THE UNIVERSITY OF CHICAGO

EXPERIMENTAL DEVELOPMENT TOWARDS THE BEACON PROTOTYPE ARRAY AND THE RADIO NEUTRINO OBSERVATORY IN GREENLAND

A DISSERTATION SUBMITTED TO
THE FACULTY OF THE DIVISION OF THE PHYSICAL SCIENCES
IN CANDIDACY FOR THE DEGREE OF
DOCTOR OF PHILOSOPHY

DEPARTMENT OF PHYSICS

BY
DANIEL SOUTHALL

CHICAGO, ILLINOIS
DECEMBER 2022

To my buddy, Nicholas Bertram. I couldn't have wished for a better friend to take my first steps into the fields of physics and astronomy with. I miss you.

TABLE OF CONTENTS

LIST OF FIGURES

LIST OF TABLES

ACKNOWLEDGMENTS

Thank you to my thesis advisor, Abigail Vieregg, for continually being a positive driving force in my life as I worked towards this dissertation. Thank you also to Stephanie Wissel, who in many ways was also my advisor. Without either of you I would not have gained the competence and confidence I have throughout my PhD. Thank you as well to my thesis committee members: Dan Hooper, Mel Shochet, and Scott Wakely. To Cosmin Deaconu, who served as a helping hand whenever it was needed, thank you for constantly displaying the embodiment of curiosity and expertise. Thanks also to Eric Oberla for enabling all of my experimental efforts. I would like to thank Dan Smith for being a constant source of inspiration, displaying all the positive traits any Dan should aspire to. Thank you also to all collaborators on the BEACON and RNO-G experiments, as well as the staff at WMRC.

My eternal gratitude to Kaeli Hughes, with whom I shared an office, a research group, and a friendship. Thank you to all of my friends in Chicago, especially Lucas Beaufore, Michael Hank, Liza Mulder, and Louis Varriano. I would like to give a special thank you to all of the guys I've spent countless nights gaming with on Discord. Your friendship has been a constant reminder that there are more important things in life than work. I would like to thank my parents, who taught me the value of kindness, a sense of humour, and persistence, all of which they needed to display frequently in raising me. Thank you also to my brothers, and friends back home. I regret that geography keeps us apart, but I love you all.

To my Love, Tracy. Thank you for sharing everything with me, and letting me share everything with you. You and Brisket are my family.

ABSTRACT

The field of experimental ultra-high-energy (UHE) neutrino physics has seen significant expansion in the past decade, with ongoing developments towards new experiments such as the Beamforming Elevated Array for COsmic Neutrinos (BEACON) as well as the Radio Neutrino observatory in Greenland (RNO-G). These experiments aim to probe production mechanisms by measuring the flux of astrophysical and cosmogenic UHE neutrinos, as well as to provide new information of neutrino cross sections at the highest energies. I discuss my role in the development, deployment, and data analysis efforts for the BEACON prototype array, which was installed at Barcroft Station in California in 2018. BEACON is designed to detect radio emission from upgoing air showers generated by UHE tau neutrino interactions in the Earth. This detection mechanism provides a measurement of the tau flavor flux of cosmic neutrinos. The BEACON prototype is at high elevation to maximize effective volume and uses a directional beamforming trigger to improve rejection of anthropogenic background noise at the trigger level. In discussion of BEACON I present details of the radio frequency environment observed by the prototype instrument, and categorize the types of events seen by the instrument, including a likely cosmic ray candidate event. In addition to BEACON I also discuss my work on RNO-G, which seeks to measure neutrinos above 10 PeV by exploiting the Askaryan effect in neutrino-induced cascades in ice. I present work towards a robust Monte Carlo simulation which was used in the early planning stages of RNO-G. I also discuss the RNO-G horizontally-polarized antenna design and outline the prototyping and development process from which they are a result.

CHAPTER 1

INTRODUCTION

Since humanity first looked up and questioned what they saw, the study of the universe beyond Earth has been a field dominated by light-based astronomy. By studying the photons generated in the cosmos we can learn of their origin, and the physics present at their genesis. However, in modern astronomy the picture is now much more dynamic; we can now view the cosmos with telescopes designed to observe messengers beyond just light. A variety of telescopes are now operational, each highly specialized to measure additional messengers such as gravitational waves, cosmic rays, and neutrinos. With the advent of multi-messenger astronomy each sub-field of observational astronomy has a role to play. In this thesis I focus on experiments within the field of neutrino astronomy, a field which has seen significant progress over the last few decades.

1.1 Neutrino Astronomy

Neutrino astronomy both leverages and laments over the key property of the neutrino: they only interact with the weak force and gravity. The advantage of this feature is that neutrinos do not interact with matter readily, and thus do not scatter as they travel from source to telescope. This gives them a long attenuation length in space and makes them ideal for pointing to the true source direction of their emission. This small interaction cross section with matter also means that detecting neutrinos is extremely difficult, as they only weakly interact with any detector volume one can construct. Unlike light, which readily interacts with the materials of the telescopes designed for detecting it, neutrinos can easily pass through mountains, with only an extremely small fraction of neutrinos stopping to acknowledge the presence of the matter. Overcoming this is the challenge neutrino astronomers face, and many interesting solutions have been proposed and implemented.

Neutrinos are one of the elementary particles listed and described in the standard model. The defining property of these spin-1/2 particles is that they interact exclusively through the weak interaction and gravity. This in-turn means that their interactions with atoms (which make up nearly all of the human experience) occur exclusively through rare interactions with the proportionately small nuclei of those atoms. Further, this results in a particle that is so hard to directly detect that it was initially only theorized to exist by Pauli to explain how beta decay is capable of conserving momentum and spin when the clearly observable particles did no such thing. The full reaction was given by Fermi as:

$$n \to p^+ + e^- + \overline{\nu}_e \tag{1.1}$$

wherein an anti-neutrino is produced as a neutron undergoes beta-decay via the weak force, converting into a proton while emitting the lepton pair of an electron and an anti-neutrino. This interaction shows one of the many ways in-which a neutrino can be produced; further modes of production are described in the following sections.

1.1.1 Solar Neutrinos

The many decades of research that followed the initial proposal of the neutrino showed its prevalence in essentially all nuclear processes. The expectation of neutrinos originating from astronomical sources then becomes immediately obvious, when one considers that every star in the universe is undergoing a lengthy exercise in converting hydrogen nuclei to successively heavier and more complex nuclei, creating an extensive and constant bath of neutrinos passing through every portion of space every instance. The relative rarity of neutrino interactions with matter results in their emission often taking a significantly more direct route from production to observation, unlike light which must fight the stochastic timeline of Brownian motion to escape the star in-which it was produced. The neutrino generally travels from the core of a star all the way to free space without any significant interactions. Should the trajectory of the neutrino intersect with the Earth it may continue undeviated through the Earth as well.

Neutrino astronomy's first major experimental success came with the Homestake experiment, which aimed to measure neutrinos which were theorized to be produced during nuclear fusion within the Sun. This experiment was built between 1965 and 1967; the main operating principle consisted of putting a massive detector volume (378 000 liters of ^{37}Cl, 615 metric tons) deep into the Earth's crust (1478 meters). Neutrinos interact with the chlorine isotopes through the inverse beta process and produce ^{37}Cl:

$$^{37}\mathrm{Cl} + \nu \rightarrow e^{-} +^{37}\mathrm{Ar} \tag{1.2}$$

The concentration of Argon isotopes in the volume could be measured through radiochemistry techniques to determine how many neutrinos interacted with the volume. The size of the volume compensated for low interactivity of neutrinos, and the depth of the experiment ensured that only neutrinos could penetrate deep enough through the Earth's crust to hit the detector, minimizing backgrounds. The size of the experiment was chosen to achieve a reasonable rate of neutrino observations based on the existing expected flux. With the 615 metric tons of ^{37}Cl the expected rate of neutrino captures was 8 ± 4 [1].

The initial rate measurements of the Homestake experiment infamously gave rise to the "Solar Neutrino Problem", wherein the expected flux of neutrinos was ∼3x larger than the measured rate [2, 3, 4]. A flurry of activity on both the theoretical and experimental side of the problem followed, with neutrino flavor oscillations being theorized as one possible explanation [5] (discussed more in Section 1.1.2). It wasn't until large water-Cherenkov detectors came online that the theory was confirmed, with the first evidence for oscillations coming from atmospheric neutrino measurements made with by Superkamiokande [6]. Figure 1.1 shows their result. These measurements demonstrated a deficit in the atmospheric muon neutrinos $\nu_\mu \leftrightarrow \nu_\tau$ oscillations.

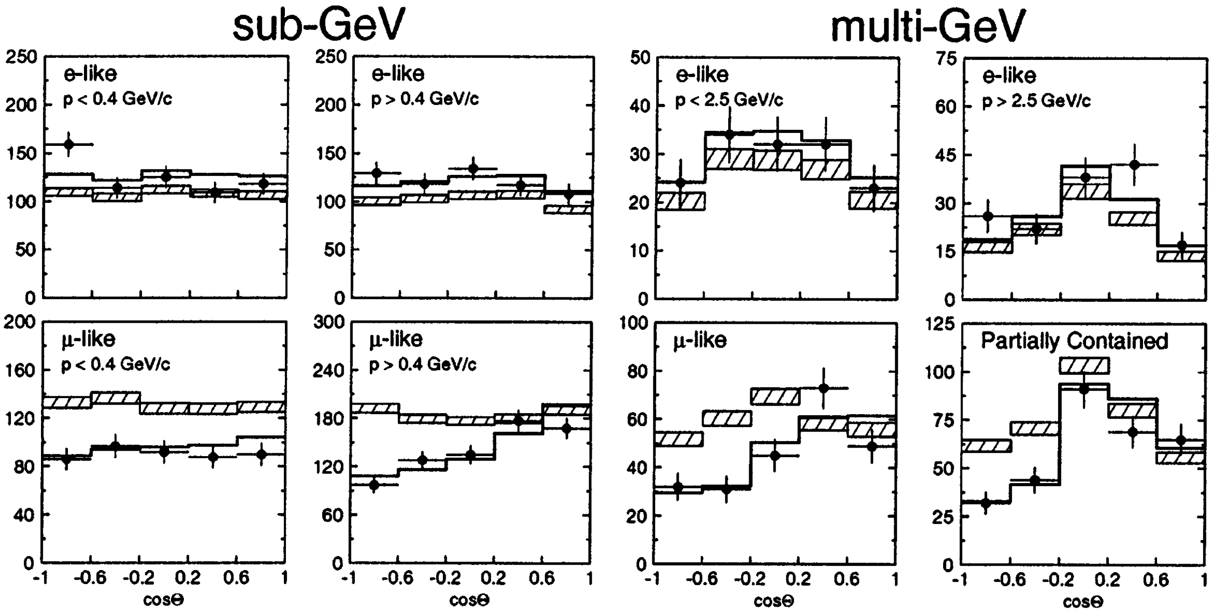

Figure 1.1: Zenith angle distributions of μ-like and e-like events for sub-GeV and multi-GeV data sets. Upward-going particles have $\cos\theta < 0$ and downward-going particles have $\cos\theta > 0$. Sub-GeV data are shown separately for $p < 400$ MeV/c and $p > 400$ MeV/c. Multi-GeV e-like distributions are shown for $p < 2.5$ and $p > 2.5$ GeV/c and the multi-GeV μ-like are shown separately for fully-contained and partially-contained events. The hatched region shows the Monte Carlo expectation for no oscillations normalized to the data live time with statistical errors. The bold line is the best-fit expectation for nm $\nu_\mu \leftrightarrow \nu_\tau$ oscillations with the overall flux normalization fitted as a free parameter. Figure and caption from Reference [6].

The finalization of the discovery of neutrino oscillations and the solution to the Solar Neutrino Problem came from the Sudbury Neutrino Observatory (SNO), which was designed to measure the flux of neutrinos produced from the ^{8}B β^+ decay, which dominates the high-energy portion of the solar neutrino spectrum [7, 8]. Specifically, SNO is capable of measuring both the total neutrino flux (through analyzing events within the detector associated with neutral-current and elastic-scattering reactions) and the electron neutrino flux (through analyzing events within the detector associated with charged-current reactions). With this information the collaboration was well equipped to measure discrepancies between the two, and managed to provide conclusive evidence of neutrino oscillation in solar neutrinos in 2004 [9]. Section 1.1.2 discusses neutrino oscillations in further detail.

1.1.2 Neutrino Oscillations

The discovery of neutrino flavor oscillations showed that neutrinos are produced exclusively in a state corresponding to one of the known lepton families of either electron, muon, or tau neutrinos, however each of these lepton flavors (ν_e, ν_μ, ν_τ) exist as a superposition of mass eigenstates (ν_1, ν_2, ν_3). The probabilistic portion of the neutrino that exists in each mass eigenstate varies as the neutrino propagates. This relationship between mixing of mass states and the lepton neutrinos can be described by the unitary matrix known as the Pontecorvo-Maki-Nakagawa-Sakata (PMNS) matrix, U:

$$\begin{bmatrix} \nu_e \\ \nu_\mu \\ \nu_\tau \end{bmatrix} = U \begin{bmatrix} \nu_1 \\ \nu_2 \\ \nu_3 \end{bmatrix} \tag{1.3}$$

U is a 3x3 unitary matrix that can be parameterized in terms of four degrees of freedom: the mixing angles θ_{13}, θ_{23}, and θ_{13}, as well as the Charge Parity (CP) violating phase, δ_{CP}. This parameterization is often written as:

$$U = \begin{bmatrix} 1 & 0 & 0 \\ 0 & c_{23} & s_{23} \\ 0 & -s_{23} & c_{23} \end{bmatrix} \begin{bmatrix} c_{13} & 0 & s_{13}e^{-i\delta_{\text{CP}}} \\ 0 & 1 & 0 \\ -s_{13}e^{-i\delta_{\text{CP}}} & 0 & c_{13} \end{bmatrix} \begin{bmatrix} c_{12} & s_{12} & 0 \\ -s_{12} & c_{12} & 0 \\ 0 & 0 & 1 \end{bmatrix} \tag{1.4}$$

with $c_{ij} = \cos\theta_{ij}$ and $s_{ij} = \sin\theta_{ij}$.

Using the assumption that the momentum of the neutrino is much larger than the mass, the state of a neutrino after travelling distance L can be represented as plane wave solutions to Schrödinger's equation:

$$|\nu_i(L)\rangle = e^{i\frac{m_i^2 L}{2E}} |\nu_i(0)\rangle \tag{1.5}$$

where this formula is represented using so-called “natural units”, which set $c = 1$, $\hbar = 1$. Here E is the energy of the wavepacket, and m_i is the mass of the neutrino eigenstate.

This assumption of small neutrino mass matches all currently available observations of neutrinos, however, may not hold for sterile heavy neutrinos which are theorized. The takeaway illustrated by the assumption holds in either case: the frequency of variations in probability for a neutrino to be in a mass eigenstate depend on the mass of the eigenstate. This is what allows for the dominant mass state to fluctuate as a neutrino oscillates, and thus for a neutrino emitted as one lepton flavor to be detected as a different flavor at some distant detector.

Neutrinos are only expected to be produced in the ν_e and ν_μ flavors for astrophysical and cosmogenic sources (discussed more in the following sections), however, flavor oscillations over the relevant astrophysical baselines should result in an observed flavor ratio flux at Earth of 1:1:1 [10]. In Section 3 I discuss the BEACON experiment, which is a neutrino observatory designed to be sensitive exclusively to the τ flavor of neutrinos. As the expected flux of neutrinos is 1:1:1, such an experiment should see a sensitivity-corrected flux that is 1/3rd that of all-flavor experiments. Any deviations in that could indicate new physics pertaining to neutrino oscillation, or even indicate variations from predicted ν_τ cross-sections at the highest energies.

1.2 Ultra-High Energy (UHE) Neutrino Astronomy

The understanding of the fundamental nature of neutrinos and the standard model that was obtained as part of the solar neutrino campaign shows the value in studying these particles with the lens of astronomy. One of the greatest advantages of studying neutrinos and creating neutrino telescopes is revealed when considering their place in the experimental astronomy landscape. As described above, astronomy in the current decade is defined by efforts towards multi-messenger astronomy, with each messenger particle providing a different method to study both those messengers and the astronomical objects and mechanisms that produce them.

When studying the Universe at ultra-high energies (UHE) in excess of 10^{17} eV this breadth of options becomes complicated however, as the universe begins to become opaque to particles interacting electromagnetically with dust and matter along the line of sight. Figure 1.2 illustrates this opacity for various messengers at various distances and energies. Above 10^{12} eV photon messengers (γ) will begin interacting with cosmic microwave background (CMB) photons and will be attenuated through pair production:

$$\gamma + \gamma_{\text{CMB}} \rightarrow e^{+} + e^{-} \tag{1.6}$$

At energies in-excess of 10^{20} eV UHE cosmic rays (UHECRs) will also undergo interactions with CMB photons. This attenuation mechanism is referred to as the GZK (Griessen, Zatsepin, Kuzmin) cutoff [12, 13] and is discussed further in Section 1.2.3, as the particles produced in this interaction are a potential source of neutrinos. At lower energies cosmic rays are prone to significant deviations as they propagate astrophysical baselines due to electromagnetic interactions with the intermediate dust, debris, and fields; this makes them imperfect narrators of their source direction, especially at high energies where they start interacting and these deviations turn to full attenuation.

Thus, to study the properties of the universe in the UHE regime we must turn to either gravitational waves or neutrinos. Though the universe is transparent to gravitational waves at all energies [14], they only carry information about the gravitational interactions at the source, and cannot provide direct information about the particle physics that governs astronomical objects.

Thus at the highest energies and distances, neutrinos stand out as the messenger of choice. Moreover, studying these UHE particles also provides a measurement of interaction cross sections at center-of-mass energies not achievable by current or planned collider experiments,

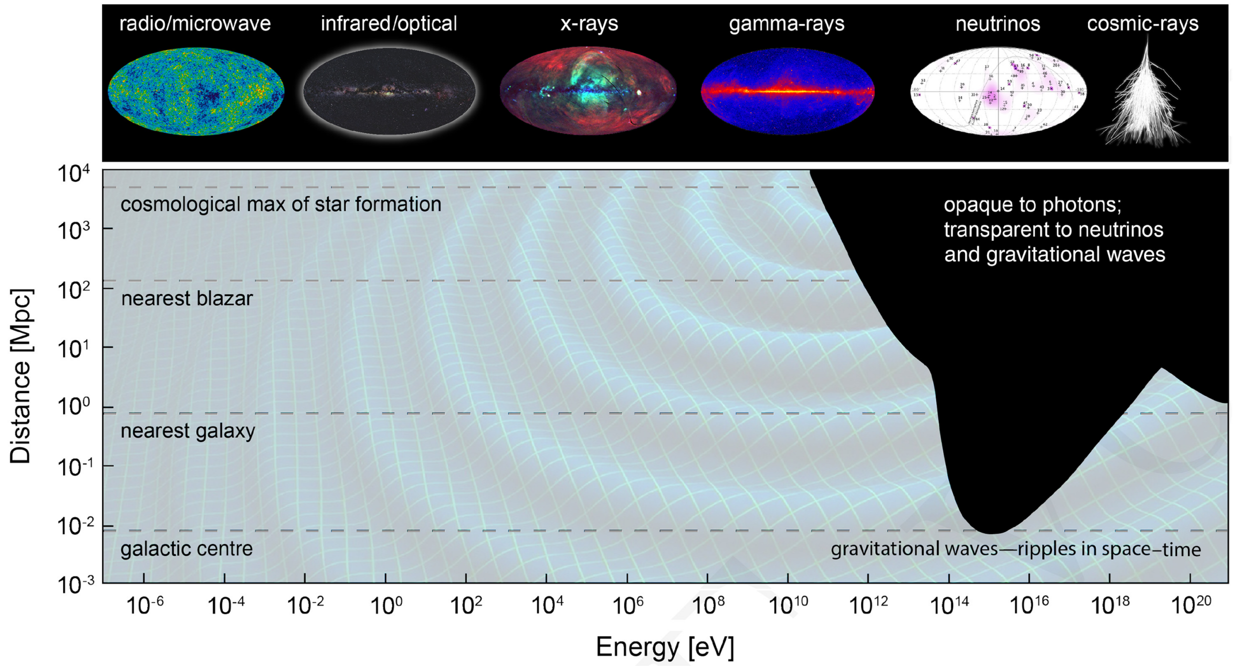

Figure 1.2: Distance horizon at which the Universe becomes optically thick to electromagnetic radiation. While lower-energy photons can travel to us from the farthest corners of the Universe, the highest energy photons and cosmic rays are attenuated after short distances, obscuring our view of the most energetic cosmic events. In contrast, the Universe is transparent to gravitational waves and neutrinos, making them suitable probes of the high-energy sky. Radio/microwave image, credit: ESA/DLR/Ducris, CC BY-SA 3.0 IGO. Infrared/optical image, credit: Axel Mellinger, www.milkywaysky.com. X-rays image, credit: X-Ray Group at the Max Planck-Institut fur extraterrestrische Physik (MPE). Gamma-rays image, credit: NASA/DOE/Fermi LAT Collaboration. Neutrinos and cosmic-rays images, credit: IceCube. Figure and caption from Reference [11].

and has the potential to reveal new physics [15, 16, 17, 18].

Solar neutrinos were previously discussed as one source candidate for neutrinos, however, when discussing UHE neutrinos they are an irrelevant source due to not producing neutrinos at sufficient energies. For higher energies we must instead turn our attention to “astrophysical” (Section 1.2.1) and “cosmogenic” (Section 1.2.3) neutrinos.

1.2.1 Astrophysical Neutrinos

Astrophysical UHE neutrinos are most like the solar neutrinos, as they are also generated at the source rather than through an intermediate interaction like cosmogenic neutrinos. This means they are produced at or near the most extreme objects in the universe, and carry with them the potential for understanding those objects. Figure 1.3 shows an overview of the various searches for high energy particles like gamma rays, neutrinos, and cosmic rays; the included red curves show the abundance of source classes predicted for astrophysical high energy neutrinos.

The increased amount of information gained through multi-messenger events is invaluable, and has already had a significant on pinning down potential source candidates for the flux of neutrinos observed at Earth. One of the major success of multi-messenger astronomy followed an alert initiated by the optical observations of Super Nova 1987A (SN1987A), which lead to searches by several neutrino detectors. Following the initial burst in 1987 excesses in neutrinos associated with SN1987A were measured by the Kamiokande II detector [34], the Irvine-Michigan-Brookhaven (IMB) water Cherenkov detector [35], and the INR Baksan Underground Scintillation Telescope [36]. Neutrinos are an expected by-product of the formation of neutron stars during the stellar collapse, where neutrons are generated from the constituent electrons and protons under the extreme pressures:

$$e^- + p \rightarrow n + \nu_e \tag{1.7}$$

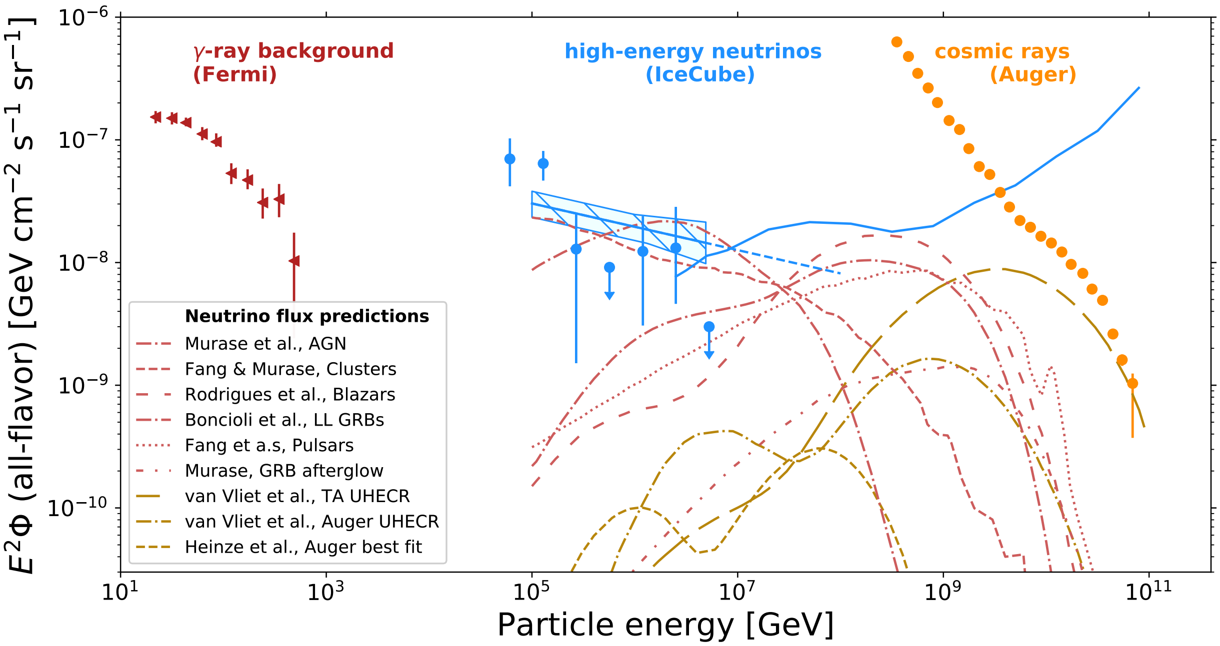

Figure 1.3: A multi-messenger view of the high-energy universe, inspired by [19], showing the science reach for radio detection of neutrinos. Shown are models predicting neutrinos from sources (in red lines) [20, 21, 22, 23, 24, 25] and those from the interaction of the ultra-high energy cosmic rays with various photon backgrounds (in dark yellow lines). Overlaid are [26, 27] the γ-ray measurements from Fermi [28], the IceCube neutrino measurements and the fit to the muon neutrino spectrum [29, 30, 31], as well as the spectrum of ultra-high energy cosmic rays as reported by the Pierre Auger Observatory [32]. Figure and caption from Reference [33].

Though the observations of SN1987A are high energy, they were not yet direct evidence of neutrinos in the UHE regime. Despite this, they introduce the promising foundation for understanding high energy phenomena in the universe using neutrino telescopes. The abundance of neutrinos observed allowed for a direct measurement of so-called neutrino light curves, which show the time variation in the neutrino spectrum following the collapse [37, 38].

The origin of astrophysical UHE neutrinos is still an open question, however, higher energy neutrinos have been observed in multi-messenger events using the IceCube observatory, which has shown promising correlation between neutrinos (IceCube-170922A) and the blazar TXS 0506+056 [39]. Blazars are active galactic nuclei (AGN) (which consist of supermassive black holes and their accretion disks) which have magnetically powered relativistic jets which serve to accelerate particles in the direction of the Earth. Additionally, there have been recent promising discoveries of a diffuse flux of astrophysical neutrinos [40, 41] and a candidate for an extra-galactic source of neutrinos [39, 42], which could all be potential sources for UHE astrophysical neutrinos.

1.2.2 Ultra-High-Energy Cosmic Ray (UHECR) Generation

The strongest evidence for UHE neutrinos comes from measurements of the cosmic ray flux in the UHE regime. Figure 1.4 shows the experimental landscape for UHECR measurements. The measurements of cosmic rays at energies up to 10^{20} eV proves the existence of phenomena in the universe capable of accelerating particles up to ultra-high energies. In particular, beyond just demonstrating the capability to produce UHE particles, measurements of particles above $10^{19.5}$ eV is of interest for UHE neutrinos. As will be discussed later, UHECRs with these energies are believed to interact with CMB photons to produce UHECRs (discussed in Section 1.2.3).

The actual mechanism within candidate sources that results in UHECRs is also an open

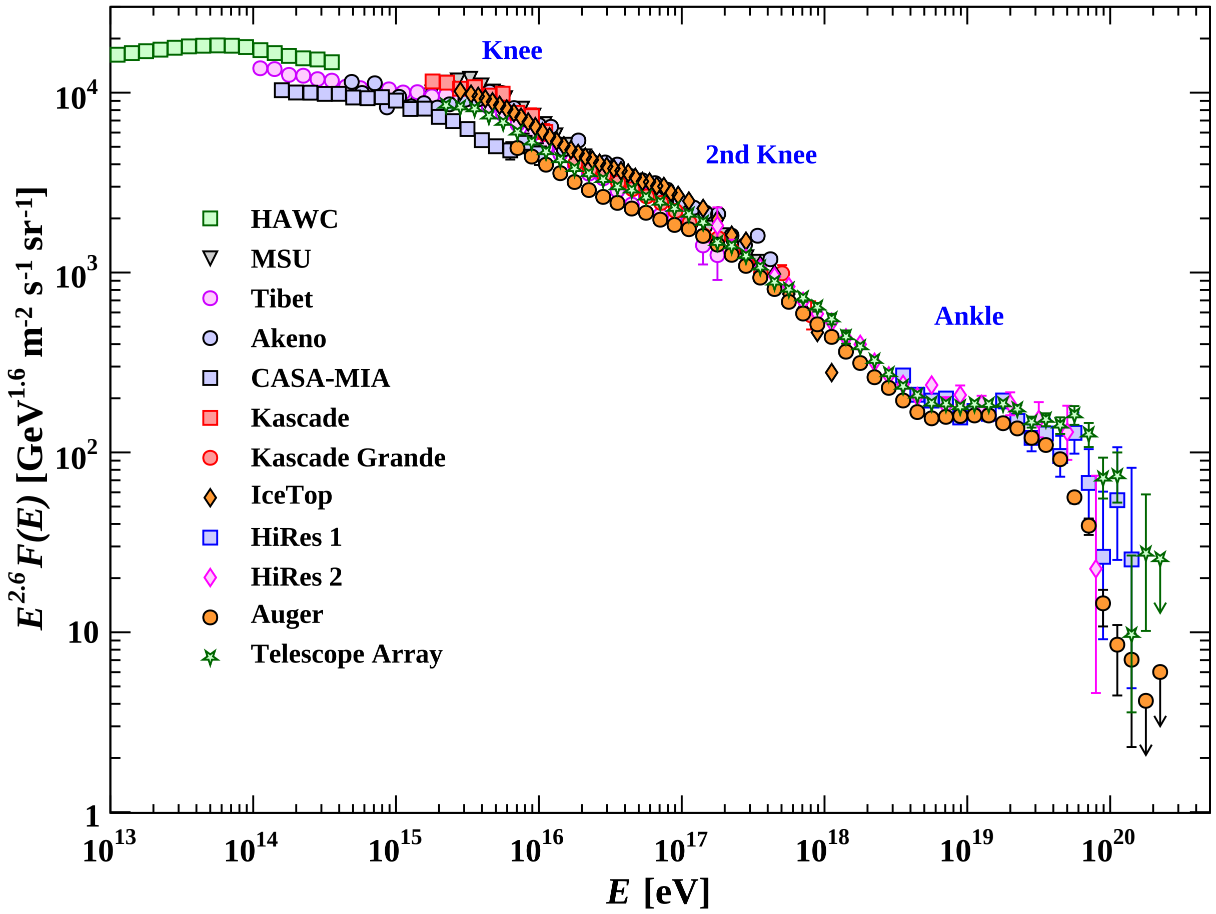

Figure 1.4: The all-particle spectrum as a function of E (energy-per-nucleus) from air shower measurements. Plot from Reference [43], which also lists the source contributions for each curve.

question, with leading theories favoring “bottom-up” models which describe the direct boosting of charged particles to UHE scales through processes like Fermi acceleration [44, 45, 46], caused by the intense magnetic fields surrounding objects like AGN [47, 48], gamma-ray bursts (GRBs) [49], pulsars [50], flat-spectrum radio quasars (FSRQ) [51, 52, 53], tidal disruption events [54], neutron star mergers [55], etc. The UHE charged particles are likely directly accelerated themselves, however, “top-down” explanations also exist to suggest that they could result as daughter particles of the decays of previously accelerated super-heavy particles [56, 57].

Some of the main mechanisms for boosting the charged particles are summarized by Reference [45] and listed below and shown in Figure 1.5:

1. One-Shot Acceleration: Continuous acceleration via an ordered magnetic field produced by objects such as blazars, black holes, or neutron stars.
2. Diffusive Acceleration: Acceleration from successive interactions with high-intensity magnetic fields.
    (a) First-Order Fermi Acceleration: Boosts obtained from the particle interacting with magnetic inhomogeneities resulting from both the leading edge and trail of stellar shock waves.
    (b) Second-Order Fermi Acceleration: A series of accelerations resulting from collisions with interstellar clouds. Each collision can result in a magnetic-mirror-like reflection of the particle off the fields of the collision, resulting in a boost and overall increase in particle momentum and energy.

1.2.3 Cosmogenic Neutrinos

Cosmogenic neutrinos are a category of neutrinos which result from interactions of UHECRs produced through mechanisms discussed in Section 1.2.2 with CMB photons above the GZK

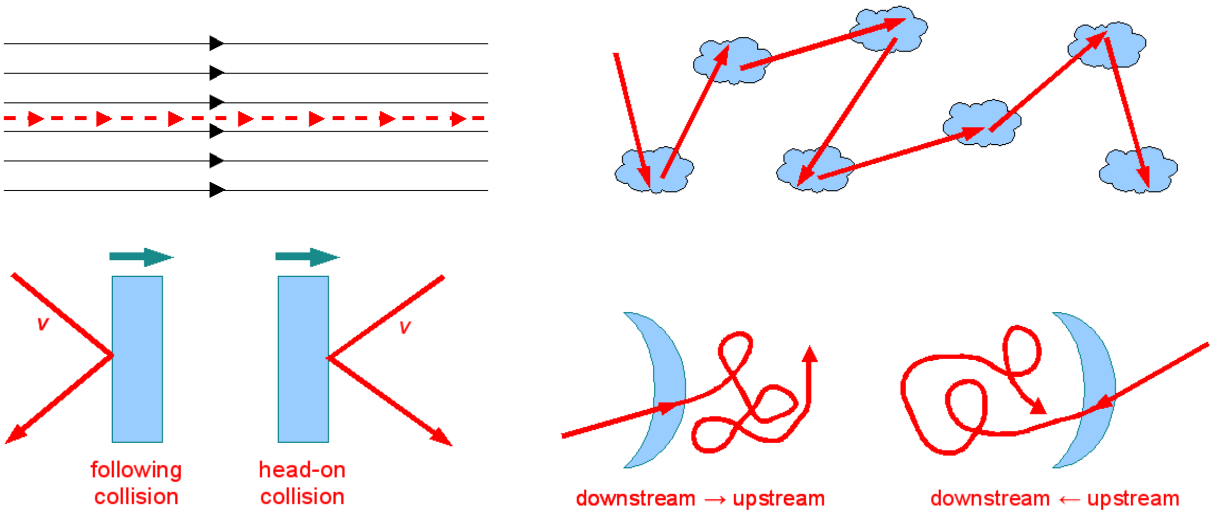

Figure 1.5: Schematic depictions of various acceleration mechanisms. Top Left: One-shot continuous acceleration in an ordered magnetic field. The maximum energy of the particle is obtained at the source from the ordered magnetic fields. Top Right: Diffusive shock acceleration. The particle undergoes a series of boosts from effects such as Fermi acceleration. Bottom Left: Second-order Fermi acceleration. The particle collides with interstellar clouds and reflects off of their magnetic fields resulting in added momentum. Bottom Right: First-order Fermi acceleration.

cutoff [12, 13]. Observations of cosmic rays above 100 EeV [58, 59, 60]) (Figure 1.4) indicate a flux of neutrinos produced through the GZK process, wherein cosmic rays undergo photon-hadron interactions through the δ-resonance which results in a chain of decays yielding a collection of particles including neutrinos [61]:

$$\gamma_{\mathrm{CMB}} + p \rightarrow \Delta^{+} \rightarrow \begin{cases} p^{+} + \pi^{0} \\ n^{0} + \pi^{+} \end{cases}$$

$$\begin{aligned} &\pi^{+} \rightarrow \nu_{\mu} + \mu^{+} \rightarrow e^{+} + \nu_{e} + \nu_{\mu} + \overline{\nu}_{\mu} \\ &n^{0} \rightarrow p^{+} + e^{-} + \overline{\nu}_{e} \end{aligned} \tag{1.8}$$

Though many candidates exist, the specific source of either astrophysical or cosmogenic neutrinos is generally difficult to determine from neutrinos alone, as observations of these high-energy neutrinos are expected at extremely low rates, however by combining neutrino measurements with observations of other coincident high energy messenger particles it is possible to strengthen the constraints on source candidates. Such searches are part of so-called multi-messenger astronomy, which promises to define the field of astronomy over the next several decades. Figure 1.3 shows the sensitivity of various experiments that are likely to contribute to multi-messenger astronomy in the high-energy regime.

With the deployment of new experiments and increased integrated observation time the UHE neutrino flux measurements will be refined, which could allow for a statistical interpretation of the source categories. Whether observed neutrinos are astrophysical or cosmogenic can be determined by interpreting the neutrino flux at various energies. Cosmogenic neutrinos serve as the baseline flux, and are believed to be a necessary flux based on current UHECR rates and standard model physics. Rates of UHE neutrinos measured in-excess of cosmogenic GZK neutrinos indicate production of neutrinos from astrophysical sources, with the exact shape of the excess determining which candidates are prevalent. If the observed rate is greatly in-excess of both cosmogenic and standard astrophysical predictions then exotic particle physics explanations are favored [62].

1.3 Radiation from Neutrino Interactions

The detection of neutrinos is an indirect process, depending not on the detection of the neutrinos or cosmic rays themselves, but rather the radio waves produced by their interactions in matter. The ability to convert radio waves into detectable oscillations in electrical current is as old as radios themselves, however our expectation of radio signals associated with neutrinos is rather modern. The mechanisms which produce the radiation that is so crucial to the field will be covered in advance in the following sections, with background on antennas and measurements of such signals covered in Appendix A and throughout the text.

1.3.1 Particle Showers

Particle showers are trails of particles produced in interactions of high-energy particles with quarks or electrons. At high energies these showers can grow in length to $\mathcal{O}$(km), and are referred to as extensive showers. These are commonly produced naturally in the atmosphere from impacting high-energy CRs. Atmospheric showers are referred to as extensive air showers (EAS). The first interaction produces many unstable secondary particles, a portion of which being neutral pions which quickly decay into photons. These energetic photons produce an excess of electrons and positrons through pair production. The effect of these accelerating charged particles is the further production of photons via bremsstrahlung radiation, the inverse Compton effect, and annihilation (in the case of the positrons). This chain reaction of particles produces a huge amount of photons which strips the atmosphere of its electrons in a wave of ionization. A self-fed cascading effect can further amplify the shower as it propagates through the air. For UHECRs these EAS can extend for kilometers through the sky and consist of billions of particles. EAS emissions have been extensively studied by numerous radio experiments (summarized by References [63, 64]).

In media denser than air (for instance ice) particle showers can still occur and propagate in much the same way, however the increased density decreases the path length of each particle (as interactions with the media are more likely). Regardless of the medium it is clear that a huge amount of photons are produced by these showers. Relevant for this thesis is the production of radio wavelength photons, which are discussed further in the following sections. EAS are particularly relevant for the BEACON experiment discussed in Section 3, which is designed to measure primarily geomagnetic radio signals produced by upgoing EAS produced by decaying τ leptons resulting from neutrino interactions in the Earth's crust. Radio-producing particle showers in ice primarily emit Askaryan radiation, which is the operating principle of the RNO-G experiment, described in Section 2. The radio emissions produced by both Askaryan radiation and geomagnetic radiation (Sections 1.3.2 and 1.3.3) are emitted in a forward boosted cone centered on the shower axis, at the same angle as Cherenkov radiation. Air shower radio signatures have been extensively studied by numerous radio experiments (see *e.g.* References [65, 66, 67, 68, 69] and References [63, 64] for recent reviews) and have been modelled at accelerator experiments [70, 71].

1.3.2 Askaryan Radiation

The flow of shower particles through matter strips the atoms in the path of their electrons, producing a core of plasma and a shower front exhibiting an excess of electrons. The time variation in electric field produced by this moving air shower produces radio emission which is polarized towards the central plasma core (Figure 1.6). This effect is known as Askaryan radiation, and was first postulated in 1961 [72], and first experimentally measured in 2001 [73]. For wavelengths greater than the dimension of the shower plasma core, the intensity of the radiation goes as ν^2 where ν is given in Reference [72] as:

$$\nu \approx \frac{n_+}{\tau_a \left(\frac{1}{T_+} + \frac{1}{\tau_-} \right)} \tag{1.9}$$

where ± refer to positrons and electrons in the material, $n_\pm$ is the average number of either, $\tau_\pm$ is lifetime before energy loss to photons, τ_a is the lifetime of the positrons prior to annihilation, and T_+ is the characteristic build-up time for the annihilating positrons (approximation made in the limit of viewing time $t \gg \tau_-$). From this it can be understood that the emitted power increases with energy (larger values of n_+) and for dense dielectric media (which are in the limit of small τ_a due to quicker interactions), though dense media also result in smaller shower dimensions meaning coherence begins at shorter wavelengths (higher frequency radiation).

Askaryan radiation is emitted at the Cherenkov angle, θ_C; for an in-ice shower where the index of refraction is $n \approx 1.7$, $\theta_C \approx 54\,\text{deg}$. Though Askaryan radiation is often thought

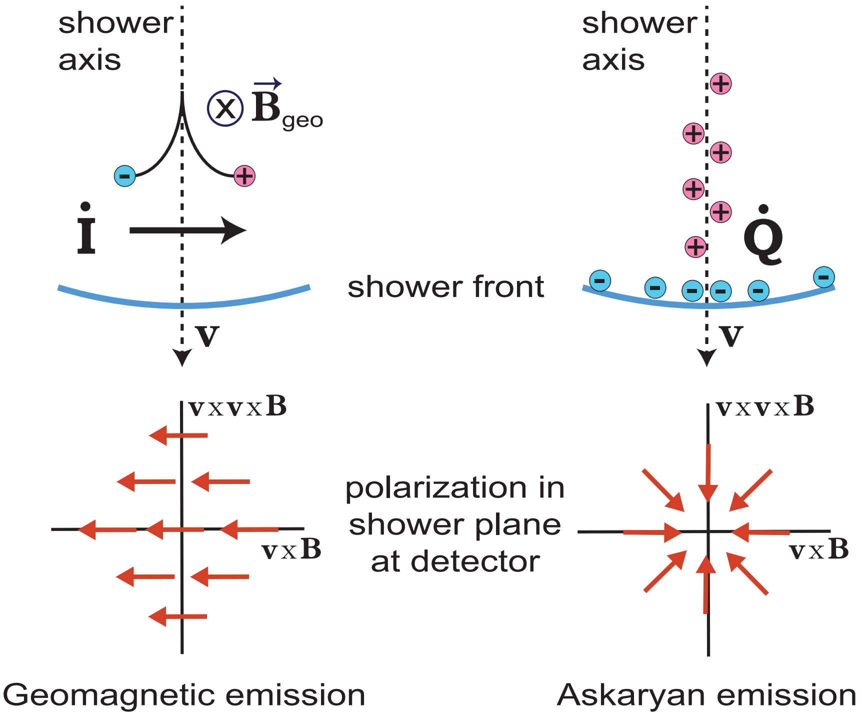

Figure 1.6: Summary of geomagnetic (left) and Askaryan (right) radiation. The geomagnetic emission is linearly polarized along the Lorentz force induced by the local magnetic field. Charged particles move under the influence of the magnetic field producing radio waves. The Askaryan emission produces radially polarized light, directed toward the shower axis. In a dielectric material a significant charge excess moves with the shower front, leaving a trail of ionized atoms near the core of the shower axis. The net effect is the emission of radio waves polarized towards the central axis. Emissions occur at many frequencies but only the radio waves (wavelengths greater than the dimensions of plasma core) add coherently in the far field, making them ideal for detecting the shower. Figure from Reference [74].

of as the radio extension of Cherenkov light (which is produced by particles moving faster than the speed of light in the medium), these shared properties are a present for any kind of coherent electromagnetic emission [63].

1.3.3 Geomagnetic Radiation

Geomagnetic radiation occurs as the charged particles interact with the local magnetic field of the shower (most often dominated by the Earth's magnetic field), where the particles experience acceleration from the Lorentz force. The deflections of the electrons and positrons are in opposite directions and induce a net current which varies as the shower develops. This flow of time varying current is the source of the linearly polarized radiation along the axis of flow. The power of this radiation increases with both the strength of the magnetic field and the duration/length of the EAS, such that highly inclined showers which spend more time in the less dense upper atmosphere will have stronger emissions [63]. Because of the dependence on the magnetic field, showers which propagate in-line with the local magnetic field are suppressed due to the projected current being nearly zero as viewed in the direction of emission (in a forward boosted cone centered on the shower axis, where θ_C is $\mathcal{O}(1\,\mathrm{deg})$ in air).

The pulses generated by geomagnetic radiation and/or Askaryan radiation are extremely impulsive, with on-cone signals having typical pulse widths of only a few nanoseconds. This results in radio signals that are extremely broadband and temporally compact. This is a key feature that is used to distinguish shower-induced pulses from anthropogenic radio signals, which are often continuous wave (CW) or narrow band.

1.4 Field Overview

The experimental landscape of UHE neutrino experiments has broadened greatly over the past decade. In Section 1.1.1 several of the experiments involved in solving the Solar Neutrino Problem were described. Each of these utilized detectors buried deep in the ground or under mountains to maintain purity of signal by shielding the main detector volume from anthropogenic backgrounds and cosmic rays. These detectors also all utilized massive volumes of matter as the main detector volume to ensure reasonable detection rates.

These two properties of "build it big" and "build it remote" are still defining characteristics of modern neutrino telescope design. Neutrino astronomy continues this tradition by utilizing radio astronomy techniques to convert glaciers and mountains into neutrino detectors. There are several classes of UHE experiments, sorted by their main detection mechanism: 1. Deep arrays (buried deep in ice or submerged in water), 2. Earth-skimming ν_τ detectors, 3. Airborne or space-borne arrays. Each category can further be broken up into optical v.s. radio arrays, with the radio arrays being targeted at UHE neutrinos and optical arrays generally being sensitive at lower neutrino energies. Figure 1.7 provides a schematic overview of the various detectors discussed in this section.

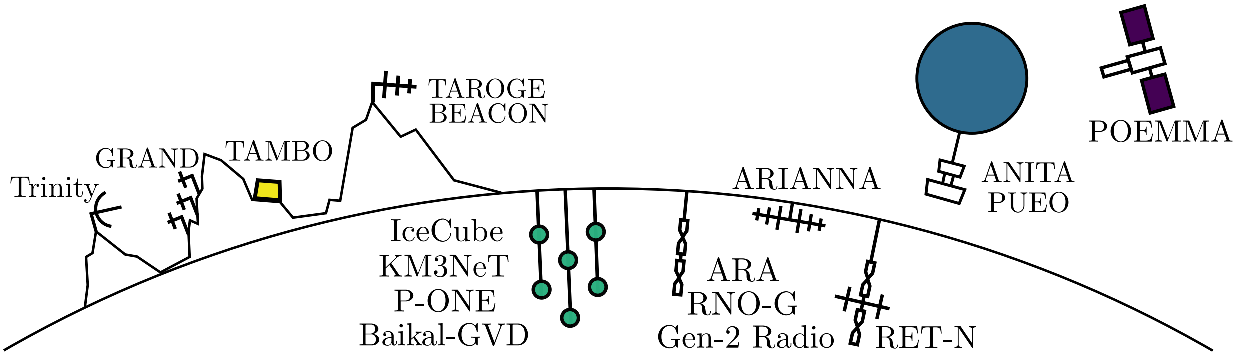

Figure 1.7: Proposed strategies to detect UHE neutrinos. The variety guarantees complementary physics opportunities. Figure and caption from Reference [18].

1.4.1 Deep Neutrino Telescopes

By far the most successful neutrino telescope in recent years has been the IceCube experiment, which is a deep array that has already been mentioned on several occasions. IceCube is a cubic-kilometer detector that consists of over 5000 digital optical modules (DOMs) buried at depths of 1450-2450 m below the South Pole. These DOMs are deployed in “strings”, with each string (86 total strings) consisting of 60 DOMs which are deployed co-linearly down boreholes. These DOMs are used to measure optical Cherenkov light produced by charged particles passing through the detector volume at speeds greater than the speed of light in ice. Other examples of optical experiments KM3NeT, P-One, and Baikal-GVD, all utilize photo-multiplier sensors similar to the DOMs, but submerged in various bodies of water throughout the world. Many of these experiments are still early in development.

The dependence on Cherenkov light means that the sensors in these experiments must be separated from each other at distances on the $\mathcal{O}(50m)$ (the absorption lengths for ice and water [75, 76]); otherwise risking a loss in sensitivity and energy reconstruction abilities, a limitation is felt strongest when attempting to measure the astrophysical and cosmogenic neutrino spectrum at UHE, where each spectra is predicted to drop off sharply [20, 21, 22, 23, 24, 25]. Thus UHE neutrino telescopes shift their sensitivity range towards the radio frequency, where attenuation lengths are $\mathcal{O}(1000m)$. This topic will be discussed in more depth in Section 2.1. The emission of radio frequency light particle cascades is discussed further in Section 1.3.

The cohort of deep in-ice UHE neutrino telescopes includes Antarctic experiments such as ARA [77] and ARIANNA [78]. ARA consists of 5 stations of deep (∼200 m) radio antennas which image the glacial ice at the South Pole. The most recently installed station, ARA Station 5, is particularly noteworthy as it utilizes an interferometric phased-array for triggering [79], which has enabled analyses to achieve the lowest threshold for a neutrino search to date [80] for an Askaryan based detector. Such a trigger will also be implemented in both of the major experiments described in Sections 2 and 3. ARIANNA is situated on the Ross Ice Shelf and maximized detector volume using only surface antennas by leveraging the reflective boundary between the ice shelf and the water underneath it. The successes of these experiments motivated the desire to expand the UHE neutrino program to the Northern hemisphere, which eventually motivated the formation of a new collaboration containing members from both the ARA and ARIANNA collaborations, the product of which is the Radio Neutrino Observatory in Greenland (RNO-G) [33]. RNO-G is still being deployed (discussed in Section 2).

Each of these experiments are radio arrays which bury antennas with the aim of measuring the Askaryan radiation produced by neutrino interactions in ice either in Antarctica or Greenland. There are also novel concepts for radio detectors such as RET-N [81], which proposes the possibility of searching for neutrino cascades with active radar techniques; this technique could have improved sensitivity over passive experiments, effectively by-passing the relatively limited detectable region that is the Cherenkov cone allowing for a wider range of detectable viewing angles. The RET-N concept has also been proposed for measuring Earth-skimming neutrinos (Section 1.4.2).

IceCube-Gen2 is the proposed expansion of the IceCube neutrino telescope, and has a planned radio component (IceCube-Gen2 Radio) which will take the lessons learned from RNO-G and extend the sensitivity of IceCube-Gen2 into the UHE regime [82]. Figure 1.8 shows the proposed footprint of IceCube-Gen2 Radio, which would consist of 200 radio stations covering an area of $\sim$500 km^2. Such an array would be a significant increase in volumetric acceptance over any current deep array, and even over a fully deployed RNO-G experiment which has a planned 35 stations and a footprint $\mathcal{O}\big(50\ \mathrm{km}^2\big)$ (RNO-G currently has 7 stations deployed following the 2022 season, with the remaining stations planned for the coming years).

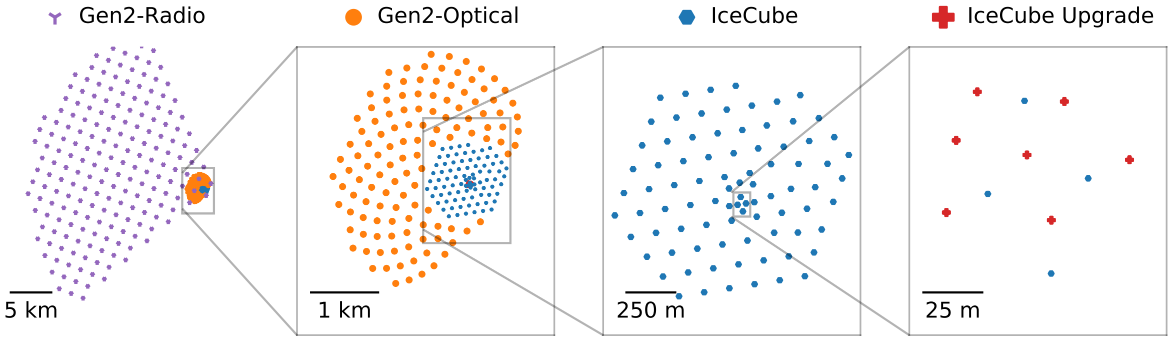

Figure 1.8: Top view of the envisioned IceCube-Gen2 Neutrino Observatory facility at the South Pole station, Antarctica. From left to right: The radio array consisting of 200 stations. IceCube-Gen2 strings in the optical high-energy array. 120 new strings (shown as orange points) are spaced 240 m apart and instrumented with 80 optical modules (mDOMs) each, over a vertical length of 1.25 km. The total instrumented volume in this design is 7.9 times larger than the current IceCube detector array (blue points). On the far right, the layout for the seven IceCube Upgrade strings relative to existing IceCube strings is shown. Figure and caption from Reference [82].

1.4.2 Earth-Skimming Neutrino Telescopes

The low cross section of neutrinos requires detectors to be large in volume and mass to ensure that neutrino interactions have tenable probabilities of occurring within the visible range of the sensors. The campaign to increase detector volume found a natural partner in glaciers and large bodies of water, as these resources provide vast and pure samples of matter which can serve as a target to induce particle cascades.

When looking for large amounts of naturally occurring dense matter as an instigator for neutrino interactions, one could also turn to the Earth itself, or more precisely the rocks and mountains which make up the Earth's crust. Attempting to monitor rock itself for neutrino interactions has obvious difficulties however, as rock is opaque to the light produced by such interactions. Earth-skimming neutrino telescopes attempt to navigate this problem by instead looking at the volume of atmosphere surrounding such massive bodies of matter, looking specifically for the decay of tau leptons in the atmosphere. At high energies, tau neutrinos interacting with the Earth via a charged current interaction can produce a tau lepton boosted enough such that it may escape the Earth and decay in the atmosphere [83, 84, 85].

Such a signal only occurs at significant levels for the tau flavor. Electrons produced in this way will readily interact with and be absorbed by the matter surrounding where they were produced, and thus do not escape the Earth's crust to be observed. Should the lepton be a muon produced by an interacting muon neutrino then the lepton can exit the Earth's crust readily, with only small radiative losses due to the muons larger mass [86, 87]. Despite escaping the Earth's crust, a muon will still have an interaction length in atmosphere of many kilometers, and thus is unlikely to interact in the lower atmosphere to create a detectable air shower. The tau lepton also has a much larger mass than the electron, and thus has no problem escaping the Earth's crust, however compared to the muon, taus has are much more prone to decaying in the lower atmosphere due to their short lifetime.

The tau lepton decay creates an upgoing extensive air shower that will produce an impulsive radio signal. The primary emission mechanism is geomagnetic radiation (Section 1.3.3), a result of the deflection of charges by the Earth's magnetic field, with contributions from Askaryan radiation [88] (Section 1.3.2). The probability that a tau lepton will exit the Earth peaks near the horizon [89].

The idea of measuring emissions from these tau leptons as a handle on tau neutrinos has been around for a while now [90, 91, 92, 84, 93], often discussed as a potential side band of existing experiments. In recent years the concept has been targeted directly as a potential mechanism around which to design neutrino telescopes. Such designs are referred to as Earth-skimming neutrino telescopes, and consist of detectors being placed on or near mountains with the goal of observing the sky for up-going particle showers produced by decaying tau leptons. The signals produced by such showers are expected to be extremely similar to those produced by down-going air showers produced by cosmic rays, however they are distinguishable by direction.

Earth-skimming telescopes provide an unambiguous measure of the tau neutrino flux. It has only been in recent years that many of the aforementioned deep neutrino telescopes have managed to distinguish events associated a the tau flavor of the neutrino (ν_T) within their data sets. The tau neutrino has a low cross section and probability of producing tau leptons, and thus is relatively difficult to measure precisely in such experiments when compared to the electron and muon flavors. As the expected observed flavor ratio flux at Earth is 1:1:1 [10], the ability to distinguish the flavors within the data can provide a key probe for understanding and testing this expectation. In addition to providing flux and flavor ratio information, such experiments provide a measurement of interaction cross sections for tau neutrinos at center-of-mass energies not achievable by current or planned collider experiments [15, 16, 17, 18],

Fluorescence telescopes such as Trinity [94, 95] aim to measure the optical Cherenkov light produced by Earth-skimming tau neutrinos. Trinity does so by monitoring mountains with Cherenkov telescopes. TAMBO [96] utilizes water-Cherenkov tanks situated within a valley to measure the particle shower directly.

Utilizing radio techniques to measure air showers has been a concept since the 1950s, with the technique being using in cosmic ray physics in the following decades [93]. Listed here are several of the experiments which aim to utilize this technique for UHE neutrino astronomy. Each of the experiments mentioned below are relatively new, with prototype efforts underway and full-scale designs outlined.

The BEACON experiment monitors the Earth's crust by situating antennas at high elevation (with a prototype currently installed in California) to achieve a large viewable horizon. This vantage point and dependence on radio signals makes the experiment prone to anthropogenic backgrounds, however the experiment utilizes a phased trigger array similar to that used in ARA Station 5 to achieve directional triggering and lower SNR thresholds despite the high rate of backgrounds. The large viewing area afforded by the high elevation allows BEACON to achieve high sensitivity with a relatively low number of antennas. BEACON is discussed further in Section 3.

TAROGE-M [97, 98] utilizes a small array of mountaintop antennas in Antarctica to measure up-going air showers. GRAND [86] utilizes thousands of antennas spread over a large area of China to observe the footprint of radio signals produced from taus leaving nearby mountains. Experiments such as ANITA [99], PUEO [100], and POEMMA [101] are also expected to be sensitive to this detection mechanism.

1.4.3 Airborne and Space-Based Neutrino Telescopes

The final category of UHE neutrino telescopes achieves high sensitivity by elevating detectors to extreme heights to achieve maximal viewing areas. Such experiments achieve sensitivity mostly in the higher end of the UHE band, as their distance from the detector volume (the Earth) means that signals must typically be of higher magnitude to be observed.

ANITA[102] is an experiment that has seen several generations of flights and has produced science in the field of UHE astronomy [103, 104, 99]. ANITA consists of a compact payload of antennas which flies above the atmosphere over Antarctica at heights of ∼35 km, looking for radio signals produced by neutrino interactions in the ice or atmosphere. Alongside constraining the UHE neutrino flux at high energies, ANITA also made observations of UHECRs during its flights via geomagnetic radiation from EAS (Section 1.3.3). Such events are visible to ANITA through reflections off of the ice, and as such have inverted polarity when compared to in-ice neutrino signals which would not undergo such a reflection.

In addition to the expected science outcomes of ANITA were observations of two so-called "anomolous" events (measured in flights of ANITA-I [105] and ANITA-III [106]), which were observed to have polarization consistent with in-ice neutrino events, but which arrived at steep angles which are expected to be heavily suppressed. These signals were unexpected, as a UHE neutrino would need to have travelled directly through the Earth (which should be opaque to neutrinos at the relevant energies) to create a shower at such a steep angle. A variety of explanations such as sterile neutrinos, dark matter, super-symmetric particles, beyond the standard model physics, etc. were all investigated by the community [107, 108, 109, 110, 111, 112, 113, 114, 115]. Alongside these explanations are several glaciology-based explanations, which propose that the signal is indeed a reflected signal, with the discrepancy in polarity being an artifact of the complexities of the Antarctic ice [116, 117].

Other airborne and space-based neutrino telescopes include PUEO [100] and POEMMA [101]. PUEO is the improved successor experiment to ANITA and which is currently under development. POEMMA takes the high elevation concept to the extreme, consisting of 2 satellite detectors which orbit the Earth looking for fluorescence signatures of EAS; POEMMA is also currently in the development stage.

CHAPTER 2

THE RADIO NEUTRINO OBSERVATORY IN GREENLAND (RNO-G)

The success of deep experiments such as ARA, ARIANNA, and RICE (Section 1.4.1) motivated the desire to expand the UHE neutrino program to the Northern hemisphere. Targeted site surveys of Greenland's ice sheet first began in 2013 for the proposed Greenland Neutrino Observatory (GNO). These surveys set out to measure the radio attenuation length, index of refraction, and general ice properties below Summit Station [118, 119] (Figure 2.1). This research station is situated atop the glacier in the center of Greenland and has an ice depth of $\sim$3000 m [120]. This massive source of naturally occurring dielectric material was an obvious fit for expansion of the UHE neutrino program into the Northern hemisphere. Though these initial surveys showed promising results, the field maintained focus on the existing Antarctic programs until later in the decade.

In 2018 members of the various collaborations encompassing the field began talks about creating a new hybrid in-ice radio array, to be named the Radio Neutrino Observatory. This array aimed combine the hardware benefits of surface detectors from ARIANNA, with the deep antenna strings of ARA, and the phased trigger system that had been developed for the ARA 5 station as well as the ANITA experiment. As is standard in the field, simulation efforts intensified to determine the optimal design of such a station, and to understand the effects of depth and ice properties on the sensitivity of such an array. Though the original conceptualization of the experiment was planned to use the existing South Pole infrastructure the concept eventually found traction for deployment at Summit Station in Greenland, being renamed to the Radio Neutrino Observatory in Greenland (RNO-G). The first 3 stations of this experiment were installed in 2021 and an additional 4 were installed in 2022 with plans for a total of 35 stations over the next few years. A schematic view of the RNO-G station layout is shown in Figure 2.2. Each station consists of 3 strings of antennas separated into

Figure 2.1: A map of Greenland, with the location of RNO-G (Summit Station) highlighted.

two categories: 1. two “support” strings which provide outlying vertically-polarized (VPol) and horizontally-polarized (HPol) antennas for direction reconstruction, and also contain a calibration pulser per string 2. one “power” string containing the main phased array trigger (similar to what was used for ARA Station 5 as mentioned in Section 1.4.1 [79]).

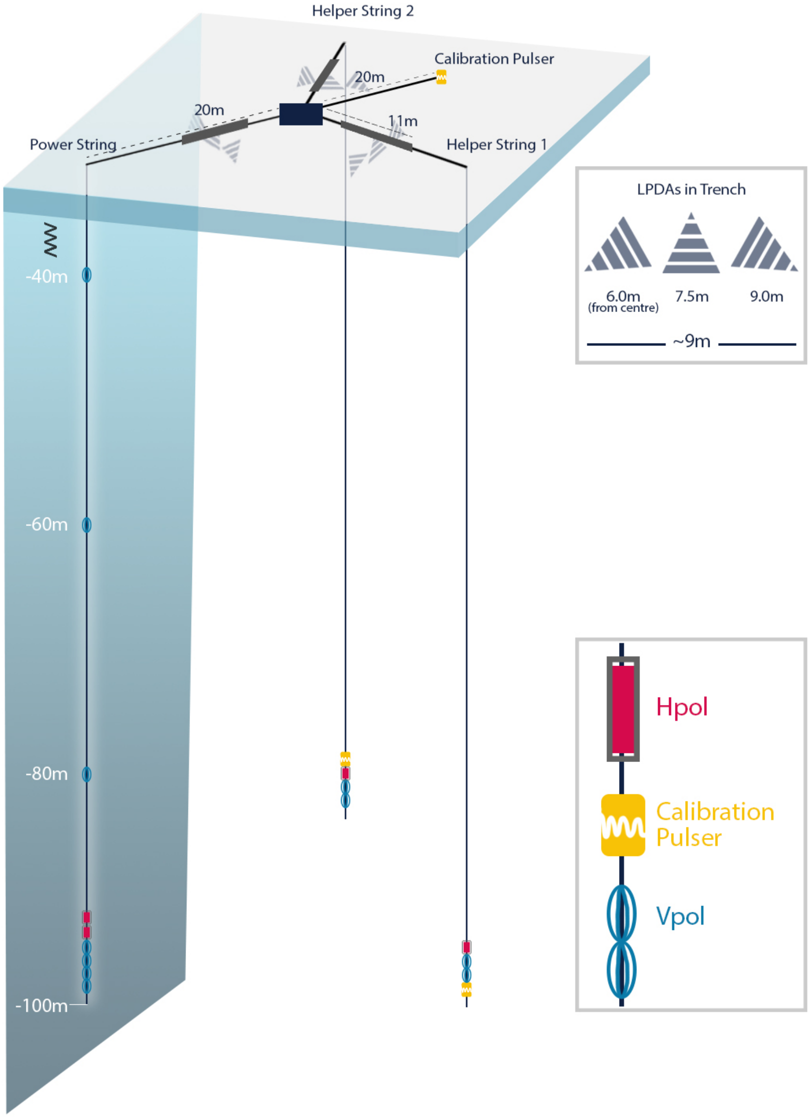

Figure 2.2: A schematic drawing of the RNO-G station layout.

This section will expand upon Section 1.4.1 and give a brief conceptual overview of in-ice UHE neutrino observatories and discuss several contributions I have made as part of my

PhD towards the RNO-G experiment. This includes the development of a custom Monte Carlo simulation package originally designed to simulate GNO and repurposed for ARA and RNO-G, as well as my efforts in developing the HPol antennas currently in-use by RNO-G.

2.1 Introduction to In-Ice Neutrino Observatories

The cohort of deep experiments described in Section 1.4.1 all aim to achieve large detector volumes by monitoring large volumes of ice or water for radiation induced by neutrino interactions. Among this cohort the most successful experiment to-date has been IceCube, which uses photo-sensitive DOMs to measure Cherenkov radiation produced by charged particles moving through Antarctic ice faster than the speed of light in that ice. The Cherenkov light that serves as the foundational measurement principle for such an experiment is in the UV and optical range, where absorption lengths for ice and water are $\mathcal{O}(50\,\mathrm{m})$ [75, 76]. The absorption length of the detected light acts as a meter stick that governs the spacing required to image the desired volume - the shorter the absorption length the more densely you must instrument it. This limitation is felt strongest when attempting to measure the astrophysical and cosmogenic neutrino spectrum at UHE, where each spectra is predicted to drop off sharply [20, 21, 22, 23, 24, 25]. This drop in the spectra means that there are less neutrinos to detect, requiring a roughly proportional increase in detector volume to achieve the same observation rate. The dense spacing required for optical experiments is thus prohibitive for measuring the UHE spectrum.

The field of UHE Neutrino Astronomy picks up the sensitivity phase space at high energies by shifting towards the radio frequency range, where attenuation lengths are $\mathcal{O}(1000\,\mathrm{m})$. Though Cherenkov light does not extend to radio frequencies with sufficient power, the emergence of additional coherent RF radiation phenomena at high energies like geomagnetic radiation and the Askaryan effect means that the showers induced by neutrinos are visible to antenna-based detectors (Section 1.3). This turn-on of radio signals conveniently enables searches for neutrinos at the same high energies that is necessary for their production. The details of Cherenkov radiation, geomagnetic radiation, and the Askaryan effect are all described in Section 1.3. Just like the optical and UV light detected by lower energy neutrino detectors, the radio frequency radiation produced by these phenomena is emitted along a cone which has maximal power at the Cherenkov angle. These radio signals are measured using arrays of radio antennas packaged into autonomously operating stations, which are equipped with power supplies and DAQ electronics to record and measure signals.

2.2 Design Principles for an In-Ice UHE Neutrino Detectors

Designing the precise layout of a station is often done by first outlining the scientific goals of the observatory. For in-ice radio neutrino observatories the most common baseline scientific goals are:

1. Direction Reconstruction: Measure the angular dependence of the flux. By understanding where these neutrinos come from, we can work towards UHE neutrinos contributing to the multi-messenger era of astronomy, adding additional pieces to the puzzle of how such high-energy particles are created. Beyond just understanding the origin of the neutrinos, directional reconstruction can be used to determine the cross sections of the particles. Neutrinos are in general considered “ghost” particles, interacting extremely weakly and infrequently, however this moniker breaks down in the UHE regime where their cross section is increased to the point that the Earth becomes opaque in most directions except glancing angles (which result in minimal integrated mass). This means that measurements of the directional dependence of detected neutrinos in the reference frame of the experiment can be used to measure how the interaction length of the neutrinos within the Earth, and thus the cross section of the neutrinos at center-of-mass energies not achievable by current or planned particle colliders.

2. Energy Reconstruction: Extend our understanding of the neutrino spectrum, extending the sensitivity to UHE neutrinos. Measurements of neutrino rates in detectors designed to be sensitive in the UHE regime allows us to test physics in the highest achievable energy regime, well beyond what is capable with engineered colliders. Spectral flux measurements provide details about the aforementioned neutrino cross section as well as sets limits on the production and propagation models of UHE particles. The currently predicted energy spectra for UHE neutrinos consists of the sum of all possible cosmogenic and astrophysical neutrino source categories, so accurate measurements of the net spectra are required to be capable of distinguishing features attributed to each source category.

With these goals in mind, we then must consider the specifics of the detectors and how to configure them into an effective array. The relatively long attenuation length of radio signals means that an antenna placed in ice can theoretically image several cubic kilometers of ice. Antennas are typically buried at depths of $\mathcal{O}(100m)$ down drilled cylindrical holes; the exact depth of the antennas is a common trade off between cost and sensitivity. The physical constraint on the extent of antennas imposed by burying them in narrow cylindrical holes results in antennas that are generally designed to have azimuthally symmetric gain patterns (Appendix A).

The data taken from a single antenna is incapable of disambiguating the various components that contribute to the strength of the observed signal, be it the energy of the neutrino-induced particle shower, how far off-cone the measured radio signal was, or from what direction within the antennas gain pattern the signal was perceived. The latter of these factors is most-often handled by situating multiple antennas nearby down the same hole, such that each antenna sees approximately the same signal, allowing for interferometric reconstruction of the source direction. Azimuthally symmetric antennas co-linearly aligned within a single hole still lack the required lever-arm to break azimuthal symmetry however, which must be done by drilling multiple holes, separated sufficiently to provide the required baselines in the horizontal plane, while being close enough to detect the same radio pulses. An array of antennas consisting of multiple strings, spread in both depth and along the horizontal plane is thus the standard configuration to create a station capable of direction reconstruction.

This general schematic for station design is effective for determining the source direction of radio pulses, however it is incomplete when attempting to determine the source direction of neutrinos. Knowing where the radio signals come from can tell you where the neutrino-induced cascade occurred within the ice but gives you a degenerate class of possible source directions due to the light being emitted along a cone. Determining the source direction of the neutrino is then a matter of determining where on-cone the signal you observed is. As discussed in Section 1.3, the polarization of these Askaryan signals has a 1-to-1 relationship with where on-cone the signal was emitted. Thus stations are designed to have both horizontally and vertically polarized antennas such that the polarization of the incident signal can be interpreted. This rough outline of a station serves as the fundamental tileable unit which is used to cover as large a volume of dielectric as possible. Stations are spaced kilometers apart with little overlap, each operating as self-sufficient experiments with complete scientific requirements and capabilities. A sparse grid of stations allows for maximal volume with minimal antennas.

Just as astronomers must precisely engineer both the sensor and its precise location near the focal plane of traditional telescopes, we must think carefully about the antennas we choose to build as well as where we position them within the ice if we wish to optimize the overall sensitivity of our detector. The first task in my PhD was to develop simulations which were used to motivate the antenna position and station design of the RNO-G experiment, the details of which are discussed in Section 2.3. I also played a key role in the engineering of the HPol science antennas used with RNO-G, which are crucial for interpreting the polarization angle and ultimately the source direction of incoming neutrino signals. I discuss the HPol antenna development project in Section 2.5.

2.3 GNOSim

2.3.1 Background

Monte Carlo simulations are a method widely used in physics to determine the outcomes of complex systems with no known analytical solution, but that are governed by relatively simple statistical laws. Simulating an entire physical system such as an in-ice radio experiment is an exercise in modular thinking and execution, breaking down complexity of the experiment into its more accessible base components, and modeling them. This involves writing scripts to place particles in ice, choosing their location, source direction, and energy all using simple appropriately chosen random distributions. Using geometry and optics we determine whether a particular event could possibly be seen by an antenna in our simulation, then combining the integrated properties of the optical path and the modeled antenna response to determine how strong that signal would be perceived, and further whether it would trigger the experiment to record and process the event. Each step is straightforward in isolation, with the combined result allowing us to understand the extremely complex ramifications of simple variations in station design.

Efforts to simulate the effective volume of the Greenland Neutrino Observatory (GNO) began in 2013 by Keith Bechtol in the production of an early version of the so-called "GNOSim". At this time the simulation could produce a simple mock radio signal at source neutrino interaction sites; this signal was then scaled using pre-calculated look-up tables which will be referred to as ray-tracing libraries. Libraries were generated for single-string co-linear antenna station configurations, consisting of simple antenna receiver models. A simple voltage trigger was in-place, with the portion of events that pass the trigger being used to determine the volumetric acceptance of the experiment (a proxy for sensitivity that will be described in more detail later). At the time this simulation was still novel, with its main benefit over competing simulations being the ability to use a generic ice model. Compared to other simulations which required simplified parameterized analytical ice models, GNOSim generated ray-tracing libraries straight from the ice property measurement curves, rather than from oversimplified integrable fits to that data.

I began work modernizing GNOSim in 2018 - updating the physics at almost every stage of the calculation, providing necessary performance improvements, and using the simulation in the early proposal phase of RNO-G to help prioritize design goals. Key among these updates were:

- Unifying the existing Antarctica and Greenland simulations
- Updating the Askaryan radiation model
- Adding realistic thermal noise, and multi-path signal support
- Adding support for generic station configurations, allowing for multiple strings, each supporting arbitrary antenna models and responses, as well as antenna orientation
- Updating the simulated DAQ to be configurable, with specific implementation to simulate the ARA Station 5 phased array beamforming trigger and DAQ
- Improving ray-tracing library generation and interpolation
- Improving surface detection in ray tracing
- Adding signal polarization calculations, ensuring accurate propagation from source to detection
- Adding a pre-trigger to exclude events early that are highly unlikely to trigger to achieve a significant speed up of the code

The adaptability of GNOSim allowed for quick iteration in station configuration design. For each configuration the all-sky water-equivalent volumetric acceptance was calculated.

This is a field-standard metric measured in units of km^3 sr$^-1$ calculated using the formula:

$$V\Omega = \frac{4\pi V_{\text{sim}}}{N} \times \sum_i \left(p_{\text{Earth}_i} \cdot p_{\text{detect}_i} \cdot \frac{\rho_i}{\rho_{\text{water}}} \right) \tag{2.1}$$

where the variables in this calculation are defined as:

- V_{sim} : The actual volume of the ice that is used in the simulation and populated with neutrino events
- N : The number of simulated neutrino events
- p_{Earth_i} : The survival probability for the neutrino passing through the Earth. This probability captures the physics which describes the opacity of the Earth and ice to neutrinos, weighting each event in the simulation by how likely such an event could actually occur. This is calculated by integrating along the chord through the Earth that represents the necessary path for a neutrino to exist at the simulated location with the generated trajectory. Density data for multiple positions along the chord is pulled from both the Preliminary Reference Earth Model (PREM)[121] and the density data for the currently used ice model. This density is combined with the neutrino cross section information[122] to calculate the net optical depth for the specific neutrino, which is then used to determine the survivability.
- p_{detect_i} : This is a weight factor that captures the probability that an event of this type would be detected. It is treated as a Boolean result in the simulation, being True if the event passes the trigger condition, and False if it does not. Whether an event triggers or not is of course only answered via the full extent of the simulation and is thus the value in this equation containing the most information, despite being only a Boolean.
- $\rho_i / \rho_{\text{water}}$: This is a ratio of densities between the ice at the interaction site and wa-

ter, effectively converting the volumetric acceptance to the standard water-equivalent metric.

GNOSim performed comparably to other contemporary simulations at the time as seen in Figure 2.3, and was used for developing the design of RNO-G in the proposal stage. Simulation efforts consolidated following the formation of the RNO-G collaboration, with other simulations continuing to progress and receive support, at which time my development of GNOSim ceased.

The details of some specific aspects of GNOSim for which I had significant contributions are outlined in greater detail in the following sections. The code for GNOSim is available at https://github.com/djsouthall/gnosim.

2.3.2 Event Generation

Event vertex center locations are generated within a simulated volume of ice which is approximated as a spherical cap, where depth is considered small compared to the radius of the sphere ($z_{\text{ice}} \ll r_{\text{Earth}}$). Using this assumption, the depth of each event, z, is sampled uniformly from bedrock to ice-air boundary. Horizontal plane coordinates x and y are generated by picking points uniformly on the surface of the spherical cap. To distribute events uniformly on the spherical surface zenith angles cannot simply be sampled uniformly due to the non-uniform (zenith dependent) surface element of the sphere $\mathrm{d}\Omega = r^2 \sin\theta d\theta d\phi$. Thus zenith angles are instead calculated as $\theta = \arccos t$ where t is uniformly distributed parameter with $t \in [-1, 1)$[125]. The azimuth angle ϕ is uniformly sampled from $\phi \in [0, 2\pi)$ radians. These are then converted to the Cartesian x and y. At this point the trajectory is also randomly generated, with unit vector angles being calculated using the same principle as populated points uniformly within the spherical cap.

The vertex position is then used to sample the ray tracing libraries for possible paths to each of the simulated antennas (discussed further in Section 2.3.3). This provides the wave

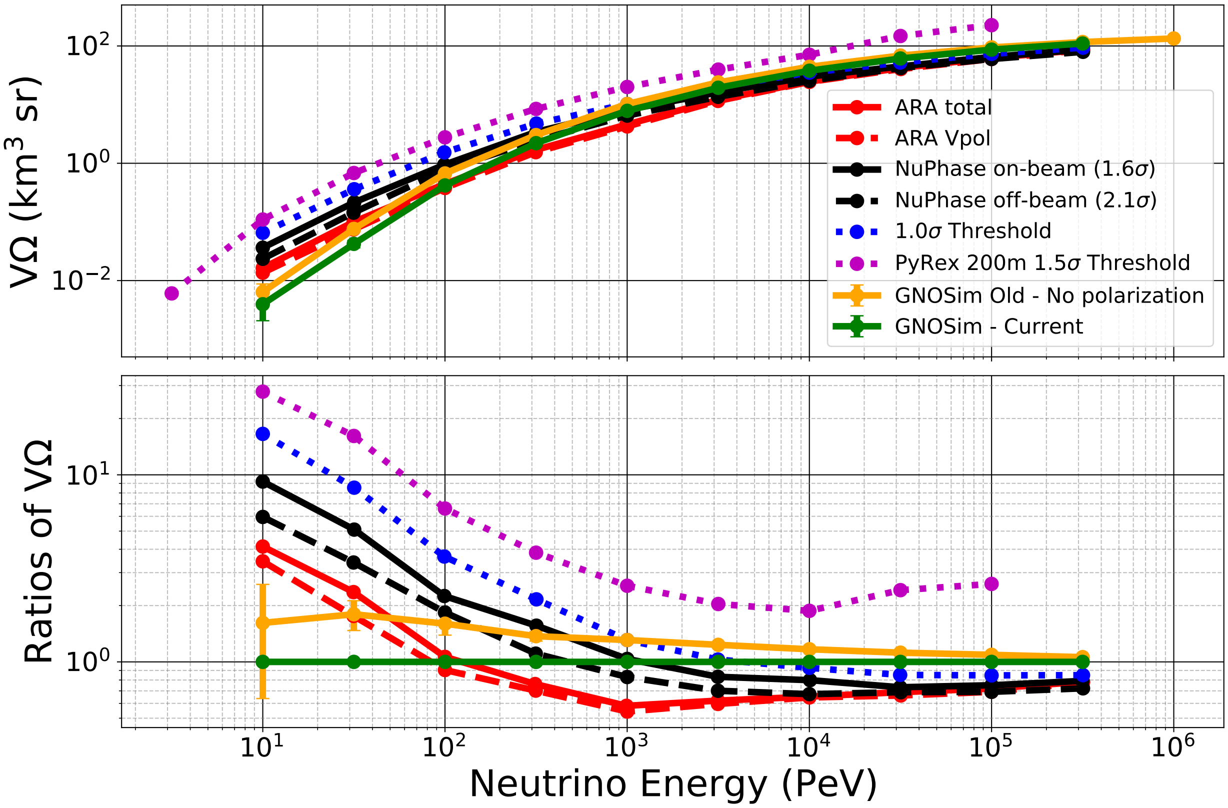

Figure 2.3: Top: Volumetric acceptance calculated for an ARA-like station as calculated using various simulations (circa 2018). Bottom: The residual when compared to an updated GNOSim which includes the updated noise, DAQ, and polarization models. The ARA, NuPhase (which refers to the ARA Station 5 phased array trigger), and 1 σ curves are all obtained from Reference [123]. The red solid line (ARA total) shows the standard ARA dual-polarization combinatoric trigger, the dashed red line is for a VPol-only combinatoric trigger, the solid (dashed) black line is for the achieved NuPhase far-field performance maximally on- (off-) beam, and the 1 σ curve represents the standard dual-polarization ARA trigger that is achievable with a 16-channel phased trigger with a 1 σ threshold (i.e. threshold at an SNR = 1). The presented PyRex [124] data was obtained from Ben Hokanson-Fasig in private communication circa 2019. The GNOSim "Old" curve represents the volumetric acceptance predicted with GNOSim prior to the addition of proper polarization handling described here. GNOSim "Current" represents the final predicted volumetric acceptance predicted by GNOSim after the inclusion of upgrades described here.

vector $\hat{k}$ for each solution, which is used to determine the observation angle of the simulated shower. This geometry goes into the Askaryan radiation model which accounts for the on-cone and observation angle geometry to calculate the perceived power of the signal for that solution (with power dropping quickly as geometry deviates from the Cherenkov angle).

The old version of GNOSim used a simple frequency domain version of Askaryan radiation [126]. Though this model gave a sense of the overall power produced and transmitted from the event vertex, it did not maintain accurate phase information for the signal which resulted in unrealistic signals in the time domain. Following the success of the ARA Station 5 phased array trigger [79] (discussed in Section 1.4.1), there was a clear desire to include such a system in any future array. As such, one of the main goals of my work with GNOSim was to refine the simulation such that an accurate representation of the ARA Station 5 phased array trigger could be implemented. Additionally, the simulation results could then be readily compared to real ARA Station 5 data as a point of reference. This goal raised the need for accurate time-domain signals such that the results of effect of adding a phased trigger to any future station configurations could be trusted.

I implemented a parameterized far-field time-domain Askaryan model [127] within the simulation. Further details about the theory of Askaryan radiation are discussed in Section 1.3. Using this model I calculate the magnetic vector potential as a function of cone observation angle θ_{obs} using:

$$\vec{A}(\theta_{\text{obs}}, t) = \hat{A}\frac{\mu}{4\pi R}\sin\theta_{\text{obs}}\int_{-\infty}^{\infty} \mathrm{d}z' Q(z') F_p\left(t - \frac{nR}{c} - z'\left[\frac{1}{v} - \frac{n\cos\theta_{\text{obs}}}{c}\right]\right) \tag{2.2}$$

where the integral is over the charge profile of the shower given by Q as a function of shower depth z'.

The charge profile Q is extremely complicated in general and requires independent energy dependent simulations to derive. For GNOSim I implemented a parameterized charge distribution profile [128]. Each event's Q is given by a normalized Γ distribution (f) defined

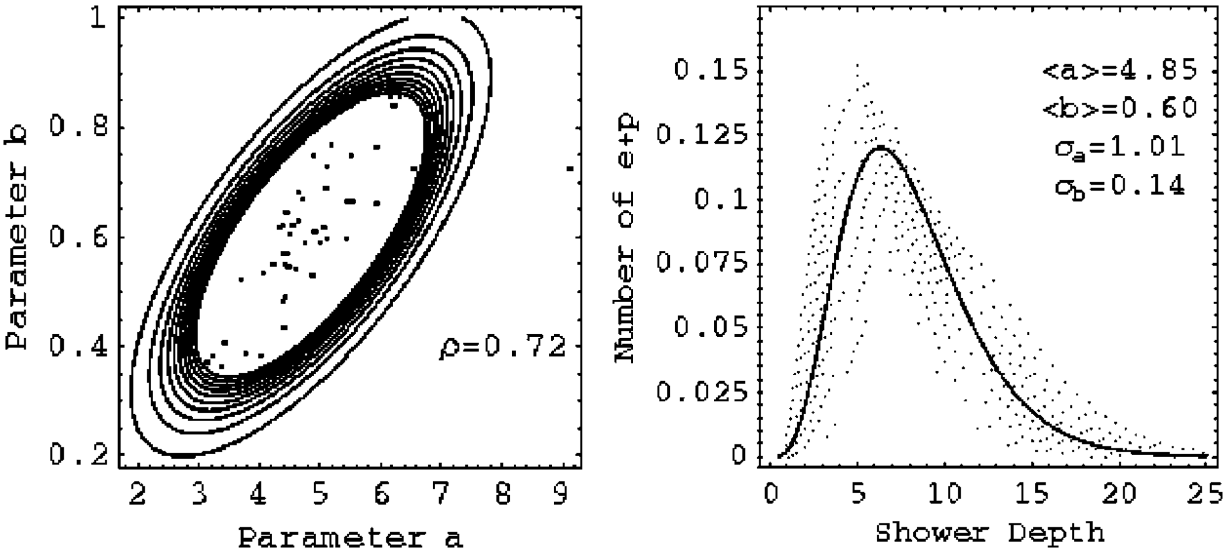

Figure 2.4: Figure and caption taken (and modified for additional context) from Reference [128]. Left: Scatter plot of the parameters a and b from the Gamma distribution fit to 50 individual shower profiles each with energy 100 GeV and 0.611 MeV threshold. The contours are from a 2-dimensional Gaussian distribution from the mean $(\langle a\rangle, \langle b\rangle)$ and standard deviation (σ_a, σ_b) obtained from the data set a, b generated as described in Reference [128]. Right: Shower fluctuations due to variation of the parameters a and b within a standard deviation. The dark solid curve is the profile with mean values of a and b. All particle numbers are normalized to 1. Shower depth $z' = \text{depth}/X_0$ is given in terms of the radiation length X_0.

in Equation 2.3, where the values of a and b are pulled from normal distributions with σ_a and σ_b being determined from GEANT simulations in the original model. Figure 2.4 is from the reference material and shows the distribution of a and b, as well as a representative charge profile distribution. The normalized Γ function is defined:

$$f(z';a,b) = b\frac{(bz')^{a-1}\exp\{-bz'\}}{\Gamma(a)} \tag{2.3}$$

where Γ is the continuous form for real a:

$$\Gamma(a) = \int_0^\infty x^{a-1}e^{-x}\mathrm{d}x \tag{2.4}$$

F_p is simplified parameterization of the shower structure containing the results radial and azimuthal integrals, and is defined as:

$$F_p\left(t - \frac{nR}{c}\right) = \frac{4\pi}{\mu}\frac{RA\left(\theta_C, t\right)}{LQ_{\text{tot}}}\frac{1}{\sin\theta_C} \tag{2.5}$$

$$RA\left(\theta_C, t\right) = -4.5 \times 10^{-14}[Vs]\frac{E}{TeV}\begin{cases} \exp\left\{-\frac{|t|}{0.057}\right\} + (1 + 2.87|t|)^{-3}) & \text{if } t > 0 \\ \exp\left\{-\frac{|t|}{0.030}\right\} + (1 + 3.05|t|)^{-3.5}) & \text{if } t < 0 \end{cases} \tag{2.6}$$

where E is the energy of the shower in TeV and t is the observer time in ns. $RA(\theta_C, t)$ is the parameterized magnetic vector potential at the Cherenkov angle. LQ_{tot} is the integrated charge profile $\int \mathrm{d}z'Q(z')$. μ is the magnetic permeability of the ice and c is the speed of light in the ice.

The magnetic vector potential in Equation 2.2 is given in terms of $\hat{A}$, which is perpendicular to the wave vector $\hat{k}$ of the emission and points inward towards the shower axis. The electric field is then calculated numerically via Maxwell's equations:

$$\vec{E} = -\frac{\partial \vec{A}}{\partial t} \tag{2.7}$$

Thus the polarization of the electric field is in the direction of $\hat{A}$ towards the shower axis.

When discussing these radio rays in ice, it is common-place to define the polarization in terms of 3 unit vectors: the wave unit vector $\hat{k}$ (the direction of the ray), the p-polarization unit vector $\hat{p}$, and the s-polarization unit vector $\hat{s}$. Both $\hat{s}$ and $\hat{p}$ are constrained to be perpendicular to $\hat{k}$, and are determined dynamically using the definitions:

$$\hat{s} = \frac{\hat{k} \times \hat{z}}{\left|\hat{k} \times \hat{z}\right|} \tag{2.8}$$

$$\hat{p} = \frac{\hat{s} \times \hat{k}}{\left|\hat{s} \times \hat{k}\right|} = \frac{\left(\hat{k} \times \hat{z}\right) \times \hat{k}}{\left|\left(\hat{k} \times \hat{z}\right) \times \hat{k}\right|} \tag{2.9}$$

where $\hat{z}$ is the upward unit vector in local station coordinates and is perpendicular to the ice surface. These are used throughout as the basis for rays in the simulation, with many values being stored for both s and p polarizations as described in Section 2.3.3.

Because ray propagation is not done on an event-by-event basis, with values being interpolated per event, this generated electric field is not literally propagated towards the antennas, but rather is scaled appropriately based on interpolated values from the ray-tracing grid. This means that all components of the electric field calculation can occur concurrently within the simulation. This process involves several convolutions, and thus is done predominantly in the frequency domain before a final Fourier transform back to obtain the processed time domain signal. To do this, the electric field is scaled by the attenuation of the ray, with individual polarizations independently being scaled based on the respective polarization's reflection and transmission coefficients (See Section 2.3.3). Signals are then scaled by the antenna-dependent gain pattern (dependent on the arrival angle at the antenna, which is stored in the ray-tracing library) and convolved with the antenna response (which was measured from real ARA antennas, however a generic response could be used). Thermal noise is then calculated in the frequency domain and added appropriately, before a final convolution with the system response (measured from the ARA station). The RMS of the thermal noise is calculated using:

$$\sigma\left(V_{\text{noise}}\right) = \sqrt{k_B \cdot T_{\text{noise}} \cdot \Omega \cdot \text{BW}} \tag{2.10}$$

where k_B is Boltzmann's constant, T_{noise} is the expected thermal noise temperate (typically set to 320 K, with the RMS being scaled to match observed RMS in ARA), Ω is the impedance of the readout (50 Ω), and BW is the system bandwidth. These values were all taken from ARA, however could be tuned to match a generic system.

This updated signal production process achieves a lot: scaling the signals, rotating the polarization appropriately, and converting signals to their final form immediately before digitization (covered in Section 2.3.4). These generated signals clearly depend heavily on the input values from the ray-tracing libraries, which will be described in further detail in the following section. Signals are ultimately processed by a simulated Station and DAQ, which are described in Section 2.3.4.

2.3.3 Ray-Tracing Libraries

The long attenuation length of radio waves in ice is a benefit, however challenges arise from the non-uniformity of the ice. The glacial ice found in Greenland and Antarctica tells the story of millennia of varying weather conditions, with varying index of refraction. Though it is impossible to fully measure all subtleties of the ice, let alone capture them in simulation, the effects of these layered variations in index of refraction are important for understanding events observed with these experiments.

A prominent example of this are the glaciology-based proposed explanations for the ANITA anomalous events (discussed in Section 1.4.3), which attributes the signals to reflections on sub-surface boundaries within the ice [116, 117]. Attempts to include complex ice models in full-experiment Monte Carlo simulations has obvious appeal, however attempts to use Finite-Difference Time-Domain (FDTD) simulations to propagate Maxwell's equations through the systems have shown the computation times to be too long for effective implementation for large volume simulations like GNOSim [129, 130].

Because of this, the standard technique used for in-ice full-experiment simulations is still ray tracing. GNOSim generates ray-tracing libraries by operating in the time-reversed regime, wherein rays are "thrown" outward from each antenna location in a defined station. By starting at the antenna only rays which are observable will be calculated. At each step the differential loss from attenuation for both polarizations are calculated alongside the transmission and reflection coefficients from the Fresnel equations, with the next step being determined via Snell's law. Snell's law is calculated between successive steps 1 and 2 via:

$$n(z_1)\sin\theta_1 = n(z_2)\sin\theta_2 \tag{2.11}$$

with the complex Fresnel coefficients for transmission (t) and reflection (r) coefficients being calculated for each of the s and p polarizations using:

$$t_s = \frac{2n(z_1)\cos\theta_i}{n(z_1)\cos\theta_i + n(z_2)\cos\theta_t} \tag{2.12}$$

$$t_p = \frac{2n(z_1)\cos\theta_i}{n(z_2)\cos\theta_i + n(z_1)\cos\theta_t} \tag{2.13}$$

$$r_s = \frac{n(z_1)\cos\theta_i - n(z_2)\cos\theta_t}{n(z_1)\cos\theta_i + n(z_2)\cos\theta_t} \tag{2.14}$$

$$r_p = \frac{n(z_2)\cos\theta_i - n(z_1)\cos\theta_t}{n(z_2)\cos\theta_i + n(z_1)\cos\theta_t} \tag{2.15}$$

here θ_i refers to the indecent angle and θ_t is transmitted angle. These values are cumulatively multiplied along the length of the ray such that more distant sources will undergo more extensive attenuation as the propagate towards the receiving antenna. The implementation of complex transmission and reflection coefficients rather than their simplified real counterparts was introduced during my addition of proper polarization handling. By using complex coefficients both the amplitude and phase information of the polarization is kept throughout the ray tracing library.

Though this depth dependence is often parameterized, in reality the dependence has many discontinuities and reflective surfaces for radio frequency light. The highest variation in attenuation length and index of refraction is observed in the first 50-100 m of ice known as the firn (Figure 2.5). The firn consists of the condensed and recrystallized snow from the most recent few seasons of snowfall.

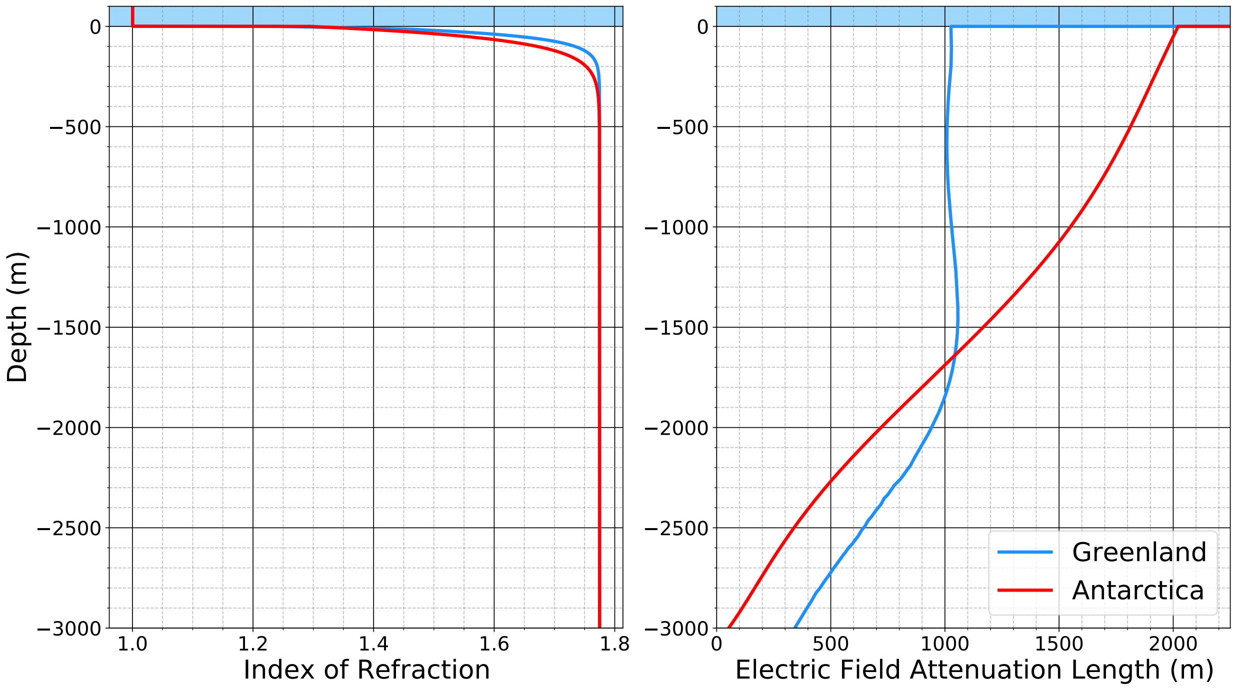

Figure 2.5: Left: The index of refraction of the main Greenlandic and Antarctic ice models used in GNOSim. Right: The attenuation length for the same models.

As radio signals propagate through ice they obey the optical laws of reflection and refraction, undergoing reflection at sharp boundaries, and undergoing gradual refraction and under the steadily varying index of refraction, slowly "bending" as they travel through the shallow layers of the ice. This often results in multiple signals paths connecting antennas buried ∼100 m in ice and radio pulses generated $\mathcal{O}(1000\text{ m})$ away: "direct" referring to the minimal distance ray tracing solution from point A to B, "reflected" referring to ray tracing solutions that depend on reflections off of any of the ice-air, the ice-bedrock, or ice-ice boundaries, to connect A to B, while "refracted" solutions refer to a situations where the ray bends heavily in the ice near the firn, inverting it's trajectory but ultimately never reflecting. This refracted solution is sometimes also referred to as a "cross" solution, as these rays are technically direct (no reflection) and can occur as a second solution path in the same locations as the shorter direct rays. These longer refracted solutions cross over the shorter direct paths creating a degenerate region where both non-reflecting solution types are valid.

GNOSim uses separate ice models for Greenland [131, 132, 133, 134] and Antarctica [131, 77] for the above calculations as necessary, with each model providing depth-dependent information for ice temperature, index of refraction, and attenuation length. Despite events being generated in 3 dimensions within the volume of ice, the fact that these models only depend on depth (z) and do not vary in the horizontal plane allows for the ray tracing libraries to be generated in cylindrical coordinates r, ϕ, z, with a fixed azimuthal coordinate ϕ (as the solution is the same for any ϕ. This heavily reduces the complexity of the simulation allowing for faster calculations. Figure 2.6 shows the stored trace positions for an example library generated for an antenna buried 200 m below the surface (where the surface defines $z = 0$). Each point in this grid contains all of the differential information necessary to describe a ray traveling along the ray from one point to the next.

The library is pre-split int the corresponding ray-tracing solution categories of "direct", "reflect", and "refract". GNOSim also supports reflections off of the bedrock layer below the ice, effectively doubling the number of solution categories, however this will not be further described for simplicity. For each library a convex hull is generated (See Figure 2.6). When an event is generated, it will see full signal interpolation calculations for each hull it is within, with the resulting waveforms being summed at the antenna with the appropriate timing offset such that multi-path solutions can be reconstructed. Each value describing the physical propagation of a radio signal from source to antenna is derived via interpolation of these ray tracing libraries.

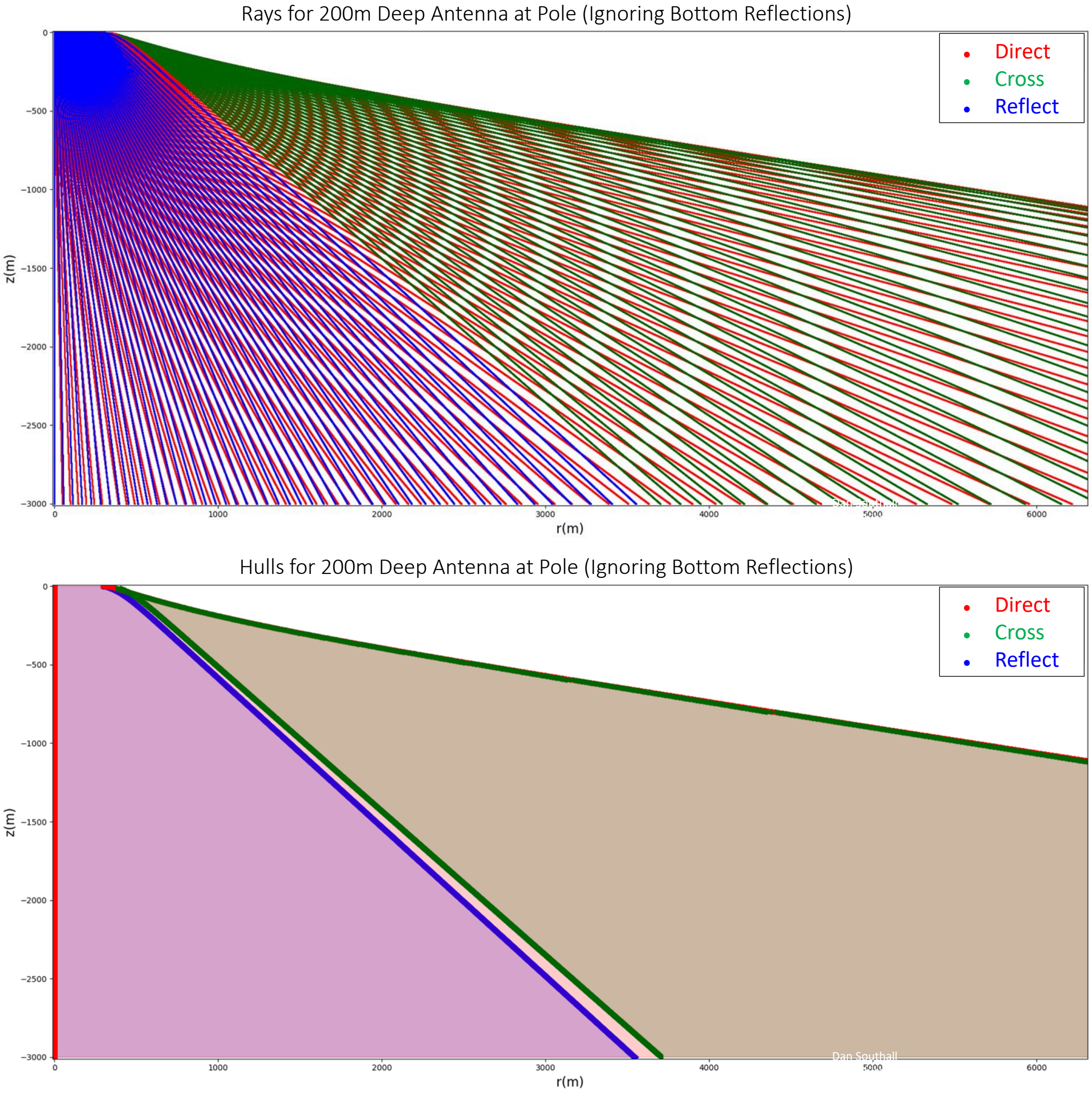

Figure 2.6: GNOSim ray tracing rays (top) and corresponding hulls (bottom).

One major bug that was present when I first began work on GNOSim was an obvious striation which arose from the simple linear interpolation of neighboring rays. This was first noticed by comparing the residual in arrival time difference between two antennas when compared to the expected uniform medium plane wave time delays. Signal arrival timing is one of the values that is stored for each point on the ray tracing grid, and thus is prone to this interpolation bug. Interpolation against the grid must be performed for every value and is one of the most time-consuming portions of the code, mitigating the problem by increasing the number of rays or with different simple interpolation methods were attempted. Increasing the ray density smoothed over the problem without solving the root cause of the behavior and does so at significant computational cost. A 3-point Delauney triangle grid was generated overlaying the grid, which was used to calculate barycentric coordinates which were used to weight 3-point interpolation. Though this significantly reduced the saw-tooth behavior from the original linear interpolation with small increases in computation it was still deemed insufficient. Ultimately the time cost of cubic interpolation was justified, however as compensation multi-threading support was added to the grid interpolation section of the code.

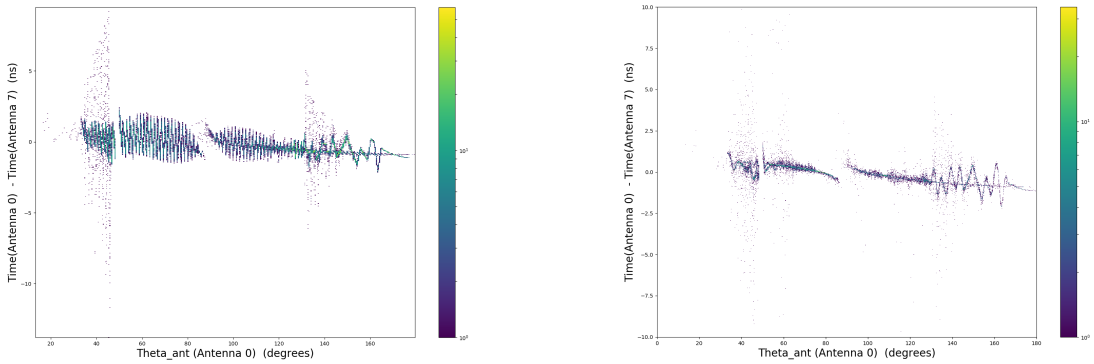

Figure 2.7: Residual in arrival time difference between two antennas when compared to the expected uniform medium plane wave time delays as function of zenith angle at the antennas. Though this plot has many features, the key feature resulting from interpolation is the saw-tooth pattern that is most visible for zenith angles near 70 degrees. Left: The residuals for 3-point barycentric interpolation. Right: The residuals for cubic interpolation.

Still visible in the right-hand portion of Figure 2.7 is large scale variations for both small and large zenith angles. These timing delays were determined to occur in reflected rays, resulting from poor surface detection in the ray tracing algorithm. An adaptive time step was implemented within the ray-tracing algorithm such that regions of significant variations in index of refraction were sampled more finely. Additional boundary identification was added, with time steps being chosen near a boundary specifically to sample with a specific tolerance of the boundary. Figure 2.8 shows the before (left) and after (right) of this improved surface detection.

2.3.4 Station Design

One of the key goals of updating GNOSim was to implement the phased-array trigger system that was deployed by ARA Station 5. This trigger is theorized to improve trigger thresholds by a factor of $\sqrt{N_{\text{antennas}}}$, where N_{antennas} is the number of antennas phased and summed within the trigger string [123]. When working towards proposing a new experiment like RNO-G it would be essential to demonstrate the effectiveness of such a system, and to better understand the effects of antenna spacing and the number of antennas in the phased array. This section will describe my efforts to expand the capabilities of GNOSim to be functional for a generic station configuration (beyond just a single string), as well as the implementation of the simulated ARA Station 5 DAQ.

A station class was developed which enables arbitrary placement of antennas within a given station. Each antenna could support a separate gain pattern, antenna and system responses, and physical orientation. Figure 2.9 shows a station layout that was made to match the ARA Station 5 configuration, with central phased-array string as well as the outlying reconstruction antennas array.

Sections 2.3.2 and 2.3.3 describe how the electric field is calculated for each antenna. These signals are digitized at 1.5 GSa/s with a 7 bit dynamic range giving a possible output adu (analog-to-digital) unit range of $\text{Range(adu)} \in [-2^{\text{bits}-1}+1, 2^{\text{bits}-1}] = [-63, 64]$. Values

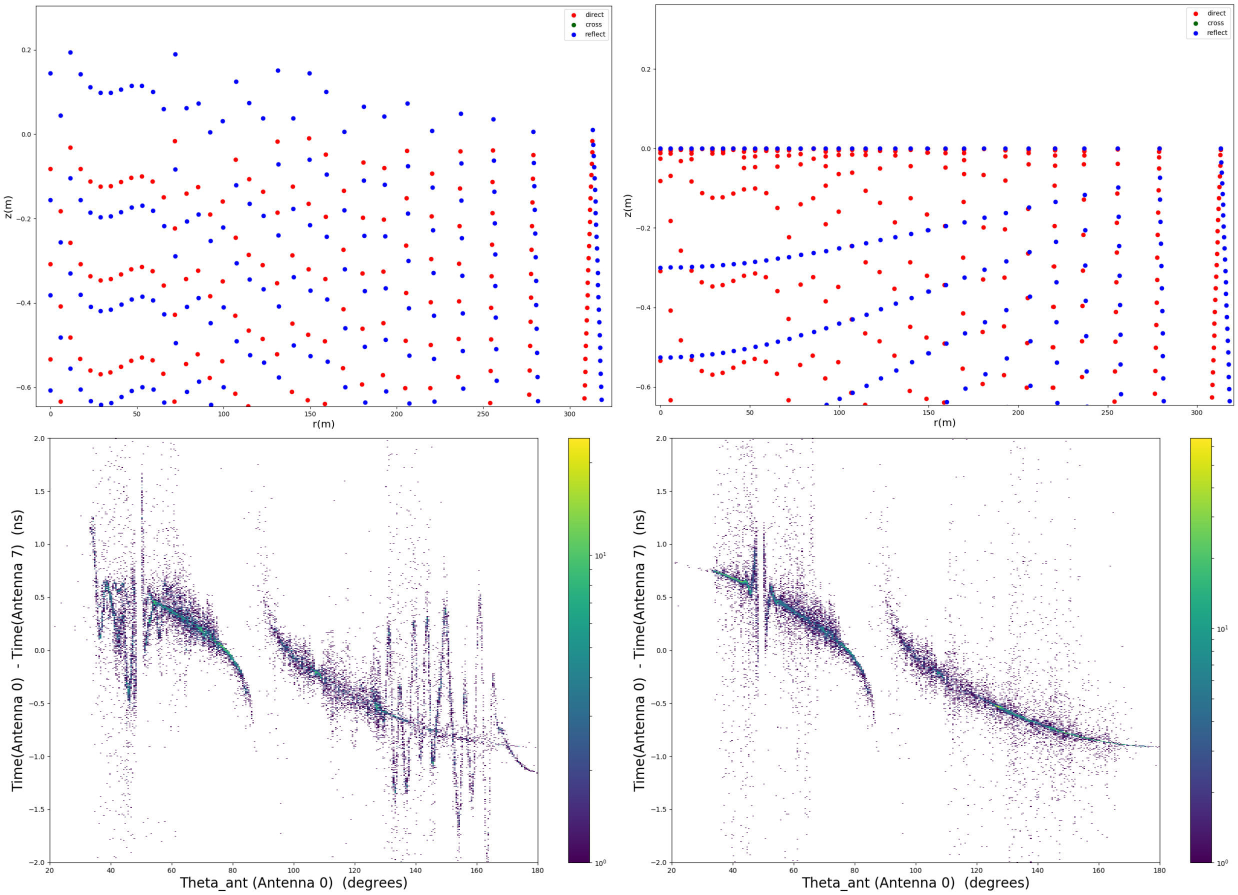

Figure 2.8: Top: Ray tracing solution points before (left) and after (right) the surface detection algorithm was implemented. Bottom: Residual in arrival time difference between two antennas when compared to the expected uniform medium plane wave time delays as function of zenith angle at the antennas. Though this plot has many features, the key one features that result from the poor surface detection are the large oscillations visible in the left plot, that have disappeared after the fix (seen on the right). The remaining gaps and features in this plot are attributed to transitions between solution type hulls. Under infinitesimal spacing of rays the separation between hulls would be a smooth transition, however with computational limitations these gaps persisted.

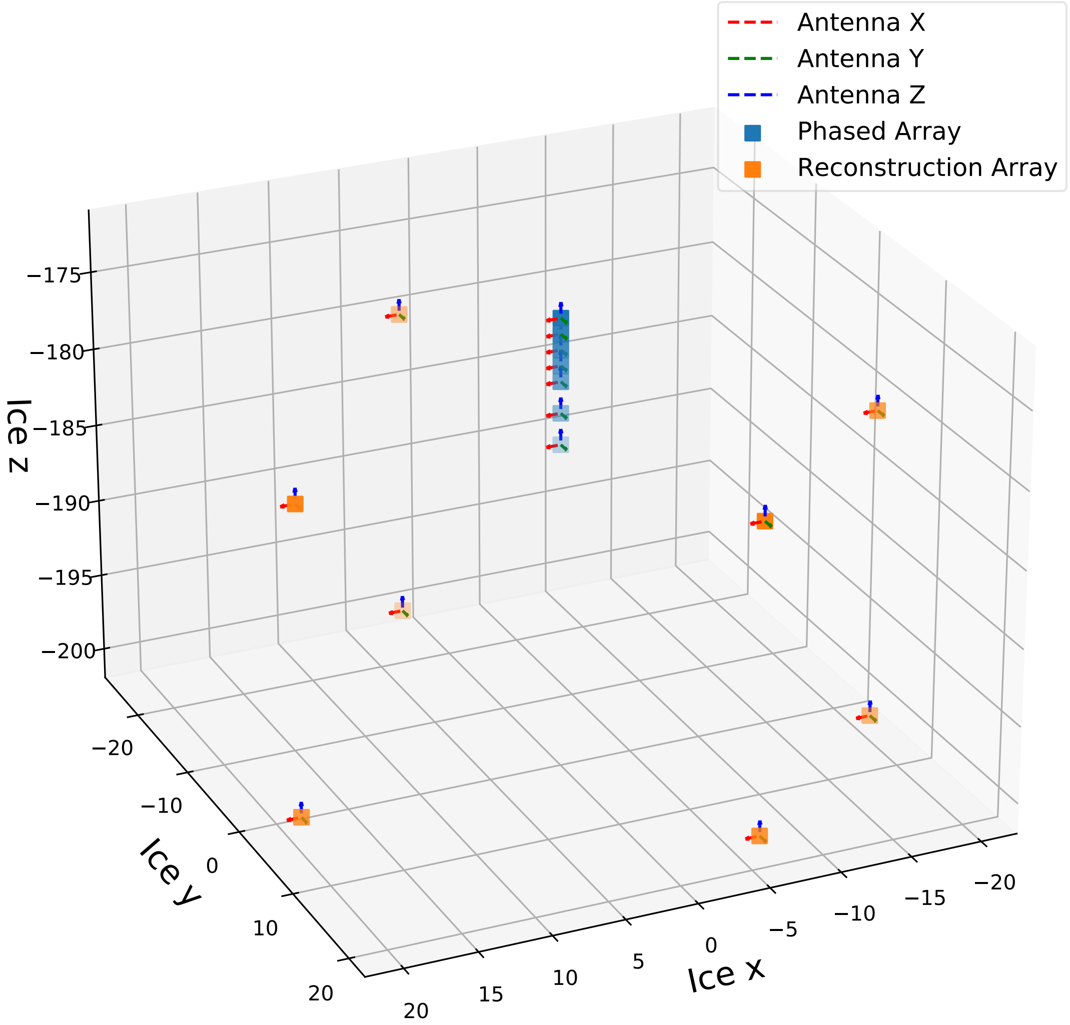

Figure 2.9: GNOSim station designed to match the layout of the ARA Station 5. The local antenna-dependent Cartesian coordinate basis are overlayed on each antenna to show their orientation. Antennas within the central blue string are flagged as being part of the phased array and are used in trigger calculations. Signals are generated and stored for each antenna for each event.

outside this range are referred to as saturated, and snap the maximum or minimum digitizer value. Figure 2.10 shows a signal before and after digitization.

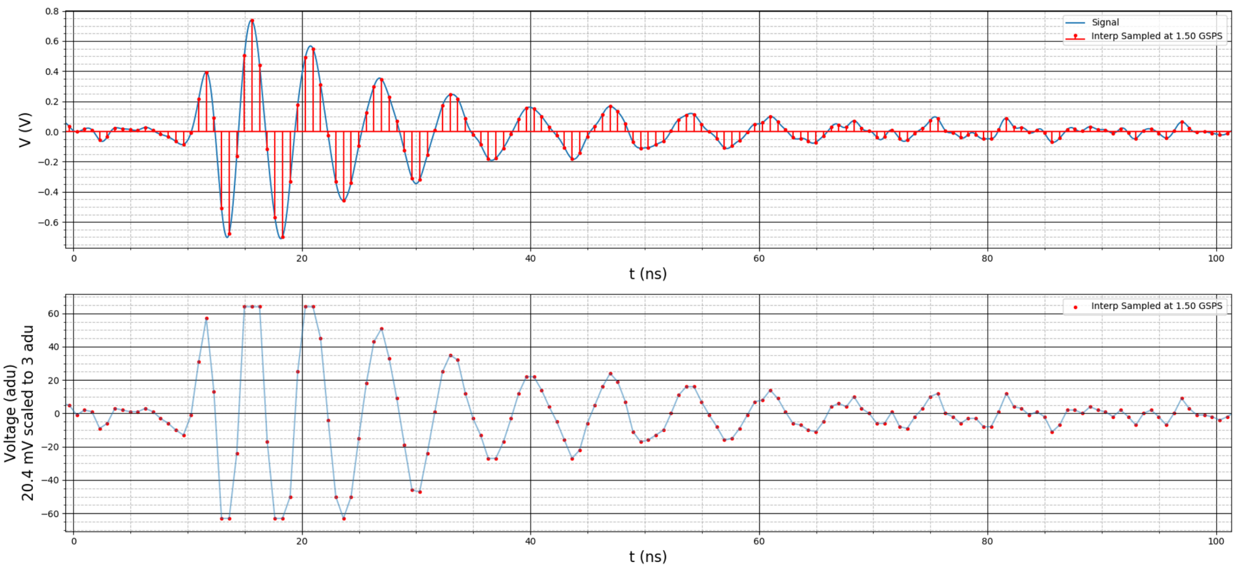

Figure 2.10: An example saturating digitized signal from GNOSim.

Signals from each channel are then processed with a simulated phased-array trigger. The details of the phased array algorithm is described in Reference [123] and with a very similar implementation discussed in Section 3. Briefly, the phased trigger array is a method of using interferometry of multiple signals at the trigger level to determine roughly the source direction of the signal based on a set of predefined expected directions known as “beams”. Each beam has a corresponding set of time delays, which are used to delay waveforms the appropriate amount to counteract any misalignment that would be expected for a plane wave arriving from that beam’s direction. These delays mean that the beam closest to the actual arrival direction of the signals will see the individual waveforms aligned. Signals are summed in each beam, with aligned signals resulting in coherent summing and a boost in amplitude of N_{ant} (while the noise of these signals only adds as $\sqrt{N_{\text{ant}}}$). The power (in arbitrary units) is then taken by squaring the summed signals. A 16 sample window then combs the power summed trace, returning the sum of each window in 8 sample steps.

The net effect of this algorithm is a boost in SNR of $\sqrt{N_{\text{ant}}}$, with the important added benefit of beam-dependent trigger thresholds. In the real world these thresholds will be set for each beam using a noise-riding threshold such that a desired global trigger rate is achieved. In simulation this is typically simplified, and a single representative trigger threshold is chosen and applied to all beams. Figure 2.11 shows an event with and without noise that has been digitized. The right side of the figure shows the resulting traces from each beams power sum, with very clear spikes in power corresponding to each of the direct and refracted ray tracing solutions for that were possible for this signal. If the power of any beam in the right-side plot exceeds the set trigger threshold, then $p_{\text{detect}_i} = 1$ for that event, whereas an event which does not trigger will be given a value of $p_{\text{detect}_i} = 0$.

As stated, the goal of GNOSim was to help understand how various station design decisions could impact the sensitivity of the proposed experiment. Using the implementation of stations above, tests could be performed not only on the effect of antenna positions, but also on the effect of variations to the DAQ and trigger algorithm. Beyond just calculating the volumetric acceptance for various designs, GNOSim could be used to understand the types of events which triggered (or did not), which could be used to motivate changes. One interesting feature that arose when expecting events which pass the trigger can be seen in Figure 2.12.

The top half of Figure 2.12 shows the frequency and polarization (as measured in the local coordinate system of the antenna) of signals which arrive at the antenna as a function of the arrival direction zenith angle at the antenna. An interesting feature is visible for events arriving at angles just about 25° zenith. This feature shows a large reduction in the number of events arriving with vertical polarization (shown by bunch of events at polarization angles of 90°). This is a result of the fact that most rays which arrive at the antenna from this direction have undergone reflections with ice-air boundary at Brewster's angle, the unique angle where the reflection of p-polarization light is completely suppressed (Figure 2.13).

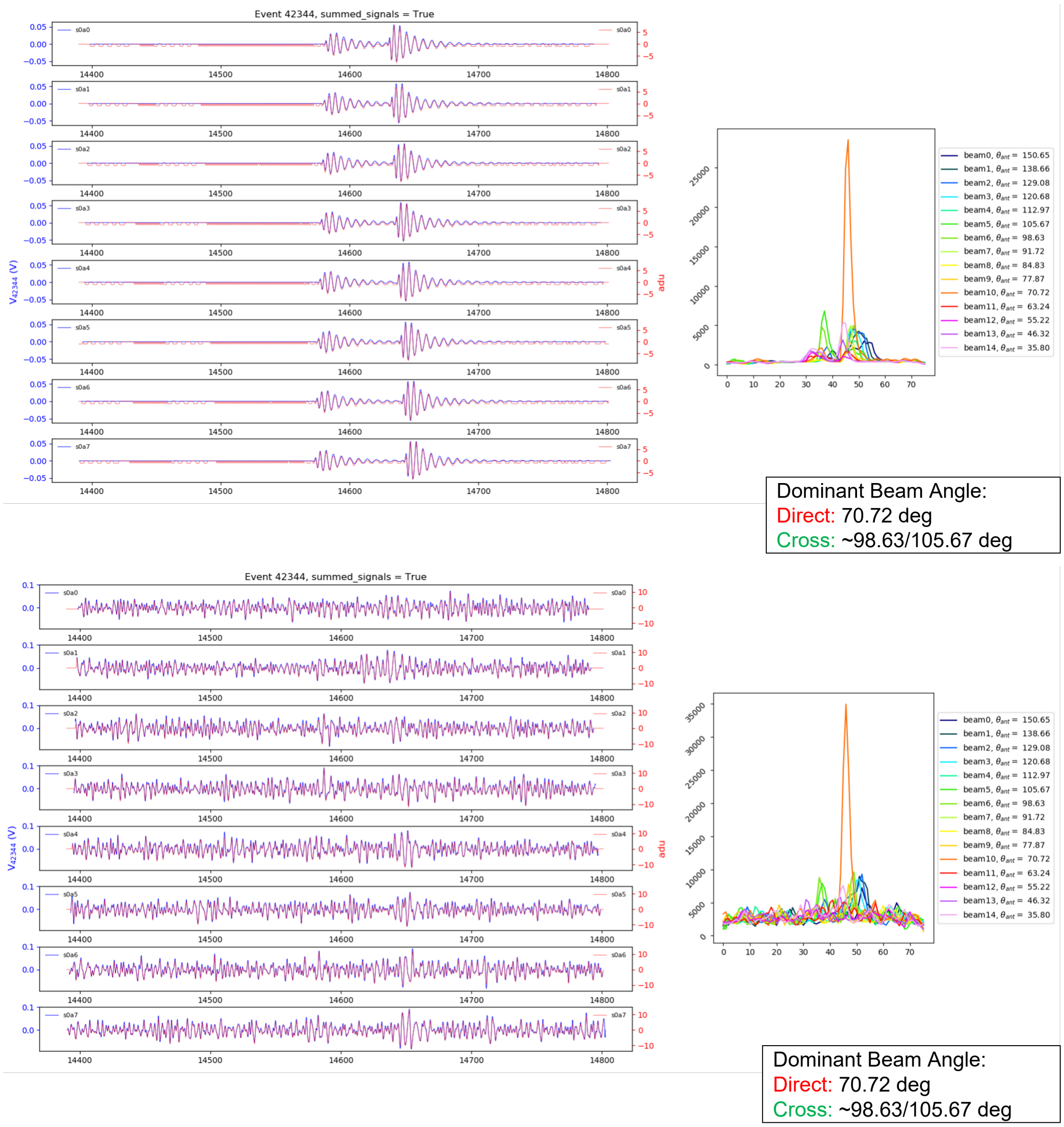

Figure 2.11: Top Left: Example GNOSim events without thermal noise. Top Right: How that signal is perceived by the simulated DAQ and beamforming algorithm. Lower Row: The same, but for the same signal with thermal noise included. This event has both direct and refracted solutions, though the geometry results in a dominant refracted solution.

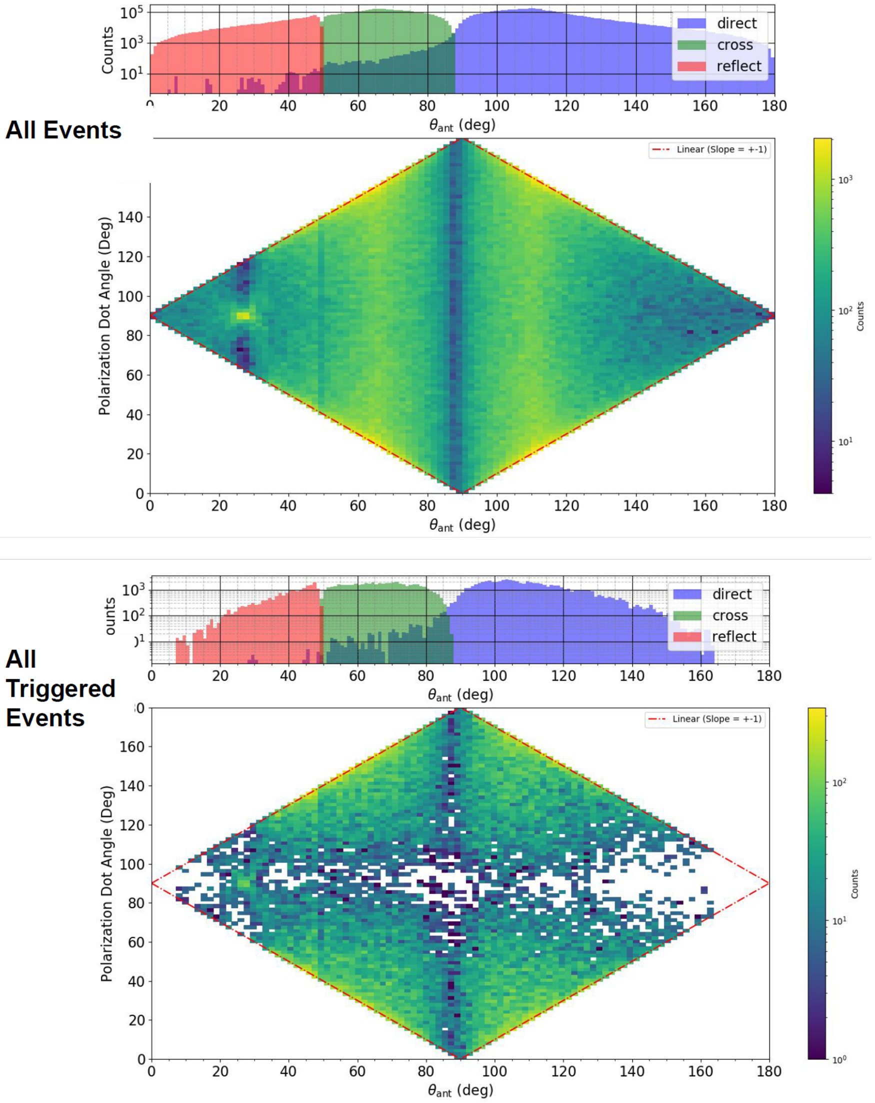
All Events

All Triggered Events

Figure 2.12: Top: Polarization of signals received at array in GNOSim. Bottom: Only the signals that pass the trigger threshold. One noteworthy feature is the appearance of Brewster's angle nearing the received zenith angle of 25 degrees. Signals approaching at this angle correspond most-often to rays which reflect off the ice-air boundary at Brewster's angle, which only allows for reflection of polarizations in the plane of the boundary. There is also clearly a dearth of signals arriving at near-horizontal zenith angles (near 90° in the x axis). This is a result of horizontal solutions being an unstable minimum in the ray-tracing solution, where slight deviations from a purely horizontal ray tracing solution result in the signal seeing a changing index of refraction, and thus deviating away from the horizontal trajectory.

Brewster's angle is defined as:

$$\theta_B = \arctan\left(\frac{n_2}{n_1}\right) \tag{2.16}$$

and is ≈ 37° at ice-air surface. Note that this angle is not the same as the arrival angle at the antenna, and occurs earlier the the rays trajectory towards the antenna.

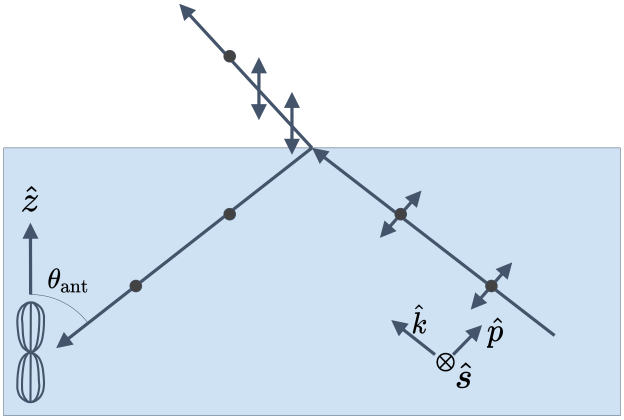

Figure 2.13: A schematic overview of Brewster's angle in ice. Reflections which occur at Brewster's angle see a complete suppression of the p-polarization.

Also visible in the plot is a lack of signals arriving at the antenna from the horizontal arrival direction (near 90° in the x axis). This is believed to due to horizontal rays existing in an unstable minimum in the ray-tracing solution set, where slight deviations from a purely horizontal ray tracing solution result in the signal seeing a changing index of refraction, and thus bending under Snell's law and deviating away from the horizontal trajectory.

Finally, this plot shows how the phased trigger results in very few triggers from events with horizontally polarized light at the receiving antennas. This is a result of the station used in this simulation being designed to match the configuration of ARA Station 5, which uses exclusively vertically aligned VPol antennas in the trigger array. The gain pattern of these antennas are maximally sensitive to perfectly VPol signals, but have a null for HPol signals (effectively suppressing their power, resulting in less triggers). Here VPol signals are aligned with the $\hat{z}$ direction, and HPol signals are orthogonal to $\hat{z}$. Both HPol and VPol dominated signals can contain portions of both s and p polarizations, which are defined in the basis of the ray, depend on $\hat{k}$, and are thus not necessarily aligned with $\hat{z}$.

Despite the interesting additional details contained within a simulated GNOSim dataset, the main use during the proposal stage for RNO-G was in understanding the depth-dependence of volumetric acceptance (sensitivity) when designing a deep trigger. Deep stations benefit from having a significant increase in ray tracing solutions (which correlates to an increase in visible volume of ice) due to having a multiplicative increase in paths from reflections from both the surface of the ice and the bedrock. In addition to an increase in reflection/reflection-based solutions, the depth of the antenna also reduces the so-called "shadow region", which is the volume of ice where there is no ray tracing solution for a smooth ice profile. This region is visible as the top right corner of Figure 2.6, where no rays propagate.

Though there are obvious benefits to a deep station, the time and financial cost of drilling holes is significant, and often times the rate-limiting step in constructing an experiment. Deep holes also constrain the possible antenna designs (discussed further in Section 2.5). To optimize sensitivity as a function of money then, a deep station is not necessarily the ideal configuration. GNOSim was used to compare the volumetric acceptance as a function of energy for various depths. Greenland had not yet been decided as the final destination for the proposed experiment, so both Greenlandic and Antarctic ice models were also compared. Figure 2.14 shows the outcome of this investigation, comparing two of the major design options at both Greenland and Antarctica. The increase in sensitivity observed for the deeper option was sufficient enough to motivate the deeper station design. This 100 m antenna depth is the nominal depth currently being used for RNO-G stations (Figure 2.2). The current status of RNO-G is described in further detail in Section 2.4.

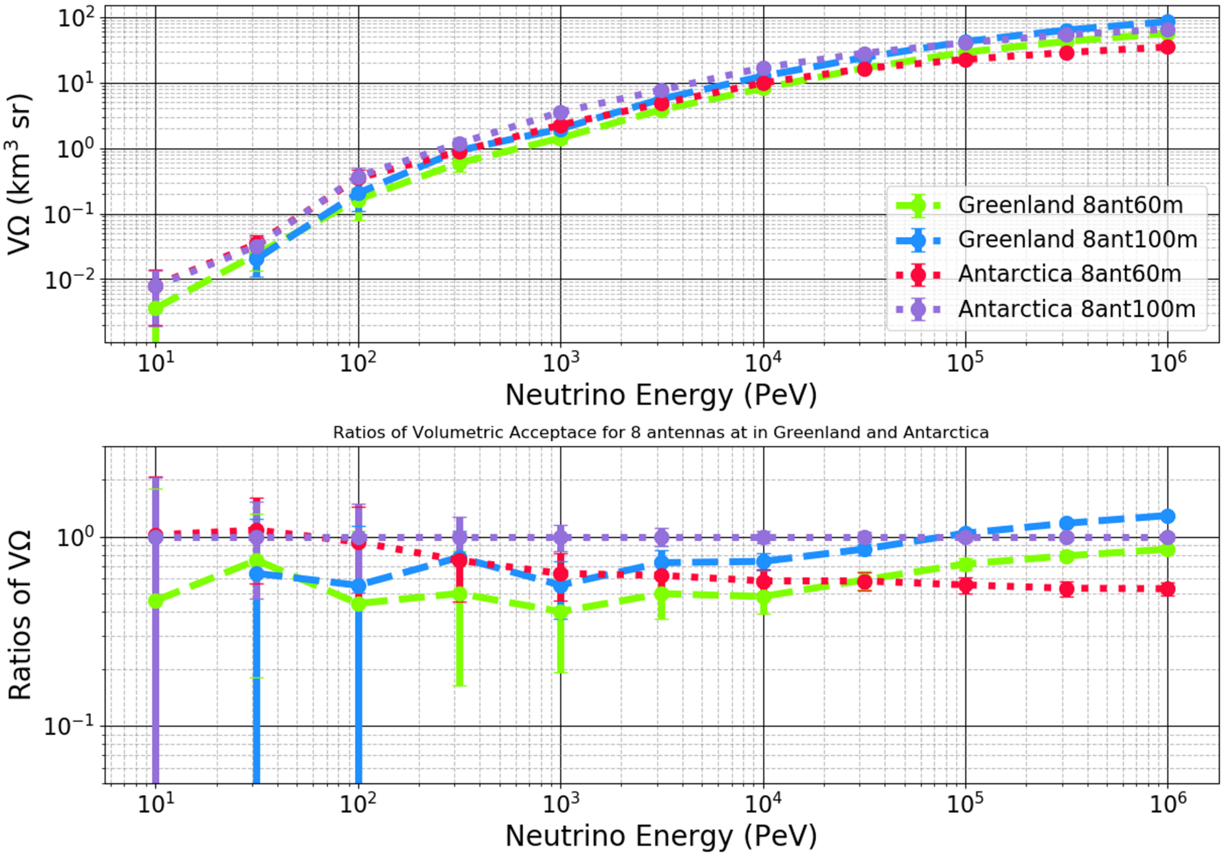

Ratios of Volumetric Acceptace for 8 antennas at in Greenland and Antarctica

Figure 2.14: Top: The volumetric acceptance as a function of neutrino energy for shallow and deep station configurations in both Greenland and Antarctica. Bottom: Residuals compared to the deep Antarctic configuration. The number of simulated events N was 100 thousand for each point above 100 GeV, with 1 million events being used at lower energies to compensate for the significantly lower detection rate. Note that the volumetric acceptance defined in Equation 2.1 is normalized by N, so this does not skew the result.

2.4 RNO-G Design and Construction

Here I provide a general overview of the current status of RNO-G. The majority of this section is directly pulled from the RNO-G concept paper [33], for which I was a co-author. Minor edits have been made where new information is available or where context needs updating. These sections go over the technical design of RNO-G.

Each station consists of three boreholes a main, each with a "string" of antennas. The most populated string is known as the "Power String" which contains the phased array trigger consisting of five VPol antennas spaced from a depth of 40 m down to 100 m; this string also has two deep HPol antennas. The other two strings are known as "Helper Strings", and each contain one VPol antenna, one HPol antenna, and a radio signal pulser which is designed for calibration. Each string is radially connected at the surface to a DAQ box. Each station also has a surface component, consisting of several log-periodic dipole antennas (LPDAs) positioned along each spoke of the station. Figure 2.9 shows a diagram of the station design. A full-scale RNO-G would consist of 35 stations, distributed in a non-overlapping grid such that each station operates independently (Figure 2.15).

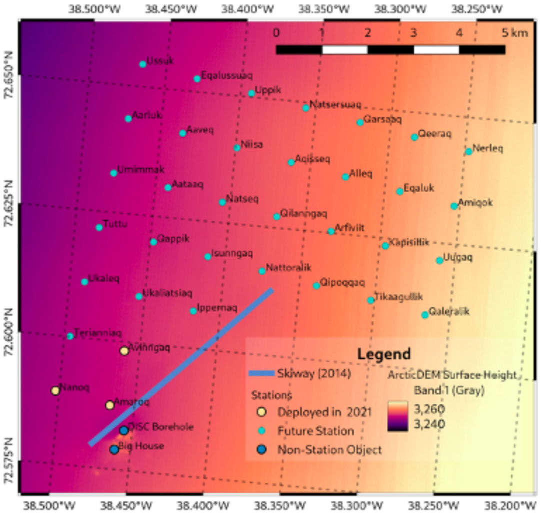

Figure 2.15: The RNO-G station deployment map following the 2021 season.

RNO-G will provide high-quality science data and a robust, low trigger threshold with

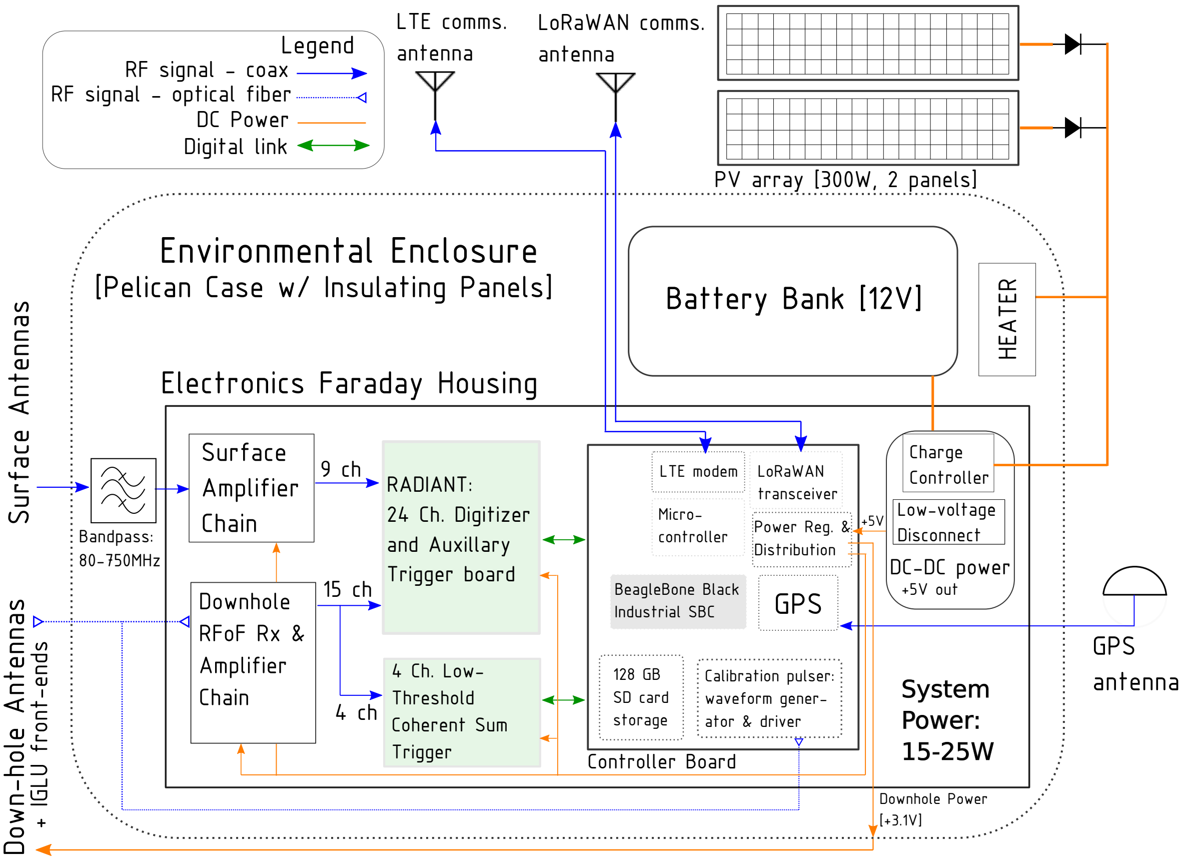

Figure 2.16: System diagram for an RNO-G station. See text for details. From Reference [33].

minimal power consumption using a station design schematically depicted in Figure 2.16. In nominal operating mode, a station will use 25 W, including DC-DC converter losses. All equipment is rated to operate at −40° C and 3200 m altitude.

The significant anticipated scientific capabilities and output of RNO-G are summarized in Section 2.4.6. The projected sensitivity for RNO-G to a diffuse flux of neutrinos is shown in Figure 2.17.

2.4.1 Antennas

The initial downhole antenna designs were driven by the 5.75 in diameter of the boreholes (ASIG drill [137]), with updated versions being designed once bigger boreholes were made available. The vertically-polarized (VPol) antennas are a “fat dipole” design (see Fig-

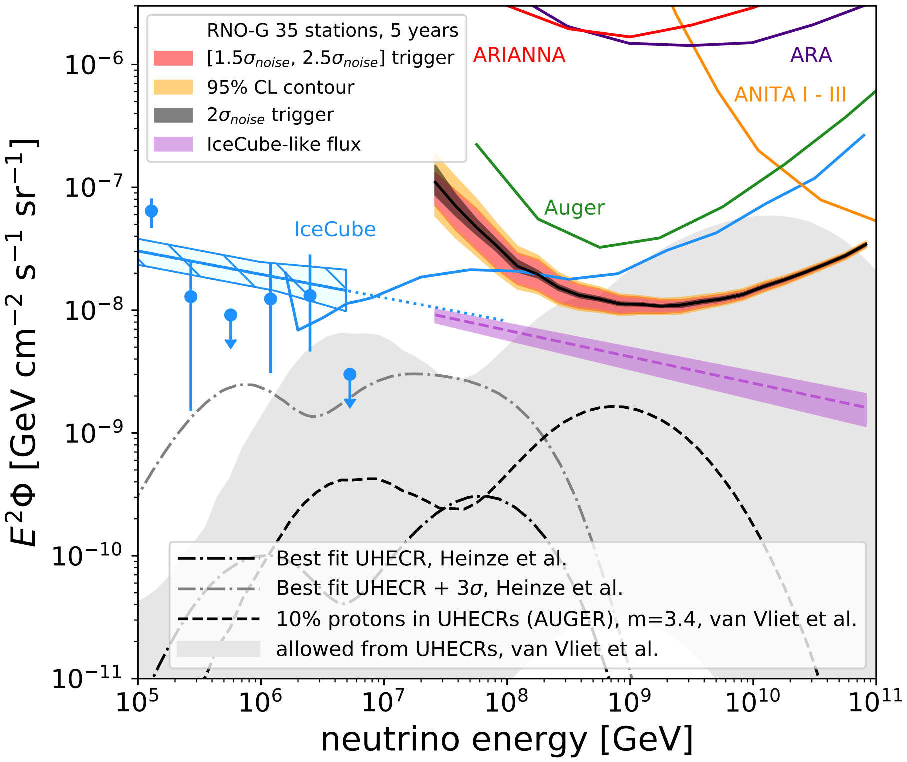

Figure 2.17: The five-year sensitivity (90% CL upper limits) of RNO-G to the all-flavor diffuse flux for 35 stations (assuming the stations are active two thirds of the total time), compared with existing experiments and several predicted fluxes [135, 103, 136, 29]. The red band represents the differential sensitivity band for a range of phased array proxies, spanning the interval from $1.5\sigma_{\text{noise}}$ to $2.5\sigma_{\text{noise}}$ using decade energy bins. 95% CL contours are represented by the orange band. The black band is the sensitivity expected for a $2.0\sigma_{\text{noise}}$ trigger, including 95% CL contours. The purple band depicts the expected integrated sensitivity (90% CL upper limits) for an IceCube-like flux, over the $[1.5\sigma_{\text{noise}}, 2.5\sigma_{\text{noise}}]$ trigger range. Figure and caption from Reference [33].

ure 2.18) previously used in neutrino detection experiments, which have an azimuthally symmetric beam pattern and usable bandwidth ranging from 150-600 MHz [138, 139]. For horizontal polarization (HPol), cylindrical tri-slot antennas were considered. They are nearly azimuthally-symmetric in gain, with differences of less than 1 dB up to 800 MHz, which corresponds to differences of less than 12% in effective length. Only VPol antennas are used for the trigger because the HPol antennas inherently have narrower usable bandwidth than the fat dipoles, as shown in Figure 2.19. With the current HPol designs, there is enough overlap with the VPol band to combine the signals for polarization reconstruction in analysis. The switch to larger boreholes (RAID drill) especially helped improve the broadband characteristics of the HPol antennas.

To take advantage of the larger holes, designs for 8 in quad-slot antennas were developed , which have a lower frequency turn-on and improved gain characteristics taking advantage of the larger allowed diameter. In Section2.5 I give a detailed description of the HPol antennas, as well as the research and development process that went into them.

The surface component employs commercially available log-periodic dipole antennas (LPDAs, Create CLP-5130-2N), successfully used by the ARIANNA experiment. ARIANNA's extensive in-field experience with these antennas will significantly simplify calibration. Owing to the high gain allowed without the borehole constraints, the nine LPDAs arranged in various orientations (see Figure 2.15) will measure all polarization components with high-precision, and provide a clear separation of upgoing versus downgoing signals. Due to their size the LPDAs have the largest gain of all employed antennas and will provide the greatest frequency coverage for the detected signals.

Particular care is taken in the placement and alignment of the LPDAs in the trenches at the surface, as well as when surveying the position of boreholes and antenna locations to ensure good starting values for the system calibration using the in-situ pulsers.

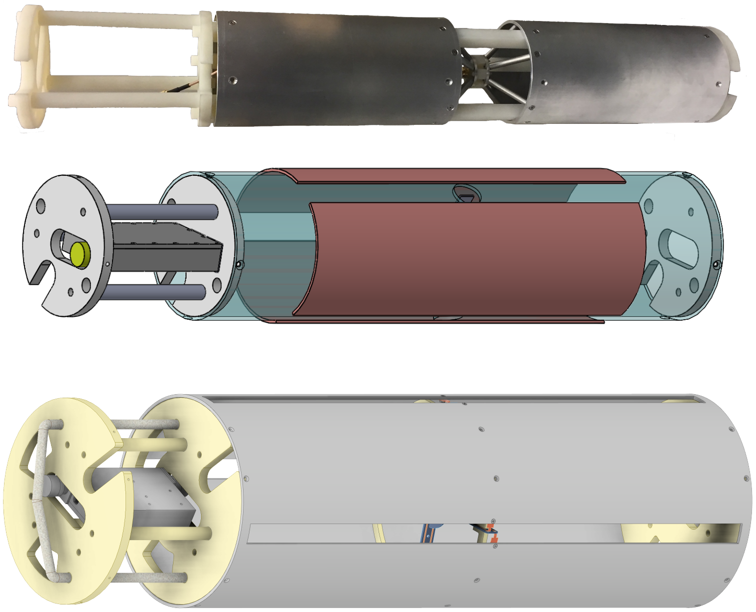

Figure 2.18: Photo of a VPol prototype (top) and technical drawings of options for the HPol antennas (tri-slot, middle, quad-slot, bottom). The VPol and tri-slot are the first iterations of the deep antennas for RNO-G, while the quad-slot is being considered for use in conjunction with larger diameter boreholes. From Reference [33].

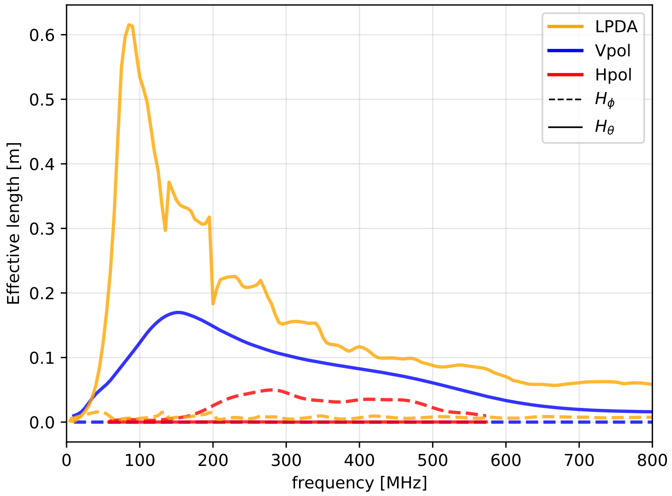

Figure 2.19: Antenna effective length magnitude for the LPDA, VPol and HPol (tri-slot) in the direction of maximum gain H_θ (V-pol and LPDA) or H_ϕ (H-pol). Results of detailed antenna simulations of the v1 iterations as shown in Figure 2.18. From Reference [33].

2.4.2 Radio-Frequency front-end design

To minimize system noise temperature, the feed of each antenna deployed in the borehole is connected with a short coaxial cable to a downhole front-end (Figure 2.16, where a Low-Noise Amplifier (LNA, type IGLU, see Figure 2.20) boosts the signal strength. To prevent a significant gain slope from long lengths of copper coaxial cable, each front-end contains a Radio Frequency over Fiber (RFoF) transmitter. The RFoF link and LNA are both powered by a DC connection from the surface, which is the only through-going coaxial cable in the boreholes. The LNA and RFoF are custom designs optimized for minimal noise temperature ($\leq$150 K) and low power. Each downhole channel consumes 140 mW, compared to 2.5 W in the previous installation of the phased-array in ARA. A total of 15 downhole antennas are distributed across three boreholes.

After being transmitted over fiber, the signals are received by another set of amplifiers in the DAQ box (type DRAB, see Figure 2.20) and converted back to analog signals. At the DAQ box, the signals from the surface channels are also received and amplified. Given the relatively short run of coaxial cable from the LPDAs to the DAQ box of less than 20 m, the signals require only one amplification stage after being fed into the DAQ box (type SURFACE, see Figure 2.20).

All amplifiers are placed in custom-designed RF-tight housings using iridited aluminium (chromate conversion coating). This significantly reduces the influence of noise on the amplifiers and protects the IGLU amplifiers in the boreholes from the environment. The amplifiers exhibit excellent uniformity in laboratory tests (see Figure 2.21). Nevertheless, all amplifiers are calibrated individually to reduce systematic uncertainties on the reconstructed signals.

2.4.3 Triggering, digitization, and data acquisition

The main trigger of RNO-G comes from a phased-array at depth of 100 m. The design of the field-proven phased-array installed at ARA [79] had to be changed to accommodate the

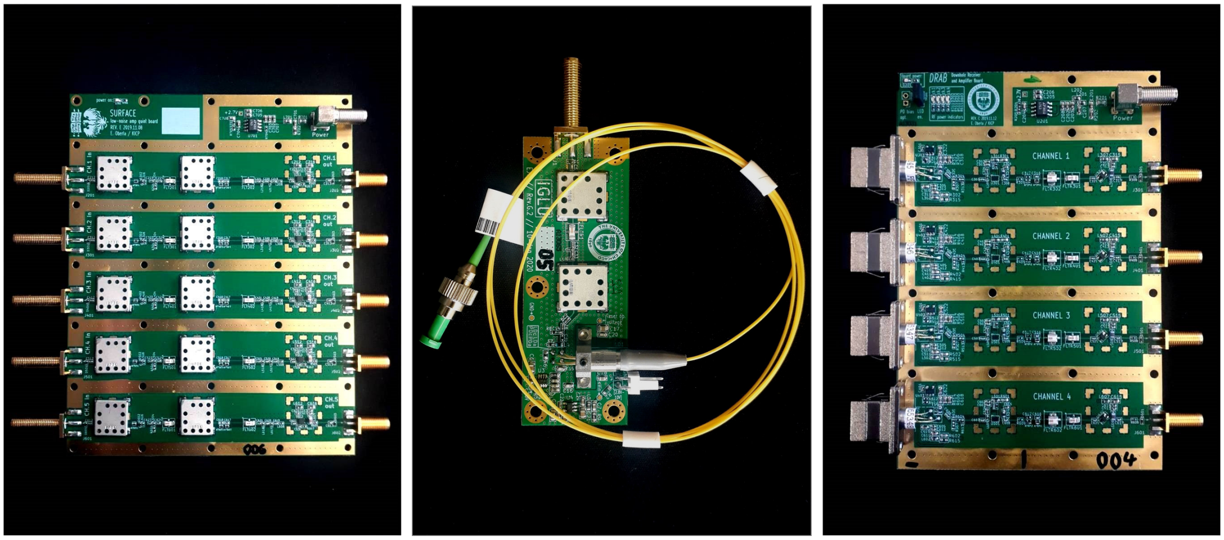

Figure 2.20: Amplifiers as designed for RNO-G. Left: SURFACE amplifiers for the signals coming from the LPDAs via coaxial cable. Middle: an IGLU board (In-ice Gain with Low-power Unit) used to convert signals from antennas deep in the ice to analog RF signals and then feed them into the indicated fiber. Right: DRAB board (Down-hole Receiver and Amplifier Board) located within the station housing. All amplifiers are shown without their environmental enclosures. From Reference [33].

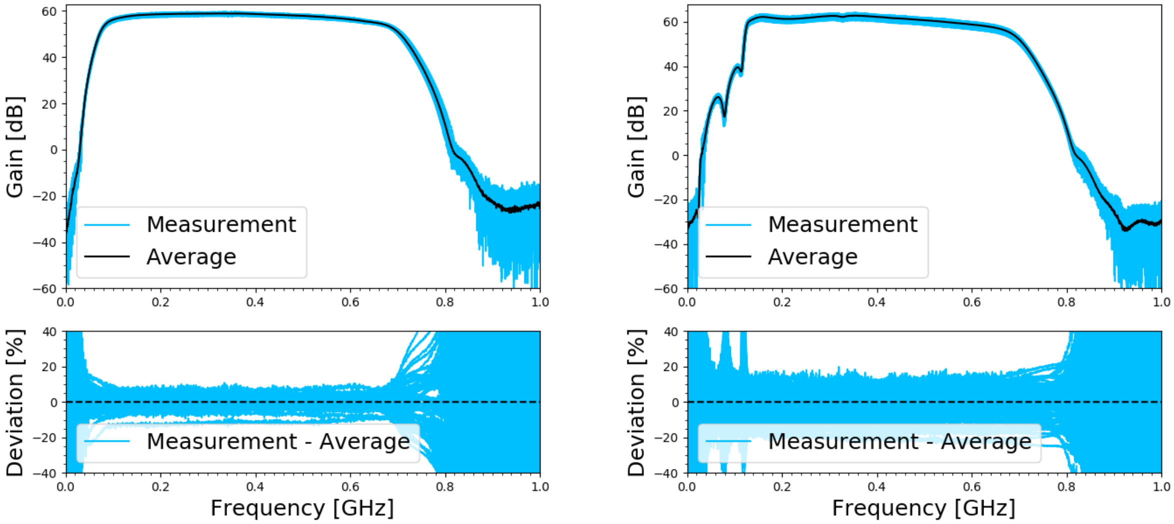

Figure 2.21: Gain of the RNO-G amplifiers. Left: 12 SURFACE amplifiers. Right: Combination of 23 IGLU and DRAB amplifiers, including a 50 m optical fiber cable. All amplifiers are revision v1 hardware. From Reference [33].

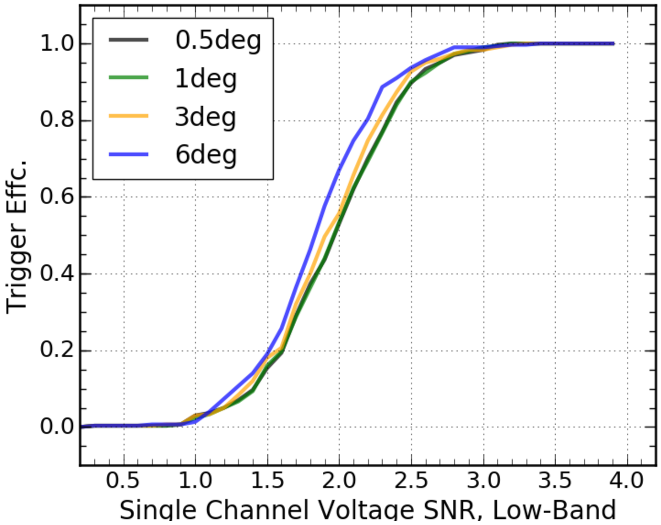

Figure 2.22: End-to-end simulation of the 4-antenna phased array trigger design for RNO-G. The simulated trigger efficiency for a number of neutrino signals at different off-cone viewing angles in the trigger bandwidth of 80 MHz to 250 MHz. From Reference [33].

lower power requirements of autonomous stations and was optimized with respect to the neutrino signals typically expected in Greenland and with respect to per-item cost for the scalability of the array.

The primary trigger is thus a coherent-sum and beam-forming trigger from a compact array of four VPol antennas installed at the bottom of the main borehole string at a depth of 100 m. A commercially available 8-bit 500 MSa/s ADC is used to digitize and continuously stream data to an FPGA. This reduces the effective band to operate at the low-end of the signal bandwidth, 80 MHz to 250 MHz. The lower cut-off is determined by the amplifier design that takes advantage of the full-range of low-frequency power that the antenna delivers.

Eight beams are formed that cover the full range of expected signal arrival directions. Compared to the previous phased-array implementation in ARA there are fewer beams, but each of them wider, thus no angular coverage loss is incurred. Overall, the power-savings total to about a factor of 10 for the trigger board, using 4 W in full operation mode.

A single-antenna voltage threshold of $2\sigma_{\text{noise}}$ can be achieved with this trigger, based

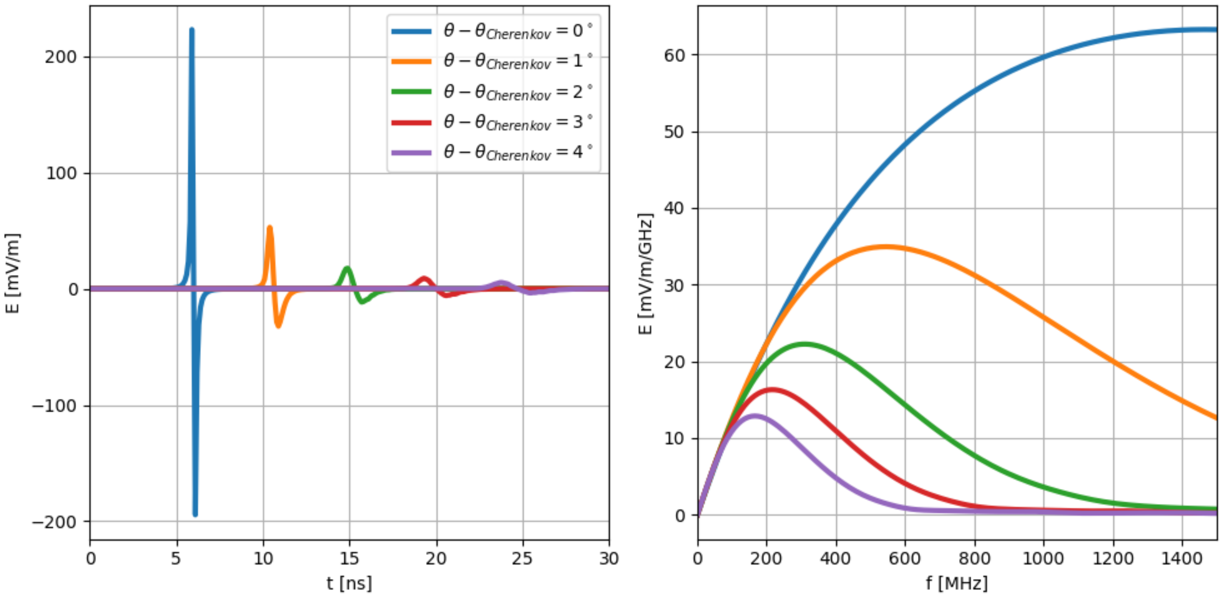

Figure 2.23: Electric-field waveforms (left) and spectra (right) of the radio signal emitted at different viewing angles relative to the Cherenkov angle, for a hadronic shower with energy deposition of 1 EeV. For enhanced readability, the waveforms have been offset in time. No propagation or detector effects have been included. From Reference [33].

on simulation studies as shown in Figure 2.22. The smaller bandwidth reduces the SNR of on-cone signals (i.e. 0.5 deg in Figure 2.22) by 10%, however, increases the SNR for off-cone events by up to 80%, thereby incurring very little loss on the absolute neutrino effective volume. This is due to the limited high-frequency content of off-cone neutrino signals (see also Figure 2.23).

The full-band waveforms for all 24 antennas within a station are digitized using the RAdio DIgitizer and Auxiliary Neutrino Trigger (RADIANT) board (Figure 2.24). The single-channel LAB4D switched-capacitor array sampling ASIC is used for waveform recording at a rate up to 3.0 GSa/s with an adjustable record length up to ∼700 ns and the capability for multi-event buffering on-chip [140]. RNO-G operates the LAB4D in 2x 2048-sample buffers for essentially deadtime-less performance.

A trigger decision can be made using input from the primary neutrino trigger board (phased-array) or an auxiliary on-board trigger using similar Schottky diode detector circuits.

The auxiliary on-board trigger is formed using a comparison between a DC voltage level and the enveloped waveform, which is fed to the on-board FPGA to build a combinatoric trigger decision. As the auxiliary trigger can have a higher overall threshold than is possible with the primary neutrino trigger board, it will predominately be used as an additional trigger for the surface antennas as an air shower trigger. In periods in which the power available to the stations is low it can serve as main trigger, however, with a much weaker sensitivity to neutrino signals.

Once an event is digitized, the waveforms and metadata are transferred to a BeagleBoneBlack Industrial, an ARMv7l Linux system, over a Serial Peripheral Interface (SPI) link, which allows data transfer at up to 20 Mbps. The operating system and acquisition software are stored on robust eMMC storage, while a 128 GB industrial SD card stage data before it is transmitted wirelessly to Summit Station. The acquisition software is an evolution of field-proven ARA phased array acquisition software.

2.4.4 Autonomous power and wireless communications

Autonomous power and wireless communications simplify logistics for an experiment of this scale and become even more efficient for even larger arrays, such as IceCube-Gen2. Each station is powered by two solar panels, with a total maximum power output of 300 W, and a 5 kWh sealed lead-acid battery bank that provides three days of full-system (24 W) running capacity during cloudy or inclement conditions, with a 60% de-rating margin. Lead-acid batteries, when lightly discharged relative to total capacity, have a proven track record in Arctic environments as demonstrated by the UNAVCO remote stations [141]. The daily solar energy delivered to a RNO-G station using a 300 W solar panel array is shown in Figure 2.25, using realistic estimates of 70% total sun fraction (including diffuse and snow-reflected contributions) and a 90% charge-controller efficiency. A low-power microcontroller (μC) manages the power system and turns parts of the detector on and off as necessary. The

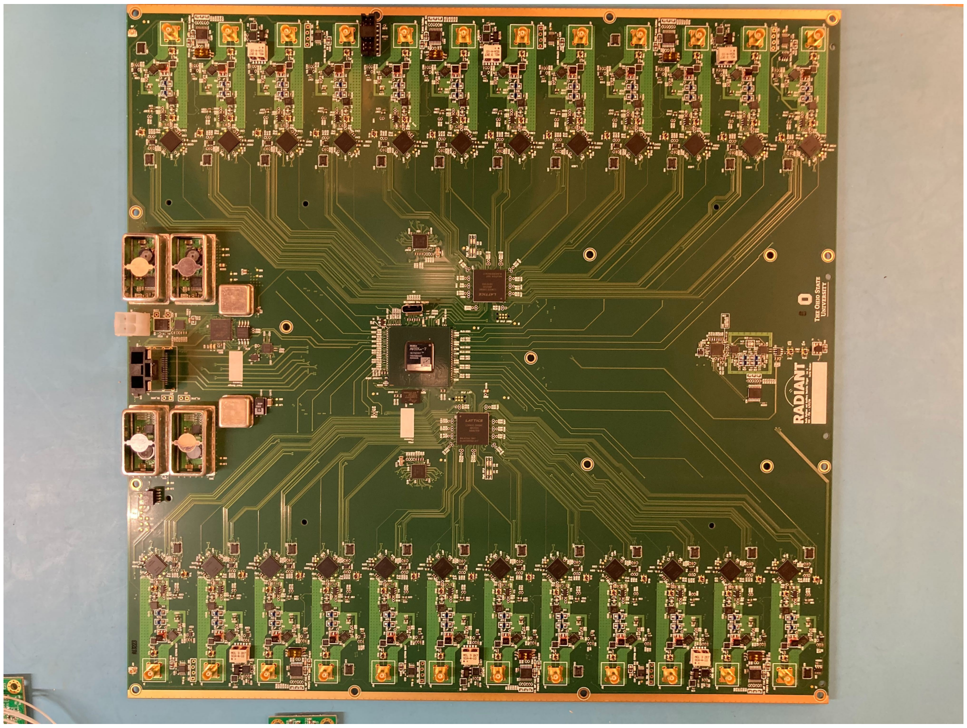

Figure 2.24: First iteration of the Radiant Board that will be the main DAQ of RNO-G. All 24 channels are accommodated on one board and read out by LAB-4D chips. From Reference [33].

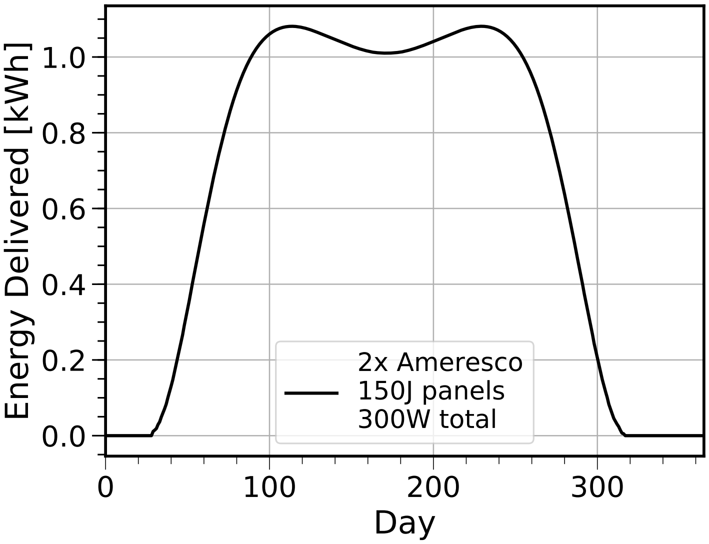

Figure 2.25: Predicted daily energy delivered by a 300 W photo-voltaic (PV) array to an RNO-G station at Summit Station. The PV array comprises two Ameresco 150J rugged panels mounted vertically and facing south. The total PV area is 2 m^2. From Reference [33].

μC communicates with the Beaglebone SBC via a serial connection so that the SBC may be shut down cleanly if necessary. Enough power granularity is available to run the detector in a low-power, lower-sensitivity mode if needed.

The RNO-G station can be operated in several different modes depending on the available solar power capacity, in order to maintain constant science data during long stretches of inclement weather and during the shoulder seasons, when the sun only rises above the horizon for short periods per day. These operating modes include:

1. **Full-station mode**: Power, trigger, and data acquisition on the full 24-channel station including the low-threshold trigger and full LTE data telemetry. Power:~24 W.
2. **High-threshold mode**: Power, trigger, and data acquisition on the full 24-channel station without the low-threshold trigger and minimal LTE data telemetry. Power:~17 W.
3. **Surface-only mode**: Power, trigger, and data acquisition only on the 9 surface LPDAs and minimal LTE data telemetry. Power:~6 W.

Figure 2.26: The station solar charge controller and high-efficiency DC-DC board for RNO-G. From Reference [33].

4. **Winter-over mode**: Operating mode during the polar night. All power is turned off except to the charge-controller, LoRaWAN network, and station-control microcontroller. Only minimal housekeeping data is telemetered over LoRa. The estimated power draw is ~70 mW.

The expected uptime for an RNO-G station at Summit Camp with the 300 W PV panel array is 216 days in operating mode 1 (59%), 25 days in mode 2 (7%), and another 20 days in mode 3 (5%) for a total science livetime of ~70% averaged over the year. For the remaining 30% of the year, the station will be put in winter-over mode. These different operating modes can be engaged by the RNO-G station controller autonomously or commanded remotely over one of the wireless networks.

Options to operate further into the winter are being explored. This R&D is particularly relevant for a potential larger array at the South Pole such as IceCube-Gen2, where the polar night is longer. Although not part of the baseline RNO-G design, wind-turbines may allow to extend the full-station mode operations of RNO-G throughout the winter. Development of radio-quiet wind turbines that can survive in the polar environment is ongoing [142]. Modeling using historical wind data [143, 144] suggests that a feasible 25%-efficient turbine at a height of 10 m would produce a daily average of 1200 Wh per square meter of collection area. Due to extended periods of low wind speeds a larger battery buffer will be needed for operation on wind power.

The main data transfer link from each detector to Summit Station uses modern cellular technology. A private LTE network provides high bandwidth (up to 75 Mbps total uplink) and long range while consuming minimal power (<1 W average) at each station. A commercially-sourced LTE base station has been deployed with an antenna on the roof of the Science and Operations Building at Summit Station. As a compromise between range and minimizing interference with our detectors, LTE Band 8 (880-915 MHz uplink, 925-960 MHz downlink) was chosen and a permit has been acquired from the Greenlandic Radio Administration. Link modeling, including terrain shielding and a 10 dB fading margin, predicts a usable range up to 10 km.

A 34-dBi roof-top sectorial antenna at Summit can cover the azimuthal extent of the array and each station is equipped with a 9 dBi antenna on a 3 m mast. A secondary LoRaWAN [145] network has also been deployed, providing a backup low-power but low-bandwidth connection for control and monitoring.

2.4.5 Operations and data systems

The acquisition software on the Single-board computer (SBC) adjusts the trigger thresholds to maintain as fast a trigger rate as possible ($\mathcal{O}(10\,\mathrm{Hz})$) without incurring significant deadtime. This high sustained rate drives system performance downstream, so second-stage filtering is applied on the SBC to reduce the rate of saved triggers to a time-averaged 1 Hz. Additionally, 0.1 Hz of forced-trigger data is recorded at regular intervals to help characterize the noise environment.

The on-disk compressed size of each event is an estimated 30 kB, implying an average data rate of around 260 kbps per station at 1.1 Hz. The LTE network can easily accommodate this rate with a relatively low duty-cycle at each modem, thereby saving power. This rate allows storage for six weeks on the local SD cards in the event of an unexpected network outage. If more time is needed, the station can be instructed via LoraWAN to reduce the rate. In the unlikely case of simultaneous LTE and LoraWAN failure, the software on the station will automatically throttle the rate. Once data is transmitted to Summit Station, it will be stored on a redundant disk array for collection each summer. At the estimated 1 TB/station/per year of data, full build-out requires a redundant storage capacity (with margin) of 35 TB, which can easily be achieved with a single commodity rack server (e.g. Dell PowerEdge R7515) .

All instrument status data and event metadata as well as a subset of the waveform data (5 GB/day total) is transmitted with low latency via Summit Station's satellite link to the University of Wisconsin for monitoring and quality assurance. A small portion of available bandwidth is reserved for remote login for any configuration changes or remote maintenance required. The JADE software [146] successfully developed and deployed for IceCube data management is also used for RNO-G. For data acquisition performance, all data is initially stored in a compressed packed-binary format resembling the in-memory format used by the data acquisition system. Converters will be maintained from the raw data format to more convenient archival formats (e.g. HDF5).

All low-latency data is readily available to the collaboration via an interactive monitoring web site[1]. A comprehensive set of checks on the metadata and system health are performed by the computer systems at Summit Station. Any anomalies will result in an email alert.

Monitoring duty is apportioned to institutes on a rotating basis. While monitoring, an institution is responsible for timely investigation of all alerts and daily checks of the low-latency data for potential issues. Weekly monitoring reports will be issued to provide historical context for any issues that may arise.

---

[1] Based on https://github.com/vPhase/monutor

2.4.6 Published and Anticipated RNO-G Results

The first three stations of RNO-G were deployed in 2021, with 4 more stations being installed in 2022. In just the short time since the first stations were deployed the RNO-G collaboration has already utilized the installation to characterize the radio properties of the ice near Summit Station [116], with additional contributions to investigating triboelectric backgrounds [147]. Anticipatory studies (such as determining the energy reconstruction capabilities of RNO-G [148]) have also been conducted in preparation of the data that will come from RNO-G as it continues to expand and operate.

In order to calculate the sensitivity of RNO-G, full 35-station array has been simulated with a detailed modelling of the baseline hardware. Simulations for radio detectors are constantly evolving, incorporating experience from air shower simulations [149, 88, 150, 68] and previous codes for neutrino radio detectors [151, 152, 153, 124]. The details of the RNO-G simulations are presented in Reference [33].

The projected sensitivity for RNO-G to a diffuse flux of neutrinos is presented in Figure 2.17, which shows the expected 90% CL upper limit to an all-flavor flux for 5 years of operation of the full 35 station array, assuming a 67% duty cycle, as expected under only solar power. This is using effective volumes for an isotropic all-sky flux and full-decade energy bins. Reference [154] provides further details on the $\mathrm{V}_{\mathrm{eff}}$ calculation, and the inclusion of the interaction length to convert from $\mathrm{A}_{\mathrm{eff}}$ to $\mathrm{V}_{\mathrm{eff}}$.

The Feldman-Cousins method [155] has been used for no detected events and zero background. RNO-G expects ~ 0.58 detected muons over the full energy range for five years of operation time (using SIBYLL 2.3C for signal generation and a $2\sigma_{\mathrm{noise}}$ proxy).

The sky coverage of RNO-G is mostly determined by the geometry of its location in Greenland. Figure 2.27 shows the effective areas for different zenith angle bands for RNO-G, as well as their projection onto equatorial coordinates. Outside of these bands, the effective area decreases rapidly (see also [156]), making RNO-G mostly sensitive to an annulus of roughly 45° just above the horizon. The ability of RNO-G to provide an accurate arrival direction for detected neutrinos depends on its ability to detect the signal arrival direction and the angle with respect to the Cherenkov cone, as well as the signal polarization, and is again a strong function of the number of antennas with detected signal and their SNR_m.

The sensitivity of RNO-G to transient events is discussed in Reference [33] and summarized in Figure 2.28. Most models predict small neutrinos fluxes in the energy range of RNO-G. However, RNO-G's location in the Northern hemisphere makes it uniquely sensitive, and complementary to other planned radio neutrino observatories in the Southern Hemisphere.

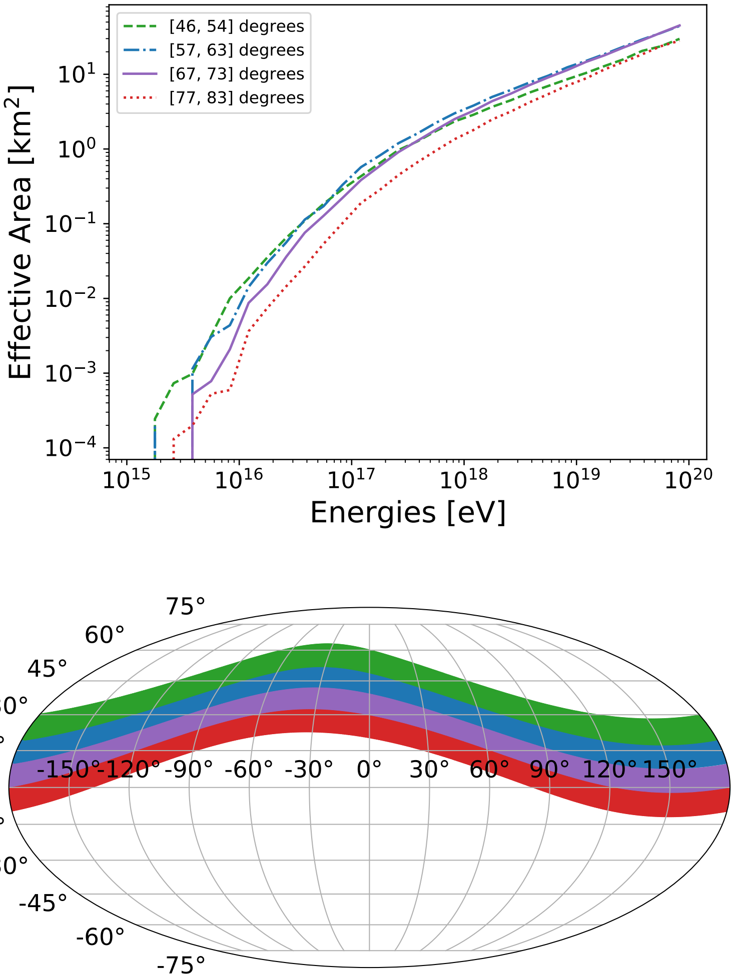

Figure 2.27: RNO-G instantaneous sky coverage. Top: Simulated effective area as a function of neutrino energy is shown for the four most sensitive zenith bands, centered at 50°, 60°, 70°, and 80°. Simulations were performed for the full RNO-G array of 35 stations with a distance of 1 km. Bottom: These bands are projected in Right Ascension (RA) and Declination (Dec) for one particular time of day to illustrate the instantaneous sky coverage. Bands outside this range still show some, albeit a strongly reduced (< 0.1 fraction of maximum effective area), sensitivity for neutrino interactions. Figure and caption from Reference [33].

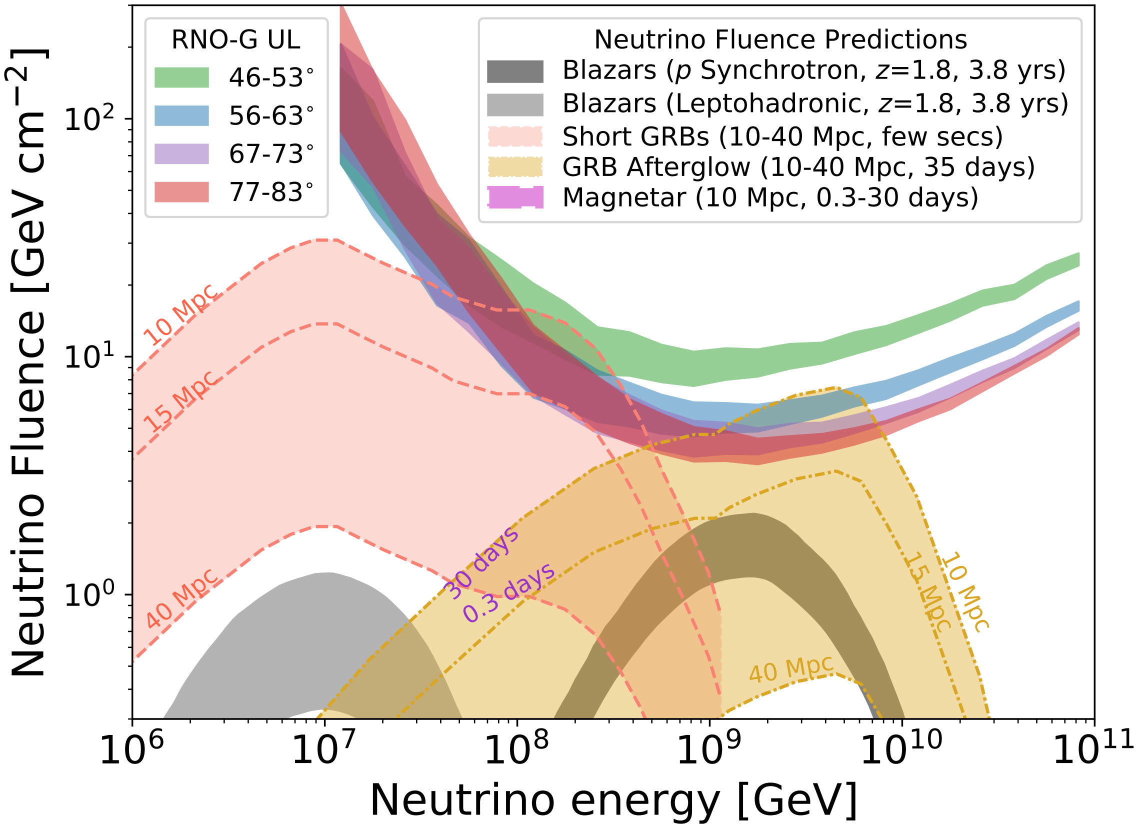

Figure 2.28: 95% CL fluence sensitivities between triggers at $1.5\sigma_{\text{noise}}$ and $2.5\sigma_{\text{noise}}$ are shown for four zenith bands centered at (top to bottom) 50° (green), 60° (blue), 70° (purple), and 80° (red). Sensitivities are calculated for a full decade in energy. Model-predicted fluences from several transient classes (bright gamma-ray blazars [157], short GRBs [158], magnetars [55], and GRB afterglows [25]) are also shown for direct comparison. We scale the short GRB and GRB afterglows by several luminosity distances to demonstrate the distance over which RNO-G will be sensitive to transients; a similar scaling can be applied to other source classes. For the calculation of sensitivities here we have used an integrated background expectation of no events. Note that for longer duration transients, integrated background may become non-negligible. Figure and caption from Reference [33].

2.5 Horizontally Polarized Antennas

2.5.1 *Principles of Spatially Constrained Horizontally Polarized Antennas*

In-order to determine the source direction of neutrino signals, in-ice experiments must be capable of reconstructing both the arrival direction and polarization of observed radio signals. The finalized station design for RNO-G aims to achieve this by equipping each string with two varieties of antennas, each specifically designed for sensitivity to either vertically-polarized (VPol) and horizontally-polarized (HPol) signals. By combining the observed signal strength in each of these antennas, the polarization of the incoming signal can be determined. Under ideal conditions these antennas would have identical performance for their respective polarizations, with no cross-pol response (cross-pol referring to signal received in an antenna by incoming waves with polarization orthogonal to the nominal sensitivity axis of the antenna).

The main design constraint governing the deep antennas used in RNO-G is the borehole diameter. As discussed in Appendix A, the frequency response of an antenna designed to measure the electric field is intertwined with the physical extent of the antenna. Thus, for an HPol antenna to achieve the same sensitivity as a VPol antenna, it must generally be of comparable scale along it's axis of sensitivity. It is thus clear that borehole constraints disproportionately impacted the design of the HPol antennas, enforcing an extremely narrow physical extent along the desired axis of sensitivity.

Because of this, HPol antennas for bore holes are often designed to achieve sensitivity not to the electric portion of the electromagnetic waves, but rather the magnetic portion. As the magnetic portion of electromagnetic waves oscillate orthogonal to the polarization (defined as the direction of oscillation of the electric field), an antenna can be designed to couple to the magnetic field, achieving sensitivity without significant horizontal extent by instead focusing on the vertically oscillating magnetic field of horizontally polarized signals. A small loop antenna is a common antenna that utilizes this mechanism. If the circumference of a loop antenna is small compared to the wavelength of radiation, then the beam pattern approximates a magnetic dipole. Figure 2.29 shows the antenna pattern for a loop antenna, which can be compared to the electric dipole pattern shown in Figure A.3. Here the nulls of the antenna are orthogonal to the plane of the loop.

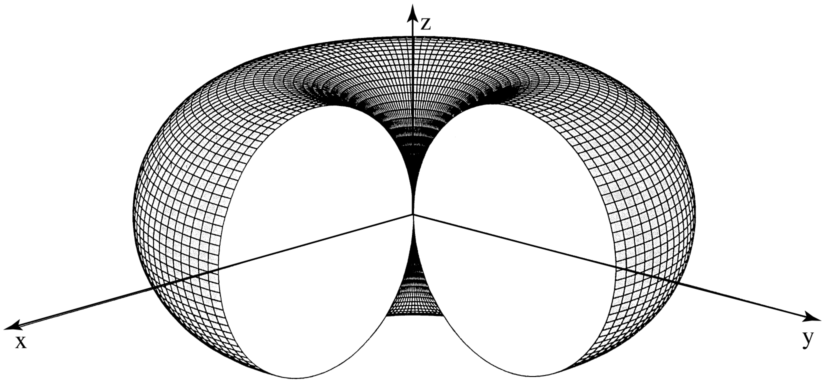

(a) $C = 0.1\ \lambda$

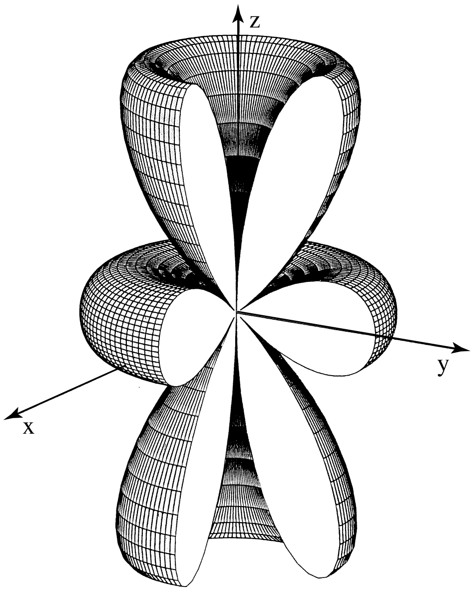

(b) $C = 5\ \lambda$

Figure 2.29: Three-dimensional amplitude patterns of a circular loop with constant current distribution. Source: Reference [159].

In Appendix A the general concept of antennas is discussed, with the example of an electric dipole being used to describe how power can be received from the electromagnetic field and fed into a transmission line for readout. The magnetic dipole produced by a loop antenna works in a similar way, however the power is received by the antenna through oscillations in the magnetic portion of electromagnetic waves. These magnetic fields induce current within the loop much like (though reversed) current in the loops of a solenoid produce a magnetic field. In this way an antenna with similar performance characteristics to the VPol antennas can be designed that is sensitive to the HPol signals but has similar radius to the VPol dipoles. The sensitivity of a loop antenna is generally poor compared to a typical electric dipole and is typically only implemented for practical reasons rather than for its sensitivity. One common way of improving the sensitivity of a loop antenna is by inserting a ferrite core, which increases the magnetic flux, magnetic field, open-circuit voltage, and overall sensitivity of the loop [159]. The addition of a ferrite core increases the radiation resistance of the loop by a factor of $(\mu_{\mathrm{ce}}/\mu_0)^2$, where μ_{ce} and μ_0 are the effective permeability of the ferrite core and of free-space respectively.

A magnetic dipole can also be produced via a slot antenna, where material can be removed from a conductive material as described in Appendix A. Even with the addition of ferrites, both the loop and patch antenna are generally lower efficiency antennas, where their application is often motivated by the practicality/simplicity of their designs. One can consider combining the two concepts in an attempt to improve the sensitivity of such an antenna. A cylindrical slot antenna is such a combination, constructed as a tube of conductive material with long slot cutout along height axis of the cylinder. This “wrapping” of the typical planar slot antenna into a cylinder results in an asymmetric gain pattern in azimuth, with sensitivity predominantly in the direction of the slot (Figure 2.30). Azimuthal symmetry can be somewhat regained with the addition of more slots, at the expense of complexity.

Such was the principle behind the original ARA HPol antenna. The ARA HPol antenna consisted of thin copper material wrapped around a non-conductive tube. Three vertical slots were evenly distributed azimuthally, with electrical connections from each panel being directed into a central feed, effectively measuring the voltage across each slot simultaneously.

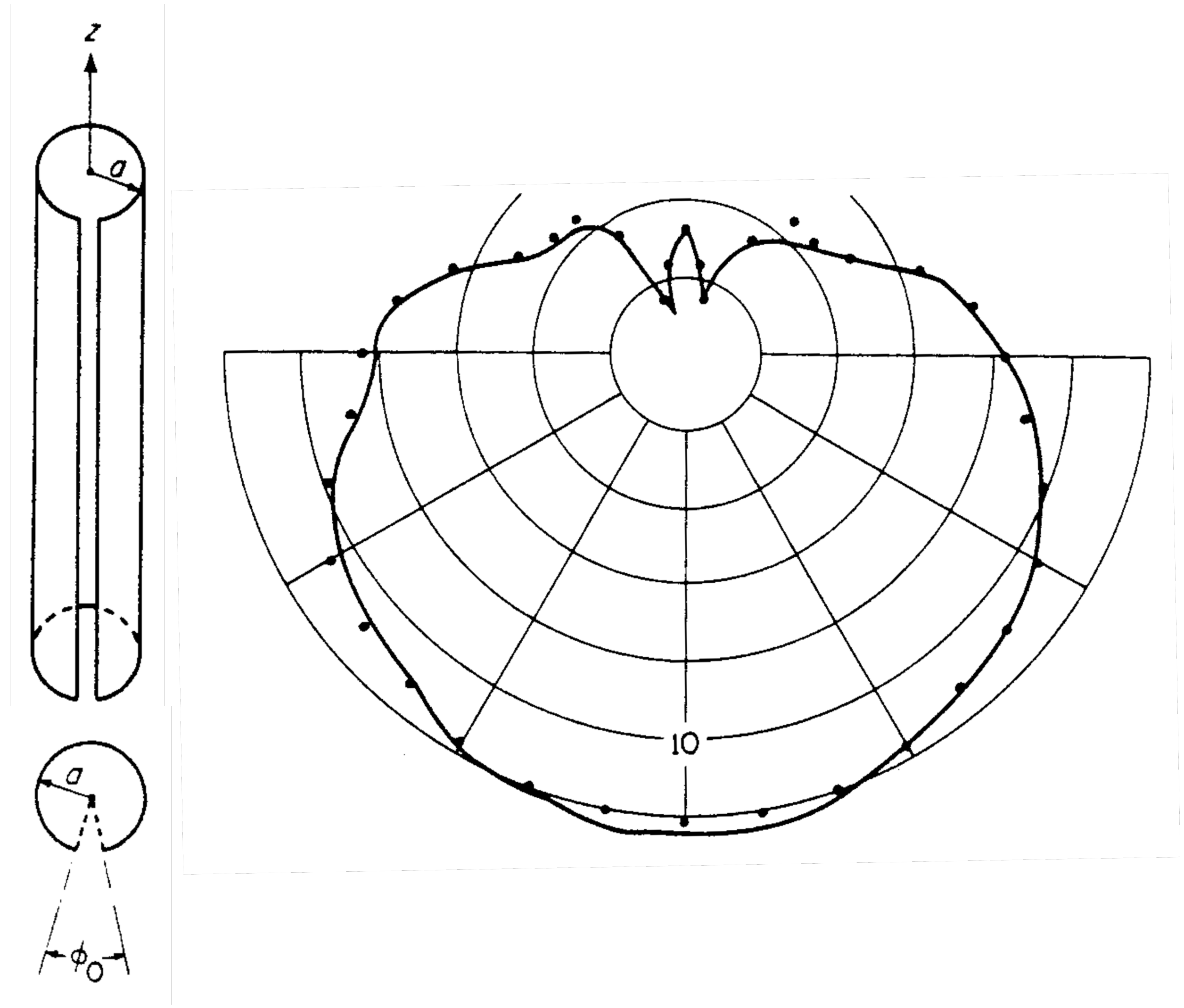

Figure 2.30: Left: An infinitely long single axial-slotted cylindrical antenna [160]. Right: The measured axial gain of a similar (but finite) antenna [161].

Several ferrite rods ran through the length of each ARA HPol antenna to improve the sensitivity of the antenna. Figure 2.31 shows the antenna as deployed. The simulated gain patterns shown in this figure show how the quad-slot design managed to imitate performance characteristics of a dipole (at a lower over-all sensitivity), at the expense of a significantly more complicated design.

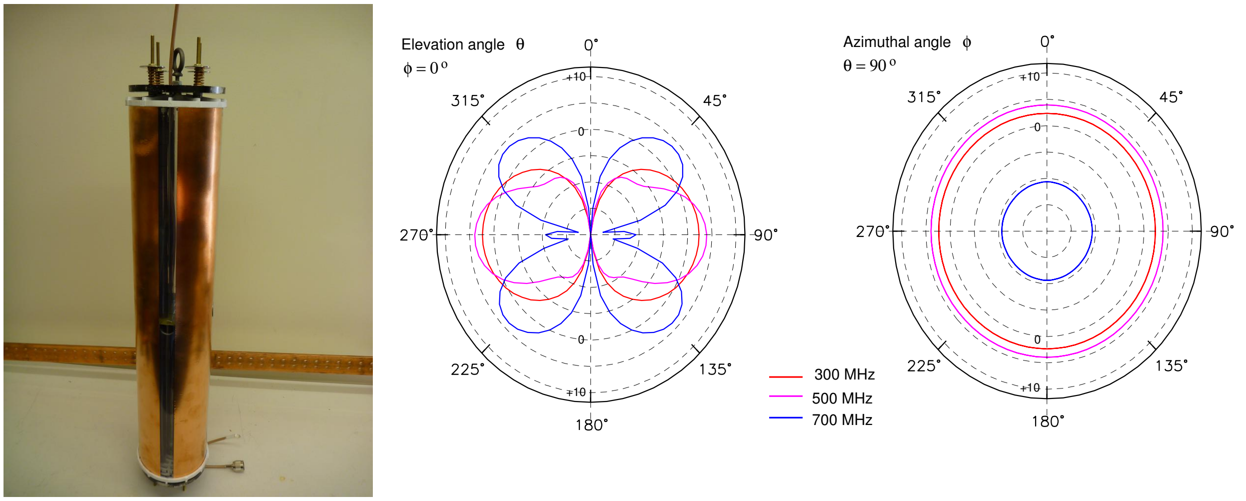

Figure 2.31: Left: The ARA quad-slot cylinder antenna used in on borehole for ARA-testbed. Center: Simulated Gain (dBi) v.s. elevation angle (zero degrees is the vertical directions) for three frequencies for the quad-slot cylinder antenna. Right: Simulated Gain (dBi) in the horizontal plane v.s. azimuth showing the high degree of uniformity of the azimuthal response. Source: Reference [162].

2.5.2 Cylindrical Antenna Design Iterations

This section provides a summary of the major steps in the research and development process towards the RNO-G HPol. Some additional details about the specific methods are discussed in Section 2.5.3, while this section aims to describe the major iterations of the prototype and how they came to be.

When the planning stage of RNO-G began in 2019, it was natural to look the ARA design as a jump-off point for the next generation of downhole HPol antennas. The goal became to maintain or improve the advantages of the design while reducing the disadvantages. Specifically, the ARA antenna was complicated, heavy, and expensive. Despite the benefit of ferrite cores, they contributed significantly to the cost, weight, and complexity of the antenna, so minimizing losses from their omission in a future design was a key development goal. The goals for designing RNO-G HPol antennas were:

1. No ferrites
2. Broadband
3. Gain matches VPols
4. Lightweight
5. Sensitivity at Low Frequencies (turn-on frequency near $\sim$ 300 MHz)
6. Maximize the available space

Though the ARA HPols were a possible starting point, the RNO-G HPol development largely started from scratch. The first iteration of development focused on simulation, comparing the simple dual-slot, tri-slot, and quad-slot antennas with no ferrite loading. These simulations were conducted by colleagues at California Polytechnic State University (Cal Poly) using a simplified antenna model corresponding to a 5 inch diameter antenna consisting of thin copper cylindrical segments connected to a central feed readout (Figure2.32). The 5 inch diameter was the maximum diameter available for the expected boreholes (with clearance considerations). From simulation it was determined that a tri-slot design achieved sufficient azimuthal symmetry in gain and had the desirable low-frequency turn-on point compare. These 5 inch diameter copper tri-slot antennas will be referred to as CTS5 (Copper Tri-Slot, 5 inch diameter, $\sim$300 mm height) antennas moving forward.

I began work on the RNO-G HPol project shortly into the prototyping phase, as the first CTS5 antennas were being built. Most of the prototyping and design work was conducted at Chicago by me, with efforts continuing at Cal Poly and later at Penn State by Bryan

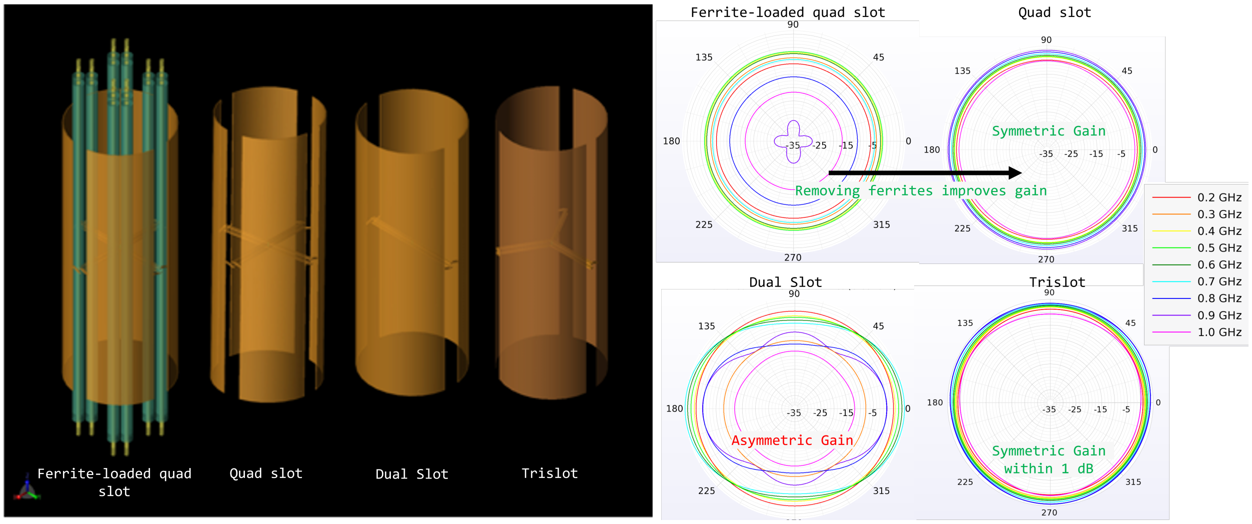

Figure 2.32: Left: Models of the simulated antennas in early HPol development. Right: Resulting azimuthal gain patterns at various frequencies. Source: Reference [163].

Hendricks, who worked on XFdtd simulations that mirrored the various iterations of prototype antennas. Short term changes were motivated by in-lab testing at Chicago, through antenna measurements and Smith charts (discussed in Appendix A and Section 2.5.3), while longer term changes were motivated by simulations from Penn State. Feedback from the simulation was initially limited due to a mismatch between simulated behavior and actual measurements in the lab, however results eventually converged late in the process. Further details on testing methodology and the general design loop are described in Section 2.5.3.

The base structure of the CTS5 antennas was provided by a polycarbonate tube. Rectangular panels of thin copper foil were cut to specified size and taped in place on the antenna. Through-holes provided access for wires to be soldered in-place connecting the conductive panels to a three-dimensional tri-wing feed. Each feed arm is a PCB with two series traces and two shunt traces which are populated by passive circuit components for impedance matching network tuning (Section A.1). The baseline non-matched configuration consists of 0 Ω resistors shorting each of the series traces, with the shunt traces remaining unpopulated. The 3 feed arms are soldered into a central PCB, which has an SMA connector for readout. The feed and antenna can be seen in Figure 2.33. Many variations of this basic antenna structure were tested, varying parameters such as the components used in the matching network, the height of panels, the size of the slot, and the shape of the slot (with attempts to replicate bow-tie like antennas).

Through this significant and lengthy iteration process it became clear that the existing CTS5 design was too fragile and inconsistent, resulting in unreliable measurements that were difficult to replicate between Chicago and Cal Poly. Significant sources of variation came from inconsistencies in the cutting of copper panels, amounts of solder, wire gauge, and matching network components. It was decided to move away from the wire connection to the feed. Instead, the copper panels would be cutout such that they could directly be soldered to the center feed. A laser-cut stencil was produced to ensure consistent panel and connection shape (Figure 2.33), with a 3D printed alignment cylinder also being produced to provide quick guidelines for consistent panel installation (Figure 2.34). Though these added tools would be insufficient if the design were to reach production scale, they significantly improved consistency during the prototype phase.

This shift aimed to solve many of the outlined issues but introduced a more delicate design by swapping sturdy cable connections to think copper tab connections. This was solved with the creation of inset braces which would be used significantly increase the structural integrity of the feed and provide convenient contact points for set screws. These braces saw several collaborative design iterations, with the finalization of the design, CAD drawings, and ordering being completed by me. These parts were water-jet nylon, and can be seen in Figure 2.33.

Efforts to produce robust and consistent CTS5 antennas proved challenging, and efforts shifted towards an aluminum design which could be professionally machined from a single cylinder for optimal consistency. For simplicity in design an electrically “closed” antenna structure was also considered at this time, meaning the top and bottom of each slot would be electrically connected. These significant changes were simulated in XFdtd by Penn State.

Figure 2.33: An overview of the 5in diameter 340 mm tall antenna prototypes. Top Left: An early CTS5 prototype, using standard slot geometry and wires for electrical connection to feed. Top Center: The CTS5 tri-wing feed with nylon braces, fastened inside non-populated polycarbonate tube. Top Right: The direct tab connection from panel to feed used in later versions of CTS5. Bottom Left: An ATS5 prototype. Bottom Center: The ATS5 tri-wing feed with tin-coated steel contacts (nylon braces not installed), fastened inside polycarbonate tube for visibility. Bottom Right: The tin-coated steel contact connection elements to ATS5 feed.

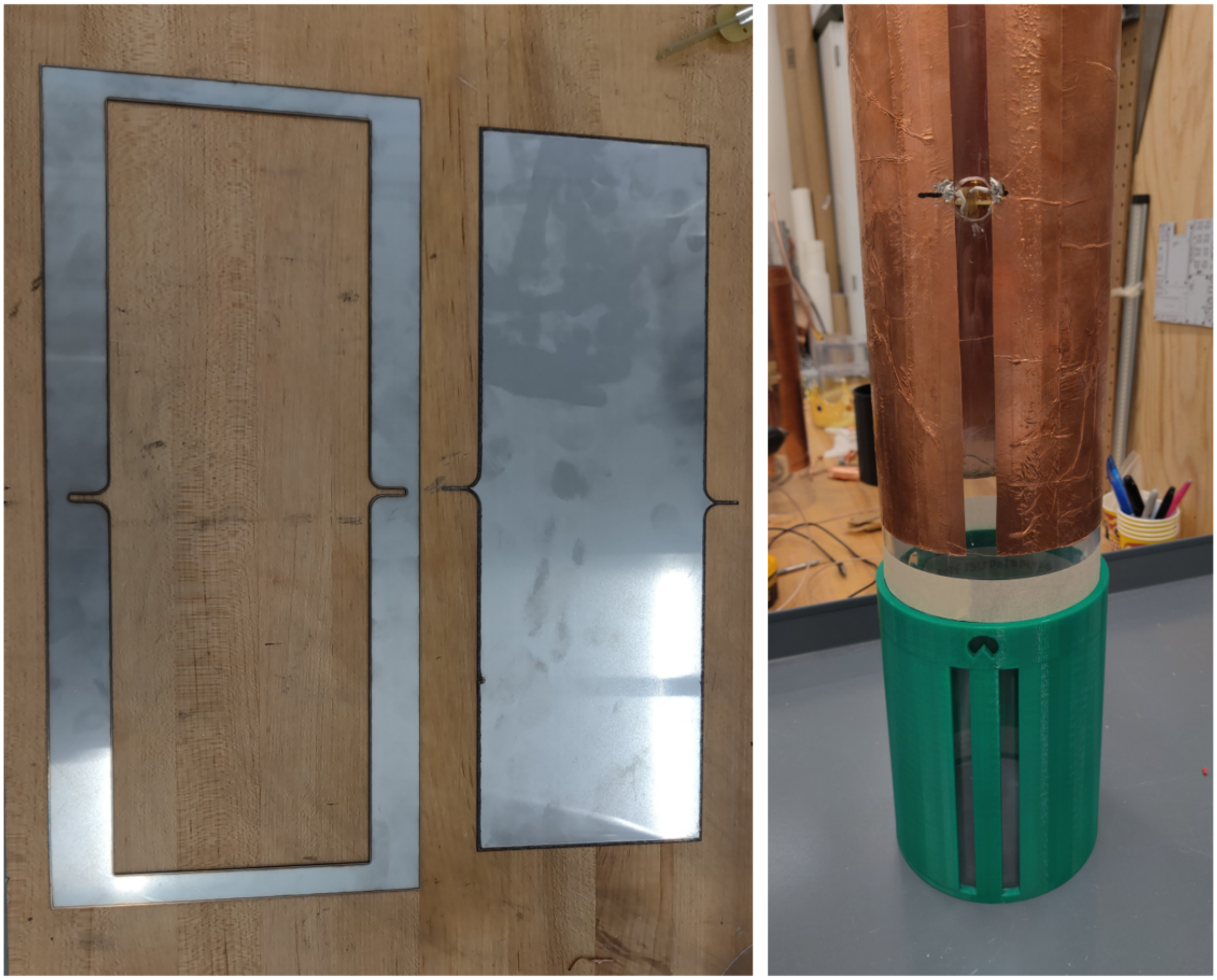

Figure 2.34: Left: The laser-cut stencil used for producing consistent copper panels. Right: The 3D printed stencil which provided guidelines for consistent panel placement and through-hole positioning.

A standard tin-coated steel tab was used for electrical connection to the feed, being screwed into the aluminum frame and soldered to the feed insert. This version of the antenna will be referred to as ATS5 (Aluminum Tri-Slot, 5 inch diameter, 300 mm height). Relevant pictures of the ATS5 prototype can be seen in Figure 2.33. The transition to a more professionally machined architecture necessitated modeling to ensure proper integration of all parts, and such that CAD drawings could be provided for manufacturers. Design drawings for these parts and others described later can be seen in Figures 2.36, 2.47, 2.44, 2.45, and 2.46.

The ATS5 antennas proved consistent and capable but were short-lived due to a change in drill resulting in a new, larger borehole size. Simulations were conducted by Penn State to investigate the potential performance of 8, 9, and 10 in diameter aluminum and copper antennas, ranging in heights of 34 cm to 70 cm (Figure2.35). XFdtd simulations were developed using a simplified feed to get a baseline measure of the unmatched performance via the reflection coefficient (S11). The resulting curves were then shifted using the commercial antenna matching software Optenni Lab to apply the effects of a matching network comparable to what had been used in previous prototypes. The increase in diameter was shown to produce gain improvements, but broke the near-asymmetry that the tri-slot was capable of providing when implemented at a lower antenna radius. Because of this a quad-slot design was considered and simulated as well, which showed improvements in azimuthal symmetry.

The extremely tight time constraints for this research and development process motivated immediate finalization of a design such that parts could be ordered in-time for deployment. Results from testing and simulations were combined with practical considerations such as cost, weight, and consistency to guide us towards the decision to produce 8 inch diameter aluminum quad-slot antennas, which had a height of 60 cm (referred to as AQS8 antennas). High-quality 3D models were created for each of the necessary parts, including a redesigned tri-slot PCB feed to support the large diameter quad-slot architecture. Designs were also drafted for nylon endcaps which house the associated electronics and provide support for

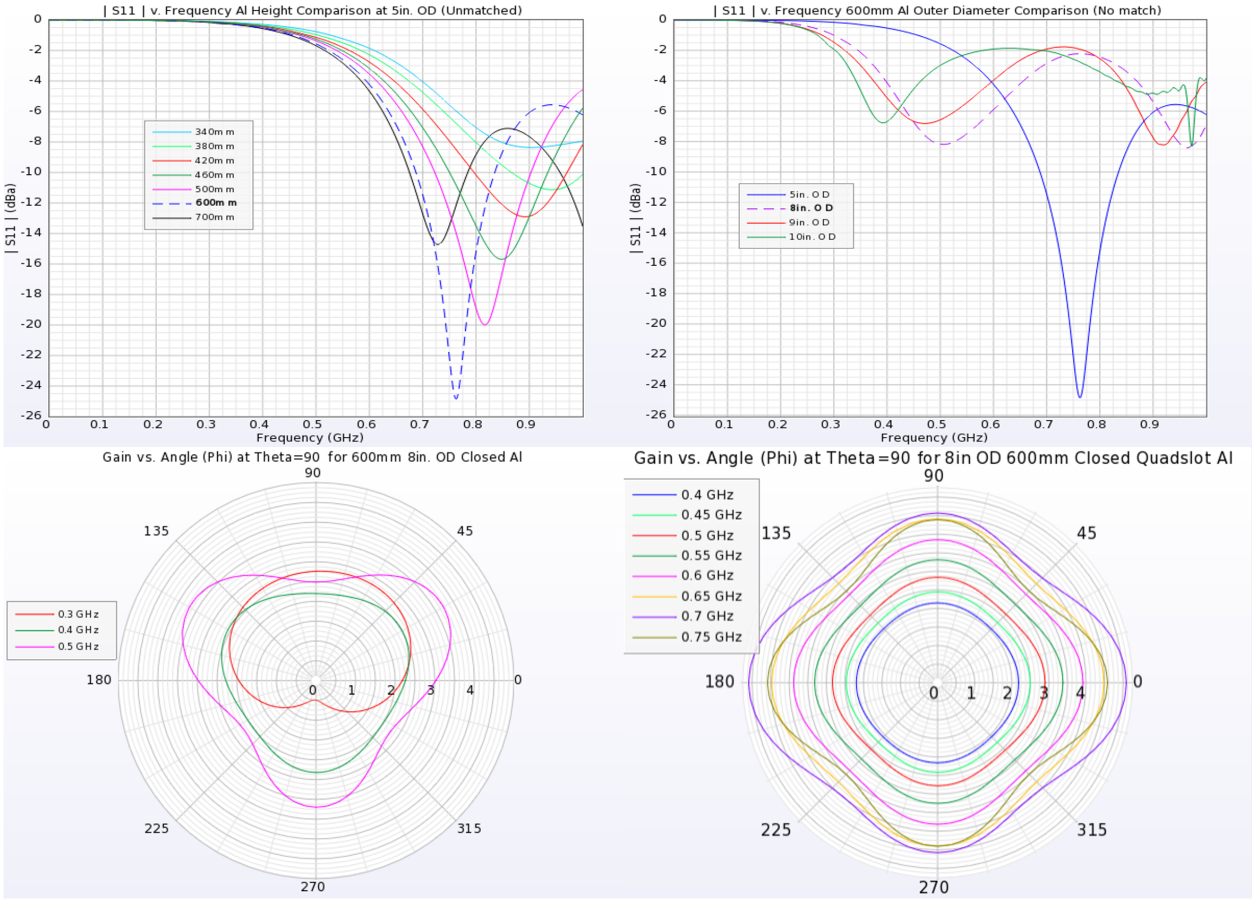

Figure 2.35: Results from XFdtd simulations performed at Penn State for various antenna lengths and diameters. The transition from ∼5.5 inch boreholes to ∼11 inch holes motivated investigation of larger antennas. Simulations, weight, and cost all contributed to the final version using an 8 inch diameter and 60 cm length.

ropes which support the antenna in the boreholes. Design drawings can be seen in Figures 2.36, 2.47, 2.44, 2.45, and 2.46. With the mechanical designs finalized my work efforts shifted to other projects, however efforts continued at Penn State with the AQS8 antenna to refine the matching network before deployment. I present the current status of the HPol antennas, as well as the final designs for the AQS8 antennas in Section 2.5.4. The fully assembled model can be seen in Figure 2.36.

2.5.3 Prototyping and Design Methodology

A summary of the major developments in the research and development process is presented in Section 2.5.2. Here I present an overview of some of the methods used in testing the prototypes and motivating design iterations.

As mentioned in Section 2.5.2, the development process for the RNO-G HPols was highly time constrained, with my efforts starting in early 2020 and largely ending by the beginning of 2021. This timeline means that the research and development phase occurred largely during the first few months of the COVID-19 global pandemic, which contributed to a development cycle that had to work around long-lead times, reduced personnel and parts availability, and limited or cumbersome access to lab spaces. The main ramifications of this were felt in early CTS5 antennas, which were largely built with spare parts. During the testing process I built these antennas by-hand, cutting copper element panels in the various shapes tested, assembling and soldering the feeds and matching network components. The range of matching network components initially consisted of the values available at Chicago, which set the zero-point reference from which variations would be motivated and new parts ordered.

The relative success of an antenna can often best be determined through frequency-dependent measurements of the so-called scattering parameters (often called S-parameters, representing elements in the scattering matrix), which measure the power emitted and re-

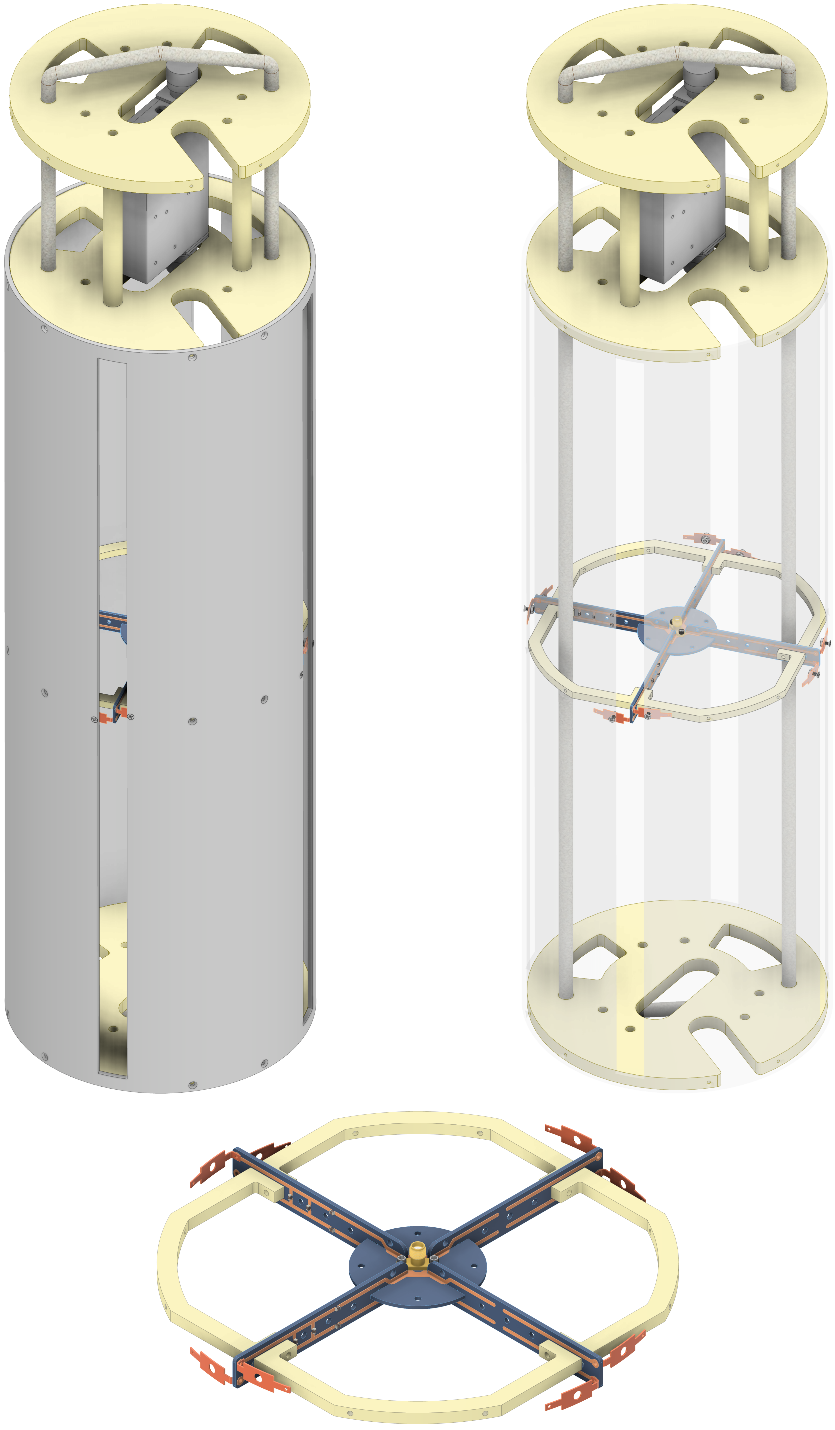

Figure 2.36: Top: Models of the fully assembled 8 inch diameter 60 cm tall quad-slot (AQS8) antenna produced in AutoDesk Inventor, with the aluminum cylinder opaque (left) and transparent (right) for visibility. Bottom: Model of the redesigned quad-slot feed with nylon bracers and tin-coated steel contacts. In-line matching network traces are visible on each spoke.

ceived through two points in a system. Relevant to testing the RNO-G HPol antennas are the $S11$ and $S21$ reflection coefficients, which refer to the power transmitted through port 1 of a FieldFox vector network analyzer and received through port 1 or 2 respectively. $S11$ is easily the most convenient measurement, as it only requires a single port and antenna for the measurement. By measuring the ratio between emitted and received power within a single antenna, $S11$ effectively measures the power that has been reflected back by the antenna, rather than being emitted as radiation. This measurement depends on the fact that the ability for an antenna to radiate power is often one-to-one with its ability receive power; for instance, a RX $\lambda/2$ dipole has peak sensitivity to signals with wavelength λ, while a pulse through the same dipole would emit predominantly wavelengths of λ.

In Appendix A I discuss the reflection coefficient Γ in the context of Smith charts. This coefficient represents the quality of an impedance match, with $\Gamma \sim 0$ corresponding to a good match with small amounts of reflections, and thus a high level of power transmission. $S11$ and Γ are equivalent, which gives rise to the value of Smith charts, where a direct measurement of $S11$ can be plotted in complex polar coordinates and superimposed with the guidelines of the Smith chart. This was done as a matter of course when developing the CTS5 and ATS5 antennas. An antenna would be built, with a matching network only being populated where necessary by 0 Ω resistors. An $S11$ measurement would be taken and interpreted in polar coordinates such that appropriate matching network components could be included. The feed would then be replaced by a feed with added series capacitors and shunt inductors, and the resulting antenna would again be measured. The overall goal of the matching network was to move as many frequencies as possible of the $S11$ values closer to $\Gamma = 0$, such that a high gain broadband match is achieved.

As the simulations were not yet reproducing the in-lab results, attempts were made to expand the predictive abilities of Smith charts by taking measured $S11$ curves and observing their behavior as matching network values are varied using the rules defined in Equation A.5.

Adjusted effective values of L, C, and R were initially used for these calculations to account for the three-fold antenna architecture (quad-fold for quad-slot), which has identical matching network components being installed on each of the 3 arms. These effective values used the typical rules for combining parallel and series components to simplify circuits. Though this initial assumption was well-founded, experimentation revealed that the effective value conversions were not necessary, and the observed variations corresponded to the raw circuit component values. This result was unexpected and shifted the way of conceptualizing the antenna from a single antenna with one feed split across three equivalent arms, to instead thinking about the antenna as three distinct antenna elements that were in electrical contact, but ultimately consisted of their own element and matching network. An example predicted $S11$ curve is shown in Figure 2.37.

The goal of matching these antennas is to achieve a broadband match with a low turn-on frequency. To quantify the quality of the match for each set of network values the portion of the band that was below a set decibel value in $S11$ was calculated for each network, with a typical value set near the goal $S11$ value of -4 dB. Figure 2.38 shows the resulting metric for a variety of series capacitor and shunt inductor values for an ATS5 antenna. Though this plot shows a clear peak, the stability of the peak is also a desirable trait such that variations in production quality has minimal performance characteristic differences for the antennas.

ATS5 Though $S11$ measurements give quick feedback, they are only a measure of the power lost through the antenna. Though most of this power can generally be assumed to be radiated, some losses can occur due to the setup and environment, as well as from thermal losses. To get a more accurate measure of the antennas performance for measuring radiation it thus preferable to perform an $S21$ measurement such that the antenna is actually used for receiving. $S21$ typically requires two antennas connected to separate isolated ports, and separated by a known distance. Signals are sent through one antenna and received by the other, with the loss in signal being a direct measure of the free space path loss (FSPL).

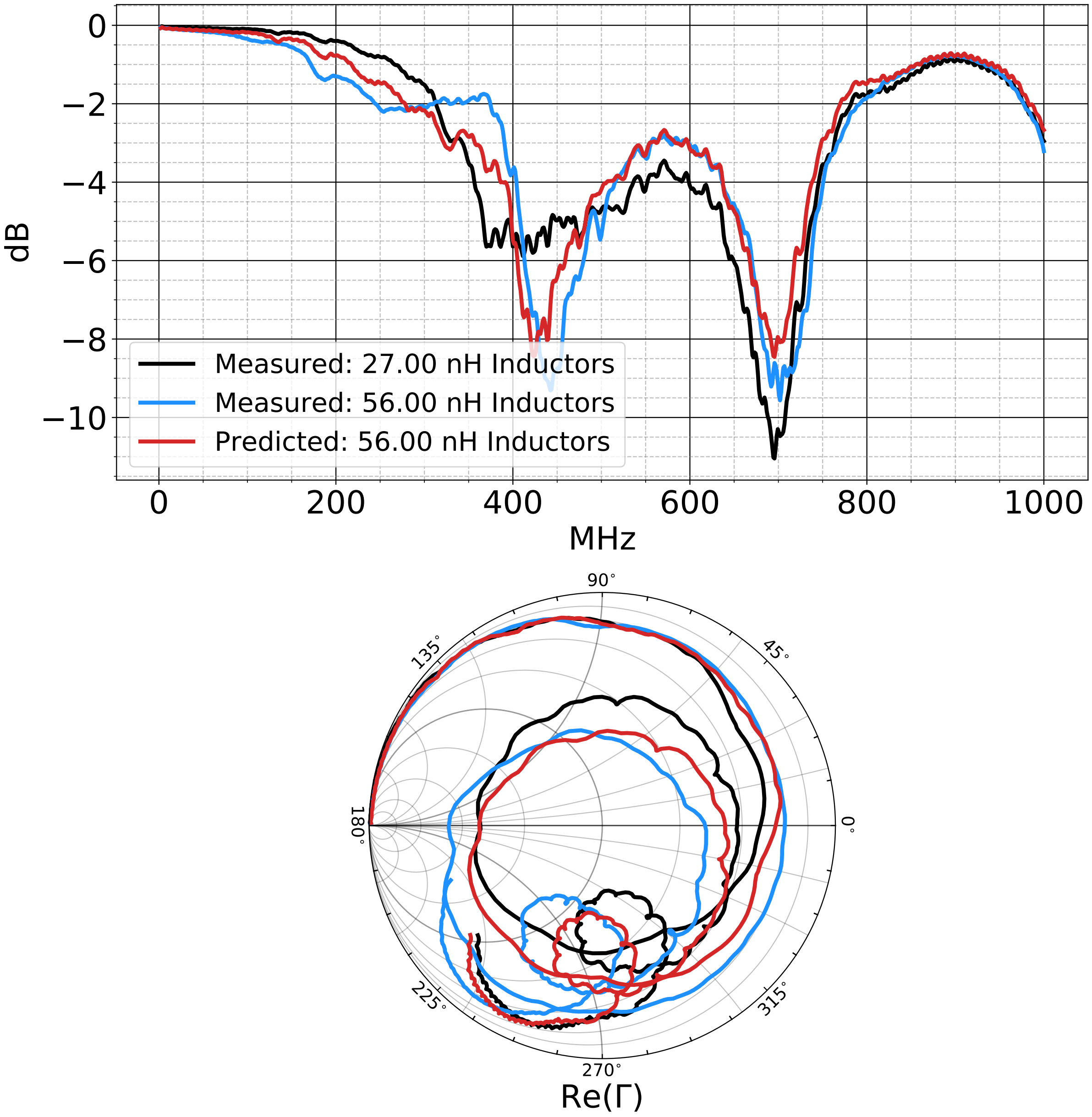

Figure 2.37: Initial measurements of an $S11$ curve for 27 nH shunt inductor, alongside the predicted $S11$ if the data was shifted to a 56 nH shunt inductor. A measurement of the same antenna with the 56 nH shunt inductor is also included for comparison. The difference between predicted and measured 56 nH shunt inductor curves is a result of unintended decreases in shunt resistance caused by the new shunt inductor.

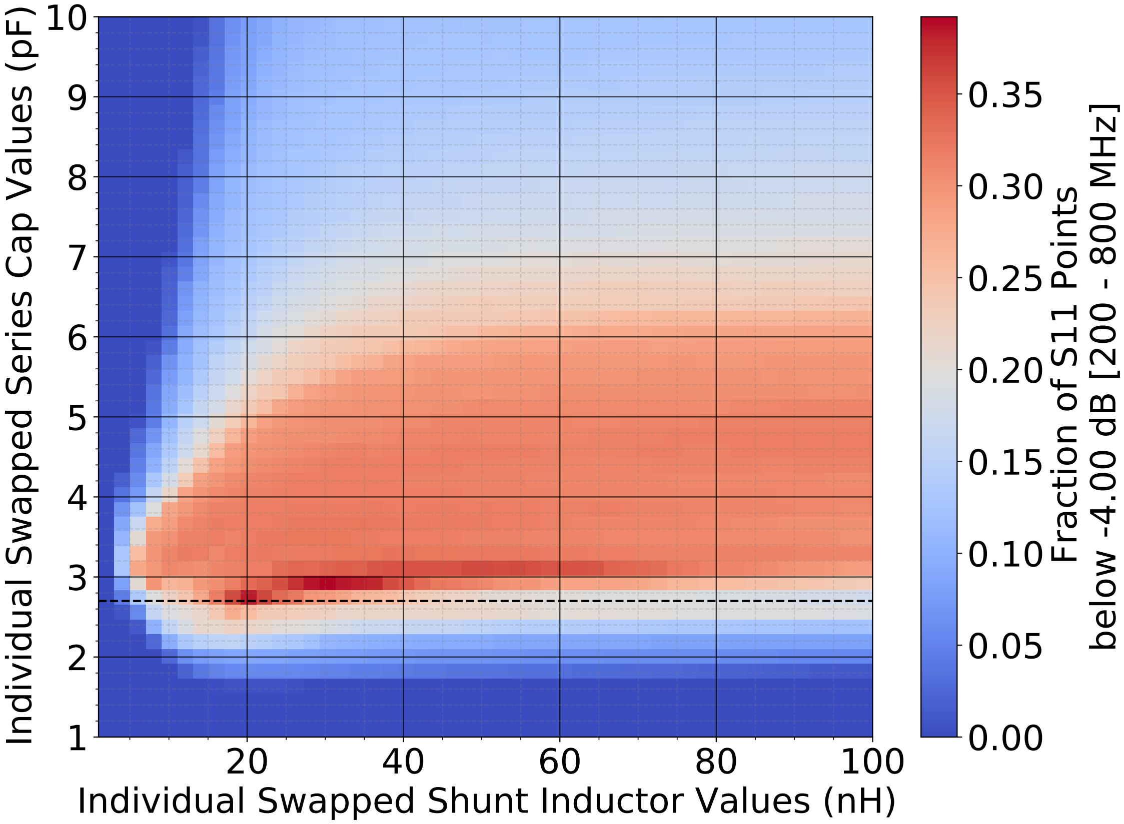

Figure 2.38: The fraction of $S11$ values below -4 dB for various shunt inductor and series capacitor values for an ATS5 antenna. Calculated by varying the $S11$ using Equations A.5 from initial measurements taken with 2.7 pF capacitors (indicated by the black dashed line).

The equation for FSPL is given below in Equation 2.17 for known transmitter and receiver gains (G_{TX} and G_{RX} respectively). To obtain the purest measure of RX performance, $S21$ measurements are typically performed using either a standardized known TX antenna, or an identical antenna to the RX antenna. If both RX and TX antennas are nominally identical (with same gain, G), then this equation can be rearranged such that the Gain can be experimentally determined through a FSPL measurement, as shown in Equation 2.18.

$$\mathrm{FSPL} = 20\log_{10}(d) + 20\log_{10}(f) + 20\log_{10}\left(\frac{4\pi}{c}\right) - G_{\mathrm{TX}} - G_{\mathrm{RX}} \tag{2.17}$$

$$G = \frac{1}{2}\left(20\log_{10}(d) + 20\log_{10}(f) + 20\log_{10}\left(\frac{4\pi}{c}\right) - \mathrm{FSPL}\right) \tag{2.18}$$

where d is the distance between the antennas, f is the frequency of light, and c is the speed of light. $S11$ measurements were taken significantly more frequently than $S21$ due to only requiring a single antenna, and being logistically easier in all ways, however $S21$ measurements were often conducted in the late stages of each antenna design. A typical setup can be seen in Figure 2.39. Both $S21$ and $S11$ measurements were done using elevated antennas with attempts to minimize local conductive surfaces. An RF quiet chamber is available at Chicago; however it is not sufficient in size for $S21$ measurements, and the time of setup requirements largely excluded its usage for $S11$ measurements which were taken quickly and often.

These techniques provided additional insight into the HPol prototypes and were used extensively. A preliminary matching network was obtained via direct measurements and the procedures outline above. With the mechanical designs of the AQS8 antennas finalized, and a preliminary matching network obtained through testing. Work continued at Penn State to refine the simulation such that it reproduced the in-lab measurements. A transition in simulation away from a simplified feed towards the actual feed that I designed proved crucial for replicating results. Figure 2.40 shows the simplified and realistic feed models. The

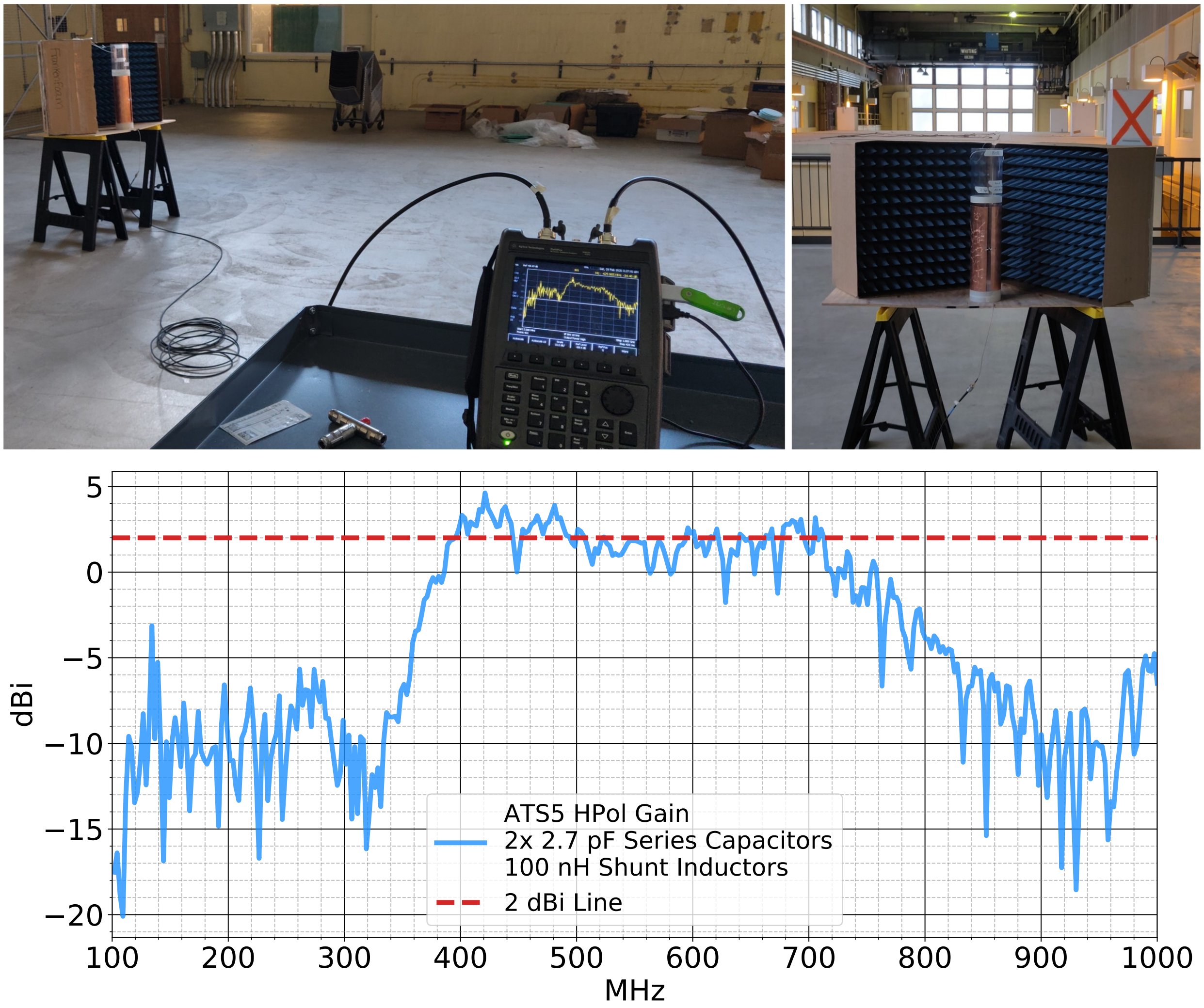

Figure 2.39: Top: HPol S21 measurement setup. Top Left: The view from the network analyzer showing the TX antenna on the left. Top Right: A frontal view of the RX antenna, which is out of frame of the left picture. Each antenna was elevated with non-conductive material and RF noise absorbing foam was used for backing. Bottom: The measured gain for an ATS5 antenna calculated using Equation 2.18.

realistic model resulted in a significant increase in run time for the simulation but eventually lead to a reliable and replicable output. The simulation was then used to motivate the final matching network which was deployed in the field. More details about the production and deployment of the AQS8 antennas is provided in Section 2.5.4.

2.5.4 Deployment and HPol Conclusions

The AQS8 HPol antennas were developed from 2019 through to early 2021. The final design consisted of an 8 inch outer diameter aluminum tube. Each tube was professionally machined to contain four 20 mm slots and a series of set-screw through holes using the designs I produced shown in Figures 2.36, 2.47, 2.44, 2.45, and 2.46. Each antenna had a feed consisting of four arms, each with two series 13 pF capacitors and one 68 nH shunt inductor. Feed arms are electrically connected to the antenna element via tin-coated steel tabs where were soldered to the feed arms and screwed into the element frame. Nylon braces subtended the feed arms for structural support, with set screws securing the braces to the frame independent of the electrical connection. Nylon endcaps were screwed into the top and bottom of the antenna, with a second end cap being used at the top of the antenna separated by nylon support columns to provide a gap for the front-end electrics to sit. This secondary top cap did not have machined and threaded edge holes to save costs as it was not inserted into the antennas. An SMA port connect the feed to the front-end electronics, consisting of an LNA and RF-over-fiber optical transmitter (RFoF) which converts the conventional electrical signal into light such that it can be transmitted to the surface DAQ over low-loss fiber-optic cables. Specifics of the RNO-G hardware beyond the HPol antenna are discussed further in Section 2.4.

For the first deployment season of RNO-G (2021) 10 stations worth of material (with extra) were ordered and constructed. For the HPols this meant a total of 60 full antennas were built in the lead-up to the 2021 deployment. Partial construction occurred at Penn

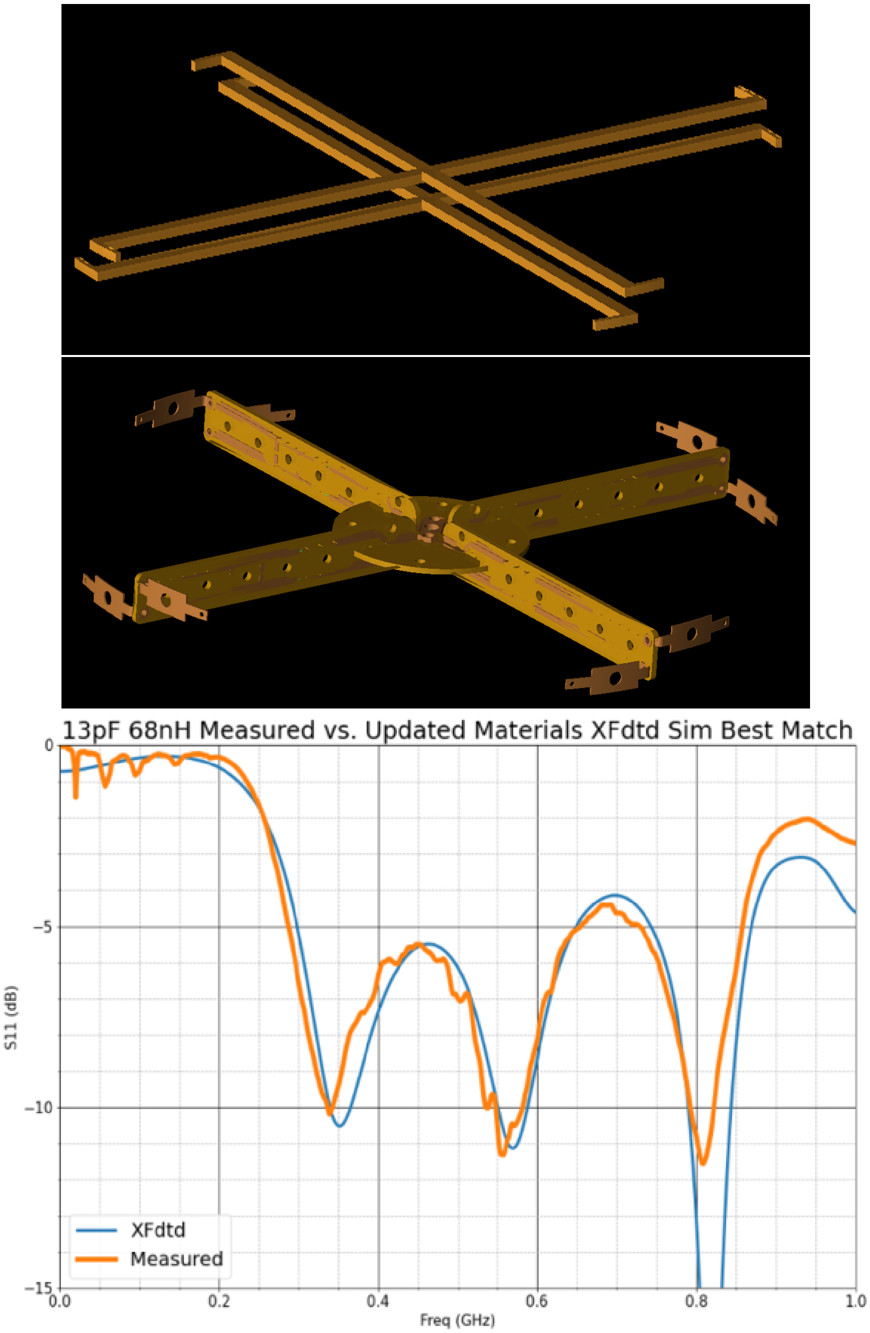

Figure 2.40: Top: The simplified simulated quad-slot feed. Middle: The realistic quad-slot feed implemented late in development. Bottom: The $S11$ measured in air compared to results from the simulation. Values below -5 dB represent a reflection of ∼50%, which was used as a reference level of merit. The deployed antenna had a turn-on frequency of 300 MHz and bandwidth of ∼475 MHz in air.

State, with all 60 antennas being shipped to Greenland in the summer of 2021 (Figure 2.41). These shipped antennas consisted just of the elements and feeds, with the endcaps and front-end electronics being added at Summit Station. The 2021 season saw the deployment of 3 stations, with the remaining hardware on-deck for installation in the summer of 2022 which saw a further 4 stations deployed. A breakdown of the raw material costs for the 60 AQS8 antenna is given in Table 2.1. Pictures of the partially assembled HPol antennas being deployed in the ice at Summit Station in Greenland are shown in Figure 2.42.

Line #	Part Name	# Ordered	Price Per Part	Price
1	Aluminum Tubes	60	\$154.51	\$9,270.60
2	Feed Inserts	240	\$44.24	\$10,617.60
3	Nylon Strut	120	\$11.30	\$1,356.00
4	Nylon Cap, Threaded	120	\$87.79	\$10,534.80
5	Nylon Cap, No Edge Holes	60	\$57.36	\$3,441.60
6	PCB Feed Hub	80	\$6.28	\$502.40
7	PCB Feed Spokes	350	\$1.72	\$602.00
	Full Assembly	~60	\$600.17	\$36,010.20 (60 Antennas) + \$314.00 (spare parts) = \$36,325.00

Table 2.1: Material costs of 60 HPol antennas as produced in preparation for the 2021 RNO-G deployment season. Cost of circuit components considered negligible and ignored.

With seven stations deployed by the end of 2022, 28 HPol antennas were buried in-ice (two on the power string, one per helper string, seven stations), each at depths below 90 m. The antennas have already proven to be functional, with the first-deployed antennas having already survived two seasons. Shortly after the 2021 deployment pulsing signals were emitted from the VPol calibration pulsers on the helper strings. As the pulser is VPol, the signal as viewed from the HPol antennas is not ideal, however it shows the ability of the HPol antennas to operate and receive radio signals in the ice. Figure 2.43 shows signals from the pulser at three of the four HPol antennas within that station (excluding the HPol which was 1 m from the calibration pulser).

Figure 2.41: Top: Several assembled quad-slot feeds before installation. Bottom: Partially assembled AQS8 HPol antennas before being shipped to Greenland. Photos courtesy of B. Hendricks.

Figure 2.42: AQS8 HPol antennas being deployed in Greenland. Photos courtesy of C. Welling.

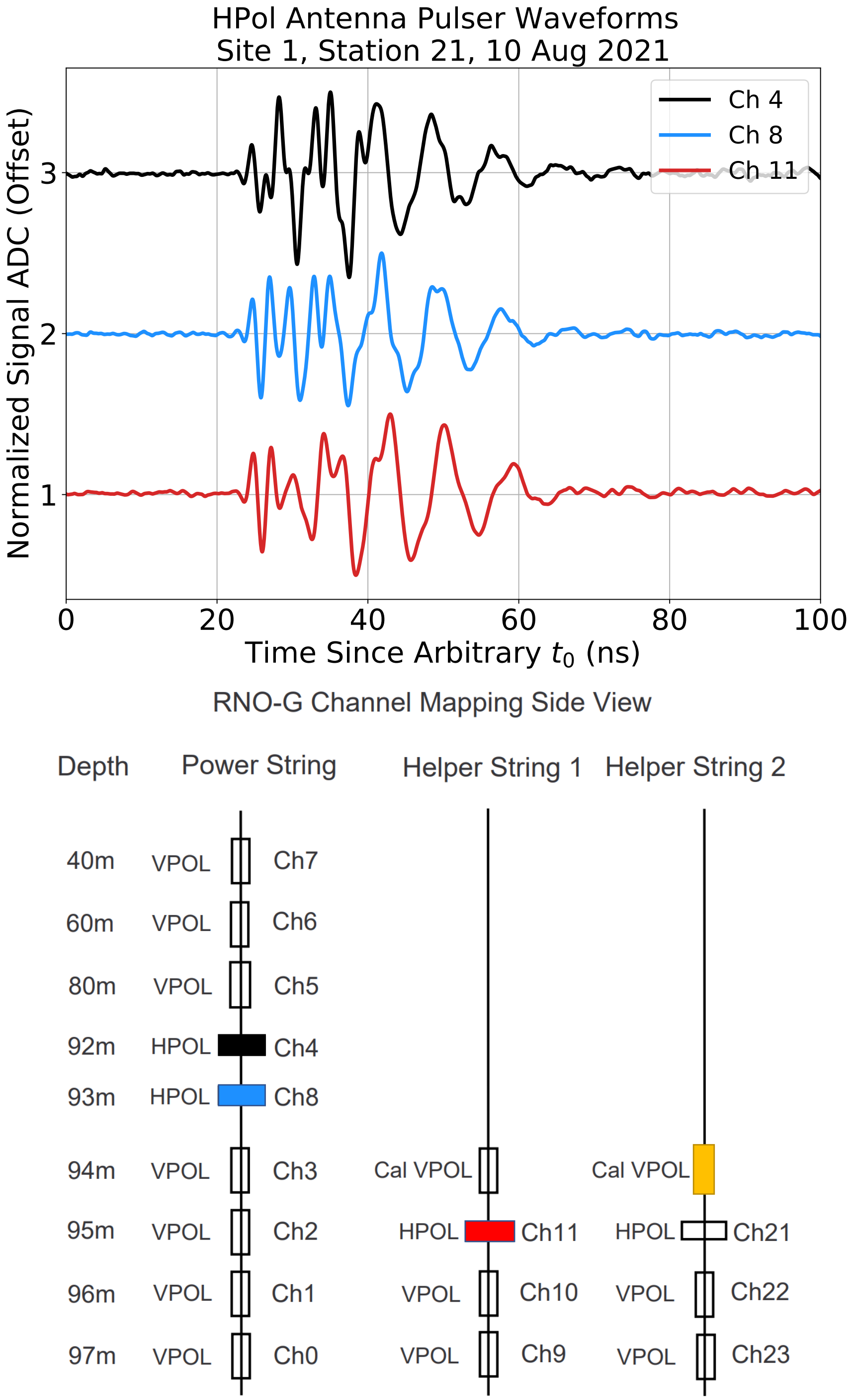

Figure 2.43: Top: Waves as seen through the several AQS8 HPol antennas in-ice in Greenland. Bottom: A schematic view of the channel mapping. The signal was emitted from the calibration pulser on Helper String 2, and was received by the HPol antennas in channels 4, 8, and 11.

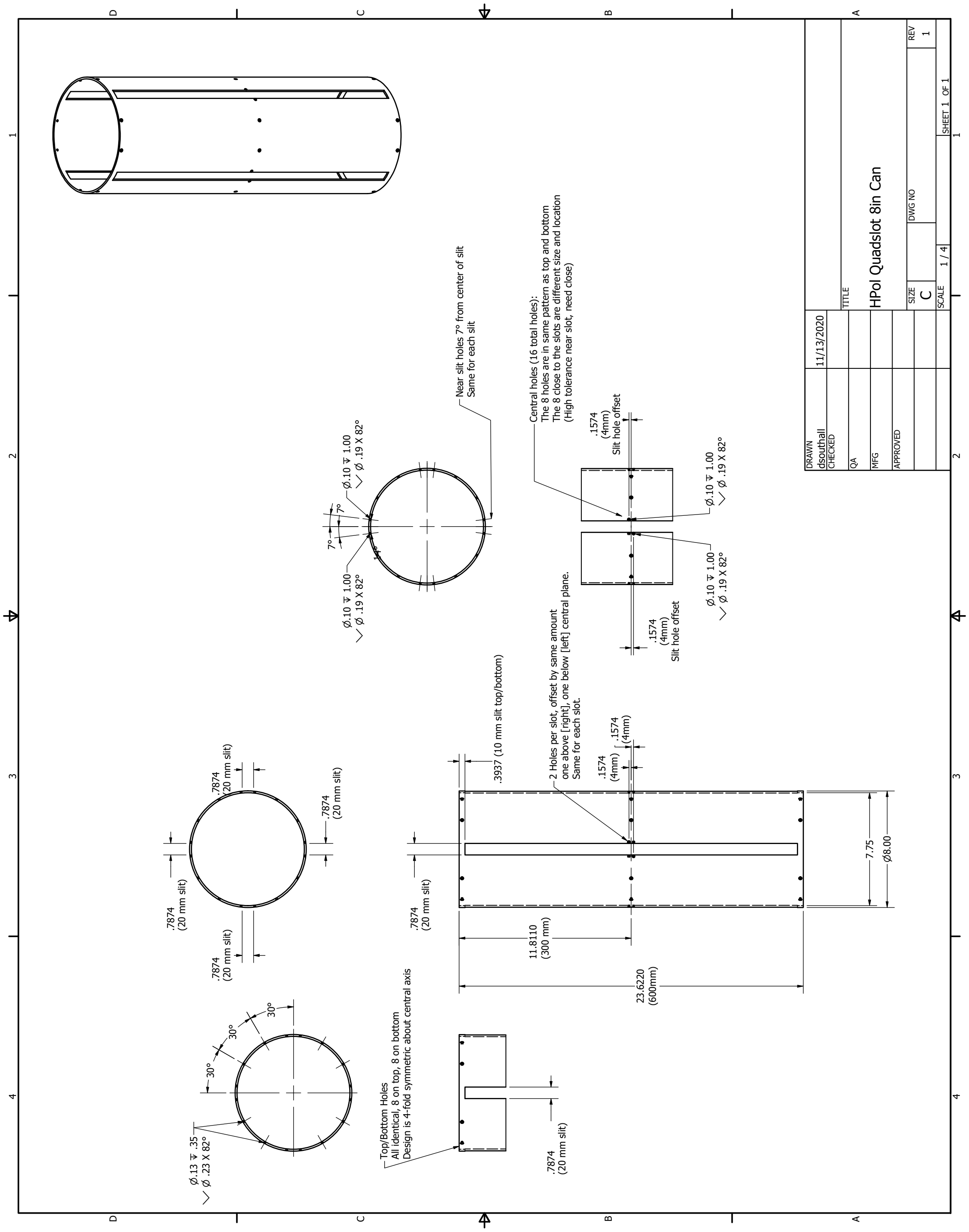

Figure 2.44: AQS8 aluminum frame design.

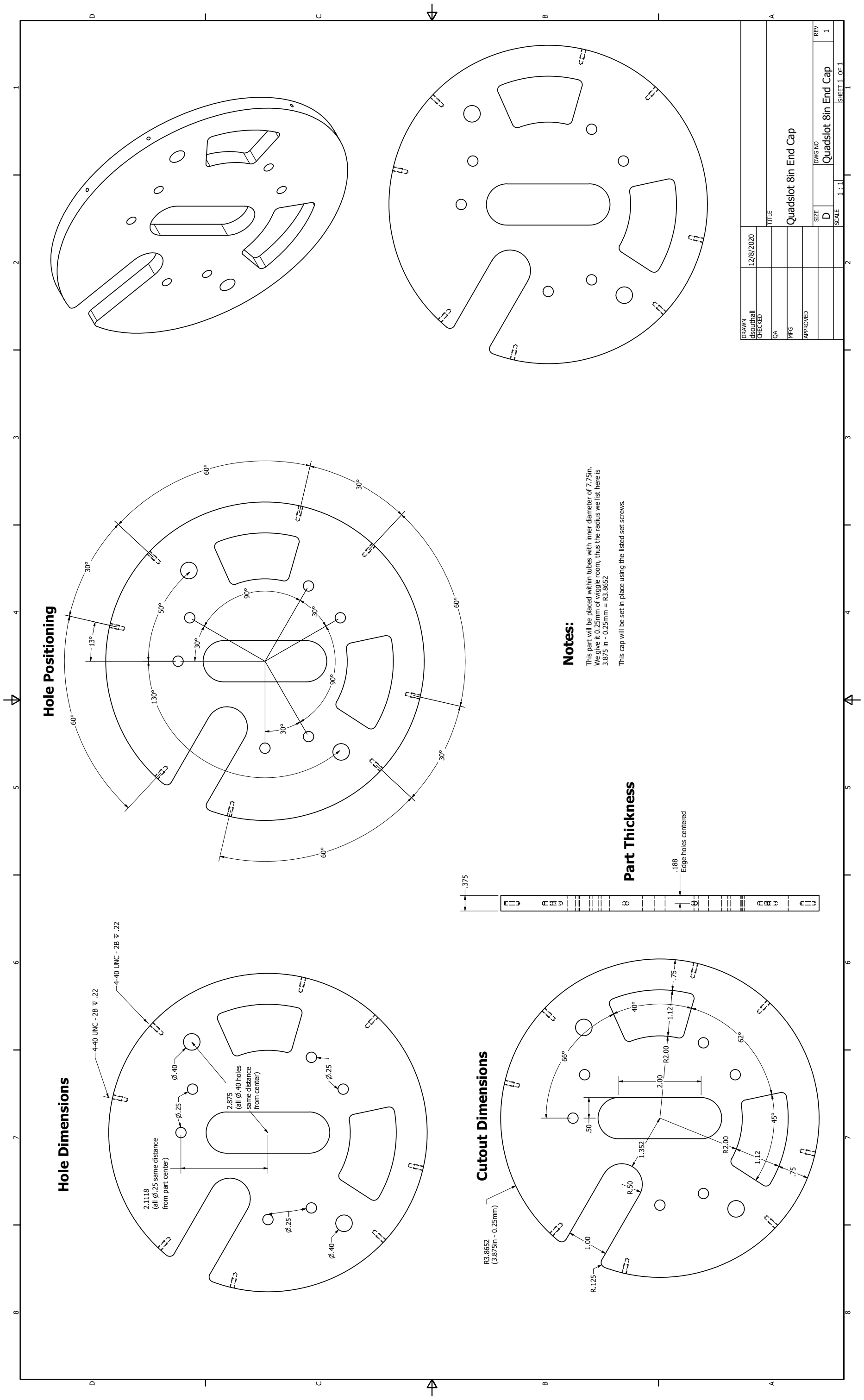

Figure 2.45: AQS8 nylon end cap design.

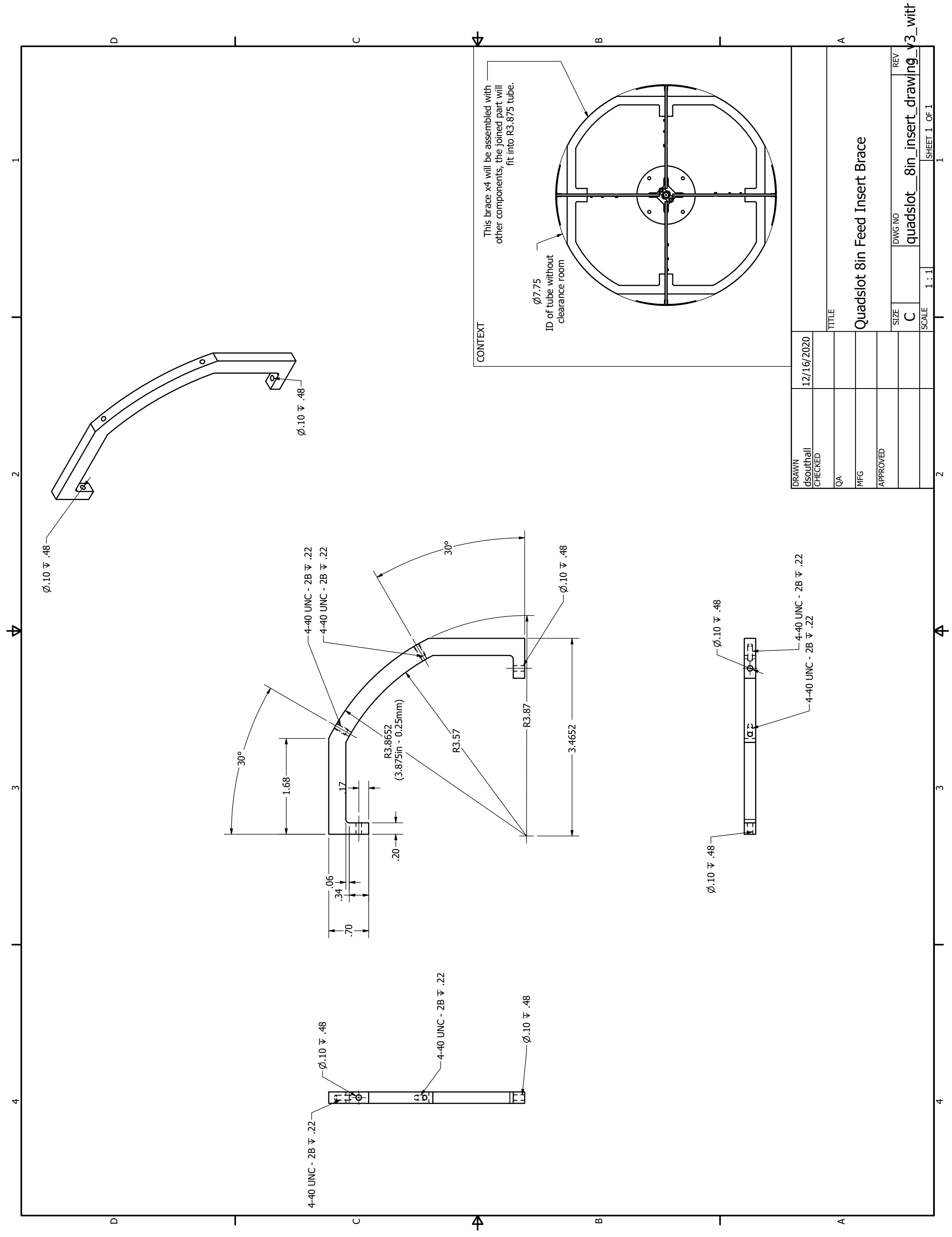

Figure 2.46: AQS8 nylon feed brace design.

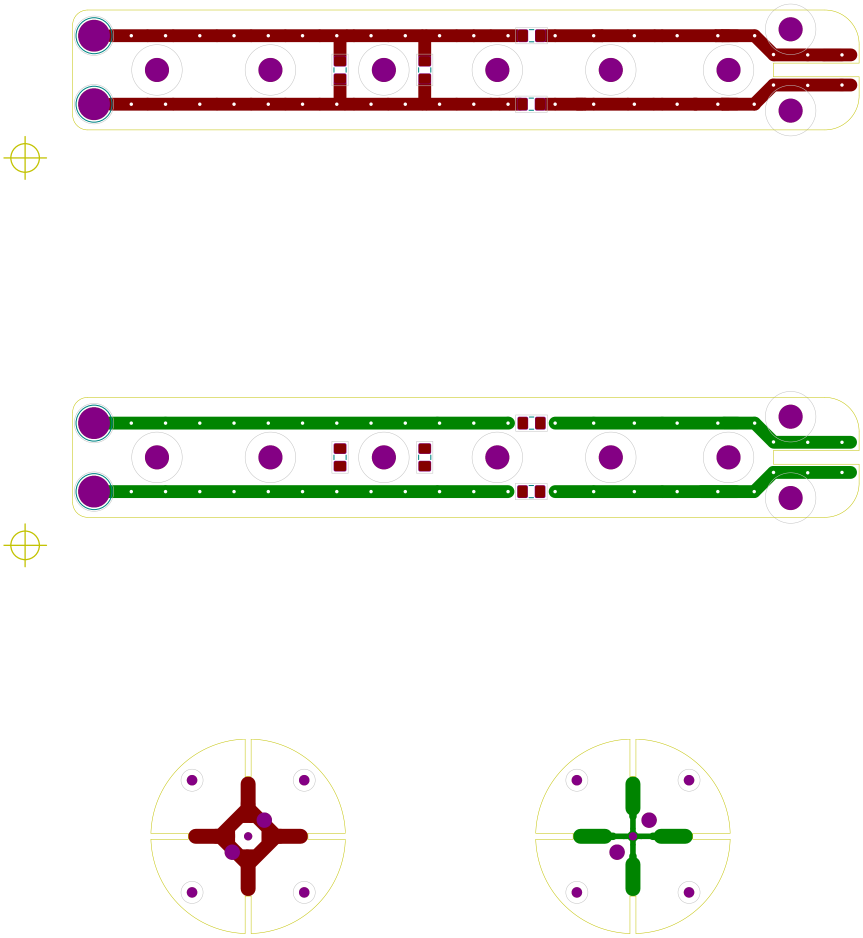

Figure 2.47: AQS8 feed PCB design. The top two plots show the traces on the front (first) and back (second) of the custom feed arm designed for the 8 inch diameter slot antennas. Each feed arm consisted of out-going and in-going traces, each with pads for series components. The out-going and in-going traces are electrically connected to each side of a single slot. Two pads are provided per feed arm for shunt components. Bottom: The front (left) and back (right) traces of the custom quad-slot feed hub. Feed are oriented orthogonal to the board and soldered in place, achieving a three-dimensional feed structure. An SMA readout connector is screwed and soldered in-place in the center of the hub. Designed exported from KiCad.

CHAPTER 3

THE BEAMFORMING ELEVATED ARRAY FOR COSMIC NEUTRINOS (BEACON)

Significant portions of this chapter are from the BEACON prototype instrument paper for which I am the primary author [164]. This thesis will expand on certain sections of this paper and add details related to my work with BEACON that are not included in the paper.

3.1 Introduction

The Beamforming Elevated Array for COsmic Neutrinos (BEACON) is a concept for an Earth-skimming neutrino telescope (Section 1.4.2) which consists of mountaintop phased radio antennas that are designed for measuring the flux of tau neutrinos above 100 PeV [165]. At these energies, tau neutrinos interacting with the Earth via a charged current interaction can produce a tau lepton boosted enough such that it may escape the Earth and decay in the atmosphere [83, 84, 85]. The tau lepton decay creates an upgoing extensive air shower that will produce an impulsive radio signal. The primary emission mechanism is geomagnetic radiation, a result of the deflection of charges by the Earth's magnetic field, with contributions from Askaryan radiation [88]. Air shower radio signatures have been extensively studied by numerous radio experiments (see e.g. References [65, 66, 67, 68, 69, 166, 167] and References [63, 64] for recent reviews) and have been modelled at accelerator experiments [70, 71]. The probability that a tau lepton will exit the Earth peaks near and below the horizon [89]. This process is shown schematically in Figure 3.1.

There are several detector concepts around the world targeting the tau neutrino flux using this Earth-skimming technique, including particle detectors [92, 168], imaging Cherenkov and fluorescence telescopes [169, 95, 170], and radio arrays both on and near mountains [171, 172, 173, 98, 69] and on balloons [174, 100]. See Reference [175] for a recent review. The BEACON concept is distinct for using phased array triggering on a high-elevation mountain. At high elevation, each BEACON station views a large area over which a tau lepton can emerge. The combination of a large prominence and a steerable phased array trigger capable of triggering on events from hundreds of kilometers away provides an optimized detector design for neutrino searches near the horizon. A full-scale BEACON array would consist of $\mathcal{O}(1000)$ independent stations, creating a global network of low-cost high-elevation mountaintop radio arrays designed to search for these signals.

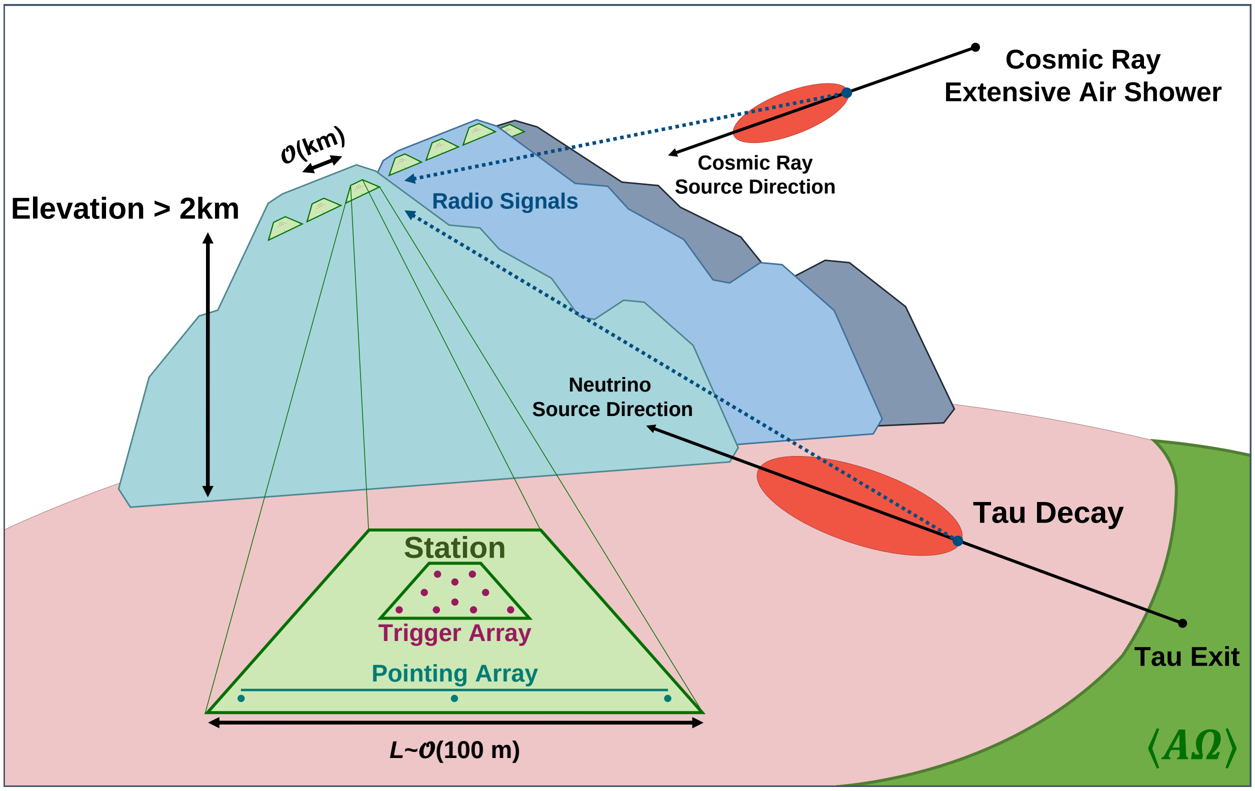

Figure 3.1: A schematic overview of the BEACON concept, adapted from [165]. Tau neutrinos interacting in the Earth can produce a tau lepton that escapes into the atmosphere, producing an upgoing air shower upon decay. Radio emission from the air shower may be detected by mountaintop radio stations, each consisting of a small antenna array used for triggering and reconstruction. BEACON stations are also sensitive to emission from cosmic ray-induced air showers, which will come from above the horizon, and may be used for detector characterization.

Phased array, or interferometric, triggering and reconstruction also offers additional benefits to the BEACON design [176]. Directional beams are formed by delaying and summing signals from individual antennas. The trigger is then formed on the coherent sum of the signals from each antenna, which has a higher signal-to-noise ratio (SNR) than the signal from each antenna for true plane-wave air shower signals, thereby lowering the energy threshold of the detector to 100 PeV [165] compared to triggering on individual antenna channels. Additionally, the trigger thresholds on each beam can be dynamically adjusted in response to changes in the local noise environment. These characteristics enhance the trigger's capability to reject anthropogenic radio frequency interference (RFI), which can help maintain sensitivity to the expected diffuse flux while in noisy environments.

A full-scale BEACON array would consist of many stations in various mountain ranges and countries. Though some sites might have existing infrastructure that can be leveraged, it is not a requirement for a BEACON site. Stations should therefore be capable of operating autonomously in remote environments at sites with little to no infrastructure. This means the system must be low-power and operate off-grid using either solar or wind energy. Stations should also be minimally capable of transmitting monitoring and house-keeping data off-site, with full data transmission desirable to remove the need for retrieval of hard disks. Finally, such an array must be easy to deploy, robust to weather and wildlife, and cost-effective.

Development towards the BEACON experiment has been focused on building a prototype. The goals of the prototype study are to evaluate the performance of an interferometric trigger used in this context, and to use the observed cosmic ray flux to measure the in-situ expected performance of the full-scale array. As shown in Figure 3.1, the prototype is also sensitive to extensive air showers initiated by downgoing cosmic rays.

Though the prototype instrument is not large enough to detect tau neutrinos, we expect to detect cosmic ray air showers with it. Cosmic ray air showers come from above the horizon, whereas signals from tau neutrinos would come from below the horizon. The observed rate of cosmic ray events in the prototype instrument can be ultimately used to determine its achieved sensitivity to tau neutrinos, allowing us to predict the sensitivity of the full-scale

BEACON experiment in a data-driven way.

Section 3.2 gives an overview of the BEACON prototype's design, hardware, and implementation. Section 3.5 discusses the performance of the array, common sources of RFI backgrounds, additional details on the phased trigger. We also present a study of common sources of RFI backgrounds at the prototype site. We also discuss the first cosmic-ray-like impulsive event triggered by an RF-only trigger at high-elevation in a noisy environment. In Section 3.7, we place these results in a broader context and discuss future work.

3.2 The BEACON Prototype Instrument

In 2018, we installed an 8-channel prototype instrument consisting of four dual-polarized antennas and an instrument that amplifies, conditions, and records triggered events. The system diagram is shown in Figure 3.2. The design described here is robust to weather and operating conditions experienced at this remote site, and scalable to larger future deployments. This section describes the instrument and its site.

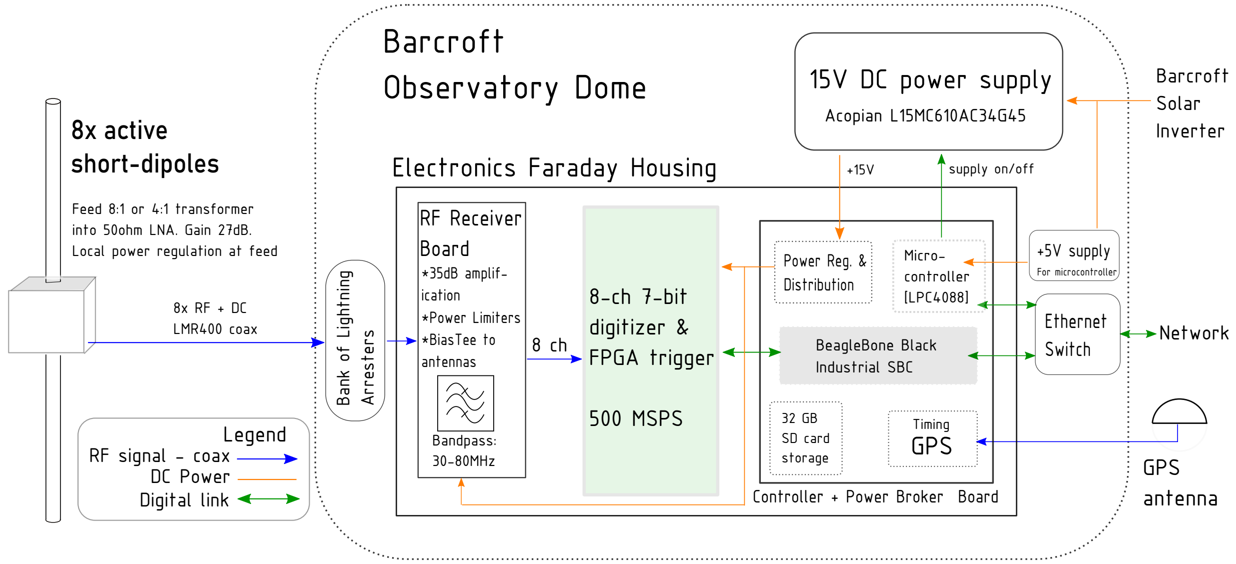

Figure 3.2: Schematic of the BEACON prototype instrument system.

3.2.1 White Mountain Site

The prototype is located at an altitude of 3.8 km in the White Mountains of California, near White Mountain Research Center's (WMRC) Barcroft Field Station. The experiment looks east from the site, overlooking the Fish Lake Valley with the valley floor having an altitude of 1.5 km. Figure 3.3 shows the local topography at the site. The antenna locations are shown in red (and also photographed in Figure 3.4), and important structures like Barcroft Field Station and the Observatory Dome are shown in gray. The Observatory Dome is an enclosed structure with power and network access where our data acquisition system (DAQ) electronics are housed.

The site provides significant infrastructure that is advantageous for BEACON, including road access, a solar-battery hybrid power system, internet access via a microwave relay to Owens Valley Station (which is also operated by WMRC), room and board during deployment, and remote support for the BEACON prototype from WMRC staff. There are engineering challenges presented by the site that have influenced the design of the prototype instrument: it is only accessible in the summer months, sees wind speeds in excess of 130 km/h, and is located on steep and rocky terrain. Additionally, the permit for the site restricts erecting permanent structures (e.g. concrete foundations) under the current agreement with the United States Forest Service.

3.2.2 Antennas and Mechanical Design

As the radio emission from air showers is broadband, several bands ranging from 30 to 1200 MHz can be used to detect them [165, 177]. Prior to initial deployment of the BEACON prototype, a site survey of RFI was conducted to help make a choice of band [178]. The antennas chosen for the first implementation of the BEACON prototype were inverted-V cross dipole antennas also used as part of the Long Wavelength Array (LWA) experiment at the Owens Valley Radio Observatory [179]. These antennas were chosen for their sensitivity

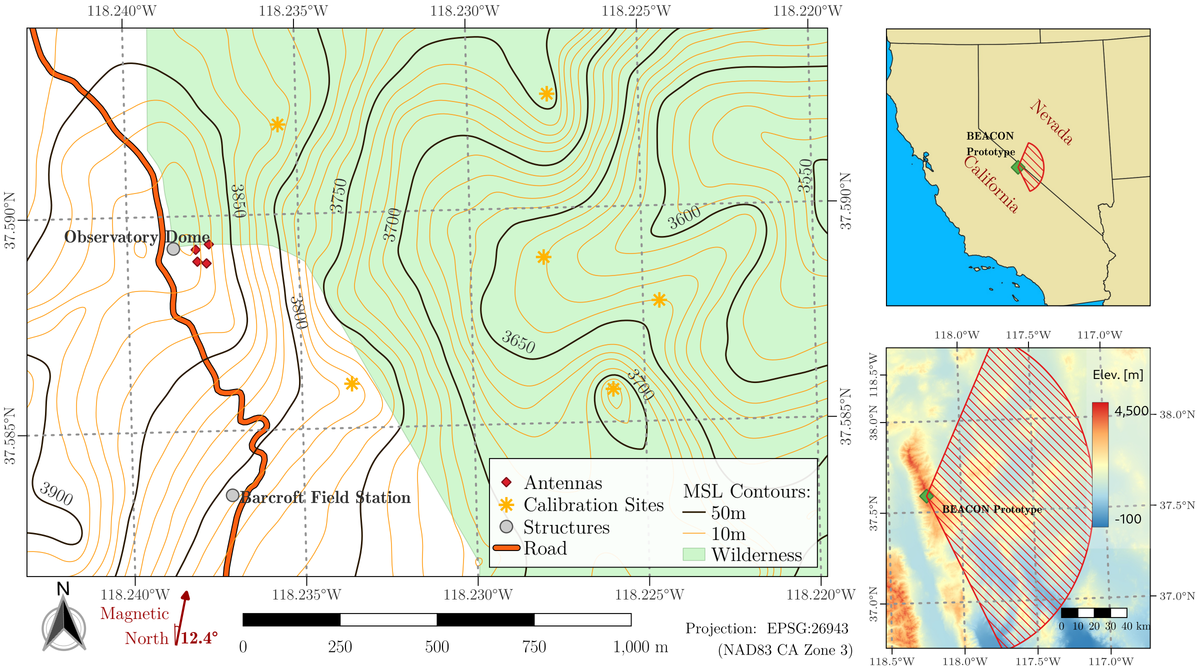

Figure 3.3: Left: A map of the immediate surroundings of the BEACON prototype at the White Mountain Research Station. Electronics are housed in the Observatory Dome. A scale bar is provided for the local terrain, as well as the direction of magnetic North. Top Right: A map showing the BEACON prototype's location within California, USA. Bottom Right: A map showing elevation profile of the region visible to the BEACON prototype. A cone extended 100 km from the site and spanning ±60° of East has been added for reference to illustrate the direction the BEACON prototype faces.

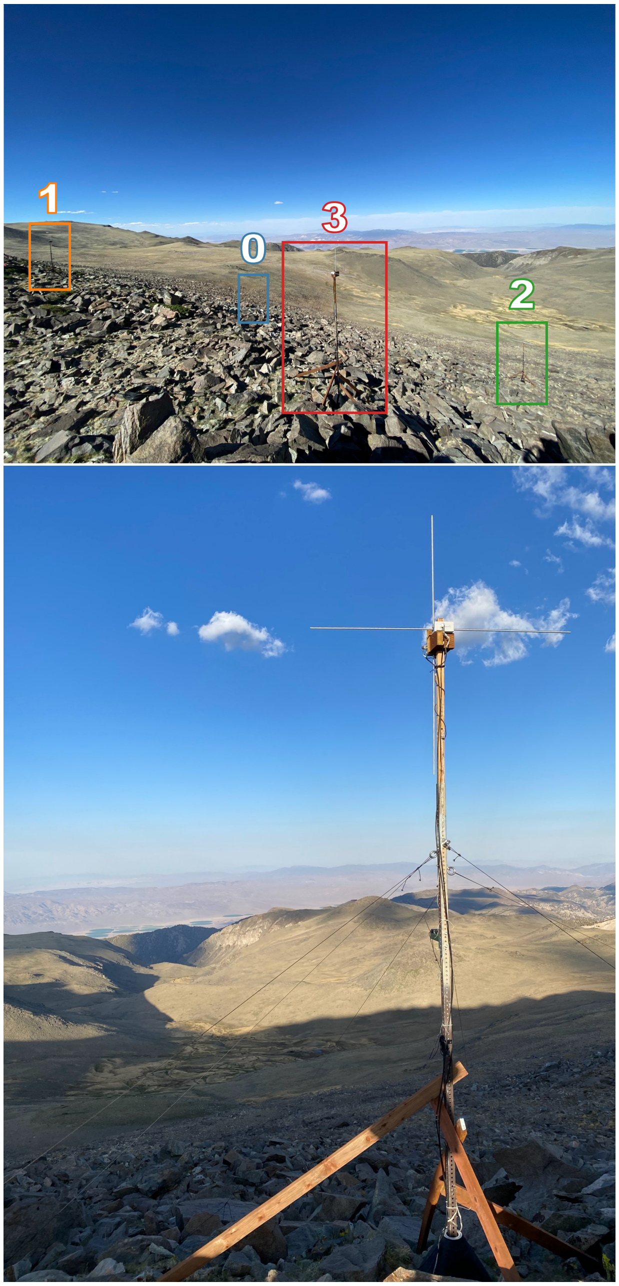

Figure 3.4: Top: The BEACON prototype array consists of four crossed dipoles each with a custom active feed. The antennas are positioned on a sloped rocky terrain; the HPol (VPol) dipoles are oriented such that their physical extent and gain nulls align in the North-South (Up-Down) direction for maximal sensitivity towards the horizon in the East. Bottom: Close-up view of Antenna 3 shows the antenna masts with two dipoles and active feeds fed with LMR240 connecting to LMR400 at the base of the antenna. The GPS patch antenna is used for the RTK-based calibration system. The antenna masts are protected against high winds while minimally impacting the local environment using ∼33 kg rubber bases, wooden struts, and six guy-lines. All four antennas are elevated ∼3.96 m above the ground and pointed toward the horizon to the East.

to 30-80 MHz frequencies, as well as their active balun that includes conversion to a coaxial cable line and amplification of 35 dB [180, 69].

Later modeling using antenna simulation packages NEC [181] and XFdtd [182] suggested that the effect of the ground when looking near the horizon was too severe for a non-elevated antenna design. Following this study it was determined that elevating the antennas off the ground was necessary to avoid ground interference; an antenna elevation height of ~3.96 m was chosen as a compromise between performance and deployment difficulty. Ground effects are still present in the beam patterns, as shown in Figure 3.5. Additional interference contributions are mitigated by avoiding any metal near the antennas in the support system.

We designed a custom short-dipole antenna with 2x76.2 cm (2x30 in) long tines with an active balun that could be mounted inside of a small enclosure on top of the mast, providing a low-profile and low-mass device capable of surviving the extreme environment. Although these antennas have a small effective height at the low-edge of the band, they provide a nearly omni-directional beam pattern across the band. Our BEACON active balun, shown in Figure 3.6, consists of a 4:1 transformer that is fed into a 50 Ω low-noise amplifier (LNA), which is followed by a second stage of amplification. The transformer not only boosts the input impedance as seen by the antenna, but also isolates the common mode ground of the amplifier and coaxial cable from the dipole. To maintain a precision voltage to the on-board amplifiers, the balun is locally regulated to 3.0 V. The board draws <45 mA with a total gain of 35 dB. Similar short dipole designs have been studied and utilized in the LOPES and CODALEMA experiments [183, 184].

Figure 3.7 shows that galactic noise is visible in the vertically polarized channel. Because of the small difference in period of the solar and sidereal days, we stacked the root-mean-squared (RMS) fluctuations in the noise over the course of a month at two periods of the year. When the galaxy rises above the horizon, the RMS noise is slightly elevated and the peak is correlated with the rising galactic center. We also note that this effect is not visible

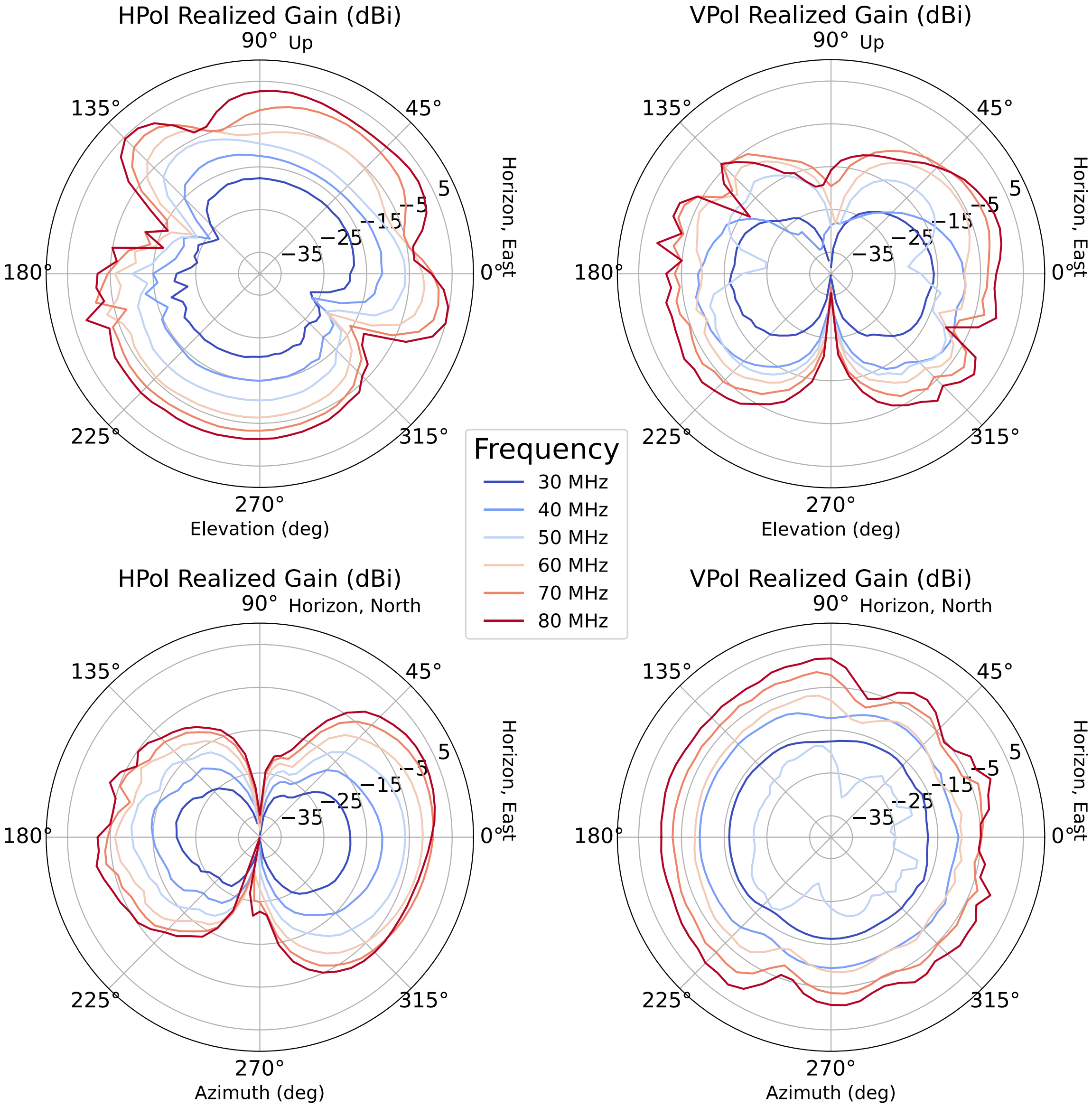

Figure 3.5: The realized gain of the crossed dipoles simulated with XFdtd. The HPol antenna gain is shown on the left, while the VPol is shown on the right. The full width of each dipole is 1.56 m, and they are elevated ∼3.96 m above the ground over a ∼3.05 m sign post. The antennas are simulated with a 200 Ω characteristic impedance to model the 4:1 transformer. The simulated antenna sits in the center of a 150 m ground plane tilted by 30° in elevation and 10° from North to south. This configuration models the two antennas lower on the hill. An azimuthal angle (shown on the bottom) of 0° corresponds to due East and an elevation angle (shown on the top) of 90° looks directly up. The HPol beam pattern develops modes at a frequencies determined by the interference of ground reflections with the main lobe, while the VPol pattern appears to be additionally affected by the presence of the steel pole.

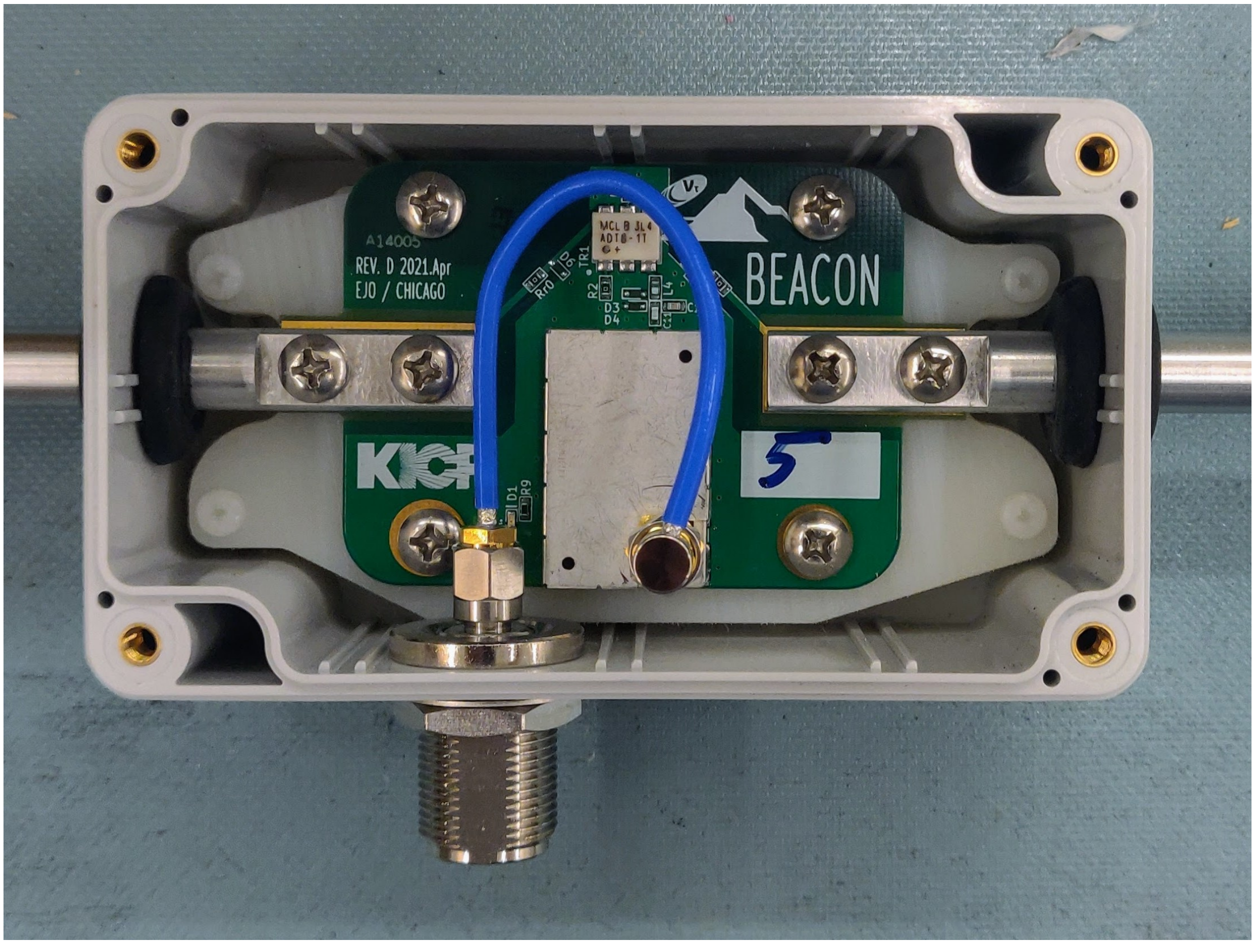

Figure 3.6: Short dipole antenna feed. The active dipole feeds each incorporate a 4:1 transformer into a 50 Ω LNA. The Polycase enclosure helps protect the front-end board from weather. The antenna elements are connected directly to the front-end board, with each extending outward through grommets in the enclosure.

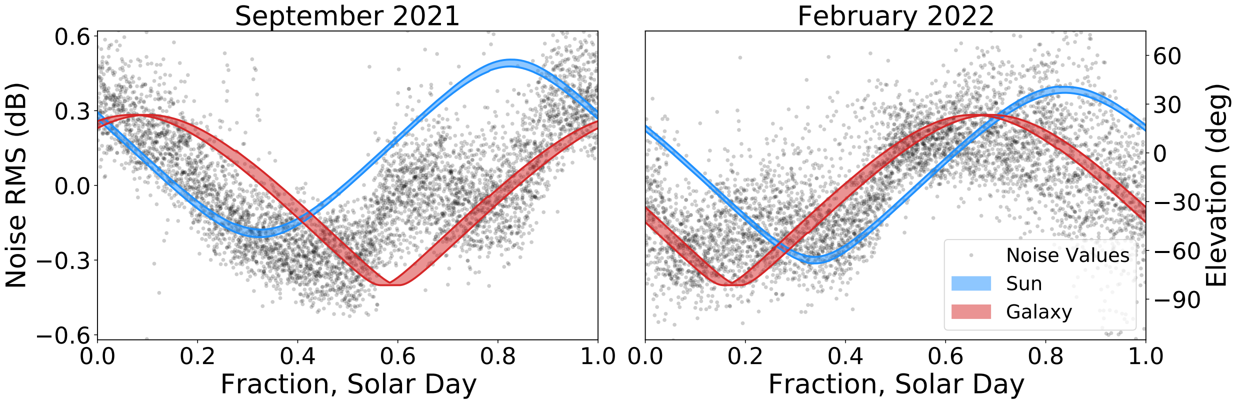

Figure 3.7: The fluctuations in the root-mean-squared (RMS) noise observed in VPol channel 5 during September 2021 (left) and February 2022 (right). Superimposed on each plot are the range in elevation of the Sun and galactic core over the sampled time. The RMS rises along with the galactic center, such that when the galaxy is visible in the antennas, the noise increases. The phase of the RMS variations follows that of the galactic center throughout the year, rather than the sun.

in the horizontal polarization, because the galactic center peaks in the South where there is a null in the HPol beam pattern. While the effect in VPol is weak, there is a clear phase shift correlated with the elevation of the galactic center at two different times of year. To be sensitive to this faint but pervasive galactic noise is a key goal of a transient radio detector like BEACON [185, 186].

The short dipoles are mounted directly onto a wooden masthead in a cross pattern for sensitivity in both horizontal and vertical polarizations; these are referred to as HPol and VPol antennas respectively. A second HPol antenna could be a future addition for full angular sensitivity. However, the array's location on a mountainside reduces the need for sensitivity in directions parallel to the mountainside where the effective area is already significantly reduced. The BEACON prototype is located on a North-South aligned ridge, so the HPol antennas are oriented North-South with the gain being maximized along the East-West axis, orthogonal to the ridge. Because the Earth's magnetic field points close to the North, this orientation of the array aligns the center of the array's sensitivity with the direction that air shower radio emission is expected to be strongest (given by $\vec{v} \times \vec{B}$).

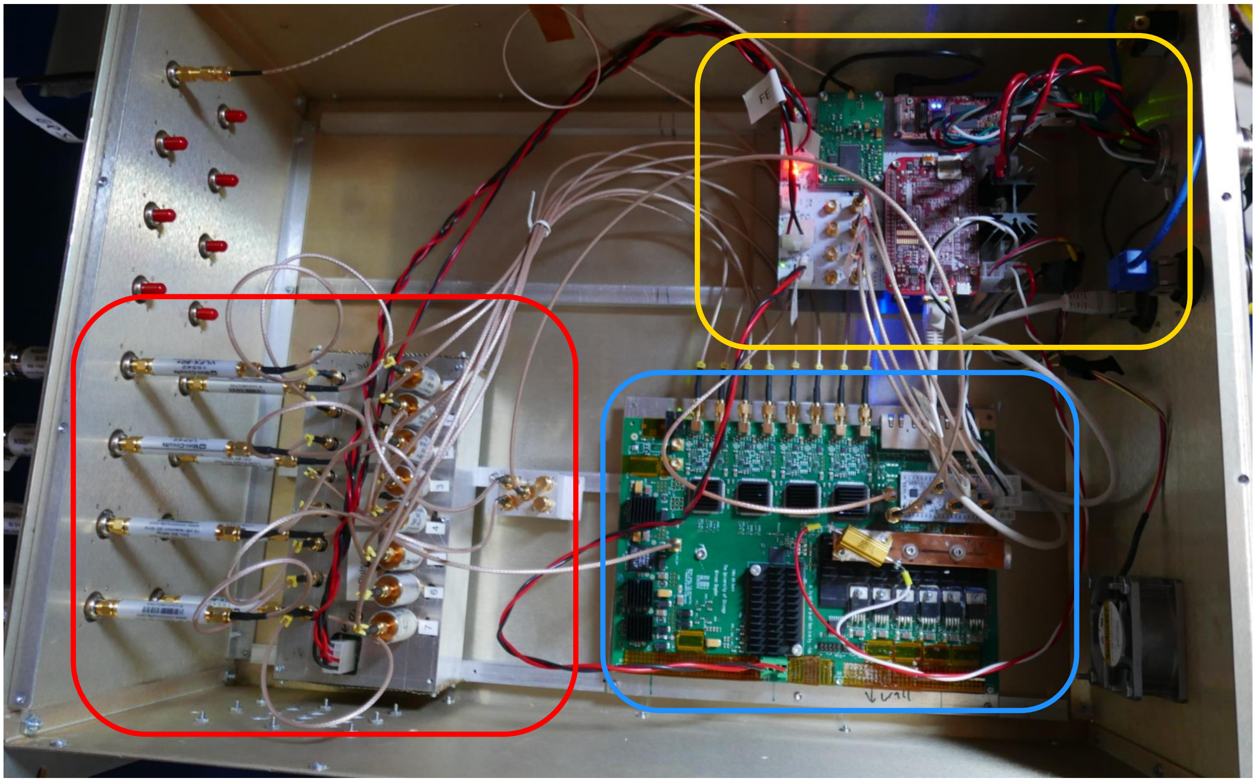

Figure 3.8: Picture of the DAQ. The yellow region in the top right contains the SBC, GPS clock, and power distribution. The red region on the left contains second stage amplification and band-pass filtering. The bottom right blue section is the custom digitizer and beamforming trigger board.

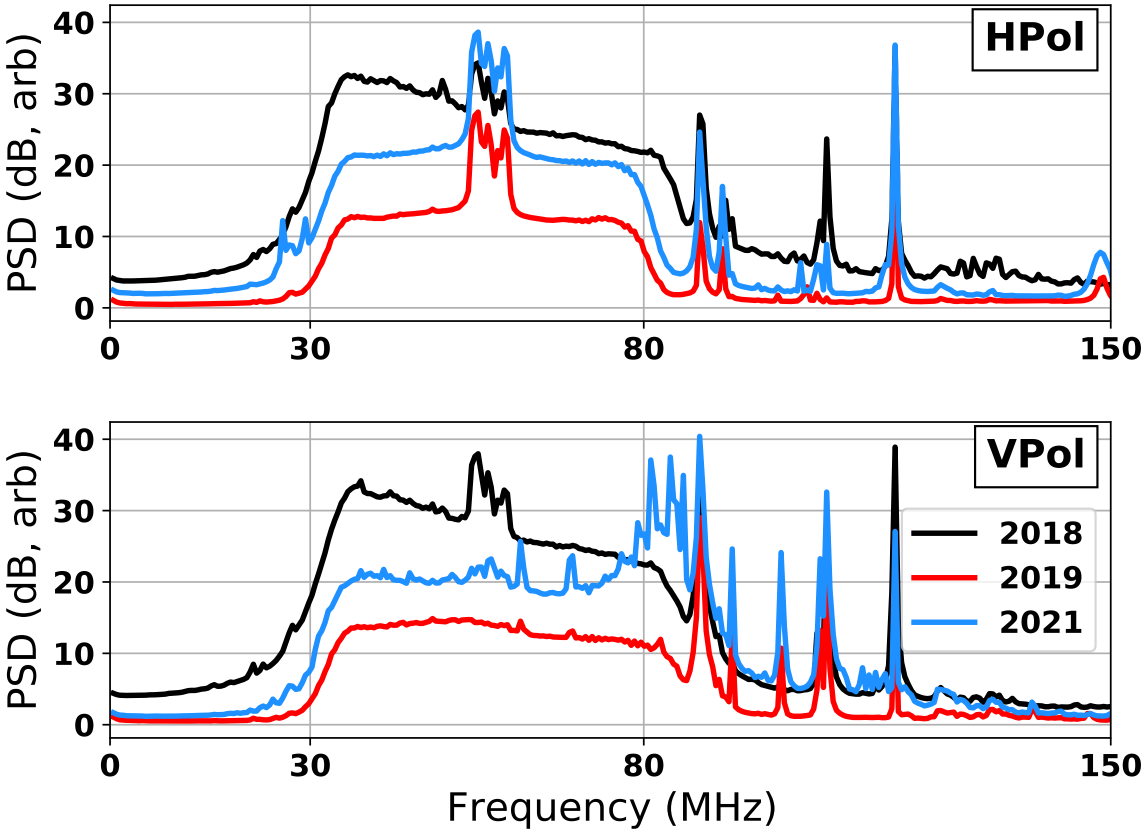

Figure 3.9: Top: Time averaged spectra for 3 generations of dipole antennas corresponding to the same HPol channel. The time covered by each is set to be 50 runs, resulting in averages covering 391 hours for 2018, 133 hours for 2019, and 153 hours for 2021. These times are sufficiently long for each generation that the differing time windows do not have a significant impact on the structure of the spectra. Bottom: The same except VPol antennas. The spectra are presented as Power Spectral Density (PSD) in arbitrarily offset dB units (a conversion between ADU and volts has not been performed). The variation in baseline power is a result of differing antenna construction and amplification which affects both signal and noise levels and is generally not representative of performance differences in SNR. The 2018 traces correspond to LWA antennas, which were significantly lower to the ground and were generally a different infrastructure. Comparing 2018 to other years it is clear that our VPol channel has significantly reduced cross-polarization power, as noticeable by the disappearance of television (TV) band noise in the VPol channel (with TV contributions ranging from ∼53 to 60 MHz, discussed further in Section 3.5.2). The antenna element lengths were increased from 2x68.6 cm to 2x76.2 cm for the 2021 model, which has resulted in additional pickup in the high-end of the band, noticeable particularly in the VPol antenna which may be experiencing additional coupling with the steel mast due to closer proximity. As the trigger operates primarily using HPol antennas this has not negatively impacted performance of the trigger.

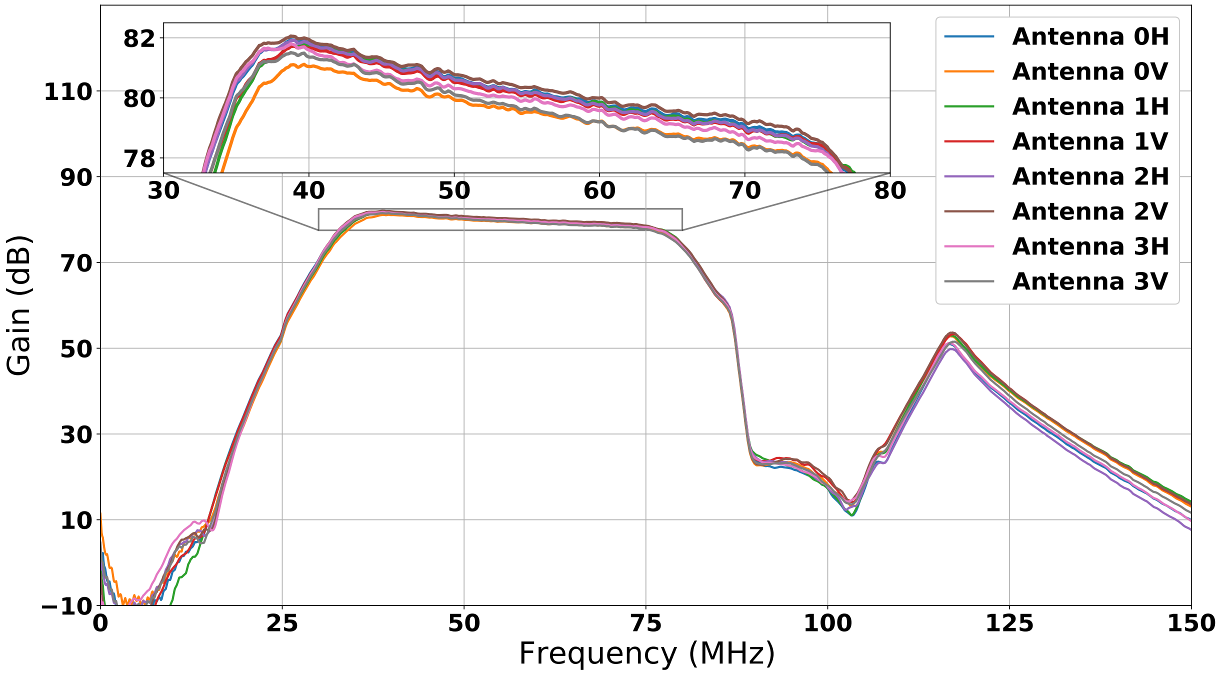

Figure 3.10: The system gain for each channel, including the active feeds with a gain of 45 dB, cable losses through LMR400 and LMR240, bandpass and notch filters (Mini-circuits SHP-50, SLP-90, and NSBP-108), and second stage amplifier board with a gain of 40 dB.

Coaxial cables ($\sim$107 m of LMR400 and $\sim$6 m of LMR240 in series) connect the antenna preamplifiers to the DAQ, carrying both the amplified signal and DC power to the preamplifiers, which have internal bias tees. These cables are jumpered across the wooden masthead to the steel mast along with grounding cables, where they are guided to the ground before being run uphill towards the DAQ. The cables are sheathed when on the ground to reduce damage from weathering as well as the local wildlife.

Reliably elevating the antennas required a number of iterations, especially as the array location within Inyo National Forest precluded any permanent structures, requiring a mast support design that avoids drilling or pouring concrete. The first iteration of this design secured the base of the mast with a commercially available $\sim$33 kg rubber base, as well as 3 guy-lines tied to local rocks for each mast. This design was improved in follow-up deployments in 2020 and 2021, which addressed issues with failed wooden mastheads and fallen masts. These issues were caused by the extreme weather at the prototype site, with gusts of up to 130 km/h, heavy snow and ice build-up, static discharges, lightning strikes, and exposure to the sun. The improved supports included ≥ 6 guy-lines per mast using higher-grade rope, and 4 wooden struts per mast. The struts are cut to length on-site such that they can be wedged securely into the local terrain (Figure 3.4).

This upgraded design is robust to animals climbing or pulling on it, is readily adaptable to varied terrain and has proven to be capable of withstanding winter conditions. In places with fewer restrictions, drilling into the ground would add additional stability. Though the wood used was high-quality pressure-treated cedar, it still showed significant weathering after just a single year, so improvements in RF-safe alternative materials to wood, such as fiberglass, for the masthead may be warranted for future deployment, while steel struts could be an option for usage away from the antennas.

3.2.3 Radio Frequency (RF) Signal Chain and Data Acquisition System (DAQ)

The BEACON prototype uses a custom DAQ housed in a Faraday enclosure, shown in Figure 3.8. At the input, signals pass through a lightning arrester bank to prevent static discharge from damaging the system. Afterwards, signals then pass through an RF receiver board, which provides 35 dB of amplification, a DC bias for the antenna feeds, filtering, and power limiting. Filters include both 30-80 MHz band-definition filters as well as FM notch filters, which are necessary due to the proximity of the FM broadcasts. Typical noise spectra for three generations of BEACON antennas are shown in Figure 3.9. Figure 3.10 shows the combined gain of the full RF signal chain.

Signals then reach the digitizer and beamforming trigger board, which incorporates 8 channels of 500 MSPS 7-bit digitization and a control FPGA responsible for triggering and buffering up to 2048 samples per channel for readout once triggered. Typically, only 1024 samples are read out per event to increase readout speed and reduce dead time and data volume. Tunable attenuators allow for gain matching between channels and tuning the dynamic range of the digitizer. A timing GPS is used to provide a reliable pulse per second (PPS) to the digitizer board, which records the number of clock cycles when the PPS is received, allowing for precise time tagging for each trigger.

The digitizer and beamforming trigger board is controlled and read out via SPI using a BeagleBone Black (BBB) single board computer (SBC), running Debian Linux. Software on the SBC manages configuration of the trigger, readout of event data and metadata, housekeeping, and transfer of the data off of the DAQ. The BBB is connected to the Barcroft network via Ethernet. Also on the network is a microcontroller which allows for remote power cycles of the entire system.

The DAQ system is powered by a 15 V DC supply, plugged into the Observatory Dome power system. The present power draw of the DAQ is $\sim$40 W, dominated by the digitizer and trigger board. Power at the Observatory Dome is provided by a solar-battery hybrid system deployed by WMRC. The typical power system capacity is considerably greater than the daily usage (∼1 kWh), resulting in nearly complete live time, except under extended extreme cloud cover or excessive snow lasting > 5 days.

Data is sent from the DAQ system to our Archive Machine computer located nearby at Barcroft Field Station. The Archive Machine archives data before it is transferred to the University of Chicago and provides local monitoring. In addition to being connected to the Barcroft network, the Archive Machine is also connected to a backup cellular network, which allows communication with the DAQ system when the normal connection from Barcroft is down, a relatively common occurrence particularly in winter. Also at Barcroft is a Raspberry Pi with a software-defined radio tuned to listen to aircraft ADS-B transmissions, which is used alongside data provided by The OpenSky Network [187] for the purpose of tracking nearby commercial airplanes. The use of ADS-B transmissions to correlate airplane locations with above-horizon RF signals in the 30-80 MHz band has been demonstrated previously by other experiments [173].

3.2.4 Trigger System

The combination of an FPGA and streaming digitizer on the digitization and trigger board allows for flexible triggering capabilities. Currently, a beamforming (i.e. phased array) trigger is implemented, similar to the one deployed as part of the Askaryan Radio Array (ARA) at the South Pole [188]. This trigger uses a pre-calculated table of expected arrival time differences between the antennas to delay signals before summing them. Each set of time delays corresponds to a beam sensitive to a particular direction, and is most sensitive to signals arriving from the specific direction where the delays result in coherently summed signals. This coherent sum will increase an incoming signal's voltage by a factor of N_{antenna}, while thermal noise will add incoherently and only increase as $\sqrt{N_{\mathrm{antenna}}}$, resulting in a net

SNR increase of $\sqrt{N_{\text{antenna}}}$ [176].

The delayed and summed waveforms are further processed in the DAQ with a "power sum". This is done by first squaring the combined signal to obtain a proxy for power, before summing the combined power signal in 16 sample (32 ns) bins every 8 samples (16 ns) such that each bin has some overlap with the previous bin. The power sum of a coherently summed signal will increase the power SNR by a factor of N_{antenna}. Hereafter we refer to the beam SNR calculated by aligning voltage waveforms and summing as the "beam voltage SNR" and the power sum performed in the triggering hardware as the "beam power SNR". Currently, the time delays for each beam are pre-calculated assuming plane wave signals, however near-field time delays could be implemented in the FPGA if desired.

The trigger rates in each beam are continuously monitored and the thresholds are adjusted to meet user-defined goals. In this way, trigger thresholds are dynamically set to be noise riding, managed by the SBC such that a global trigger rate of 10 Hz is maintained. With a target rate of 10 Hz and temporary system outages accounted for, we conservatively estimate our dead time to be ∼1.5-2% over the span of time used in the analysis discussed in Section 3.5. The thresholds for each beam are adjusted automatically and in nearly real time so beams with consistently loud sources of RFI do not dominate the trigger. The rates of the individual beams can be further refined by the user. This directional trigger is essential in RFI-rich environments and has allowed the BEACON prototype to maintain relatively low thresholds in the majority of beams despite prevalent RFI from certain directions.

Currently we use 20 beams, distributed as shown in the upper panel of Figure 3.11. These beams were optimized for triggering on above-horizontal events in the region expected to be populated by cosmic rays. A full-scale BEACON station would be targeting the near-horizon region where tau neutrino events are expected. Moreover, the total number of beams would be expanded to uniformly fill the aperture. The trigger logic for the original implementation with ARA is described in more detail in Reference [188].

The trigger implementation allows for additional calculations to be performed in order to form noise-rejection vetoes to improve performance. Some examples of vetoes that have been considered:

1. a “side-swipe” veto, which can actively veto events where the amplitude on one antenna is significantly larger than others;
2. a saturation veto for high-power events which are clipped significantly;
3. a rear-facing veto which would avoid triggering when an event hits both western antennas first;
4. and a “band ratio” veto which compares relative power seen through 2 finite impulse response (FIR) filters in the low and high portions of the band to reduce triggers from narrow band events.

Beams pointed at specific known sources of RFI can also be used as a veto. As shown later in Figure 3.25, regular anthropogenic sources can be localized to well within the beam width. A veto could be implemented that disallows events from a certain beam direction if it also triggers a sideband.

The performance of the phased trigger can be seen in Figure 3.11, which illustrates each beam’s definition and dynamic thresholds. Thresholds are computed as the power sum over a 16 sample (32 ns) window in each beam and are shown here referenced to the RMS noise in a beam, which is monitored continuously by the DAQ. In the middle and bottom panels of Figure 3.11, the power SNR thresholds are compared to the voltage SNR thresholds in the beams. The translation between the power thresholds used in the triggering hardware and the voltage thresholds shown on the left are computed from simulations of cosmic rays modeled with ZHAireS and propagated through the prototype signal chain [189]. The translation is $V_{\mathrm{SNR}} = 1.8\sqrt{P_{\mathrm{SNR}}} - 0.38$. We make this comparison because prior simulation studies used beam voltage SNR thresholds for modeling the tau neutrino sensitivity [165], while the trigger hardware uses thresholds on the beam power SNR. The thresholds achieved on the instrument approach the nominal thresholds assumed in the simulation studies (5σ in voltage) [165]. While the thresholds are often in the range assumed by the simulations, there are also periods of time dominated by loud RFI in the field of view.

Comparing the beam map to the thresholds, we can see that there is some variation in the thresholds in each beam, corresponding to the observed rates in those beams. Some beams, like beams 0 and 4, point near a source of RFI below the horizon and maintain a higher mean threshold compared to other beams at the same elevation. Other beams, like beams 5, 9, and 17, point well above the horizon but may be triggering on sidelobes from RFI below the horizon. The impact of sidelobes is expected to be reduced with the increased number of antennas in a full-scale BEACON station trigger array.

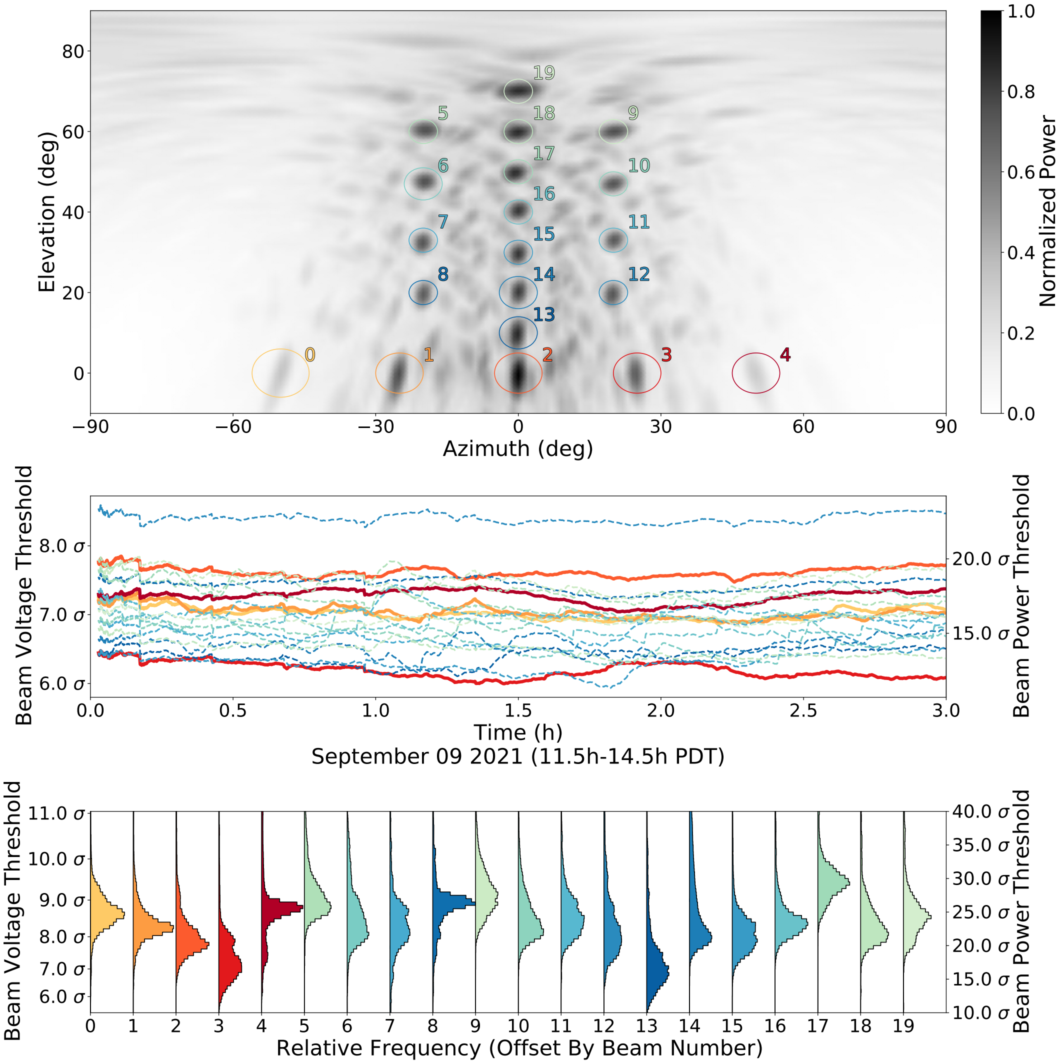

Figure 3.11: Top: The current beam map, with gray-scale color map corresponding to the normalized maximum power perceived in any beam for a mock signal arriving from each point on the map; maximal sensitivity/power is achieved in the nominal directions of each beam. Each beam is labeled and circled with radius set to 3 dB below that beam's max power. Middle: The thresholds for each beam during a quieter run. The measured power SNR, referenced to the instantaneous noise from the DAQ, is shown on the right axis. Beam voltage SNR is shown on the left axis and is computed from cosmic ray simulations as described in the text. Colors of each line correspond to the same colors used in the top plot, with beams near the horizontal being solid red lines, and above horizontal beams being dashed blue and green lines. The near-horizon beams generally exhibit a higher power threshold, as expected from anthropogenic noise. Some above-horizon beams point to prominent sidelobes of below-horizon RFI, and will also show elevated thresholds. Bottom: The long-term distribution of thresholds in each beam over the ∼112 day period discussed in Section 3.5.

3.3 Overview of Antenna Position Calibration and Direction Reconstruction for BEACON

This section provides a conceptual overview of the BEACON position calibration procedure. Specific iterations of using this technique are covered further in Sections 3.4.1, 3.4.3 and 3.4.4.

BEACON uses interferometry of waveforms from each of its 8 channels to determine the source direction of signals. Accurate source direction reconstruction (both at the trigger level and in analysis) requires precise knowledge of the array timing, including the location of each antenna and signal cable lengths. A calibrated array can use pointing for RFI rejection of permanent sources or airplanes, as well as for characterization of the polarization and source properties of the initiating radio source. The typical method of calibrating an array consists of the following process:

1. Perform initial position measurements using a Global Positioning System (GPS) system.

2. Measure cable delays using a vector network analyzer or time-domain reflectometer (TDR)

3. Send radio pulses at the array from a known location (also measured with comparable system to antennas), recording the pulses through the DAQ for later analysis

4. Perform a χ^2 minimization targeted at matching predicted arrival time differences in each channel with the actual measured delays through the DAQ for various pulser locations or sources. A typical χ^2 takes the form:

$$\chi^2 = \sum_{j}^{n_{\text{sources}}} \sum_{i}^{n_{\text{baselines}}} \frac{\left[t_{\text{geometry,i,j}} - t_{\text{measured,i,j}}\right]^2}{\left[\sigma\left(t_{\text{measured,i,j}}\right)\right]^2} \tag{3.1}$$

where the antenna positions (geometry of the array) are adjusted at each iteration until minimization has been obtained.

The number of degrees of freedom (DoF) for the minimization parameters is equal to 3 axes of movement + 1 cable delay per antenna, leading to 16 total DoF. The number of distinct measurements provided by N_{site} pulsing sites is given by DoF $= N_{\text{site}} \cdot C(N_{\text{antenna}}, 2)$ where $C(n, r)$ is the choose operator, which determines the number of arrival time differences (baselines) that can be calculated when comparing 2 antennas from a set of N_{antenna}. Minimization was performed independently for each polarization, allowing for variations in phase centers between HPol and VPol antennas. Pulsing locations are chosen to be far from the array such that variations in timing from uncertainties in their locations are negligible and do not add additional DoF to the minimization.

Initial position measurements of the antenna masts were made with the Real Time Kinematic (RTK) technique that compares GPS positioning of two nearby GPS antennas - resulting in cm level precision by correcting for the propagation conditions in the local atmosphere [190]. Each antenna mast includes a dual-band GPS patch antenna, which may be connected to a GPS receiver on demand. We use a u-blox C099-F9P application board (ZED-F9P GPS [191]) to measure the position of each antenna, with corrections provided by a UNAVCO GPS station permanently installed ~30 m away from the BEACON site at 37.58915N, 118.23844W [141].

Pulsing data was taken over the course of 3 days during a calibration campaign in 2021, during which pulsing data was taken for 6 separate sites in both polarizations. The transmitter included a high-voltage pulser (FID technologies FPM 10-1PNP) driving a biconical antenna (Aaronia BicoLOG 30100E) at known rates, with varying fixed attenuators. These pulsing data are used in the fit described in Equation 3.1. The resulting errors on the phase centers are estimated to be less than 5% of the shortest relevant wavelength.

The source direction is reconstructed using interferometry [192]. Cross correlations are calculated for each pair of antennas in separate polarizations. The cross correlation for a given antenna pair is expected to peak at a time delay consistent with the arrival direction of the signal. A "correlation map" is formed by sampling these cross correlations at delays expected for each direction. Each direction in the map corresponds to the average correlation value from each baseline when sampled at the expected time delay for that direction. The expected time delays depend on the geometry of the array and source direction on the map and are often calculated assuming a plane wave for distant sources. The peak value of the map corresponds to the direction which has sampled each baseline's cross correlation nearest the maximum. Each baseline is weighted equally and is normalized such that identical signals result in a maximum cross-correlation value of 1; a map generated with identical signals in each channel would also result in a peak value of 1. Real signals vary slightly across antennas, so the optimal map value depends on each event and is typically < 1.

A perfect impulse would have a single peak in a cross correlation, resulting in a single ring of possible arrival directions on the sky for each baseline due to the symmetry around the axis connecting those 2 antennas. By averaging maps of all 6 baselines, the degeneracy of these rings is broken, with all baselines overlapping only in a single location for an impulsive plane-wave in a properly-calibrated array. This requires a sufficient number of baselines to fully break degeneracy, or ambiguities in pointing can occur. Though the BEACON prototype has a sufficient number of antennas to accurately point to most impulsive RF sources, narrow-band signals result in highly periodic cross correlations which in turn produce a series of concentric rings on the maps per baseline, increasing the degeneracy of potential source directions. This problem can be exacerbated by the presence of unrelated continuous wave (CW) noise, coincident signals from other RFI, or by the source signal itself being insufficiently impulsive.

After minimization, signals from the mountainside pulsers show maximal reconstruction offsets of $\sim 1^\circ$, with the majority of sites showing offsets $< 0.5^\circ$. The accuracy is discussed further in Section 3.5.2 when presenting airplane reconstructions, which provide an external source of signals with known directions and show a systematic offset of 1-2°. The mountainside pulsers provide a limited range of elevation angles for the calibration minimization, which could contribute to the observed reconstruction error. Additionally, the cable delays can have a degenerative effect with antenna position within the minimization for adjusting baseline timings, which also could be the source of the discrepancy. In future efforts we aim to address these issues with a drone pulser (Section 3.7), which would provide a significant increase in angular range used for calibration.

The precision of the prototype to reconstructing the arrival direction of stationary radio signals was experimentally determined by reconstructing arrival directions of below-horizon RFI sources, the majority of which arrive from a few very loud stationary emitters. A 2D Gaussian was fit to 7 of the most prevalent sources, with an average 90% integral area for the fits of < 0.1 sq. degrees (see Figure 3.25).

3.4 Field Deployments

Section 3.2.1 gives a brief overview of the BEACON prototype instrument construction, and some of the intermediate stages of development. I expand on the development process in this section, providing additional details relevant to my work on BEACON.

During my time working with on the BEACON prototype I went of 3 deployments to the site, each approximately a week in duration. As described in Section 3.2.1 the BEACON prototype site is located at high elevation in a remote portion of California on the border of Nevada. The remoteness of the station make it essential that all necessary tools and supplies are brought with deployment team. This makes the logistics of planning a deployment important.

3.4.1 2019 Deployment and Calibration Efforts

As described in Section 3.2.1 the prototype array transitioned from LWA antennas to custom short-dipole antennas in 2019. This was done over two separate deployments, with the first team removing the old hardware, and the second team installing the new masts and antennas. Additionally, the installation deployment was scheduled to perform calibration pulsing for the new antennas, which would be separated at longer baselines than the original LWA layout. This installation deployment was my first field deployment for BEACON. In the lead-up to the 2019 deployment I worked on the mechanical construction and testing of the custom dipole antennas.

Testing included measuring the performance of the antennas. The general procedure for S-parameter measurements was described in Section 2.5.3; however, BEACON antennas differ from the RNO-G HPol antennas due to being "active" antennas (as they have powered amplifiers on-board in the front-end electronics). The powered on-board preamplifier effectively makes the flow of signal in the antenna uni-directional, meaning the BEACON antennas do not work as TX antennas. Because of this, measurements were instead performed using an RSA3045 RIGOL Spectrum Analyzer, which allowed for real-time measurements of observed spectra with the antenna in RX mode. For testing the antenna typically connected to a ZKL-1R5+ amplifier, a ZDBT-282-1.5A+ bias-tee, and filters such as the SLP-90+ low pass filter (all from Mini-Circuits). A power supply was connected to the bias-tee which then transmitted the power as DC current to the amplifiers, while allowing for simultaneous readout of RF signal through the same cable; this setup can be seen in Figure 3.12.

Measurements were performed both in the RF quiet chamber at UChicago, as well as outside on a rooftop; measurements were taken both with and without the elements attached with the goal of isolating the performance of the front-end electronics. Images of these measurements can be seen in Figure 3.13. These measurements validated the first iteration design of the BEACON custom short-dipole antennas, showing they were capable

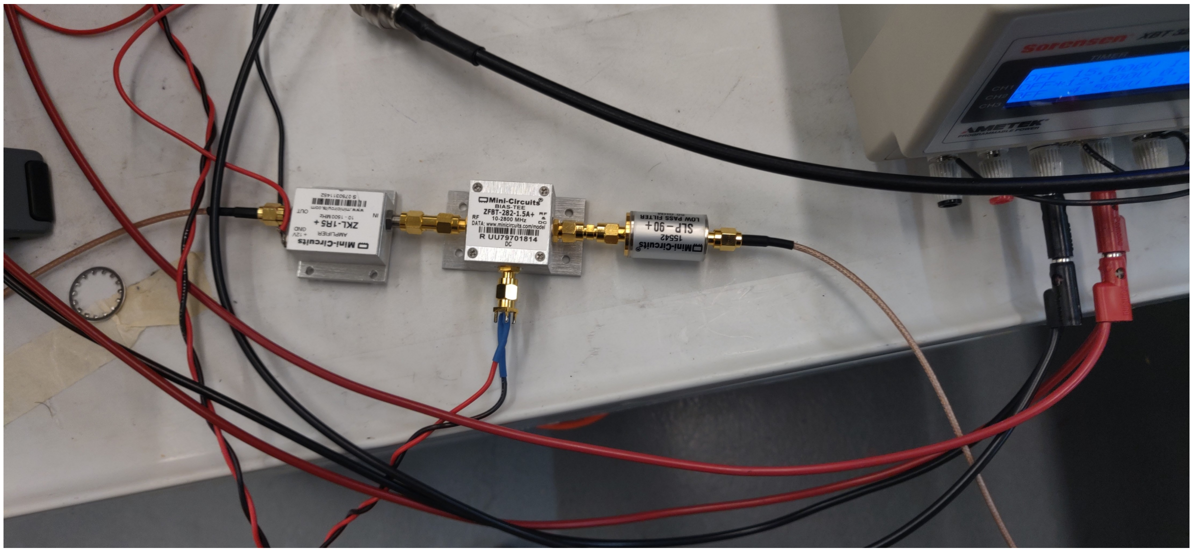

Figure 3.12: Electronics used in testing BEACON antennas.

of measuring impulsive RFI signals from within the noisy Chicago Southside. One goal of the antenna designs is to be sensitive to the RF noise produced by the galactic core. As this noise can never be removed, achieving an antenna that has noise dominated by the Galaxy is the effective ceiling for performance, as any improvements to sensitivity only make you more sensitive to that noise. The rooftop measurements were unable to demonstrate sky-noise dominance however. Later iterations of the antenna from the 2021 deployment were shown to be sensitive to the Galaxy (Section 3.2.1, Figure 3.7).

Following testing I was also responsible for final assembly (Figure 3.14) and verification of the antennas to be deployed, and also aided in the planning and packing for the deployment. During this deployment in October 2019, we installed 8 individual antennas, 2 per mast in a crossed-dipole configuration. Antennas were installed on the east-facing slope adjacent to the Barcroft Observatory dome. The dipoles were installed atop a mast with a height of 11.5 feet using a 10 foot metal sign post with a custom wooden post extension and antenna mount as shown in Figure 3.15. The actual antenna height is roughly 11 feet 7 inches for the VPol; 11 feet 9 inches for the HPol. This was slightly shorter than the planned 12 feet, with the change being made in the field during the construction of the mast and wooden

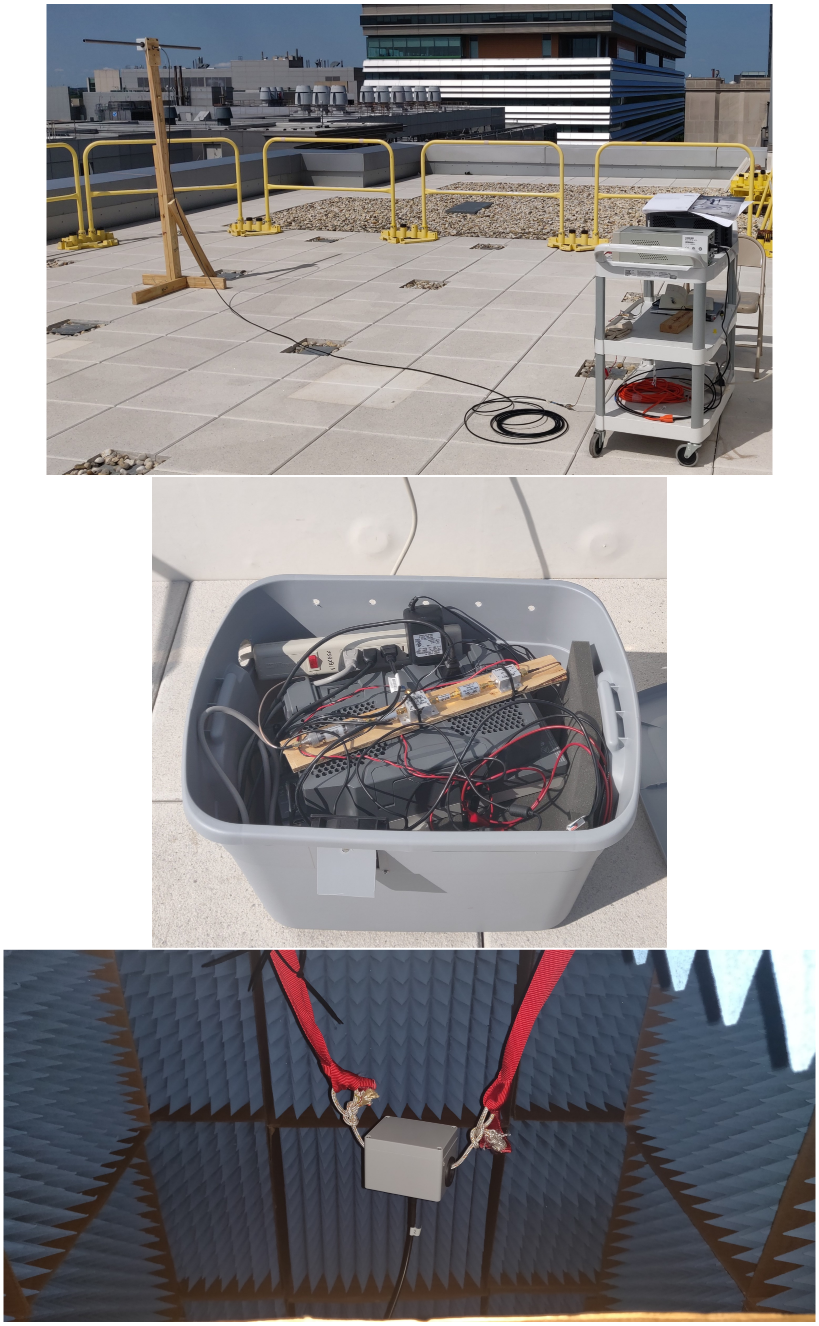

Figure 3.13: Top Left: The setup used for rooftop antenna measurements. Top Right: An enclosure containing network analyzer, power supply, electronics, and cooling. This was used for overnight measurements of the BEACON antenna, specifically targeted at investigating whether the Galaxy was visible in the antenna. Bottom: A 2019 BEACON antenna without elements being tested in the RF chamber. These measurements served as a baseline for the performance observed by a fully assembled antenna in rooftop measurements.

extensions; the intention was to increase stability. At this time the masthead design was largely improvised, with last minute additions of 90° rafter brackets joining the wooden mast to masthead.

Suitably flat patches were found on the slope to allow the use of commercial rubber sign bases, which allowed rapid installation of the antenna stands. In accordance with Forest Service guidelines, the antenna masts were guy-lined via nylon para-chord to local boulders in-situ, without moving rocks. After installation, it became clear one of the VPol antennas (installed on the Ant_3 mast) was flipped relative to the other three channels – this was also observed in the first RFI pulses. The 2019 BEACON array covered a substantially larger area than the 2018 installation.

GPS measurements were taken of antenna positions using cellular-phone GPS systems that were later determined to be inconsistent and unreliable. Baseline measurements were taken with a long tape measure as well; this measurement was done in windy conditions with considerable slack, so these measurements were likely an upper-limit measurement of the antenna separation distances (Table 3.1).

Antenna Pair	Distance (ft)
0 and 1	129
0 and 3	181
0 and 2	163
1 and 3	102
1 and 2	151
2 and 3	85

Table 3.1: Approximate 2019 Baseline Distances as measured with tape measure.

In addition to GPS measurements, a calibration pulsing campaign was performed at this time such that antenna phase center positions could be determined in analysis (described further in Section 3.3). Four sites, three of which with confirmed impulses in the data, were used for calibration pulsing. A GPS-synced FID pulser was used for all sites and configurations. The pulser setup was highly mobile and could be transported with two packs

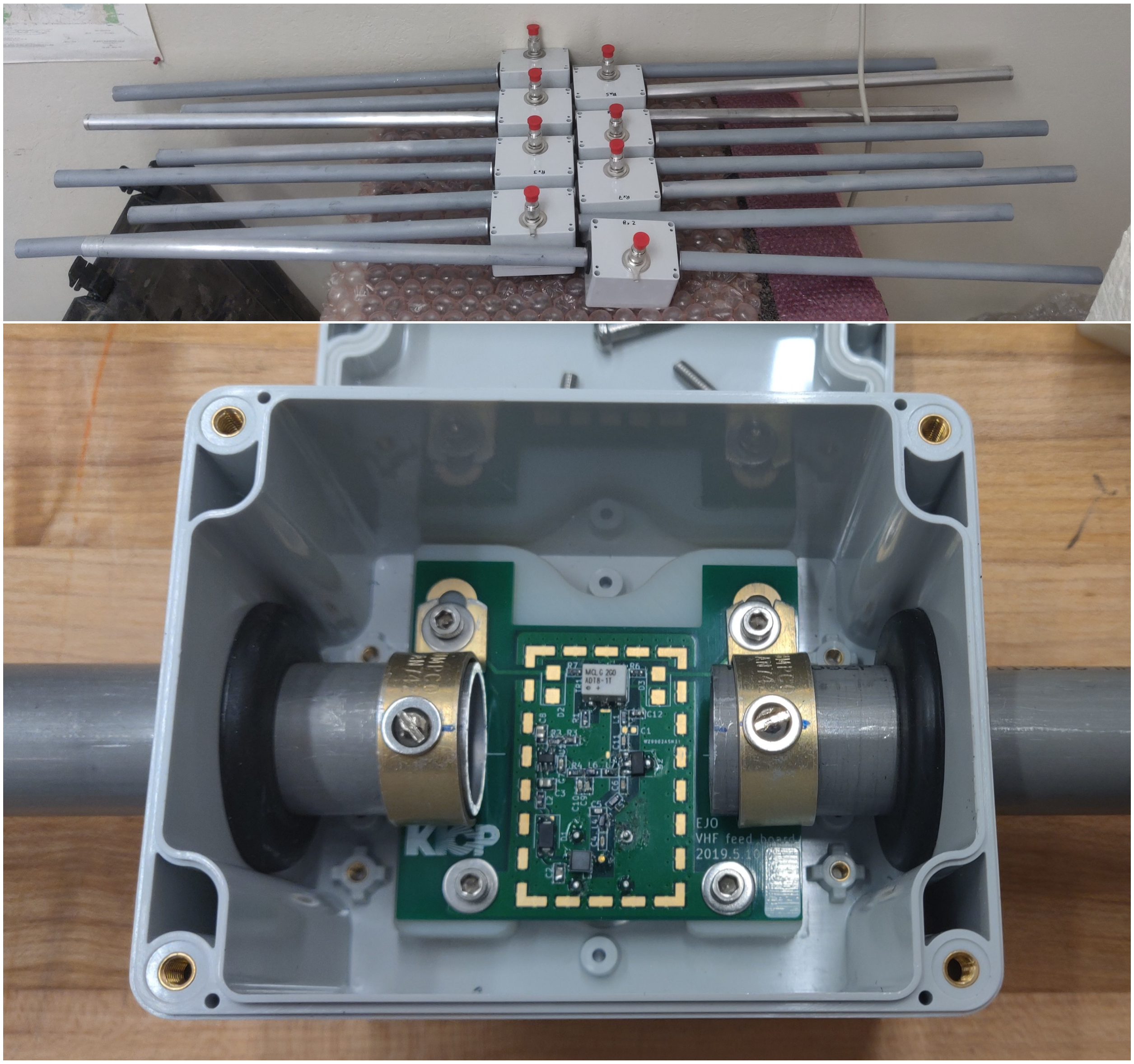

Figure 3.14: Top: The fully assembled 2019 antennas prior to mountainside installation. Bottom: An open antenna enclosure showing the front-end electronics board. The enclosures were custom PolyCase containers (with modifications designed by me) which had pass-through holes for the antenna elements and N-connector readout. The antenna elements connected directly to the board, which was raised to the appropriate height with a backing I custom designed; this backing was professionally waterjet cut, and brass threaded inserts were installed for mechanical connection to the antenna board.

Figure 3.15: The BEACON crossed dipole, as initially installed in 2019. Photo courtesy of E. Oberla.

plus hand-carrying the antenna and the tripod. Pulses were sent under various configurations using either a bicone antenna or a dipole antenna. Various degrees of filtering were also utilized to avoid saturating the system. A photograph of the pulsing setup is shown in Figure 3.16. Table B.1 in Appendix B gives the various configurations for each pulsing site, as well as the approximate run and eventid where the pulses are first observed in the data. The location of the four pulsing locations are presented in Table 3.2.

Site	Date	Latitude	Longitude	Altitude WGS-84	Altitude MSL
1	Oct. 5, 2019	37°35’9.3700”	-118°14’2.1050”	3762.9 m	3789.32 m
2	Oct. 5, 2019	37°35’9.4370”	-118°14’1.828”	3763.1 m	3789.53 m
3	Oct. 5, 2019	37°35’8.4690”	-118°13’33.3920”	3690.70 m	3717.04 m
4	Oct. 6, 2019	37°35’31.2067”	-118°14’7.6129”	3806.25 m	3832.55 m

Table 3.2: The measured location of each pulsing site during the 2019 deployment.

Figure 3.16: The 2019 calibration pulser setup.

This deployment season was overall a major success, and established the baseline design and construction for the BEACON prototype moving forward. This design would be iterated on in following seasons, which are discussed elsewhere in this text. The 2019 deployment was fully operational for a few weeks before the first antenna channel died. Over the course of the next few months various channels stopped working. Though the site is generally inaccessible during off-season, WMRC staff were able to access the site and send back broken antennas for studying. Several of the masts had fallen under the excessive winds at the site, with apparent damage from weather and local wildlife all contributing to the antenna failures. A 2020 iteration of the antenna was developed with modifications to the front-end electronics, with the overall structure of the antennas also being refined. The new antenna was more compact with longer and thinner elements.

A full deployment was planned for the summer of 2020 to replace all antennas, and add additional structural support to the antennas, however these plans were ultimately made impossible due to the travel restrictions imposed by the global COVID-19 pandemic. Some repairs were instead performed by WMRC on our behalf, for which we are very grateful, however this was undoubtedly a set-back for the experiment. Much of the time between the 2019 and 2021 deployments (discussed in Sections 3.4.4 and 3.4.3) was spent on attempting a calibration with the pulsing data taken in the 2019 deployment. Though the χ^2 minimization technique being used for antenna position calibration (discussed more in Section 3.3) is standard within the field, great difficulty was had in obtaining a reliable calibration. As this was the first position calibration with the BEACON system, the precise source of this difficulty was unclear.

Possible sources of problems could occur from having inconsistent antenna performance, large unknowns in cable lengths and other internal system timings, etc. Ultimately the dominant source of issues were determined to arise from inadequate initial position measurements for both antennas and pulsing sites. A variety of GPS systems were used, including various cellular phones and the GPS receiver which was used for synchronizing pulser emissions to the GPS second. Any single one of these may have provided a systematic offset or uncertainty on their own, but in reality no single GPS measuring device measured all points of interest - resulting in a mixed dataset. Baseline measurements taken with measuring tape were also highly unreliable and only served as an upper bound.

In an attempt to compensate for the large uncertainty in initial position of both the antennas and pulsing sites, modifications to the χ^2 minimization were attempted (Equation 3.1). A summary of some of these efforts is presented below:

- Pulsing positions were also included as moveable parameters in the calibration minimization using Equation 3.1. Each of the 4 pulsing sites added an additional 3 DoF to the system. The number of degrees of freedom (DoF) for the minimization parameters is equal to 3 axes of movement + 1 cable delay per antenna, leading to 16 total DoF per polarization. It was common to set one antenna position as the origin, removing 4 degrees of freedom resulting in a 12 initial degrees of freedom.

  Each pulsing site provides constraining information as described in Section 3.3 to reduce the remaining DoF by $C(N_{\text{antenna}}, 2)$ where $C(n, r)$ is the choose operator, which determines the number of arrival time differences (baselines) that can be calculated when comparing 2 antennas from a set of N_{antenna}. By including the positions of the pulsing antennas in the minimization each additional site then adds 3 DoF (one for each axis of movement, with cable delays not being relevant for pulsing antennas). The unconstrained DoF with this method was thus:

  $$\text{DoF} = 4 \cdot (N_{\text{antenna}} - 1) - N_{\text{site}} \cdot (C(N_{\text{antenna}}, 2) - 3)) \tag{3.2}$$

  For $N_{\text{antenna}} = 4$ and $N_{\text{site}} = 4$ this still results in a net negative DoF, and thus theoretically the system should be over-constrained and solvable.

Despite being over-constrained, the magnitude of variation in uncertainty of the initial antenna positions still resulted in results which had positions warped to unrealistic extremes. No satisfactory calibration was obtained from these attempts

- A ground-based RFI calibration was also attempted. This attempted to use RFI signals observed from the East as effective pulsing sites. Though the calibration was not accurate, maps created from signals still generally spatially clustered. Thus various sources could be isolated and used as independent effective pulsing sources. Despite their source direction being unknown, each RFI source theoretically still provided more constraining power than unknowns. This is similar to the previously described method of allowing pulsing positions to vary, but taken to the extreme where N_{site} was increased greatly. Additional weighting factors were introduced for each source to emphasize matching for sources which were trusted more. This method was applied iteratively, with intermediate calibration being used to explore potential sources for each RFI signal. Google Earth images we scanned in detail for potential RFI sources within the surrounding 100 miles, with candidates such as towns, power plants, substations, cellular towers, and industrial facilities all being highlighted and stored. Later iterations attempted to associate candidate RFI sources with signals; however, the speculative nature of the potential source catalog made this difficult.
- An airplane-based RFI calibration was also attempted. Several airplane candidates were identified in the data by plotting single baseline time delays of all RF-triggered events v.s. time. As most RFI is stationary (resulting in consistent arrival directions and thus observed time delays), such a plot will produce various horizontal lines with each line corresponding to a difference RFI source. Airplanes can be found by carefully inspecting such plots for small numbers of events that seem to be close in time but show a steady drift in arrival time delay (indicating the source is moving). We record our own airplane tracking data, which was used to associate airplane trajectories with

these events. Each identified airplane then served as a series of moving pulsing sites with "known" locations provided by the self-reported airplane trajectory. Though this method is sound in theory and could likely be used for validation at future sites.

An analysis which combined results from both airplane-based and the ground-based RFI methods described above lead to the calibration which was used until improved measurements were performed, however the results were later shown to be inaccurate - with three antennas being relatively near their true positions but one antenna being dramatically higher in elevation than it should have been. This is likely a result of the extremely untrustworthy initial conditions.

Throughout this lengthy calibration effort, it became clear that improved antenna site measurements were required, and the calibration would benefit from a more detailed calibration pulsing effort. These issues and desires were raised relatively early in 2020, but the pandemic removed the possibility of new and improved measurements until the 2021 deployment discussed in Sections 3.4.4 and 3.4.3.

3.4.2 2020 Partial Deployment

Though travel restriction did not allow for BEACON scientists to visit the site during 2020, WMRC staff were extremely cooperative. A strategy was developed to instruct WMRC staff through a partial deployment, which focused on bare-essential refurbishment of the antennas following the various structural and electrical failures observed from the 2019 season. I was instrumental in this planning process, working with colleagues to develop a plan. Three plans of varying complexity were developed such that the WMRC staff member could choose the amount of effort that they deemed safe and reasonable when on-site. All necessary hardware and supplies were shipped to OVS.

Under the guidance of these plans all 4 antenna masts were resurrected, with new antennas being installed. All masts were raised to 13 feet, an increase from the $\sim$ 12 feet implemented in the 2019 deployment. Each of the 4 masts was reinforced with varying degrees of support such that an in-situ test of each method could be performed. The structural integrity of each strategy would be studied in a future deployment to motivate the best design. Several of the broken antennas were shipped back to Chicago for inspection (Figure 3.17). The tested mast reinforcements included a new masthead design, the addition of wooden support struts (Figure 3.18), and the addition of more guy-lines (with higher quality rope). The observations made from this partial deployment were critical for making the necessary improvements for a successful 2021 deployment. Observations made during the first 2021 deployment validated the added reinforcements, which were all applied to each mast moving forward.

3.4.3 2021 Deployments

As travel restrictions began to lift in the second year of the global pandemic, the BEACON collaboration was overdue and eager for a deployment. In 2021 two separated deployments were planned and executed. The first of these deployments was focused on observing and characterizing the status of the array, which had not been visited by BEACON scientists in two years. Significant damage was observed in some of the antennas that were refurbished over the 2020 partial deployment (Figure 3.19). All damaged masts were fixed and resurrected with improved structural supports following the lessons learned, and the newly revised 2021 antenna models were installed (which saw iterative improvements upon the 2020 model). A pulsing campaign was also attempted during this deployment, however the large amount of planned tasks meant this campaign was constrained in scope. The first deployment occurred in June 2021, while the follow-up dedicated calibration deployment occurred in August 2021. This second deployment also saw additional guy-lines being added to the antennas following observations of weather-related loosening of lines in just the few weeks since the first 2021 deployment.

Figure 3.17: The 2019 antenna as imaged in 2020 following a winter of deployment. The visibly bent antenna element was a common occurrence which was mitigated in later iterations of the antenna design.

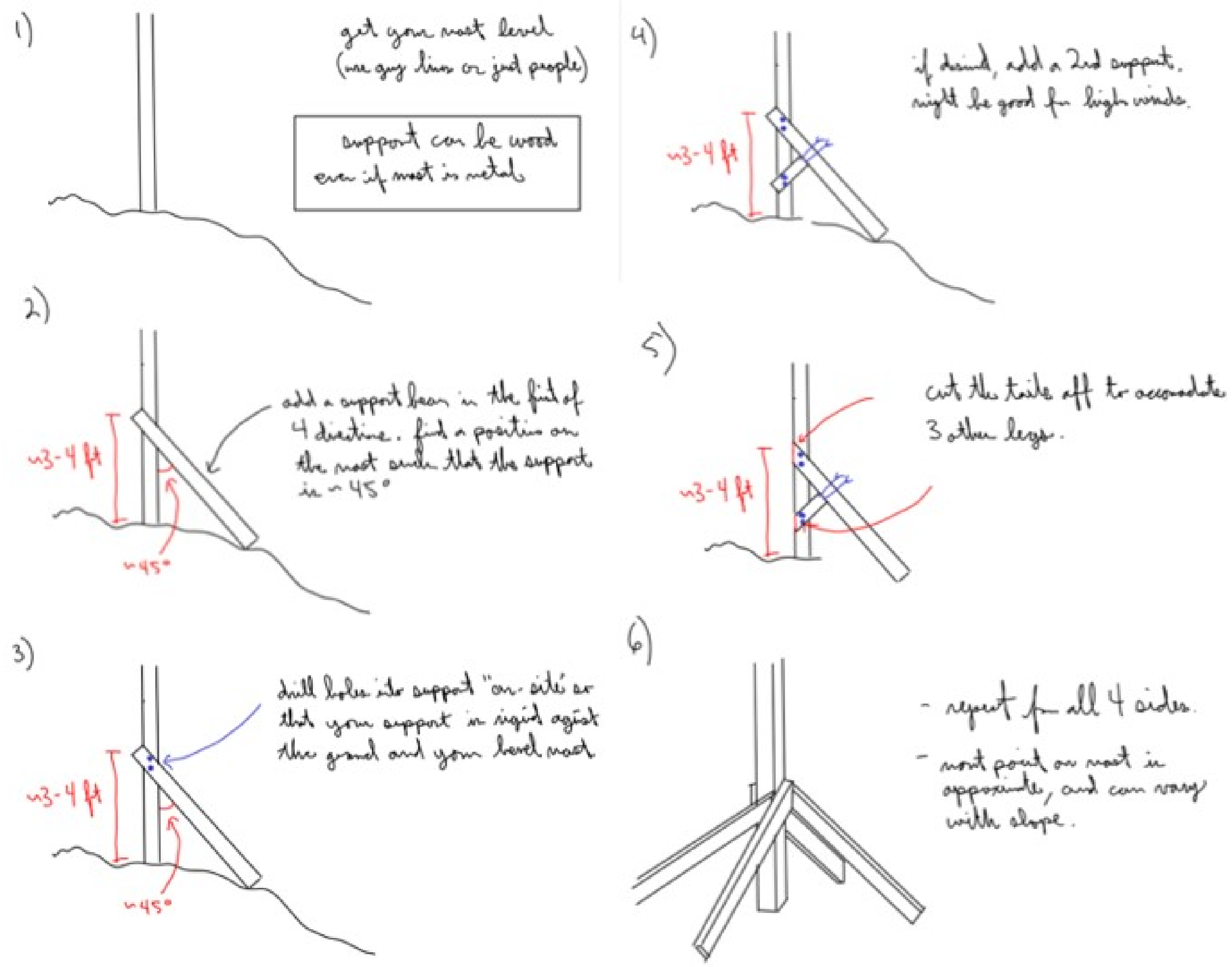

Figure 3.18: A sketch of instructions which were used for constructing the first iteration of wooden strut supports for the BEACON masts. These were first implemented on a subset of antennas during the 2020 partial deployment, and later used on all masts in 2021.

Figure 3.19: The 2020 antenna as imaged in 2021 following a winter of deployment. The structural connection between the element and front-end board failed completely. The visible singeing inside the enclosure indicate that a lightning strike is a possible candidate for the source of the damage.

As a senior member in the collaboration I was intricately involved with the planning and execution of both deployments. Under my direction a series of internal instruction documents and notes were made in the lead-up to each of these deployments to provide detailed instructions for every procedure that was planned for the deployments.

As stated, one of the main focuses of these deployments was to resurrect the status of the prototype and to perform accurate measurements of the antenna positions such that new data could be taken and accurately analyzed. A brace was designed for the permanent installation of GPS patch antennas on each mast (Figure B.5. These braces and antennas were installed in equivalent position on each mast, and could be used for initial position calibration measurements.

In both 2021 deployments initial position measurements of the antenna masts were made with the Real Time Kinematic (RTK) protocol that compares GPS positioning of two nearby GPS antennas - resulting in cm level precision by correcting for the propagation conditions in the local atmosphere [190]. As stated above, each antenna mast now included a dual-band GPS patch antenna, which was connected to a GPS receiver on demand. We used a u-blox C099-F9P application board (ZED-F9P GPS [191]) to measure the relative position of each antenna to a UNVACO GPS station permanently installed ~ 30 m away from the BEACON site at 37.58915N, 118.23844W [141].

Data was taken over the course of both 2021 deployments, however here we focus on the dedicated pulsing deployment. Pulsing data was taken over the course of 3 days during the dedicated calibration campaign in 2021, during which pulsing data was taken for 6 separate sites in both polarizations (the 6 sites are highlighted in Figure 3.3 and listed in Table 3.3). I was one of two members on the pulsing team which hiked equipment to each of these sites over the course of 3 days. The transmitter included a high-voltage pulser (FID technologies FPM 10-1PNP) driving a biconical antenna (Aaronia BicoLOG 30100E) at known rates, with varying fixed attenuators. Other antennas were used briefly in testing (See Figures B.3

and B.3). The pulser was controlled by a combination of a laptop and Raspberry Pi with GPIO board. At each site the laptop would also be connected to a dual-band patch antennas to perform accurate measurements of the pulsing site location. As the pulsing sites were far from the Observatory Dome an internet connection was not available, so RTK corrections were not utilized here. The pulsing configuration can be seen in Figure 3.20.

Site	Runs	Latitude	Longitude	Altitude WGS-84
1	5630, 5631, 5632	37.58602450°	-118.23354200°	3768.1 m
2	5638, 5639, 5640, 5641, 5642	37.58575767°	-118.22592267°	3697.4 m
3	5643, 5644, 5645, 5646, 5647	37.58779650°	-118.22452000°	3619.0 m
4	5648, 5649	37.58885717°	-118.22786317°	3605.9 m
5	5655, 5656, 5657, 5659, 5660	37.59264500°	-118.22765817°	3741.7 m
6	5658, 5659, 5660	37.59208167°	-118.23553200°	3804.9 m

Table 3.3: The measured location of each pulsing site during the 2021 deployment.

Figure 3.20: The view of the pulsing setup. The bi-cone antenna is visible standing atop a tri-pod stand above the other pulsing gear. The BEACON prototype is installed on mountainside in the background, however it is not easily visible at this distance.

One major challenge when pulsing is ensuring that the array can see the pulses. To ensure this was possible, both the array and pulsing kit were designed to trigger (and pulse) at 1 Hz, synced to the GPS second. Though this would ensure that both were occurring at the same rate, ensuring that the pulse was measured meant shifting the measurement trigger window such that the short pulse was visible within the digitized 8 μs waveform window. For 1 Hz pulsing this alignment has a chance of randomly occurring of 1 in 125,000, so achieving alignment was sometimes tricky. For the pulsing campaign the 5 members were split into 3 teams: the pulsing team (which I was a part of), the site team (which served as an intermediary communicator and provided timing information described below), and the analysis team (which was responsible for looking for pulses in the data and adjusting the DAQ parameter accordingly). The site team member was positioned within walkie-talkie range of the pulsing team, while also being within WiFi range of the Observatory Dome, and thus could serve as an communicator between the pulsing and analysis teams. This was situated near the array with an RX antenna hooked up to a network analyzer capable of taking longer trace windows and independently triggering; this was used to quickly hone in on the signal, providing provide relative timing information for the analysis team which could then tune the DAQ triggering to measure signals. For ease of analysis later the analysis team started a new run for each pulsing configuration.

Following the deployment I used the pulsing data for position calibration of the antenna phase centers. The quality of data was evaluated for each configuration; Figure 3.21 shows the peak-to-peak values for force triggered events for various configurations of a single pulsing cite. 2 configurations in this image show saturating signals, 3 show signals of lower magnitude, while 1 configuration appears to not have seen signals whatsoever (with peak-to-peak dominated by noise). This sort of analysis was performed for each calibration run, with the highest quality configuration being used for each site in calibration.

3.4.4 2021 Position Calibration

Changes in the calibration campaign procedure significantly improved the resulting dataset and enabled the successful execution of the process outlined in Section 3.3 (compared to the

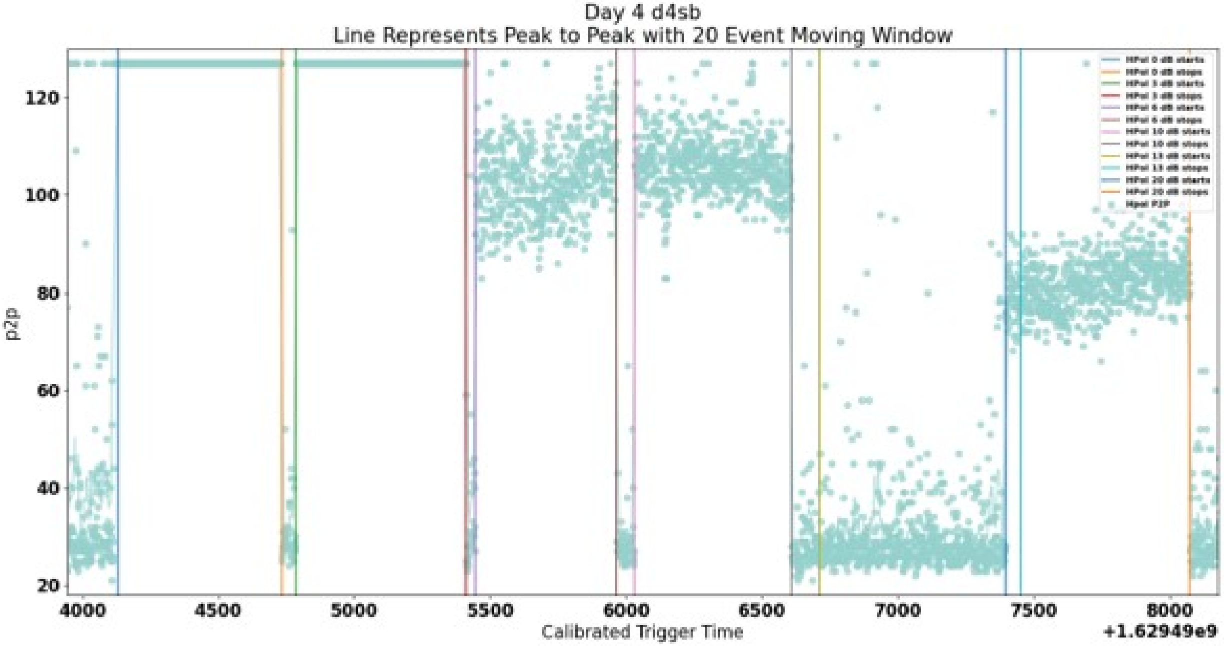

Figure 3.21: The peak-to-peak values for force triggered events for various configurations of a single pulsing cite. 2 configurations in this image show saturating signals, 3 show signals of lower magnitude, while 1 configuration appears to not have seen signals whatsoever (with peak-to-peak dominated by noise).

less successful 2019 calibration effort discussed in Section 3.4.1). As such, these pulsing data were used in the fit described in Equation 3.1. To be used in this minimization the arrival time delays $t_{\text{measured,i,j}}$ must be accurately determined for each site. This is typically done by cross correlating waveforms from each pulse across channels, with the maximum value aligning with the corresponding timing offset. This simple approach relies of the waveforms appearing similar in shaped across channels, otherwise the true timing can be ambiguous due to prominent sidelobes in the correlation. Unfortunately this was the case for the pulsing data taken, so a modified approach was taken.

Waveforms from a single pulsing site are extremely consistent within a single channel. The waveforms for each channel/site were aligned and averaged to create a per-channel reference template. These templates were of more consistent shape, and each pair was cross correlated to obtain an initial time difference: $t_{\text{template,i,j}}$, where i and j refer to the antennas in the cross correlation/baseline. Each individual pulse received for antenna i was then correlated with its corresponding template to obtain secondary time differences δt_i. Though each signal was consistent in shape, the timing within the event window resulted in jitter for the values of δt_i which would contribute to jitter in the final time delay calculations. If $t_{\text{measured,i,j}}$ is defined as the difference in arrival times at antenna i and j given by $t_i - t_j$, then the final time delays were calculated for each baseline using:

$$t_{\text{measured,i,j}} = t_{\text{template,i,j}} + (\delta t_i - \delta t_j) \tag{3.3}$$

the resulting distribution could be fit per baseline, giving a mean and associated error bars for the measurement. This method leverages the consistency in signal appearance within a single channel and leverages it to overcome the visible differences across channels. A set of 6 $t_{\text{measured,i,j}}$ values were calculated per polarization per pulsing site, and were used alongside the initial GPS measurements as input into the χ^2 minimization.

Minimization was performed using the iMinuit in Python. The final calibrated antenna phase center positions are presented in localized East-North-Up (ENU) coordinates in Tables 3.4 and 3.4. Figures 3.22 and 3.22 correlation maps for each of the pulsing sites as perceived by the prototype array using this calibration, which show a reconstruction accuracy of $<\sim 1$ degrees. The resolution errors on the phase centers are estimated to be less than 5% of the shortest relevant wavelength. Differences occur between the HPol and VPol calibrations (which were executed separately). This is expected, as each antennas beam pattern will be slightly different due to local terrain and orientation on the mast. The resolution of the prototype to reconstructing the arrival direction of radio signals was experimentally determined by reconstructing arrival directions of below-horizon RFI sources, the majority of which arrive from a few very loud stationary emitters. A 2D Gaussian was fit to 7 of the most prevalent sources, with an average 90% integral area for the fits of < 0.1 sq. degrees (see Figure 3.25).

Parameter	Value	
HPol Antenna 0 East	0.0	m
HPol Antenna 0 North	0.0	m
HPol Antenna 0 Up	0.0	m
HPol Antenna 1 East	-34.33	± 0.10 m
HPol Antenna 1 North	-13.308	± 0.030 m
HPol Antenna 1 Up	15.88	± 0.26 m
HPol Antenna 2 East	-6.96	± 0.09 m
HPol Antenna 2 North	-48.895	± 0.032 m
HPol Antenna 2 Up	3.96	± 0.26 m
HPol Antenna 3 East	-30.46	± 0.11 m
HPol Antenna 3 North	-43.77	± 0.04 m
HPol Antenna 3 Up	13.72	± 0.29 m
HPol Cable Delay Antenna 0	462.59	ns
HPol Cable Delay Antenna 1	465.11	± 0.29 ns
HPol Cable Delay Antenna 2	454.63	± 0.26 ns
HPol Cable Delay Antenna 3	462.95	± 0.34 ns

Table 3.4: Calibrated HPol phase center positions. Errors presented are the 1 σ bounds given by minimization (iMinuit). Initial errors were input into the minimizer at 10 cm for each spatial coordinate and 0.05 ns for cable delays. The scale of errors are set by $\sigma(t_{\text{measured,i,j}})$ from Equation 3.1 which are are derived as described in the discussion around Equation 3.3. Coordinates are given in East-North-Up (ENU) coordinates with the original set as the initial location of antenna mast 0.

Parameter	Value	
VPol Antenna 0 East	0.0	m
VPol Antenna 0 North	0.0	m
VPol Antenna 0 Up	0.0	m
VPol Antenna 1 East	-33.57	± 0.09 m
VPol Antenna 1 North	-13.218	± 0.028 m
VPol Antenna 1 Up	16.67	± 0.17 m
VPol Antenna 2 East	-6.87	± 0.09 m
VPol Antenna 2 North	-48.918	± 0.026 m
VPol Antenna 2 Up	4.22	± 0.22 m
VPol Antenna 3 East	-30.16	± 0.11 m
VPol Antenna 3 North	-43.794	± 0.032 m
VPol Antenna 3 Up	14.72	± 0.27 m
VPol Cable Delay Antenna 0	459.16	ns
VPol Cable Delay Antenna 1	469.81	± 0.27 ns
VPol Cable Delay Antenna 2	463.79	± 0.25 ns
VPol Cable Delay Antenna 3	463.83	± 0.30 ns

Table 3.5: Calibrated VPol phase center positions. Errors presented are the 1 σ bounds given by minimization (iMinuit). Initial errors were input into the minimizer at 10 cm for each spatial coordinate and 0.05 ns for cable delays. The scale of errors are set by $\sigma(t_{\text{measured,i,j}})$ from Equation 3.1 which are are derived as described in the discussion around Equation 3.3. Coordinates are given in East-North-Up (ENU) coordinates with the original set as the initial location of antenna mast 0.

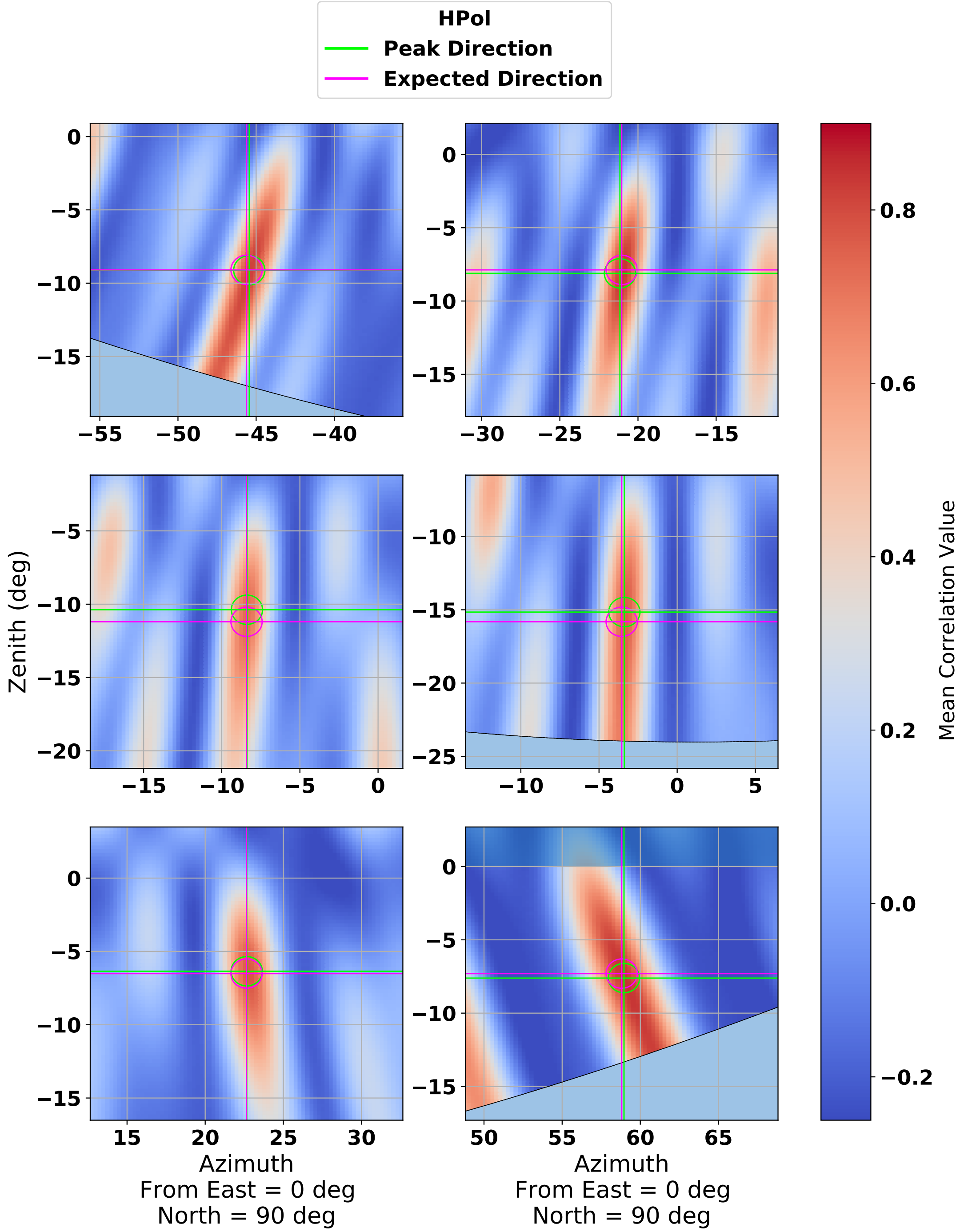

Figure 3.22: Calibrated HPol maps for pulsing events from each of the six pulsing sites. The expected signal direction (fuchsia reticle) and the peak direction (green reticle) are presented for each pulsing site. The circles associated with each reticle have a radius of 1°.

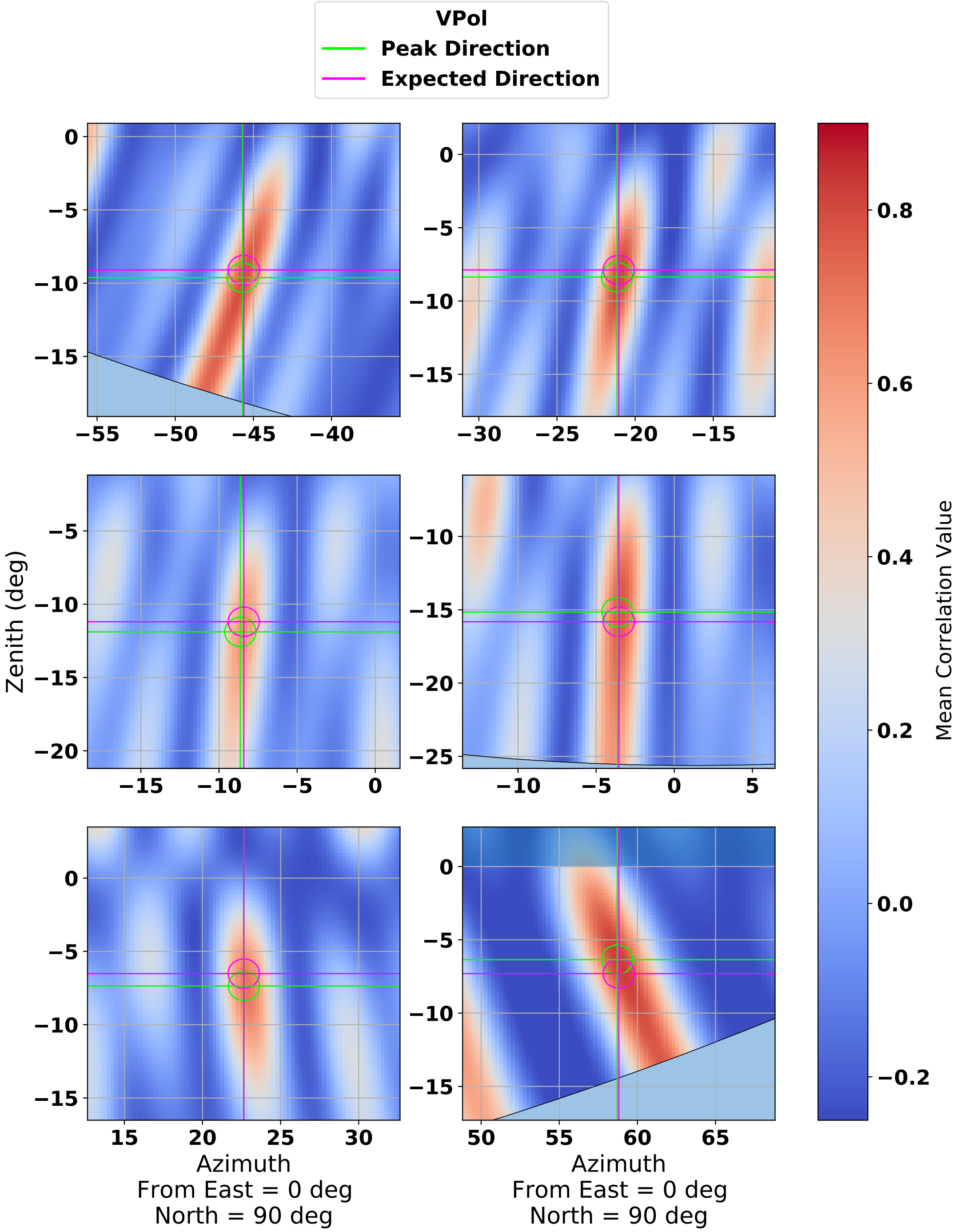

Figure 3.23: Calibrated VPol maps for pulsing events from each of the six pulsing sites. The expected signal direction (fuchsia reticle) and the peak direction (green reticle) are presented for each pulsing site. The circles associated with each reticle have a radius of 1°.

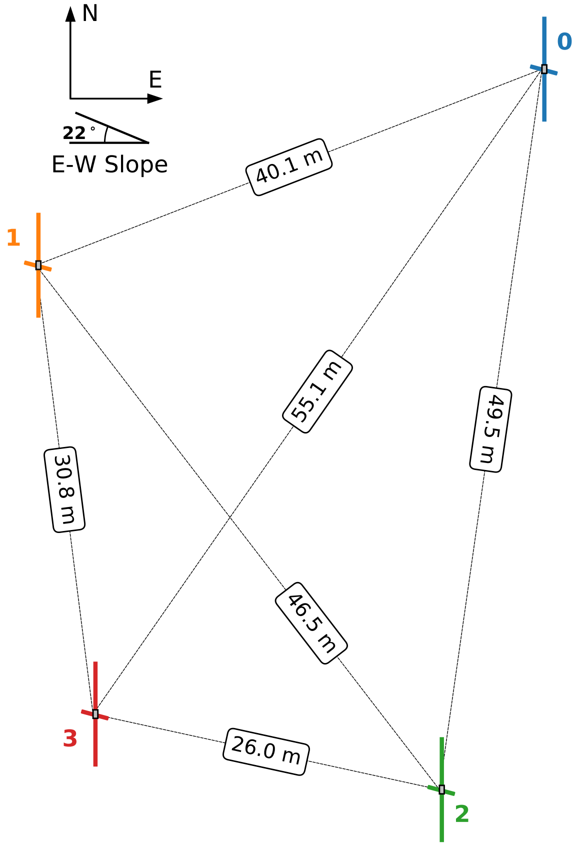

Figure 3.24: A top-down view of the array layout in local East-North-Up (ENU) coordinates. Positions correspond to calibrated HPol phase centers. Baseline distances have been labeled for each antenna pair. The slope the antennas are situated on is rugged and generally amorphous, however the approximate downhill slope across the array in the East-West direction is 22°. Relative to the lowest antenna (mast 0), the heights of 1, 2, and 3 are approximately 15.9 m, 4.0 m, and 13.7 m respectively. The size of each antenna has been magnified 5× compared to baselines for visibility.

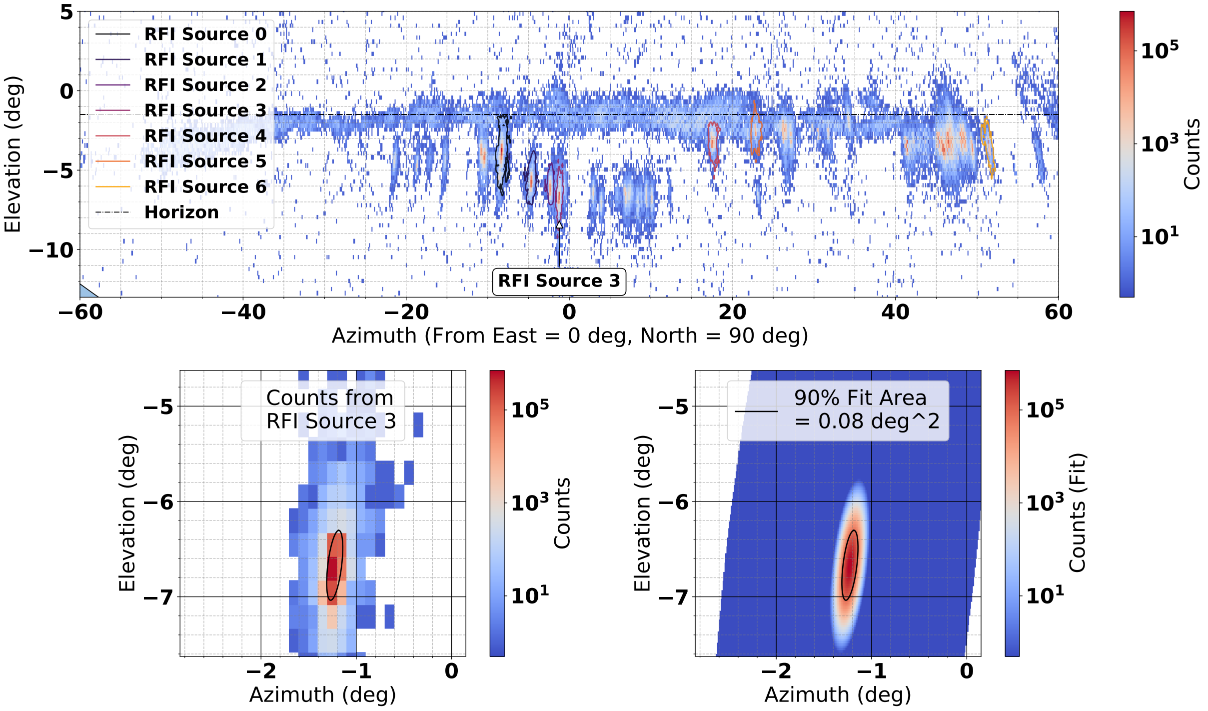

Figure 3.25: Top: Reconstruction direction of events from one week in September 2021. Seven of the most populated RFI sources have been highlighted. These sources are fit with a two-dimensional Gaussian after isolating the events in each region. Bottom Left: Isolated events from RFI Source 3 (arbitrarily chosen as an example). Bottom Right: 2D Gaussian fit (color map), with outline of the 90% integral area of the fit plotted on top. Note that the color scale is logarithmic and represents counts for all 3 plots. The average fit 90% integral area for all 7 sources was < 0.1 sq. degrees. The approximate location of the horizon has been indicated at an elevation angle of -1.5°.

3.5 Instrument Performance and Data Analysis

3.5.1 BEACON Analysis Code

BEACON data is stored in ROOT files, however the vast majority of the analysis is performed using Python code. The general structure of the code is described here, with the code being available at https://github.com/djsouthall/beacon. It is common in the radio astronomy community to interpret and process waveforms both in the frequency and time domain, so many techniques related to signal processing are used throughout as a matter of course.

As will be described in Section 3.6.1, the majority of BEACON waveforms are processed in analysis with a series of notch and band pass filters. Prominent contributions from CW backgrounds are removed using sine subtraction filtering [193], where the signals are filtered by fitting sine waves in the time domain with floating phase and amplitude, and remove any frequencies with amplitude above a threshold set in the analysis. The sine subtraction process is time consuming, and so is typically performed in advance for all waveforms, with the resulting filter parameters being cached. BEACON data is read in using the `Reader` class, which provides helper functions for interfacing with the ROOT data using Python. This classes is used for loading in waveforms, as well as accessing run and meta-data such as trigger information, or house-keeping data. To process the sine subtraction filtering as waveforms are loaded into Python a wrapper class `SineSubtractedReader` was created, which automatically applies the cached sine subtraction filters to any requested waveform. These `Reader` classes form the base element of the analysis, with run-specific `Reader` objects being produced whenever a script is processing data from that run.

The helper functions of the `Reader` classes are left to the minimum, with the majority of additional signal processing and interpretation related features being included in the `FFTPrepper` class. This class and the associated daughter classes `TimeDelayCalculator` and `TemplateCompareTool` provide support for defining arbitrary filters for each channel, upsampling, calculating time delays and cross correlations, performing template comparisons, calculation of impulsivity, time domain plotting, frequency domain plotting, etc. If a waveform is being processed it is often done through one of these classes.

Another major pillar of the BEACON analysis is the use of interferometric correlation maps, which have already been described. All maps are created using the `Correlator` class. The `Correlator` class uses the `Reader` and `FFTPrepper` classes for loading and processing waveforms. The `Correlator` loads in a calibration `.JSON` file which contains the antenna position and cable delay information, which is necessary for pre-calculating the expected arrival time differences used for generating maps (Section 3.3). The `Correlator` provides a significant tool set that allows for plotting and interpreting maps.

Various parameters are calculated for each event using the aforementioned tools and stored in `HDF5` files. The values from these files are loaded with the `dataSlicer` class, which provides tools to easily interpret the parameters for several runs with single commands. This class handles all loading for `HDF5`, and provides support for parameter transformations and comparative calculations such as adding/subtracting parameters, calculating minimums or maximums across channels or between parameters, taking the mean of parameters, or any other user defined arbitrary transformation. Functions are provided to easily interpret these parameters, such as 1D and 2D histograms. This class has support for user-defined regions of interest (ROI), which are defined by a dictionary of arbitrary length containing various parameter names and their associated upper and lower bounds. With a defined ROI the use can quickly access all events which satisfy that ROIs cuts. This feature can also be used to plot contours of the subset ROI values atop superset histograms, such as is shown in Figure 3.25. All cuts described in the following sections were applied using the ROI cut functionality of this class.

The `dataSlicer` class also provides the event display functionality used throughout the analysis. Event displays like shown in Figures 3.27, 3.31, and 3.37 are all produced using this class. Depending on the purpose of the event display, two modes are provided: "verbose" and "reduced". Verbose was used more often in analysis as it includes a higher density of information about the event. Figure 3.26 shows a verbose version of reduced Figure 3.27, displaying a table of relevant parameters the right. Each event is clearly separated with more informative scale. Circles corresponding to each time delay (calculated for each baseline) are shown overlaying the maps in the lower left, which can be helpful for interpreting maps and identifying the source of sidelobes. The maximum position of each map is also highlighted with a cross-hair.

Additional features that are not visible in Figure 3.26 but are available for maps and event displays created using the `Correlator` and `dataSlicer` include 1. the ability to regenerate maps by temporally cropping waveforms to their adjusted x-axis range (helpful for isolating source directions for coincident events), 2. the ability to double click anywhere on the maps to plot the waveforms as if aligned from that direction (helpful when interpreting visible sidelobes or coincident events), 3. the ability generate the map using a subset of antennas or baselines, 4. the ability to generate the map using Hilbert enveloped waveforms, 5. the ability to display in-view airplane trajectories (Figure 3.31), 6. the ability to dynamically adjust the assumed source distance, 7. the ability to weight the map correlation values by angular proximity to predicted arrival time delay curves, 8. the ability output projected line-of-sight ellipses from correlation map pointing directions into `.KML` files which can be loaded into Google Earth to highlight potential source directions, 9. the ability to also plot a combined all-channel map. Such features were were used regularly throughout the analysis.

Analysis scripts were written for various tasks throughout the analysis, importing the above classes as necessary. Parameters which are stored in the `HDF5` files are calculated in such analysis scripts. When processing a significant amount of data for the first time, the general analysis procedure is performed using an automated `BASH` script which calls the various analysis scripts in order for each run. This `BASH` script is executed for each run on

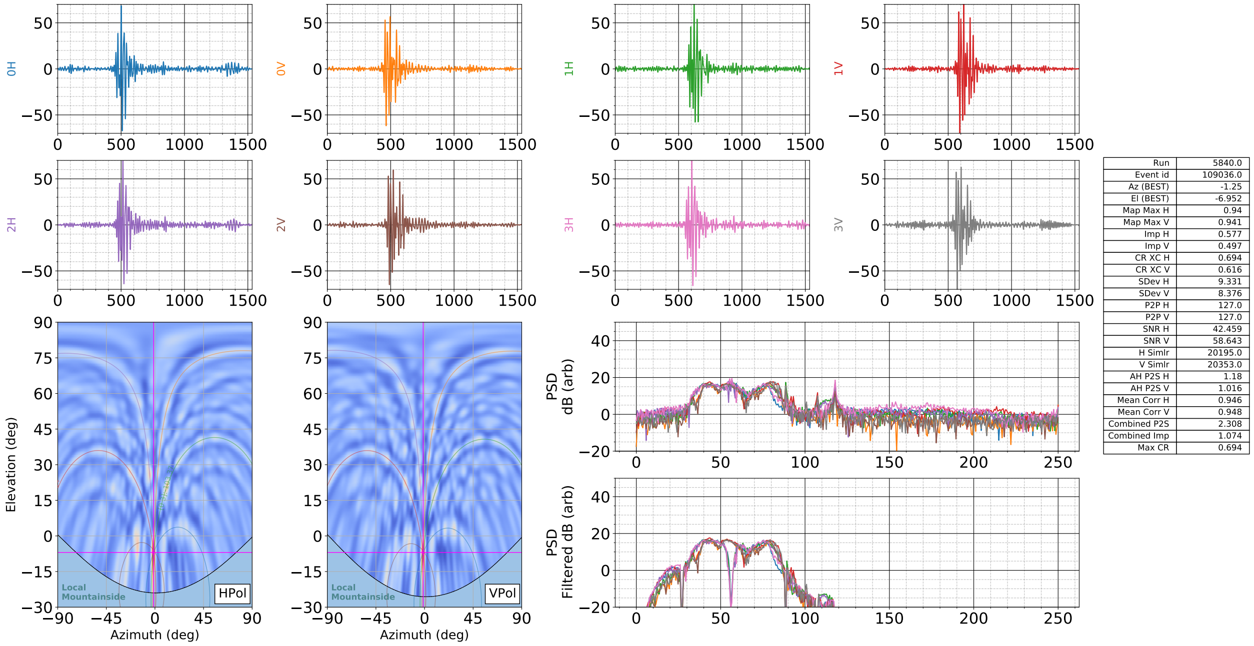

Run	5840.0
Event id	109036.0
Az (BEST)	-1.25
El (BEST)	-6.952
Map Max H	0.94
Map Max V	0.941
Imp H	0.577
Imp V	0.497
CR XC H	0.694
CR XC V	0.616
SDev H	9.331
SDev V	8.376
P2P H	127.0
P2P V	127.0
SNR H	42.459
SNR V	58.643
H Simlr	20195.0
V Simlr	20353.0
AH P2S H	1.18
AH P2S V	1.016
Mean Corr H	0.946
Mean Corr V	0.948
Combined P2S	2.308
Combined Imp	1.074
Max CR	0.694

Figure 3.26: Event display of a signal flagged by the 60 Hz algorithm (discussed in Section 3.5.2). This event is shown in the "verbose" event display mode which is more useful when performing analysis. This display includes a table of relevant parameters on the right, has each waveform fully displayed. Circles corresponding to each time delays (calculated for each baseline) are shown overlaying the maps in the lower left. This event has also been presented in Figure 3.27 in the reduced format. Top: Waveforms corresponding to each of the 8 channels. Waveform y-axis represents voltage in units of ADU. Bottom Left: HPol and VPol correlation maps. The colorscale of each map is individually normalized, and the region of the maps pointing into mountainside is masked out. Bottom Right: The Power Spectral Density (PSD) before and after filtering. The data has been filtered as described in Section 3.6.1. Right: Table of relevant parameter values.

the University of Chicago Midway High-Performance Computing cluster, with each run's analysis framework being performed on a separate node.

3.5.2 Characterization of Radio Frequency Interference (RFI)

The BEACON prototype instrument is positioned near the border of California and Nevada and looks East over the Nevada desert. This region is populated by a series of small towns with agricultural and mining industries, military bases, and power infrastructure like the Crescent Dunes Solar Project. The site is also just south of a common commercial air flight path. Though all of these anthropogenic sources are tens to hundreds of kilometers away from the site, many sources are visible to BEACON due to its high elevation and sensitivity to radio signals at signal strengths near thermal levels.

In this Section, we discuss several ways this anthropogenic activity appears in the data taken with the prototype instrument. The vast majority of anthropogenic signals in the data can be easily separated from cosmic-ray and neutrino signals due to signal shape, polarization, spatial and temporal clustering, and other event characteristics.

Static Sources: The most common category of events come from towns and infrastructure. These events cluster spatially, are expected to be localized to a single beam, and therefore can be cut based on their direction. The signal shapes observed from different RFI sources can vary significantly, however signals from a single source are generally very consistent.

Continuous Wave Sources and the Television Band: Continuous wave (CW) signals are narrow band, arriving at the array with very little temporal variation. Because of this they are often not directly responsible for activating the trigger (which is designed for temporally impulsive signals); however, they are commonly visible in the spectrum of triggered broadband signals. We typically remove these from the data in offline analysis via notch filters and the sine subtraction technique described in Section 3.6.1. The nominal band of the BEACON antennas overlaps with common radio communication frequencies, as well as the low-VHF television (TV) broadcasting range. Signals from the KHSV TV station in Las Vegas are pervasive in all HPol data, despite the transmitter being over 300 km away and lacking a direct line of sight to BEACON. A notch filter is currently used in analysis exclusively in HPol channels to combat this signal. Figure 3.28 shows the spectra of HPol and VPol antennas over the course of a few hours. Bright horizontal lines in these plots correspond to CW sources. The TV band is visible in HPol from ∼53 to 60 MHz. Intermittent short bursts of activity can be seen at 42 and 48 MHz, which are associated with communication systems for the California Highway Patrol and the Los Angeles Department of Water and Power, respectively.

Periodic Noise Sources: An excess of events have been observed to arrive at the BEACON prototype with time differences corresponding to multiples of 1/(60 Hz). These signals can be associated with arcing or similar discharges from power infrastructure, which operates at 60 Hz in the US. A 55 kV high-voltage transmission line connecting Nevada with the Owens Valley runs within the field-of-view of the prototype, with several substations. When there is snow on the valley floor, this class of signal largely is suppressed, perhaps because the snow is acting like an insulator to prevent arcing.

Similar to CW, this category is a subset of static sources and can be removed with directional cuts. However, since it may be advantageous to keep those directions in some searches, an algorithm was developed to demonstrate removal based on timing alone. We define a temporal test statistic (TS) which gives a measure of the relative abundance of temporally nearby events with trigger times consistent with a period of T. For each event, i, the difference in trigger times is calculated for a range of nearby events, indexed by j, within a specified time window w. To allow for multiples of the period, we calculate the absolute difference to the nearest multiple of T using:

$$d_{i,j} = \left| \left(t_i - t_j + \frac{T}{2} \right) \% \, T - \frac{T}{2} \right|, \tag{3.4}$$

where % refers to the floored modulo operation ($a\%n = a - n\lfloor \frac{a}{n} \rfloor$), resulting in $d_{i,j}$ being near zero for times close to an integer multiple of T. Within each window w containing $N_w(i)$ events, we construct a histogram with 20 bins ranging from 0 to $T/2$. The top right portion of Figure 3.29 shows an example histogram, with red highlighting the bin, $c_{i,0}$, containing the $d_{i,j}$ most consistent with a periodicity of T and green highlighting the 50% of bins least consistent with T. The test statistic for that event (TS_i) is defined as the difference between the red region and the mean of the green region, given by:

$$\text{TS}_i = c_{i,0} - \frac{1}{10} \sum_{k=10}^{19} c_{i,k} \tag{3.5}$$

Arrival times from a uniform distribution would result in no significant difference in counts between the red and green regions, resulting in a TS near 0, while a set of perfectly periodic events would all lie within $c_{i,0}$, resulting a TS of 1. Datasets contaminated with periodic noise sources are in-between these two extremes, resulting in a distribution of TS that is broadened when compared to uniform arrival times. Periodic events can thus be highlighted from within a contaminated set of data by cutting on high TS values. In Figure 3.29 we show how this algorithm can separate events observed arriving at a regular 60 Hz rate in data taken from September 2021. This figure also shows how the baseline timing of the periodic events fluctuates with time as the 60 Hz drifts, which is handled by choosing a value for w that is short relative to the fluctuations. Depending on the desired efficiency, this algorithm will not flag all events arriving with a periodicity of T, but can isolate a clean subset of those events, which can then be used to motivate further targeted cuts based on template matching, direction, and signal properties to further improve the efficiency for removing this form of RFI.

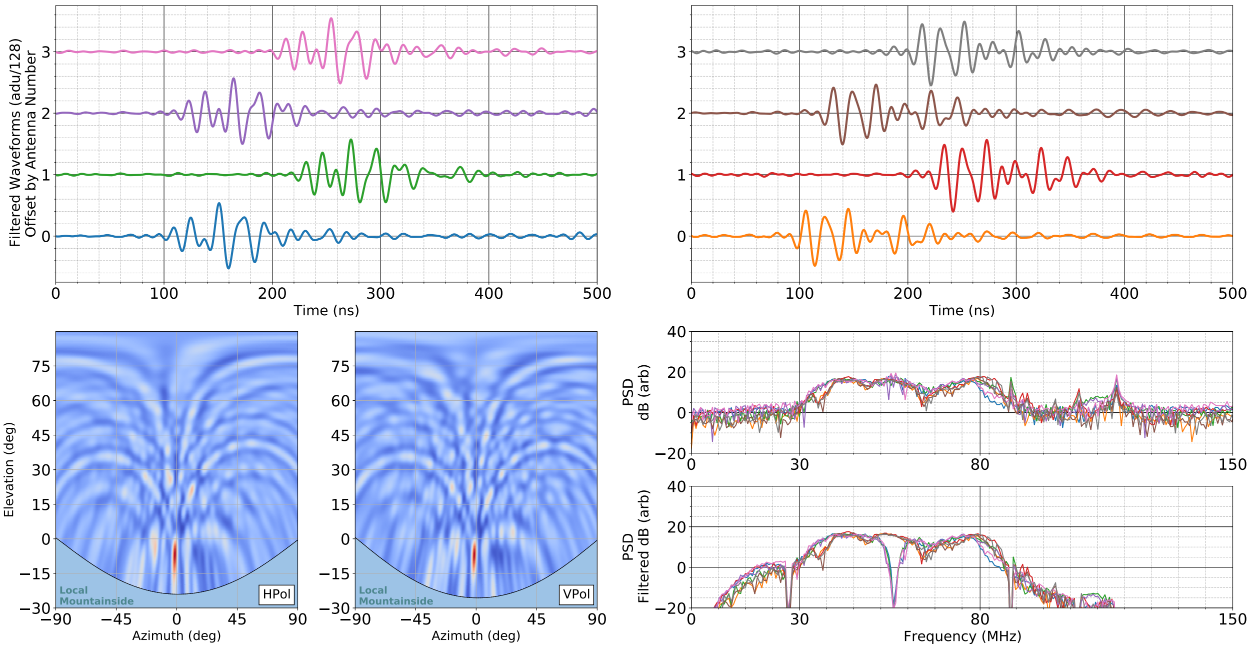

Figure 3.27: Event display of a signal flagged by the 60 Hz algorithm. This event has also been presented in Figure 3.26 to show the more verbose event display. Top: Waveforms corresponding to each of the 8 channels. Waveforms are divided by the digitizer dynamic range (128 ADU) and offset by channel number for visibility. Bottom Left: HPol and VPol correlation maps. The colorscale of each map is individually normalized, and the region of the maps pointing into mountainside is masked out. Bottom Right: The Power Spectral Density (PSD) before and after filtering. The data has been filtered as described in Section 3.6.1.

Airplanes: One of the few above horizon sources of RFI is airplanes. As part of the above-horizon impulsive events search discussed in Section 3.6.2, over 1000 RF triggered events were associated temporally and spatially with airplanes, corresponding to >100 individual airplanes, an approximate observation rate of $\mathcal{O}(1)$ airplane per day. Airplane signals have been identified by other experiments [173]; though several potential sources have been described, no definitive cause for these signals has yet been determined. The signals differ greatly in shape between airplanes and are not present for the majority of airplanes passing by the site. Because of this we believe that the airplanes are not the source of these signals but rather serve as reflectors to signals originating on the ground. Therefore, we do not expect to see signals from all airplane tracks in our band. An example airplane-associated series of events is shown in Figure 3.30, which also shows the self-reported trajectory of the airplane superimposed [187]. Apparent in this figure is a systematic offset in reconstruction direction for airplanes. This offset is approximately 1° in HPol and 2° in VPol (where each polarization is calibrated independently). This offset is small and does not significantly impact the results of this analysis, however understanding and fixing it is a priority for future analysis (see Section 3.7).

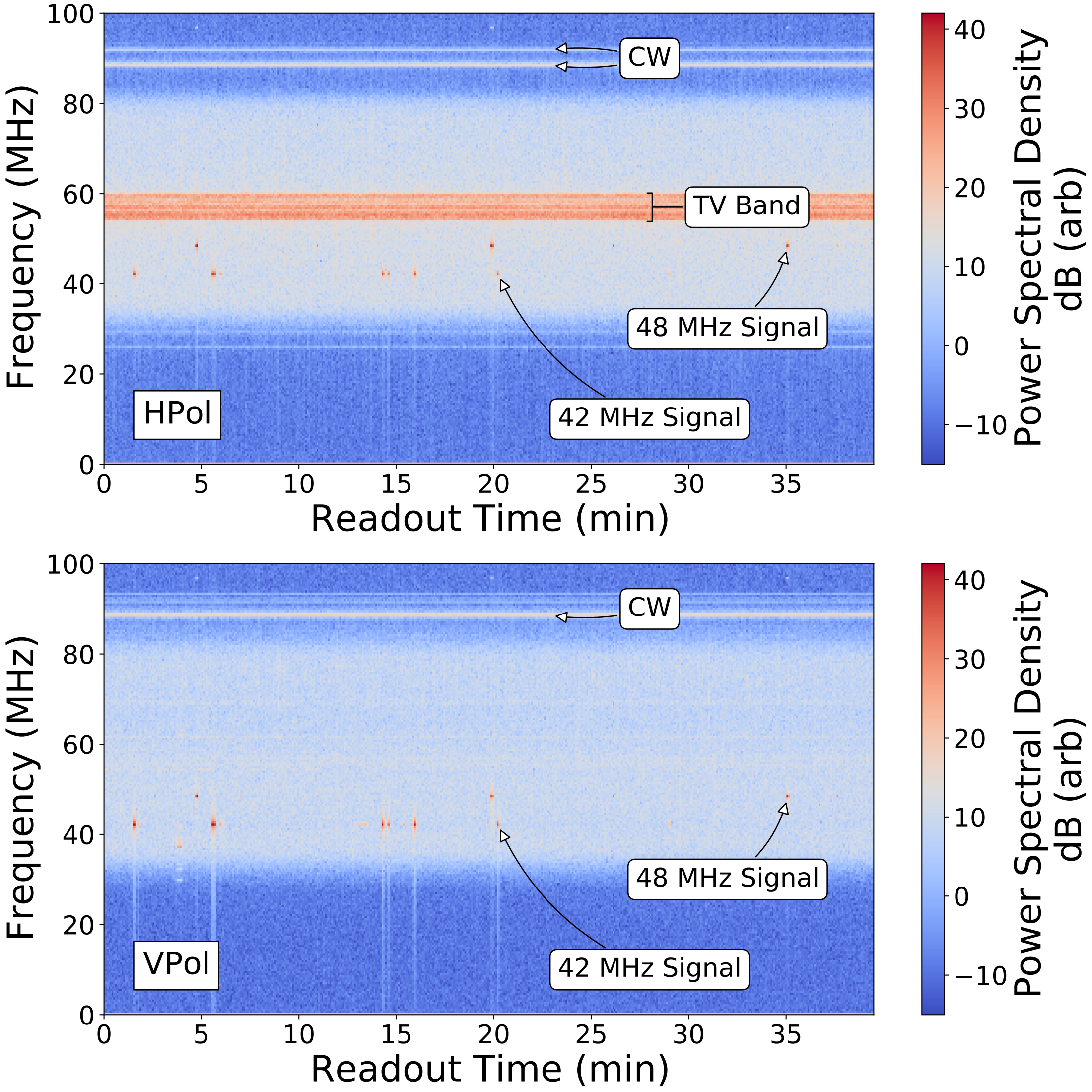

Figure 3.28: Spectrograms of the HPol (top) and VPol (bottom) channels of antenna 0 generated using force-triggered events (taken at 1 Hz) from a run in October 2021. Several features are highlighted in the spectrograms, including examples of CW noise, the TV broadcasting band, and intermittent RFI at 42 and 48 MHz that we believe is associated with radio communications. The color map is presented in arbitrarily offset dB units (a conversion between ADU and volts has not been performed).

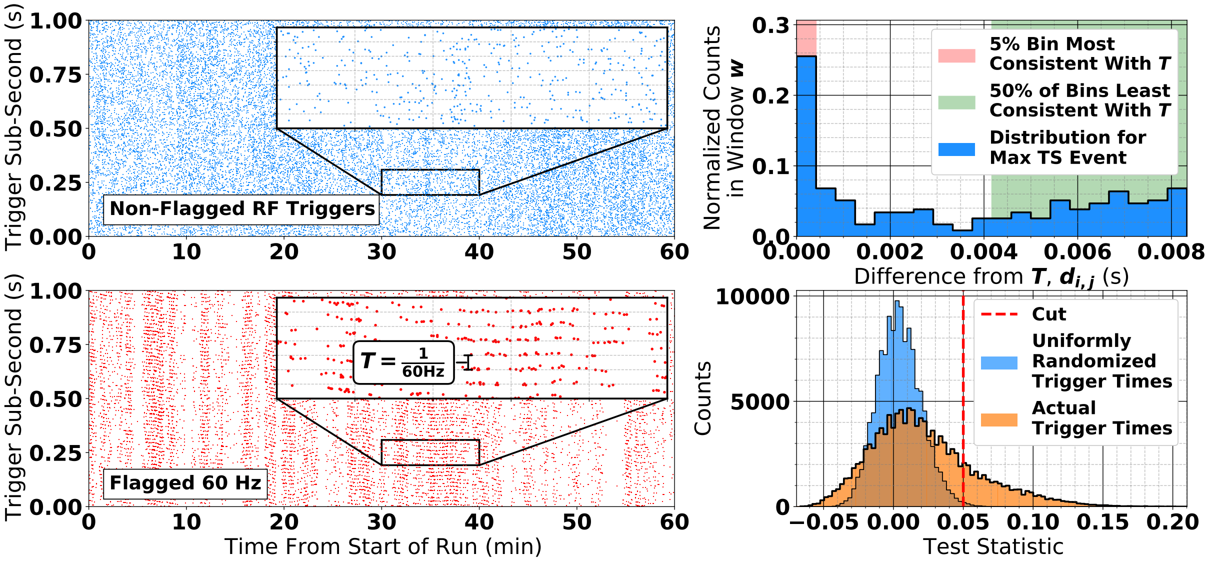

Figure 3.29: Left: The arrival time of RF-triggered events within a run from September 2021, with sub-second timing plotted on the y-axis; events not flagged are shown in the top left, with events flagged by the algorithm to be consistent with an arrival rate of 60 Hz (with corresponding periodicity of $T = 1/60$ s) shown in the bottom left. Insets show striations in the bottom plot consistent with the expected periodicity. These flagged events represent ∼20% of the total events in the 1 hour span shown. Top Right: Histograms showing the portion of events arriving at an interval consistent with T for the highest test statistic (TS) event. The TS is the difference in counts in the red region to the mean of the green region. Histograms created using window $w = 20$ s. Bottom Right: A histogram of all TS values for this run. An example cut has been applied near the limit of the TS as calculated for uniformly distributed trigger times, beyond which events are highly likely to be consistent with T. The events flagged will be used to motivate further targeted cuts based on direction, template matching, and signal properties, to further improve the efficiency for removing this form of RFI.

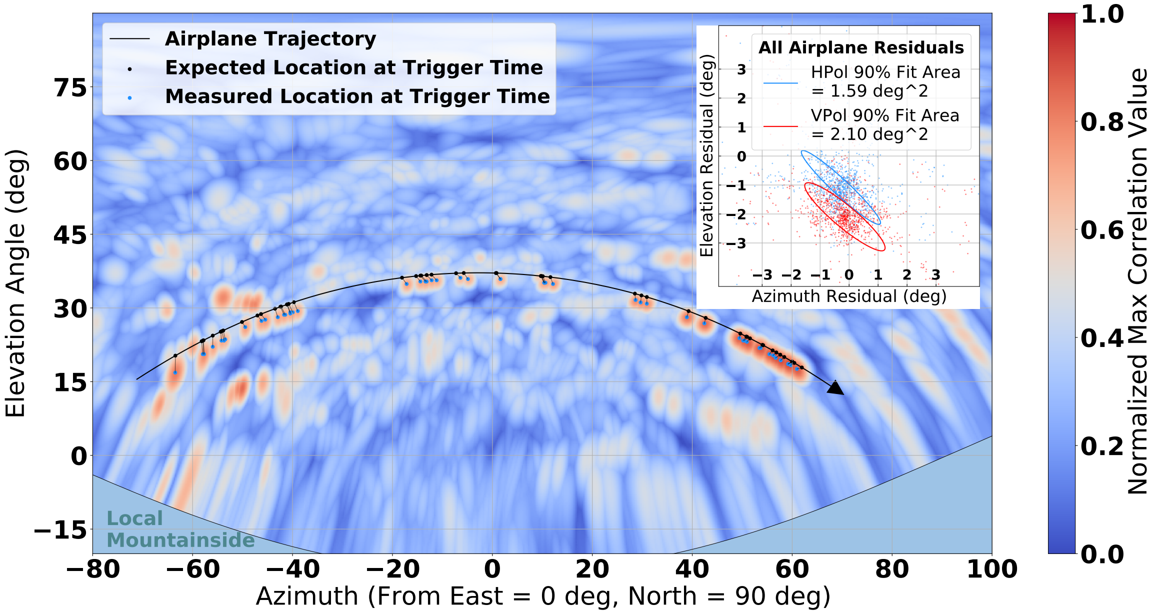

Figure 3.30: Left: The stacked correlation map of 52 events corresponding to a single airplane track, with a colorscale corresponding to maximum correlation map value obtained from any event's individual map generated using all 8 channels. The track of the corresponding airplane using ADS-B data obtained from The OpenSky Network [187] is shown with the black line, and spans ∼3.5 minutes. The expected location of the airplane at the time of each triggered event in the map is shown with the black dots, and the measured location of the peak correlation value of each triggered event is shown with the blue dots. Upper Right Inset: Scatter plots showing the reconstruction offset observed for all airplanes when observed using either HPol (blue) or VPol (red) antennas, with a corresponding 2D Gaussian fit for each. This plot demonstrates an observed systematic offset of approximately 1° in HPol and 2° in VPol (each polarization is calibrated independently). This offset does not show significant angular or temporal dependence and is likely a result of the calibration. Additionally, the 90% integral area of the Gaussian fit observed for these events is larger than the < 0.1 sq. degrees observed for static sources in Section 3.4.4. The original calibration was performed using mountainside pulsing and showed maximal reconstruction offsets of ∼1°. Future calibration campaigns using calibration sources mounted on drones would allow us to better constrain antenna positions by providing a large range of elevation angles for fitting and validation. Calibration is discussed further in Section 3.4.4.

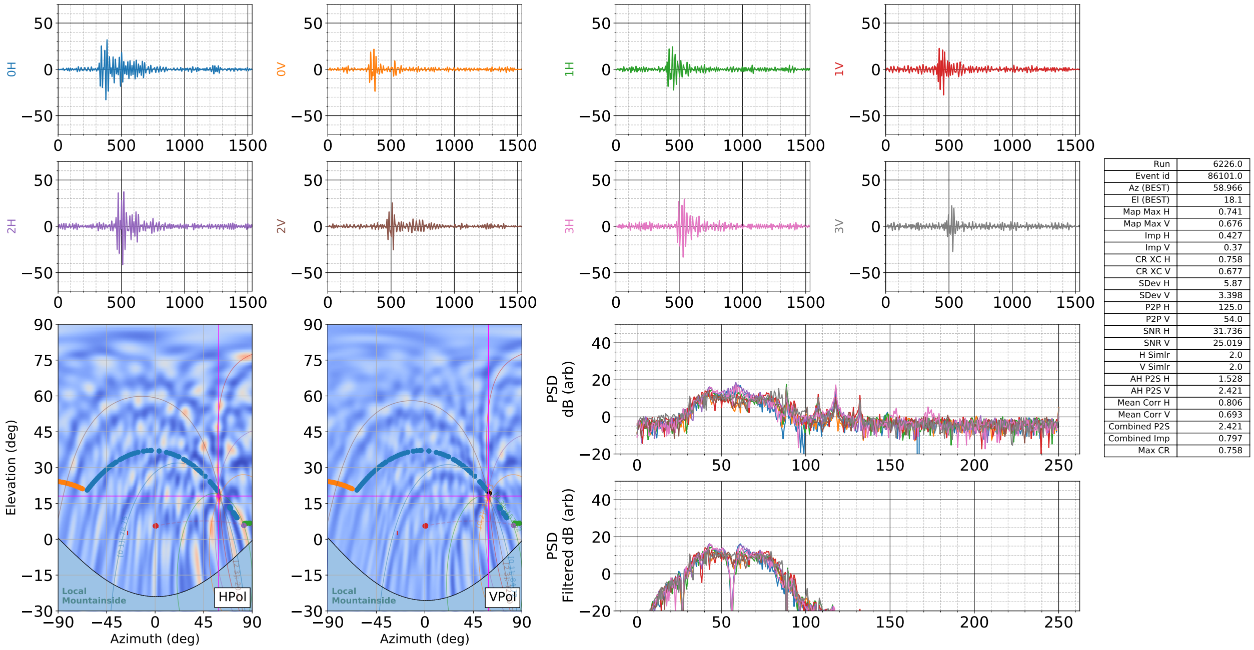

Run	6226.0
Event id	86101.0
Az (BEST)	58.966
El (BEST)	18.1
Map Max H	0.741
Map Max V	0.676
Imp H	0.427
Imp V	0.37
CR XC H	0.758
CR XC V	0.677
SDev H	5.87
SDev V	3.398
P2P H	125.0
P2P V	54.0
SNR H	31.736
SNR V	25.019
H Simlr	2.0
V Simlr	2.0
AH P2S H	1.528
AH P2S V	2.421
Mean Corr H	0.806
Mean Corr V	0.693
Combined P2S	2.421
Combined Imp	0.797
Max CR	0.758

Figure 3.31: Event display of an airplane signal. This event is also one of the events presented in Figure 3.30. Trajectories of in-view airplanes are plotted on-top of the map, showing. Top: Waveforms corresponding to each of the 8 channels. Waveform y-axis represents voltage in units of ADU. Bottom Left: HPol and VPol correlation maps. The colorscale of each map is individually normalized, and the region of the maps pointing into mountainside is masked out. Bottom Right: The Power Spectral Density (PSD) before and after filtering. The data has been filtered as described in Section 3.6.1. Right: Table of relevant parameter values.

3.6 Above-Horizon Impulsive Events

We have categorized impulsive, above-horizon events in the prototype instrument data, identifying a variety of event classes [194]. We are especially interested in above-horizon impulsive events because they contain a sample of cosmic ray air shower events, which can be used to determine the nominal sensitivity of the prototype instrument.

We expect a few cosmic ray events per day to trigger the prototype given nominal beam voltage SNR thresholds of 5σ [189]. Cosmic ray candidates will appear as isolated above-horizon events that are not identifiable as RFI events and do not cluster spatially or temporally. Additionally, cosmic ray events are expected to be impulsive signals that correlate well with cosmic ray templates from simulations. They will also have a polarization angle correlated with the source direction and the direction of radio emission from air showers in the local Earth's magnetic field (*i.e.* $\sim \vec{v} \times \vec{B}$ [63]).

Though the prototype instrument has insufficient sensitivity to detect tau neutrinos, our Monte Carlo simulation, called Cranberry [189], predicts that cosmic ray air showers should be detectable with the prototype instrument. For example, using the measured cosmic ray flux from Auger [58], Cranberry predicts that for a threshold of a beam voltage SNR of $\sim$5, we expect to see a few events per day with the prototype instrument [189]. Cosmic ray air shower signals are similar to the signals that would be made by tau neutrinos, but they can be distinguished via their incident elevation angle at the array. Cosmic ray air showers come from above the horizon, whereas signals from tau neutrinos would come from below the horizon. The observed rate of cosmic ray events in the prototype instrument presents a in-situ validation of the threshold of the instrument. The threshold is an important factor in determining the expected sensitivity to tau neutrinos, allowing us to better predict the sensitivity of the full-scale BEACON experiment in a data-driven way.

The concept for each BEACON station includes more antennas and longer baselines than the prototype and is expected to achieve a significantly better threshold per station. Measurements of correlation map characteristics, SNR, pointing resolution, and trigger thresholds all benefit from the additional antennas and longer baselines of a full station, allowing for better separation of below-horizon and above-horizon events. Additionally, multiple stations with differing views of overlapping effective volumes can be used to veto human-made noise, compared to air shower signals, which are highly beamed.

Here we describe our classification process for above-horizon impulsive events, and show a likely cosmic ray candidate event from the data. We present an analysis of ∼112 days of data taken from the beginning of September to the end of December 2021, consisting of ∼100 million RF-triggered events.

3.6.1 Identifying Above-Horizon Impulsive Events

We first filter the data to remove both known frequencies of anthropogenic noise with static notch filters (at 27, 88.5, 107, 118, and 126 MHz in both polarizations, and additionally from 52.5 to 60.25 MHz in HPol channels, which removes RFI associated with the TV band). We use a method called sine subtraction filtering [193], where we filter the signals by fitting sine waves in the time domain with floating phase and amplitude, and remove any frequencies with amplitude above a threshold set in the analysis. This method preserves causality in the data. We then remove the group delay added by the RF signal chain in the data to recover the original phase of the incident signals.

We then create a correlation map for each event and identify the most likely incident arrival direction for each by selecting the location of the peak cross-correlation value from one of three maps: 1) HPol channels only, 2) VPol channels only, and 3) the average of the two polarized maps. We choose to use the peak location from the map that has the maximum *peak-to-sidelobe ratio* multiplied by the *normalized map peak value.* The peak-to-sidelobe ratio is the ratio of the main peak to the second brightest peak in the correlation map. The *normalized map peak value* is the ratio between the peak value and the optimal possible map value for that event, which would be obtained if a particular direction perfectly sampled the peak of each baseline's cross correlation. Normalizing map peak values in this way counteracts the trend for low SNR events to have lower correlation values and thus lower map peak values. For each map we mask out the direction of the mountainside itself (defined as the area below a simple plane fit to the antenna locations).

We then separate above-horizon from below-horizon events, which removes the vast majority of triggered events, which are dominated by static below-horizontal RFI sources (see Section 3.5.2). We keep events in our sample that have an arrival direction between $[-90^\circ, 90^\circ]$ in azimuth (East = 0°, North = 90°), and $[10^\circ, 90^\circ]$ in elevation as shown in Figure 3.32. The lower bound in elevation of 10° above the horizontal is chosen to be far from the true horizon (which is $\sim$1.5° below the horizontal), to create a cleaner sample of downgoing events. The azimuthal cut restricts the search to the direction that the array is most sensitive to, which is to the East, since it is on an East-facing slope. Sources of RFI are finely resolved, suggesting that clustering could remove backgrounds in future searches.

We then develop a series of cut parameters to select for impulsive, isolated events that correlate with a cosmic ray template. We intentionally keep these cuts loose so any one cut is not overly restrictive, in order to investigate a variety of classes of events of interest above the horizon, while keeping a high fraction of triggered cosmic ray events in the remaining event sample. After all cuts, the data set is reduced to 5,440 events. We list the cuts below, and in Table 3.6, along with the numbers and fraction of events that survive each cut. The cuts are defined as:

Time Delay Clustering Cut: Remove events that are in runs with more than 10 events that have the same measured arrival time delays between antenna pairs (with an absolute tolerance of 2.5 ns per baseline). Runs in the data set are 1 to 3 hours long. This cut is used to remove events that come from the same direction.

Peak-to-Sidelobe Ratio: Remove events for which the ratio of the main peak to the

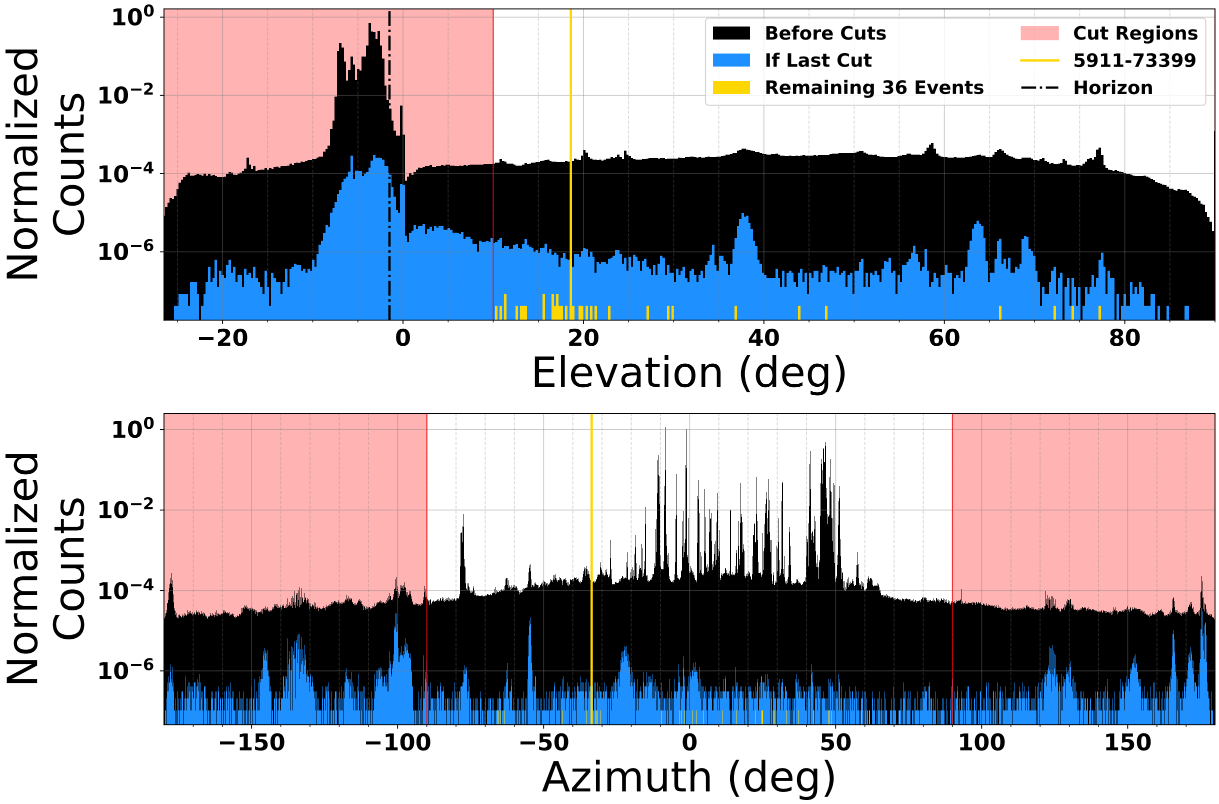

Figure 3.32: Arrival directions of the received radio signal at the BEACON prototype for the full data set (black), the data set remaining after all other cuts have been applied (blue), and the 36 remaining events discussed in Section 3.6.2 (yellow). The reconstructed elevation (azimuth) for each event are shown in the top (bottom). Regions shown in red are excluded by the cut value placed at the red line. For reference, the parameter values for the likely cosmic ray candidate event (discussed in Section 3.6.2) is shown with the yellow vertical line (Event 5911-73399). The approximate location of the horizon is shown on the top plot at an elevation angle of -1.5°.

second brightest peak in the HPol and VPol correlation maps sums to less than 2.15. A peak-to-sidelobe ratio near 1 indicates two peaks with comparable brightness. This cut removes events where it is likely that the event could be mis-reconstructed, i.e. the main peak is indistinguishable from the sidelobes.

Impulsivity: Remove events that have summed HPol and VPol impulsivities ($\mathcal{I}$) below 0.3. $\mathcal{I}$ is a metric for measuring the impulsiveness of a signal [103], defined here as $\mathcal{I} = 2A-1$, where A is the average of the cumulative distribution of fractional power contained within a 400 ns window centered on the peak of the Hilbert envelope of the aligned and averaged waveforms for a particular polarization.

Cosmic Ray Template Correlation: Remove events for which neither polarization obtains a normalized correlation value of 0.4 with a simplified cosmic ray template. The template used was a bipolar impulse with duration and amplitudes motivated by an off-axis angle of 1.37° for a slightly upgoing air shower [195]. This signal is then convolved with the appropriate channel-dependent responses of the prototype instrument, before undergoing the same filtration and cleaning as the waveforms, to create a template for correlation.

Likely Mis-Reconstructions of Known Below-Horizon Sources: To remove events that mis-reconstruct above horizon due to prominent sidelobes of below horizon sources, a set of bright below horizon sources were identified. Events are cut if their best below-horizon reconstruction direction is associated with a known RFI source.

Signal Amplitude Differences: Remove events that have significant peak-to-peak (P2P) voltage differences between HPol channels, where the $\mathrm{Max}(\mathrm{P2P_H})$ is 95 adu or more above the $\mathrm{Min}(\mathrm{P2P_H})$. This removes events where a subset of channels is significantly brighter than the rest (indicative of local noise at the array or electronics issues), and small sample of events where one channel is not functioning properly.

Combined Normalized Map Peak Value: Remove events that do not achieve a threshold percentage of their optimal achievable map value, using a combination of VPol

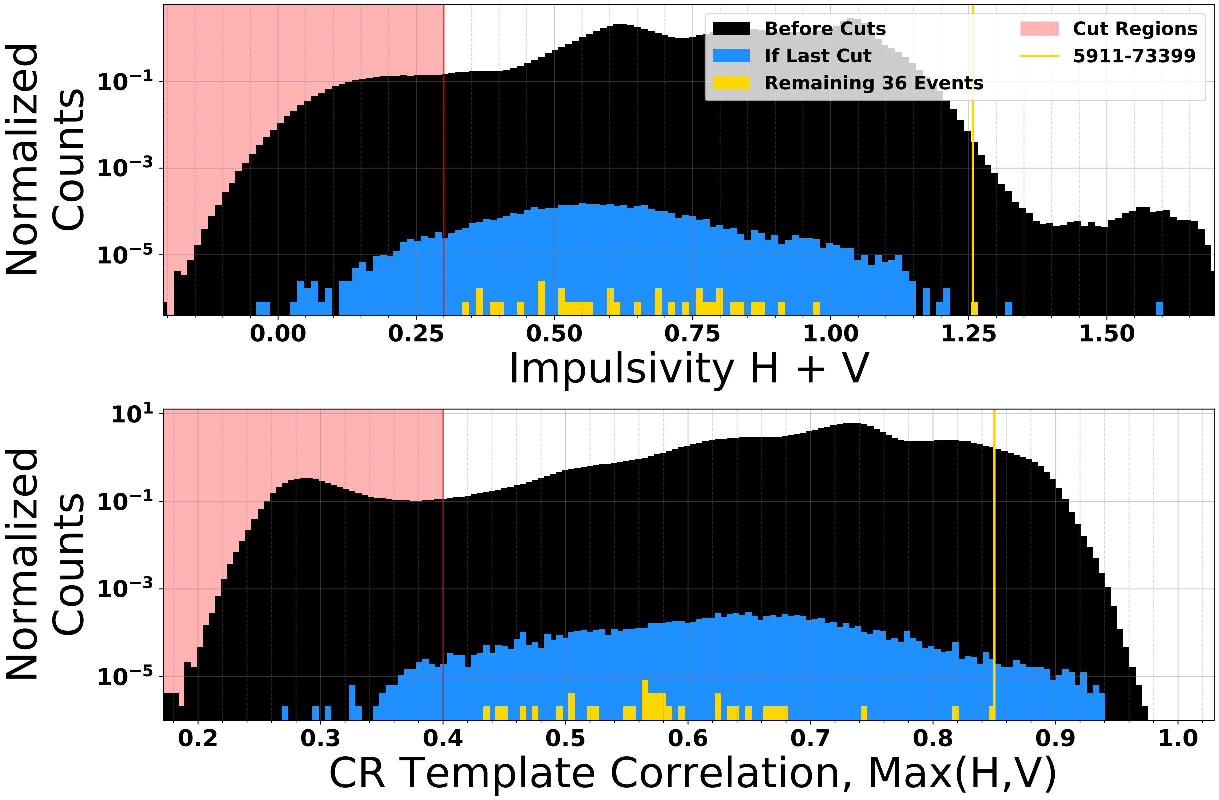

Figure 3.33: Representative distributions of the impulsive character of the full data set (black), the data set remaining after all other cuts have been applied (blue), and the 36 remaining events discussed in Section 3.6.2 (yellow). The red line and region represents the cuts on both the combined impulsivity in HPol and VPol channels and a correlation with a CR template. These cuts require the signal to be impulsive but are loose enough to allow for a variety of signal classes to classify above-horizon events. For comparison, the parameter values for the likely cosmic ray candidate event (discussed in Section 3.6.2) is shown with the yellow vertical line (Event 5911-73399).

and HPol maps. We remove events where $0.768m_{\mathrm{H}} + 0.640m_{\mathrm{V}} - 0.960$ is less than 0, where the normalized map peak value of the above-horizontal region in each polarization is m.

Combined Peak-To-Peak / (2 · Standard Deviation): Remove events where the signal amplitude (calculated as peak-to-peak divided by 2) is not sufficiently above the standard deviation of the observed ADC counts in that waveform. Note that the standard deviation is calculated on the entire waveform, which includes the signal, so this metric is distinct from the SNR. We remove events where the parameter $0.878r_{\mathrm{H}} + 0.479r_{\mathrm{V}} - 5.267$ is less than 0, where r is the ratio of half of the peak-to-peak over the standard deviation in each polarization.

We show histograms of event distributions for a representative set of cut variables targeting impulsive events in Figure 3.33, specifically for impulsivity and the correlation with a cosmic-ray template as defined above. The cuts in these two metrics were relatively loose, allowing us to investigate the varied signals we observe with the prototype. We highlight one event in particular that has a high value in both of these metrics.

3.6.2 Remaining Above-Horizon Events

The remaining 5,440 events were inspected by hand. We found that three broad categories of events remained, as shown in Table 3.6. This hand-categorization of impulsive events that appear to come from above the horizon is important for understanding the RFI environment of the BEACON prototype site, to inform future design decisions and future analyses of the data. Events were categorized into three broad categories: likely mis-reconstructions of RFI that originates from below the horizon, events associated with airplanes, and other impulsive above-horizon events.

Likely Mis-reconstructions of below-horizon events and events with amplifier instability: The largest category is events that are likely to be mis-reconstructions of below-horizon sources of RFI and events that exhibit instability in the amplifier chain, constituting

Cut Name	Number of Events Remaining	Fraction Cut Sequentially	Fraction Cut if Applied First
Full Data Set	96,483,288		
Elevation	1,830,144	0.98	0.98
Azimuth	1,145,593	0.37	0.0075
Time Delay Clustering, HPol	1,116,064	0.026	0.95
Time Delay Clustering, VPol	1,104,002	0.011	0.85
Peak-to-Sidelobe Ratio	201,926	0.82	0.065
Impulsivity	57,669	0.71	0.029
Cosmic Ray Template Correlation	42,184	0.27	0.028
Associated with Below-Horizon Sources	38,274	0.093	0.79
Signal Amplitude Differences	15,809	0.59	0.0038
Combined Normalized Map Peak Value	7,894	0.50	0.23
Combined Peak-to-Peak/(2 · Standard Deviation)	5,440	0.31	0.044
Hand-inspection breakdown of the 5,440 passing events:		Number of Events	Fraction of Events
Likely mis-reconstructions from below the horizon and Events with unstable amplifiers		4,081	0.75
Events associated with airplanes		1,323	0.24
Remaining above-horizon events		36	0.0066

Table 3.6: Summary of analysis cuts. There are two stages of analysis: application of a variety of cuts (above the double line in the table) and a hand-inspection of events that pass those cuts (below the double line in the table). The cut parameters and cut values used in the first stage of the analysis are described in Section 3.6.1. The table shows the number of events remaining after each cut is applied sequentially, the fraction of events rejected by each cut when applied sequentially, and the fraction of events that are rejected if a given cut is applied first in the analysis. The categorization of events by subsequent hand-inspection of the passing 5,440 events is also shown.

75% of the data set that passed all cuts described in Section 3.6.1. The vast majority of triggered events originate from below the horizon, as shown in Table 3.6, and if the correlation map peaks on a true sidelobe of the signal, it is possible for such events to appear to come from above the horizontal and pass the elevation cut applied to the data. Manual inspection of the correlation map can identify these events. Additionally, events are identified that have features in the data that are a result of instability in the amplifiers used in the electronics chain as well as events containing multiple impulses which can create false cross-correlations above the horizon.

Events associated with airplane tracks: The next largest category is events that were associated temporally and spatially with over 100 known airplane trajectories from The OpenSky Network [187], which contains an extensive database of ADS-B airplane data that most airplanes are required to transmit [196, 197]. An example airplane track seen in the data is shown in Figure 3.30. 64 individual airplanes were associated with at least four triggered events, and six airplanes caused 50 or more triggered events. Additional events created other temporally clustered trajectories across the sky, but with no known corresponding airplane track in the database; these events have also been tagged as likely airplane events. This category of events constitutes 24% of the sample.

Remaining events: Of the 5,440 events which passed the cuts aimed to identify impulsive above-horizon signals, only 36 (less than 1%) were not associated with airplane tracks and were not categorized as likely mis-reconstructions of below-horizon events or events with unstable electronics; parameter distributions of these events are included in Figures 3.32 and 3.33. The events are uniform in azimuth and show some structure in the elevation angle. The structure could be consistent with either sidelobes from below-horizon sources or cosmic rays, which are expected to be highly inclined on average for the BEACON geometry. Understanding this distribution will be the subject of future analyses (Section 3.6.3). One event of interest from this sample is shown in Figure 3.37 (event 5911-73399), and is a likely

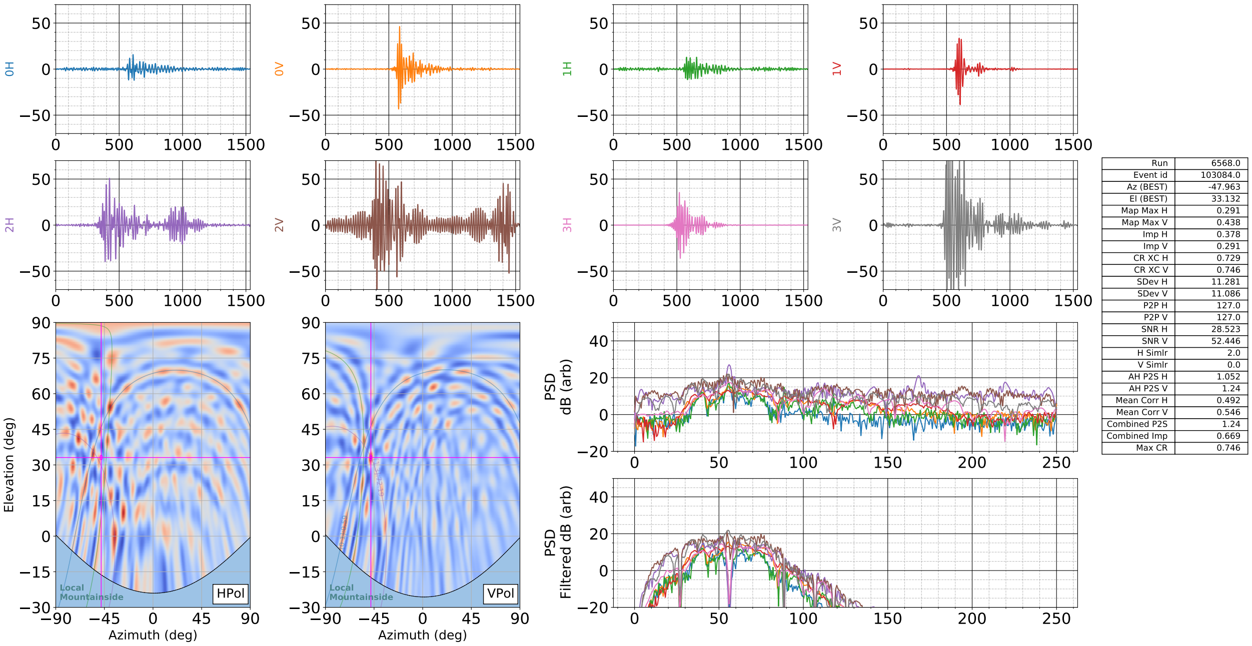

Run	6568.0
Event id	103084.0
Az (BEST)	-47.963
El (BEST)	33.132
Map Max H	0.291
Map Max V	0.438
Imp H	0.378
Imp V	0.291
CR XC H	0.729
CR XC V	0.746
SDev H	11.281
SDev V	11.086
P2P H	127.0
P2P V	127.0
SNR H	28.523
SNR V	52.446
H Simlr	2.0
V Simlr	0.0
AH P2S H	1.052
AH P2S V	1.24
Mean Corr H	0.492
Mean Corr V	0.546
Combined P2S	1.24
Combined Imp	0.669
Max CR	0.746

Figure 3.34: Event display of an event which did not pass the by-hand inspection. This event is believed to have a misbehaving amplifier which results in extremely inconsistent signal shapes, included extended portions of waveforms showing voltage of 0 ADU, while other channels show an excess of power. This also leads to non-sensible waveform time delays which do not overlap on the maps. Despite this event have parameter values which pass the cuts, it is clear upon inspection that the pointing direction cannot be trusted, and the observed behaviour does not match nominal behavior for the array. Events of this style tend to occur in high volume within one or two runs before the nominal behavior of the array returns. Top: Waveforms corresponding to each of the 8 channels. Waveform y-axis represents voltage in units of ADU. Bottom Left: HPol and VPol correlation maps. The colorscale of each map is individually normalized, and the region of the maps pointing into mountainside is masked out. Bottom Right: The Power Spectral Density (PSD) before and after filtering. The data has been filtered as described in Section 3.6.1. Right: Table of relevant parameter values.

cosmic ray event. The remaining events are of as yet unknown origin and will be the subject of future study; these events are impulsive and above horizon and may include a combination of unidentified backgrounds and additional cosmic ray events.

The candidate cosmic ray event has the third highest impulsivity of all 5,440 events that pass cuts, and the highest among the 36 remaining events. Further inspection of the two events with higher impulsivity categorized them as a likely mis-reconstruction of a below-horizon event and a likely airplane event. The candidate event also has the highest SNR (beam voltage SNR of $91\,\sigma$ in HPol; $58\,\sigma$ in VPol for the processed waveforms), peak-to-sidelobe ratio (> 1.7 for each polarization), and template correlation values (> 0.83 for each polarization) among the 36 remaining events. This event also does not occur during a time of significant lightning activity.

Figure 3.38 shows the waveform from the event of interest alongside an event waveform generated with the cosmic ray simulation [189] and compares the observed linear polarization angle and arrival direction with simulated distributions. The tangent of the polarization angle is calculated as the ratio of the maximum of the aligned and averaged de-dispersed waveforms in VPol to HPol when upsampled and symmetric filtering is applied across polarizations (such that VPol is filtered with the TV notch filter as well, ensuring similar power is lost in both averaged waveforms and a representative ratio is preserved). In this way the measured polarization angle of $\sim$28° is consistent with the purely geometric expectation of $\sim$30°, with an uncertainty in the polarization measurement of $\sim$2°, corresponding to the $\sim$10% observed variance in gain matching among channels. The geomagnetic expectation is for a signal arriving from the appropriate arrival direction and local magnetic field for this event.

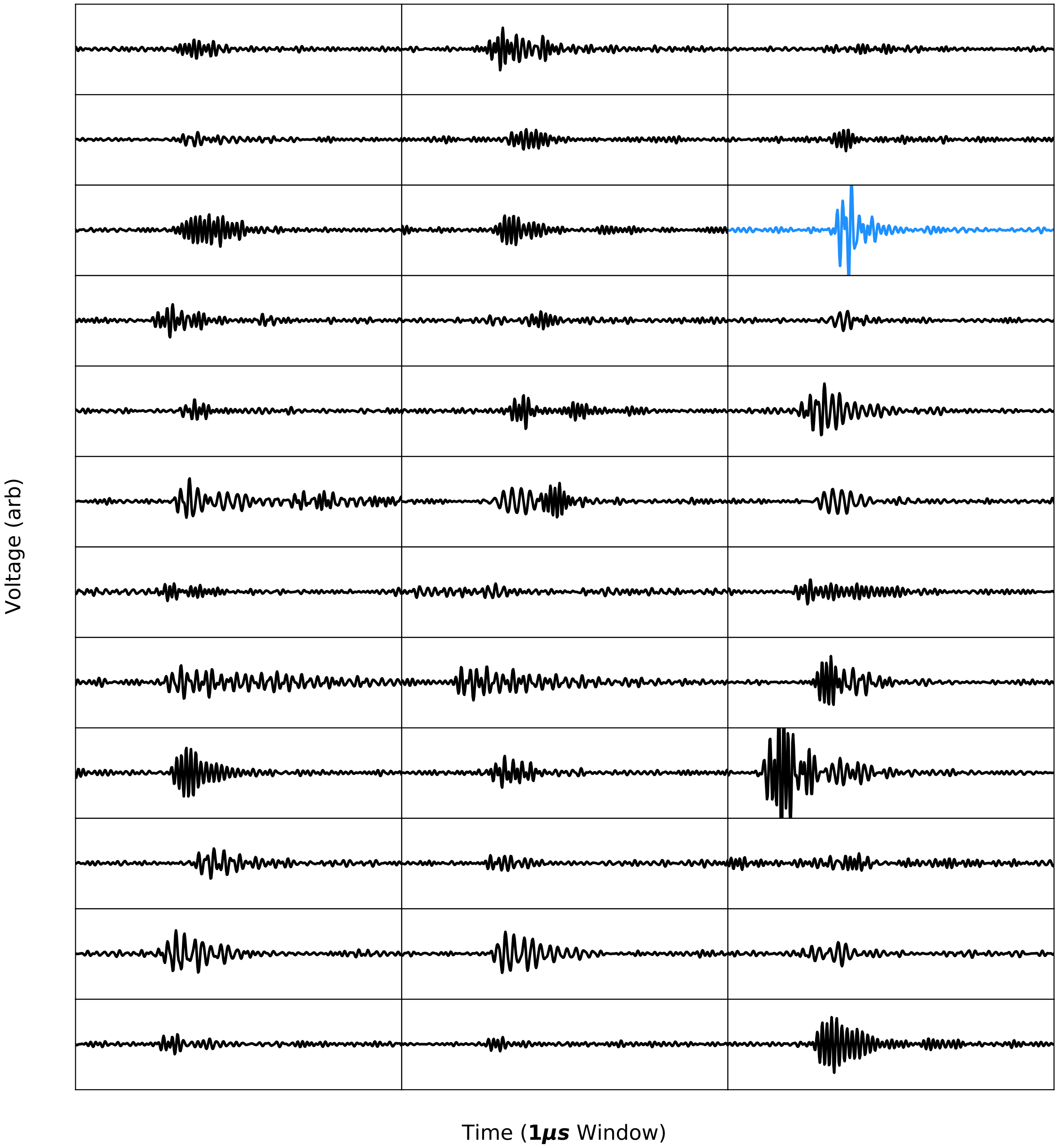

Figure 3.35: Waveforms for channel 3H for each of the remaining 36 events discussed in Section 3.6.1 (each cropped to 1 μs in length). Event 5911-73399 is highlighted in blue. This event stood out on all metrics used to identify a cosmic ray candidate. Classification of the other 35 events is reserved for future analyses by the BEACON collaboration. Distributions for the 36 remaining events can also be seen in Figure 3.36.

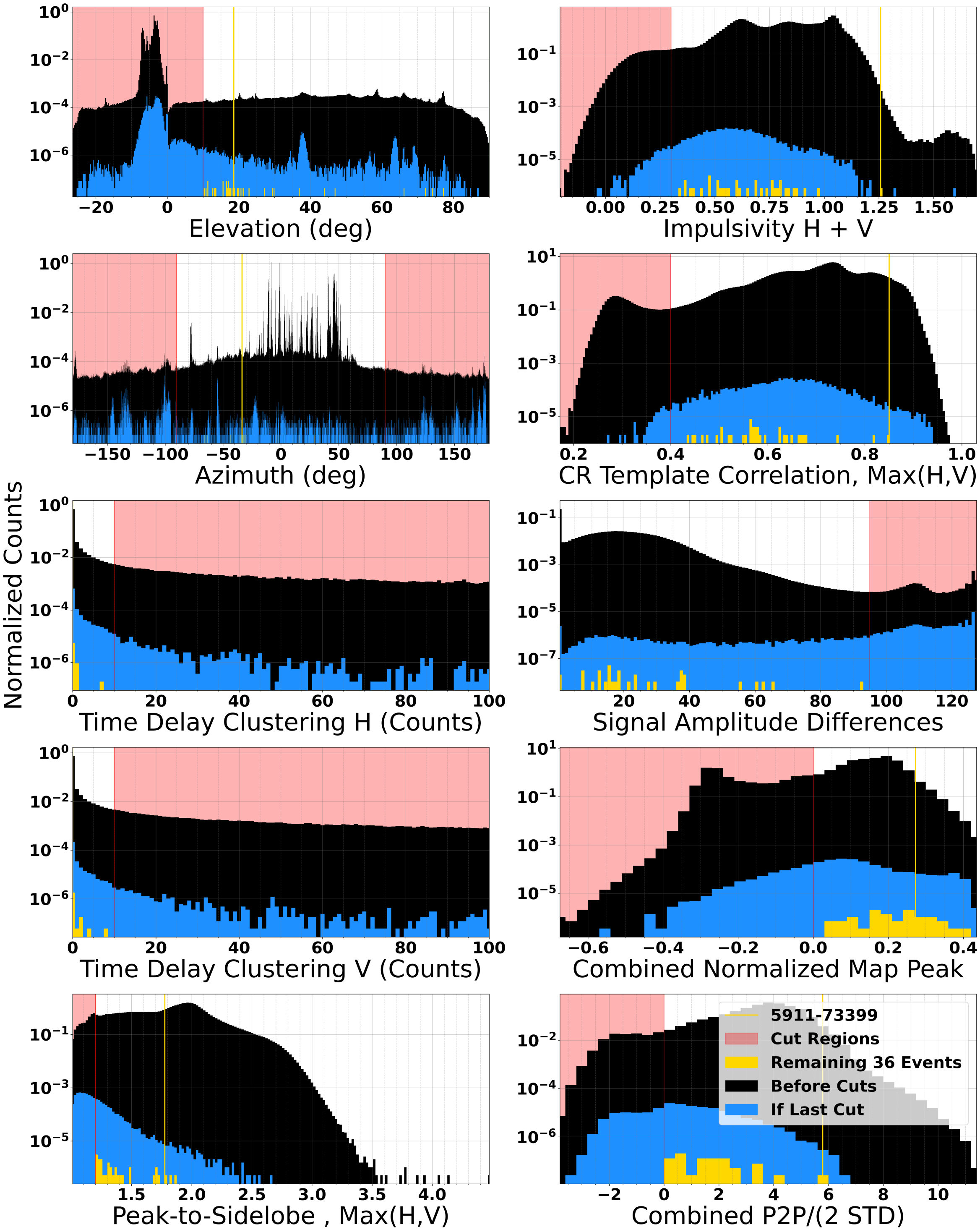

Figure 3.36: Distributions for all specified cut parameters for the impulsive event search. The full data set (black) and the data set remaining after all other cuts have been applied (blue) are shown alongside the 36 events which remained after the hand-categorization (yellow). For reference, the parameter values for the likely cosmic ray candidate event (discussed in Section 3.6.2) is shown with the yellow vertical line (Event 5911-73399).

3.6.3 Future Work

The categorization of impulsive above-horizon events in the prototype instrument data set is a critical step in defining cuts for future cosmic ray searches. While informative for this analysis, the hand-inspection of events after cuts are applied indicates that additional automated cuts would need to be made to perform a true cosmic ray search. For example, the structure in the spatial distribution of events seen above the horizon (e.g. the elevation distribution in Figure 3.32) indicates that a set of clustering cuts to remove events associated with below-horizon sources would be effective. We are planning further analyses that will leverage our understanding of the prototype system and local RFI sources to perform a cosmic ray search with the data. These searches will benefit from search metrics that are efficient at removing backgrounds and identifying cosmic ray events with low SNR. Cuts that take advantage of the directional and temporal clustering in RFI sources may be sensitive to weaker signals; however, confidence in identification can be improved when clustering is combined with cuts that emphasize the impulsive characteristics and predictable polarization of cosmic-ray signals. Combining the results of that search with input from the cosmic ray simulation will lead to an updated sensitivity estimate to tau neutrinos of the full-scale BEACON array.

3.7 BEACON Conclusion

The BEACON prototype instrument has been in operation since 2018. The current station design is robust and with its custom antennas and phased array trigger represents important first steps towards a scalable implementation of the full BEACON array.

We have used data from the prototype instrument to verify the performance of the array and understand the RFI environment at the BEACON prototype site. We have developed analysis techniques to identify above horizon RFI sources such as airplanes, and to isolate events consistent with the expected properties of a cosmic ray. The results of this analysis have already validated the phased trigger's ability to maintain sensitivity to above horizon events using a small number of antennas in a noise-dominated environment like the Californian and Nevada deserts. While the RFI rates at the current prototype site are higher than would be beneficial for a larger instrument, the environment provides an important stress test of the trigger's capabilities.

The next stage for the BEACON prototype is to develop a full cosmic ray search trained on simulated data and building on the background studies presented here and on techniques from other autonomous searches for radio signals from air showers. The dominant source of backgrounds come from below the horizon and are well clustered both spatially and temporally, suggesting that they may be removable as has been done in prior searches [69, 198, 65]. In a future work, we expect to conduct a template search based on simulated radio emission from cosmic rays and exploiting clustering cuts.

It is important to note as well that since anthropogenic noise predominantly comes from below the horizon and constitutes the main source of background, we expect that there will be a need for more background rejection power in a search for upgoing tau neutrinos compared to downgoing cosmic rays. This ultimately could translate to a loss in analysis efficiency for a given background rate. However, we may be able to further exploit differences in the characteristics of the signals – their spectra, their isotropy, and impulse response – relative to the backgrounds. We can also further tune the beamforming trigger to down-weight or directionally mask regular sources of RFI at a given site. These studies will also be important to pursue in future works.

The concept for each BEACON station includes more antennas and longer baselines than the prototype and could therefore achieve lower thresholds and improved background rejection. Measurements of correlation map characteristics, SNR, pointing resolution, and trigger thresholds all benefit from the additional antennas and longer baselines of a full station, enabling better separation of below-horizon and above-horizon events. Additionally, multiple stations with differing views of overlapping effective volumes can be used to veto anthropogenic noise, compared to air shower signals, which are highly beamed.

Finally, we note that we are exploring hardware upgrades for the prototype. Antenna position calibration and trigger validation using an RF source mounted on a drone can enable a more complete calibration of the in-situ antenna beam patterns [199]. This drone pulser will also be used to further understand the observed elevation offset in above-horizon events from airplanes (see Figure 3.30), and determine whether this offset is intrinsic to the hardware, current calibration, or in our interpretation of the airplane database, which is important for trusting above-horizon reconstruction accuracy in future analysis. While not cost-effective for a full-scale detector, adding scintillators to the prototype can improve cosmic ray identification and validation at the prototype stage. Signals from scintillator detectors could be digitized alongside the existing RF channels and serve to validate RF-only triggered events [200]. Finally, an updated DAQ is being designed, which because it is modular and flexible, can form the basis of autonomous stations with more antennas. This will allow us to scale the BEACON detector to the hundreds or thousands of stations needed to detect the tau neutrino flux.

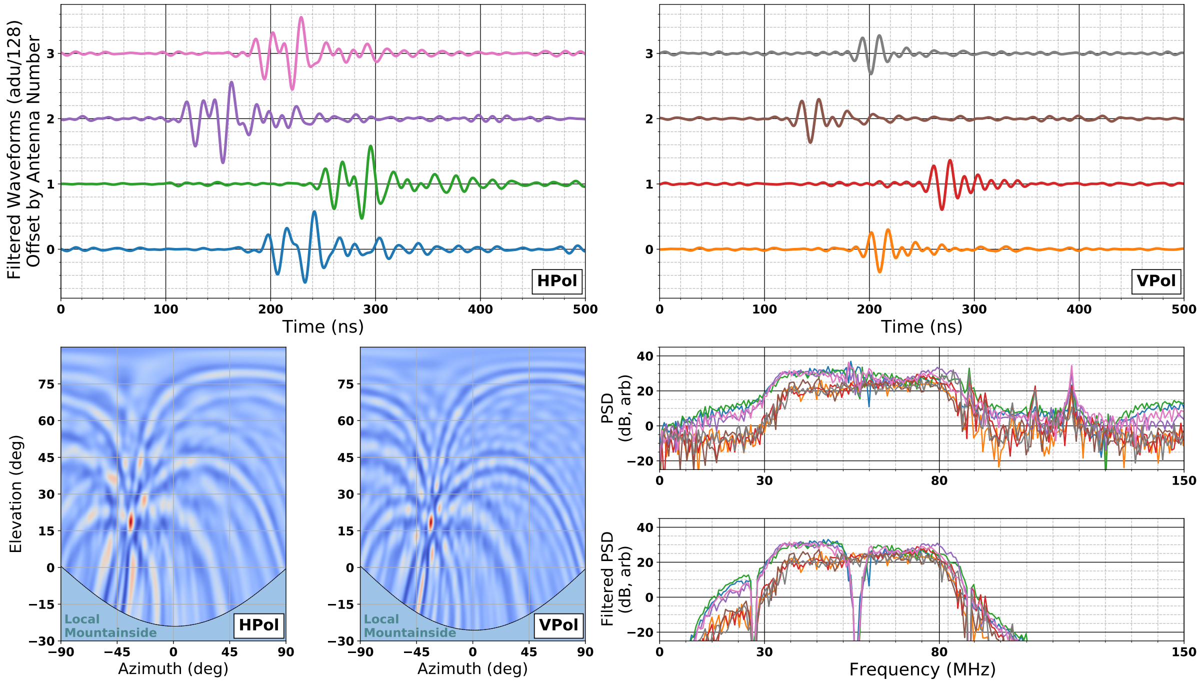

Figure 3.37: Event display for a likely cosmic ray event (Event 5911-73399). Top: Waveforms from each of the 8 channels, normalized and offset such that the y-scale indicates the antenna number for each waveform. This event has an averaged single-channel voltage SNR of 42.5 in HPol and 38.6 in VPol. Bottom Left: HPol and VPol correlation maps. The colorscale of each map is individually normalized, and the region of the maps pointing into the local mountainside is masked out. Bottom Right: The Power Spectral Density (PSD) before and after filtering. The data has been filtered as described in Section 3.6.1.

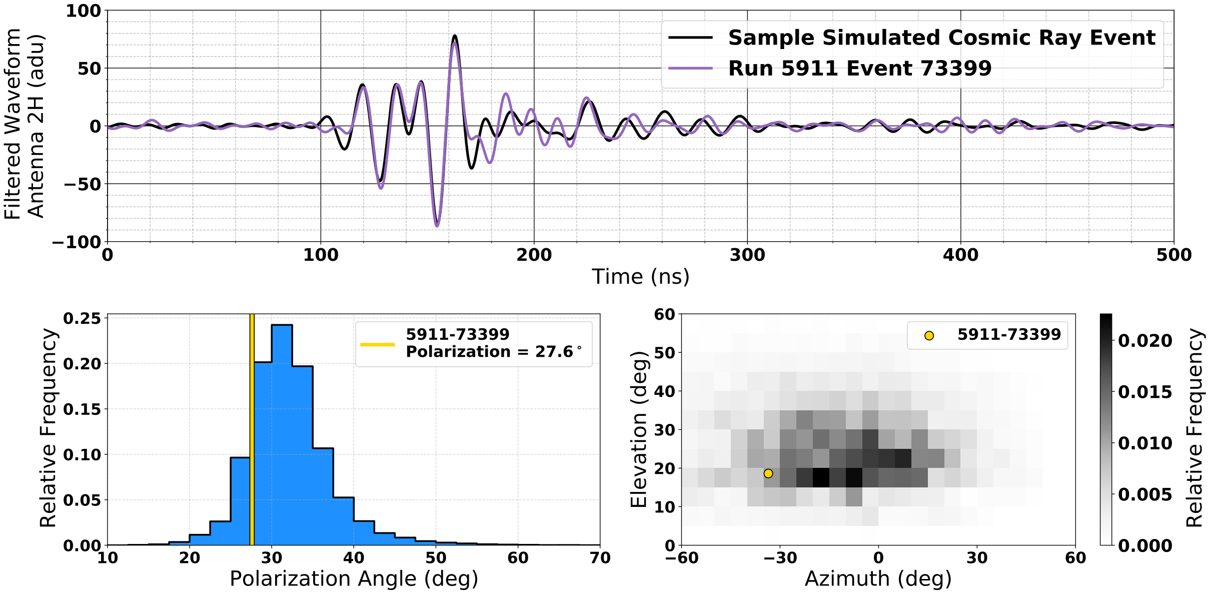

Figure 3.38: Top: The waveform for Event 5911-73399 from Antenna 2H superimposed with a sample simulated cosmic ray signal with realistic thermal noise levels [189], which has been convolved with the system response of the same channel. Both waveforms have been filtered as described in Section 3.6.1. Bottom Left: The distribution of expected observed linear polarization angles for triggered simulated events. The polarization angle of the cosmic ray candidate event is shown with a yellow line. The measured polarization angle of ∼28° is consistent with the purely geometric expectation of ∼30°, calculated assuming a geomagnetic signal arriving from the appropriate arrival direction and local magnetic field. Bottom Right: The distribution of expected azimuth and elevation for simulated events compared to the candidate cosmic ray event (in yellow).

APPENDIX A

RADIO METHODS FOR NEUTRINO ASTRONOMY

The experiments described in this thesis are radio-based, and utilize antennas to detect the radiation produced by UHE particles as described in Section 1.3. As such, antennas of various constructions will be discussed throughout this thesis. In this section a brief foundational understanding of the antennas is established. Variations on these general ideas will be given as required throughout the remainder of the text.

Antennas are an application of the concept of radiation in electromagnetism. Radiation at radio wavelengths is an extremely useful way of transmitting information/energy over long distances with a generally low amount of loss. Radio antennas are designed to both transmit (TX) and to receive (RX) radiation at radio wavelengths, with RX antennas being of particular interest for their application as radio detectors in the physics experiments discussed throughout this thesis.

The general purpose of an RX radio antenna is to detect variations in the electromagnetic field strength caused by waves passing through a medium like air or ice, and to incite these variations into current or voltage that can be readout from a cable. For this discussion I use the simple model of a dipole antenna, which consists of two conducting "elements" extending along a specified axis. These elements provide a source of motile electrons that can produce current under the influence of variations in the electric field. They are connected at the center by a transmission line which serves as a propagation medium for the generated alternating current towards a readout system. A transmission line consists of two conductive materials in proximity but separated by an insulator. This construction results in field variations down one line of the conductive material largely cancelling out the fields of the other when viewed from a distance, allowing for a near lossless transmission of electromagnetic waves.

Radio waves travel across the antenna with a single polarization (that is aligned with the antenna for simplicity). The presence of the electric field will induce a potential difference across the length of the antenna elements, which results in a force on the electrons within the material, inducing a standing wave current. The specific properties of how a transmission line interacts with this standing wave is largely characterized by the impedance of the line, Z. Impedance is defined as:

$$Z = R + iX \tag{A.1}$$

where R is the resistance of the material (to a direct current) and X is the reactance, which is similar to the resistance of a material but specifically describes the affinity for opposition to changes in current caused by the inductance and capacitance of the material. In this model, the antenna then serves the role of "impedance matching" the radio signal to the transmission line. If the wave is not matched then reflections can occur within the antenna-transmission line system, which can result in the reflected power being radiated outward through antenna rather than being readout by the measurement side of the transmission line.

As with most driven systems, resonant frequencies exist within each antenna-transmission line system. Near these resonant frequencies minimal reflections occur, and the highest portion of the received power is readout. The precise frequency of this resonance will depend on the precise structure of the antenna and details of the transmission line. For a simple dipole consisting of thin conducting elements with total length ℓ, resonance occurs for incoming signals with wavelengths that are integer fractions of ℓ given by:

$$\lambda_{\text{res}} = 2\ell/n \tag{A.2}$$

where n is a positive integer. Though the above relationship is only generally true for the simple dipole, it conveys the underlying principle that the sensitivity of an antenna to a particular wavelength of incident radiation is tied to the dimensions and construction of the antenna.

A.1 Antenna Matching and Smith Charts

Commonly a "matching network" will be used at the interface between the antenna and main transmission line, with circuitry specifically designed to tune the impedance matching between the antenna and transmission line. Most often these matching networks aim to achieve a perfect match by shifting the apparent impedance seen by the antenna by varying the resistance, inductance, and capacitance of the connecting circuit. This matched network ensures the response of the network closely represents the pure geometrically determined response of the antenna, with minimal reflections and maximal power transfer.

One powerful tool for working with matching networks that will become relevant in Section 2.5.3 is the Smith chart, a nomogram which can be used for easily interpreting the cause and effect of varying matching network components. The Smith chart expresses the complex plane of the reflection coefficient, Γ, which is defined by the following transformation of impedance:

$$\Gamma = \frac{z-1}{z+1} \tag{A.3}$$

in terms of the normalized impedance $z = Z/Z_0$, with Z_0 being the reference impedance (the 50 Ω of the transmission line here). Under this transformation, all impedance values for which $\text{Re}(z) > 0$ (positive resistance) lie within the unit circle and thus can be compactly displayed and understood.

Inspecting Equations A.1 and A.3 reveals some points of interest on the Smith chart:

- $\Gamma = -1$: The reflection coefficient of a short circuit ($R = 0$, $X = 0 \rightarrow z = 0$)
- $\Gamma = 1$: The reflection coefficient of an open circuit ($R = \infty$, $X = 0 \rightarrow z = \infty$)

- $\Gamma = 0$: A load perfectly matched to the characteristic impedance ($Z = Z_0 \rightarrow z = 1$)

Along with the helpful reference points, the complex plane is superimposed with two grids: the admittance grid and the impedance grid (Figure A.1). Admittance (Y) is reciprocal of impedance and is defined as:

$$Y = \frac{1}{Z} = G + iB \tag{A.4}$$

where G is the conductance and B is the susceptance. For use in Smith charts the normalized versions of these are used where $y = 1/z = g + ib$.

The reference curves give easy visual guidelines for the impact on Γ of varying the series/shunt inductance, capacitance, or resistance of an antenna/matching network (Figure A.1). Changes in the reflection coefficient are calculated in terms of the normalized impedance, resistance, and susceptance (x, r, b) as functions of the inductor, capacitor, and resistor values used (L, C, R). These variations are determined via the following equations:

$$\begin{aligned}
\text{Vary Series L} : \Delta x &= \frac{2\pi f \left(L_f - L_i\right)}{Z_0} \\
\text{Vary Series C} : \Delta x &= -\frac{1}{2\pi f Z_0}\left(\frac{1}{C_f} - \frac{1}{C_i}\right) \\
\text{Vary Series R} : \Delta r &= \frac{\left(R_f - R_i\right)}{Z_0} \\
\text{Vary Shunt L} : \Delta b &= -\frac{Z_0}{2\pi f}\left(\frac{1}{L_f} - \frac{1}{L_i}\right) \\
\text{Vary Shunt C} : \Delta b &= 2\pi f Z_0 \left(C_f - C_i\right) \\
\text{Vary Shunt R} : \Delta r &= Z_0\left(\frac{1}{R_f} - \frac{1}{R_i}\right)
\end{aligned} \tag{A.5}$$

To use a Smith chart the impedance or reflection coefficient of an antenna must be

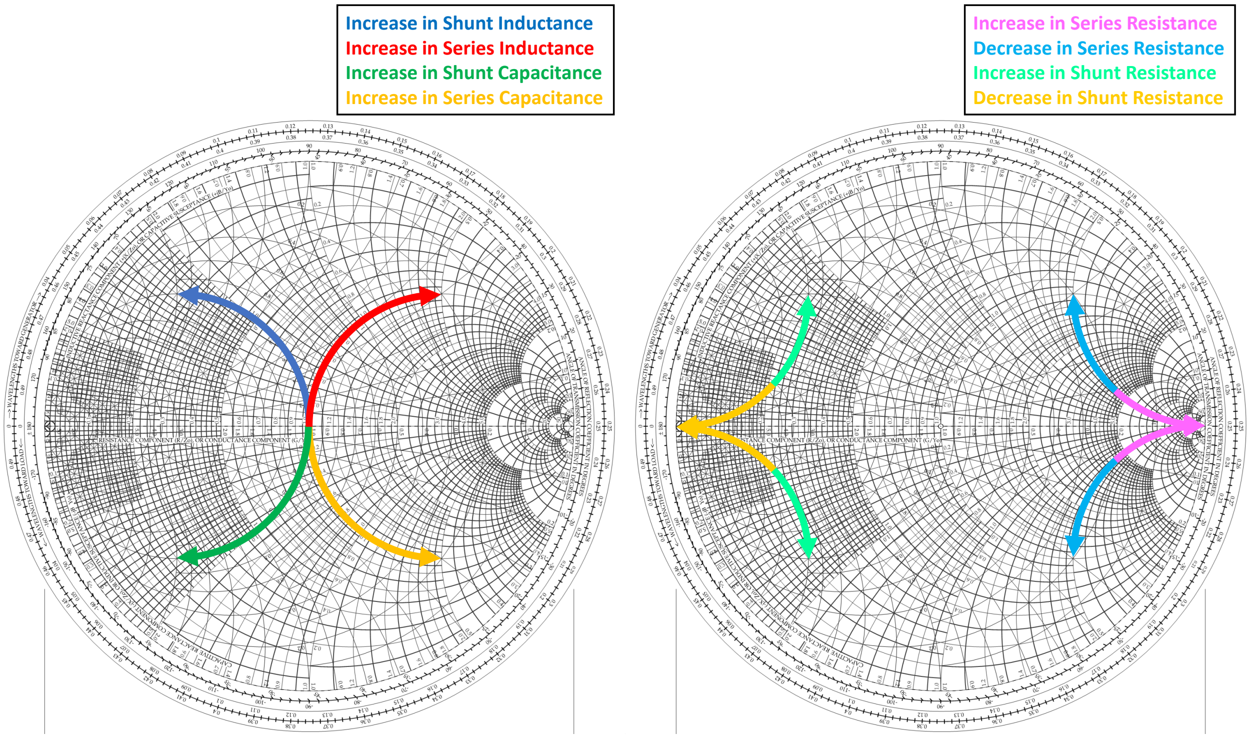

Figure A.1: Smith charts with arrows showing how an impedance values under changes to various matching network components. Any point on the Smith chart can be navigate along these curves by varying the values of their associated matching network components.

known via either simulation or through measurement with network analyzer. This is then normalized and plotted within the chart. For a perfect match, the goal is to determine what changes to the matching network would result in shifting the known normalized impedance towards $\Gamma = 0$. Figure A.2 shows an example where the match is obtained through additional shunt inductance and series capacitance. The specific length that must be travelled along each guideline (determined by guideline axis labels) sets the required change in component value.

Measurements of reflection coefficient (be it through simulation or via a network analyzer) are often performed for a range of frequencies of interest, resulting in a curve of several points on the complex plane. The effect of each adjusted circuit component is frequency dependent as well (see the dependence on f in Equations A.5), so the behavior of a curve can be considerably more unpredictable than a single frequency measurement. As such it is generally only feasible to match a single frequency, meaning the measured curve only intersects $\Gamma = 0$ at a single frequency.

Though achieving $\Gamma = 0$ is desirable in many applications (ensuring maximal power transfer for the nominal frequency of the antenna), a common trick of the trade is to intentionally mismatch an antenna at the nominal frequency such that a larger number of frequencies can be near $\Gamma = 0$ (where transmitted power increases with proximity to $\Gamma = 0$). In doing so, a trade-off has occurred where the peak sensitivity of the antenna is reduced but the bandwidth of the antenna is increased (a sufficient sensitivity has been obtained in many frequencies). This technique is used to achieve a broadband antenna.

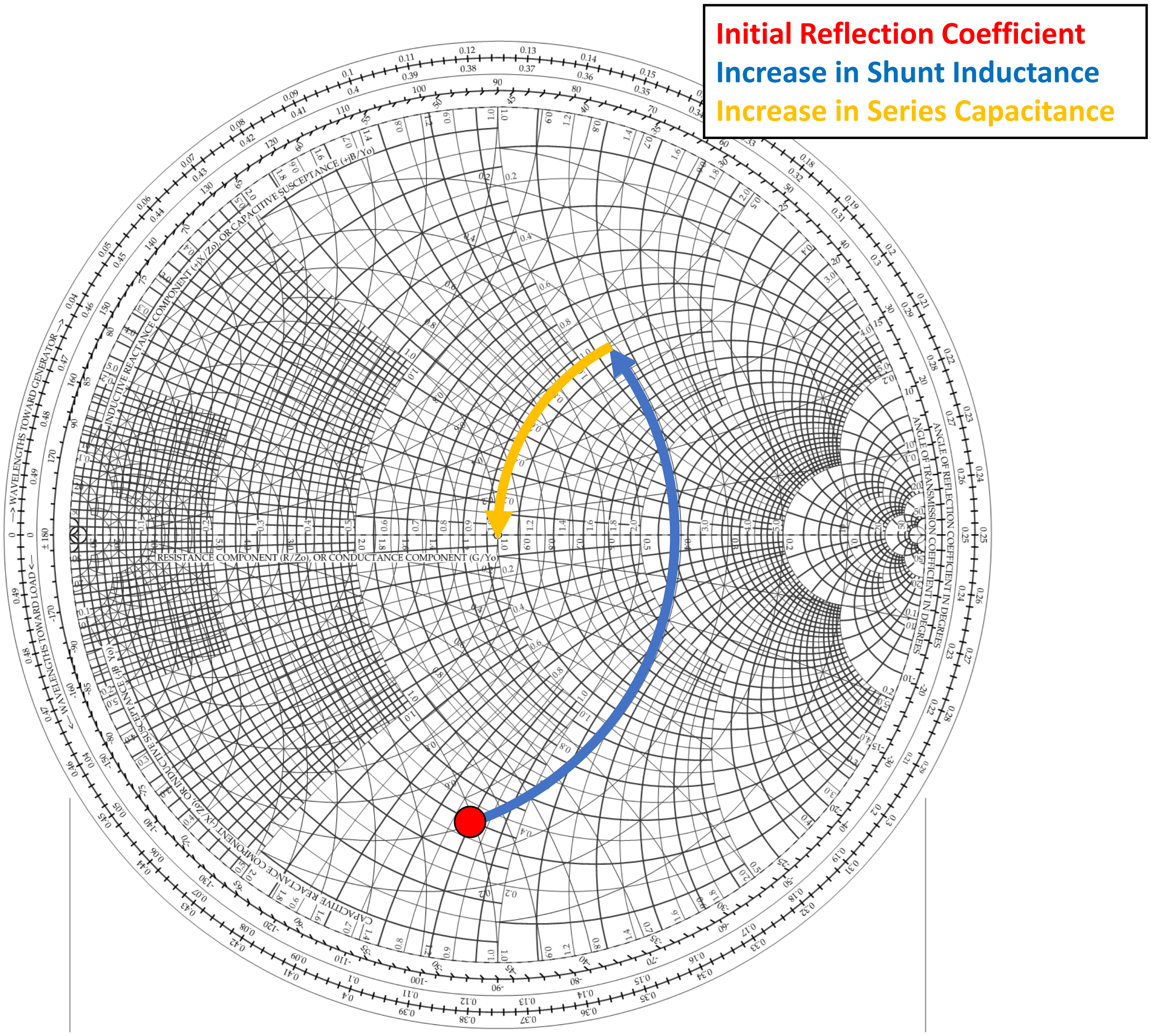

Figure A.2: An example Smith chart showing how an impedance match can be obtained by adjusting the matching network components. In this case the shunt impedance and series capacitance were increase. The specific length of each each of these curves is determined by the change in inductor and capacitor values between the old match and new, and can be calculated used the known rules.

A.2 Antenna Design and Gain Patterns

Another major component in understanding the performance of an antenna is the gain pattern. A gain pattern is a measurement of the antenna sensitivity to signals arriving at various incident angle and is both a function of frequency and polarization. For a simple dipole antenna this dependence can be understood by performing a dot product of the electric field vector with the physical extent of the antenna. When aligned (both from arrival direction and polarization) the field can achieve a larger potential difference across the antenna, and produce the nominal standing wave behavior, while an orthogonal polarization or arrival direction will result in no potential across the antenna, and thus no power transmitted from the wave. For more complex antenna the shape can be designed to achieve a highly directional gain pattern (significantly more gain in a specified direction), or to achieve a more broadband antenna. Figure A.3 shows example three-dimensional antenna patterns for a simple $\lambda/2$ dipole antenna as well as a more complex 10-element linear array antenna.

Another important principle in antenna design is the optics concept known as "Babinet's Princple". This states: "when the field behind a screen with an opening is added to the field of a complimentary structure, the sum is equal to the field when there is no screen" (Reference [159]). Here a complimentary structure refers to a structure created by the negative space of the original structure, such that a superposition of the two shapes has complete coverage of the plane. This essentially states that the shadow produced by a flat piece of material of any shape is the compliment of the light pattern produced by a hole of the same shape, such that the summed light of both patterns would be as if no material existed to block the light.

This optics concept can be extended to radio frequency light using conducting screens and vector fields to include the effects of polarization. From Reference [160]: "Let sources s_1 to the left of an infinite screen S_1 produce a field on the right of S_1, and let U_1 be the ratio of this field to the field strength tat would exist there in the absence of the screen, then

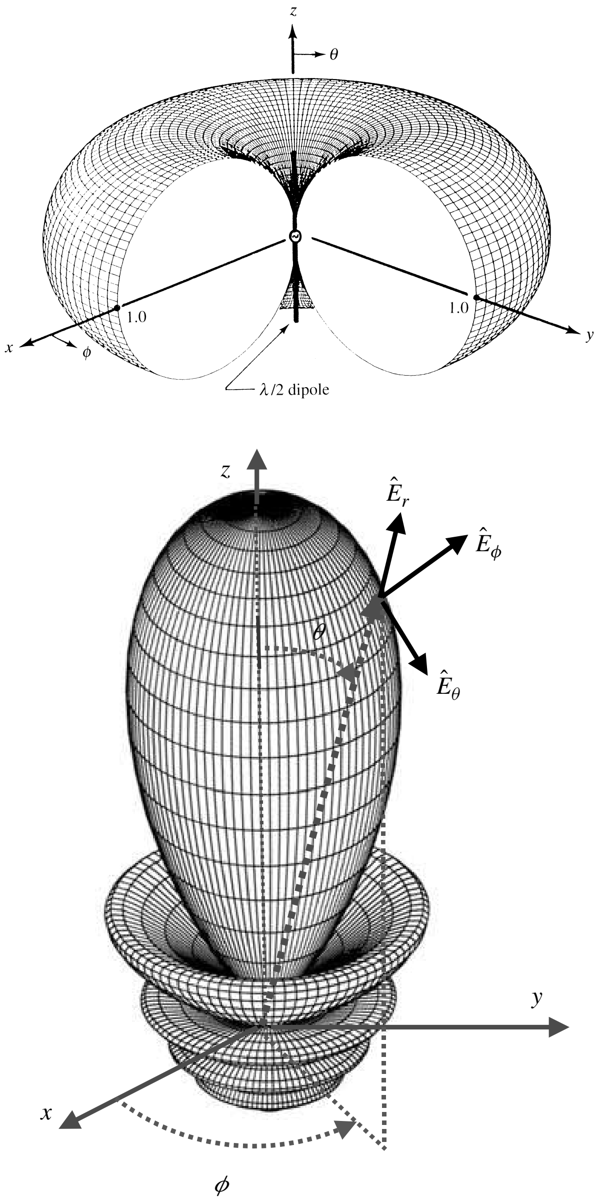

Figure A.3: Top: Three-dimensional pattern of a $\lambda/2$ dipole (dipole's physical extent aligned with z axis). Bottom: Normalized three-dimensional amplitude field pattern (in linear scale) of a 10-element linear array antenna with a uniform spacing of $d = 0.25\lambda$ and progressive phase shift $\beta = -0.6\pi$ between the elements. Source: Reference [159]. The radius of the antenna pattern shows the normalized gain (sensitivity) of the antenna to signals from that particular direction. The 10-element antenna uses a significantly more complicated geometry to obtain a directional pattern, with significant gain in a single direction.

consider a conjugate source s_2 to the left of the complementary screen S_2, and let U_2 be the ratio of the field on the right of S_2 to the field that would exist there in the absence of the screen; then $U_1 + U_2 = 1$". Here a conjugate source refers to a source with swapped incident fields $\vec{E}$ and $\vec{H}$.

Though this principle is rather hard to articulate plainly, the effects of it are important, as it implies the existence and performance of "slot" antennas, which are an extremely common genre of antennas. A slot antenna is often constructed by removing material from a conducting plane. The resulting slot acts as an antenna that behaves similarly to if the cutout material was used to produce an antenna, except the characteristics are governed by the magnetic field rather than the electric field. This swap also means that a vertical hole that is shaped like the electric dipole described in FigureA.3 would have a similar gain pattern shape, but for the orthogonal polarization. A basic understanding of slot antennas important for Section 2.5, wherein I describe the development process of cylindrical slot antennas for the RNO-G experiment.

APPENDIX B

SUPPLEMENTARY BEACON MATERIALS

Site	start time (PDT)	antenna	pol	atten.	start run/event	note
1	11:10	bicone	HPol	40dB	1504/8287	
1	11:17	bicone	HPol	20dB	1504/9126	
1	11:23	bicone	HPol	3dB	1504/9846	
1a	11:35	dipole	HPol	30dB	1505/$\cdots$	
1a	11:56	dipole	HPol	10dB	1506/929	
1a	12:04	dipole	HPol	2dB	1506/1889	
1a	12:25	dipole	HPol	42dB	1507/1035	
1a	12:27	dipole	HPol	22dB	1507/1275	
1a	12:31	dipole	HPol	20dB	1507/1755	off at 1:39
1a	1:40	dipole	HPol	20dB	1507/10034	w/ filter (NHP-50+, NLP-90+), off at 1:49
1a	1:54	bicone	HPol	10dB	1507/11714	
1a	1:59	bicone	HPol	16dB	1507/12314	
1a	2:04	bicone	HPol	16dB	1507/12914	w/ filter
1a	2:27	bicone	HPol	16dB	1507/15711	w/ filter + elevated antenna[1]
1a	2:41	bicone	VPol	16dB	1507/17354	w/ filter
2	3:30	bicone	HPol	5dB	1508/1632	w/ filter
2	3:40	bicone	HPol	15dB	1509/721	w/ filter
2	3:44	bicone	HPol	25dB	1509/1201	w/ filter
2	3:49	bicone	HPol	20dB	1509/1801	w/ filter
2	3:54	bicone	HPol	22dB	1509/2401	w/ filter
2	4:05	bicone	VPol	22dB	1509/3722	w/ filter
2	4:08	bicone	VPol	19dB	1509/4082	w/ filter
2	4:09	bicone	VPol	17dB	1509/4201	w/ filter
3	9:25	bicone	HPol	20dB	1511/892	w/ filter
3	9:40	bicone	HPol	30dB	1511/2690	w/ filter
3	9:52	bicone	VPol	20dB	1511/3892	w/ filter
3	10:06	bicone	VPol	30dB	1511/5812	w/ filter

Table B.1: 2019 BEACON calibration configurations and meta data.

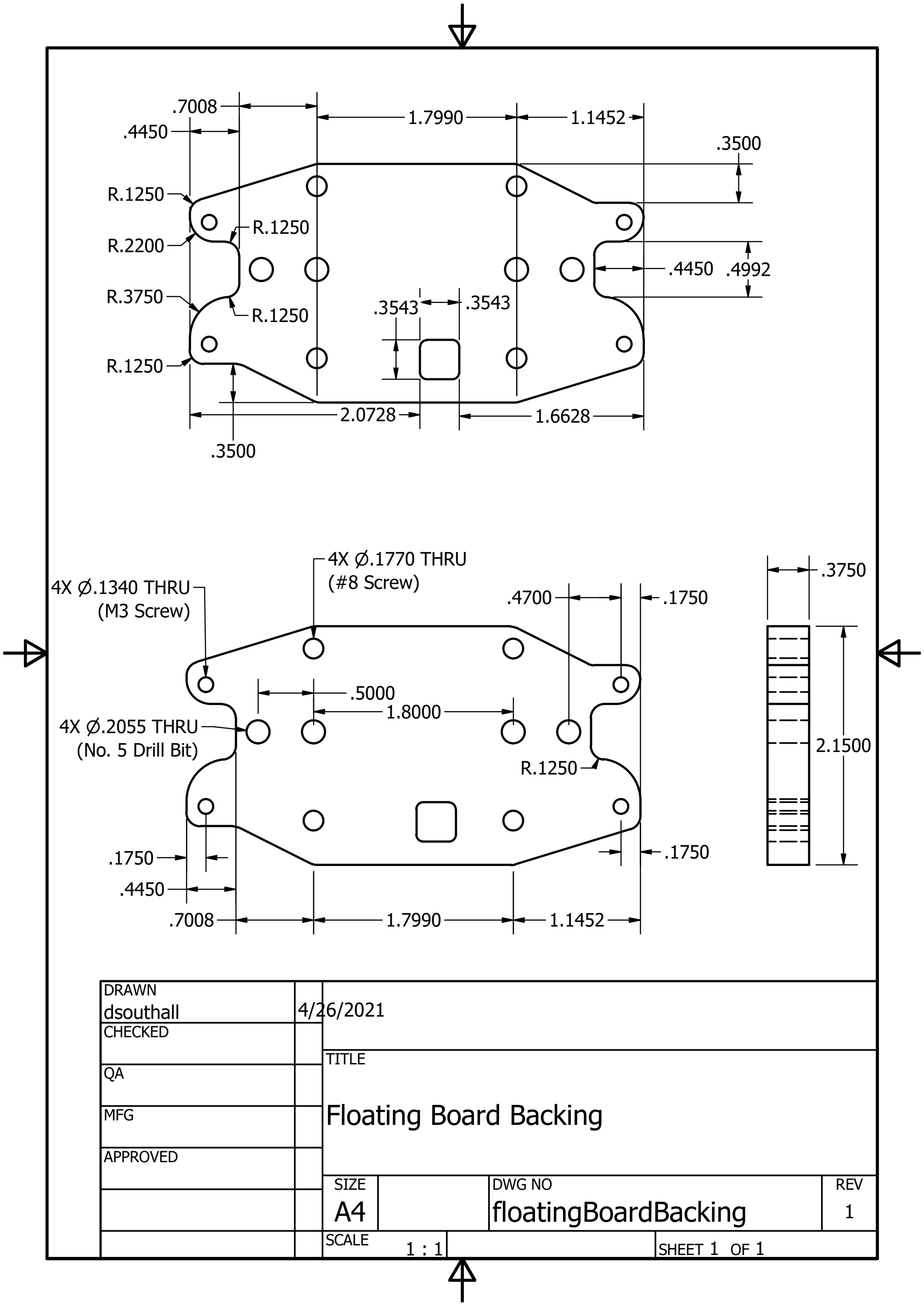

Figure B.1: Nylon board backing design used for supporting the front-end board at the appropriate height for direct connection to antenna tines. The shape is largely governed by the enclosure used (Figure B.2).

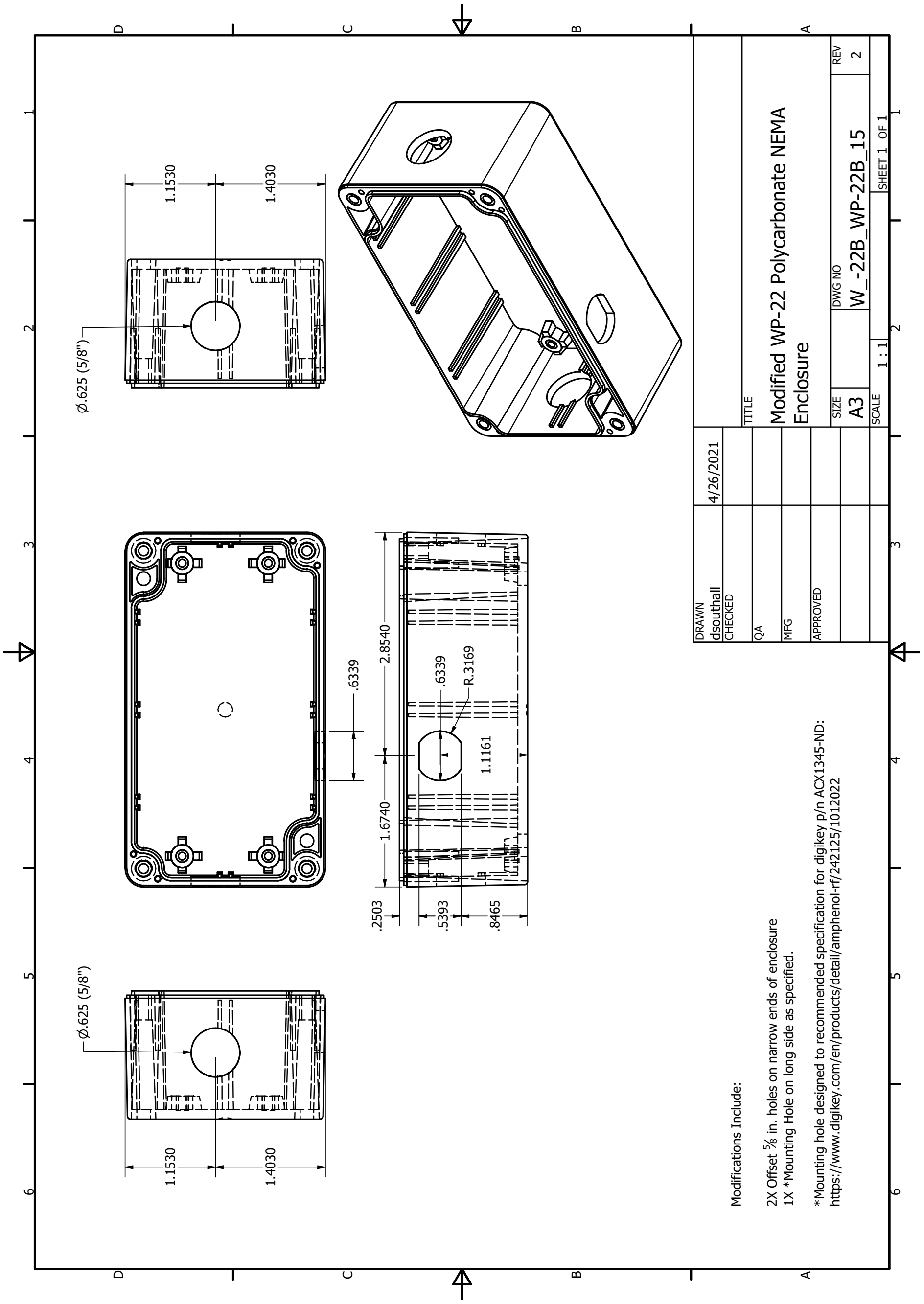

Figure B.2: Modifications to the PolyCase enclosure, providing pass-through holes for antenna tines and readout bulkhead adapter. These enclosures were designed to provide protection from the elements for the front-end electronics, and provide a means for fastening antennas to the masts.

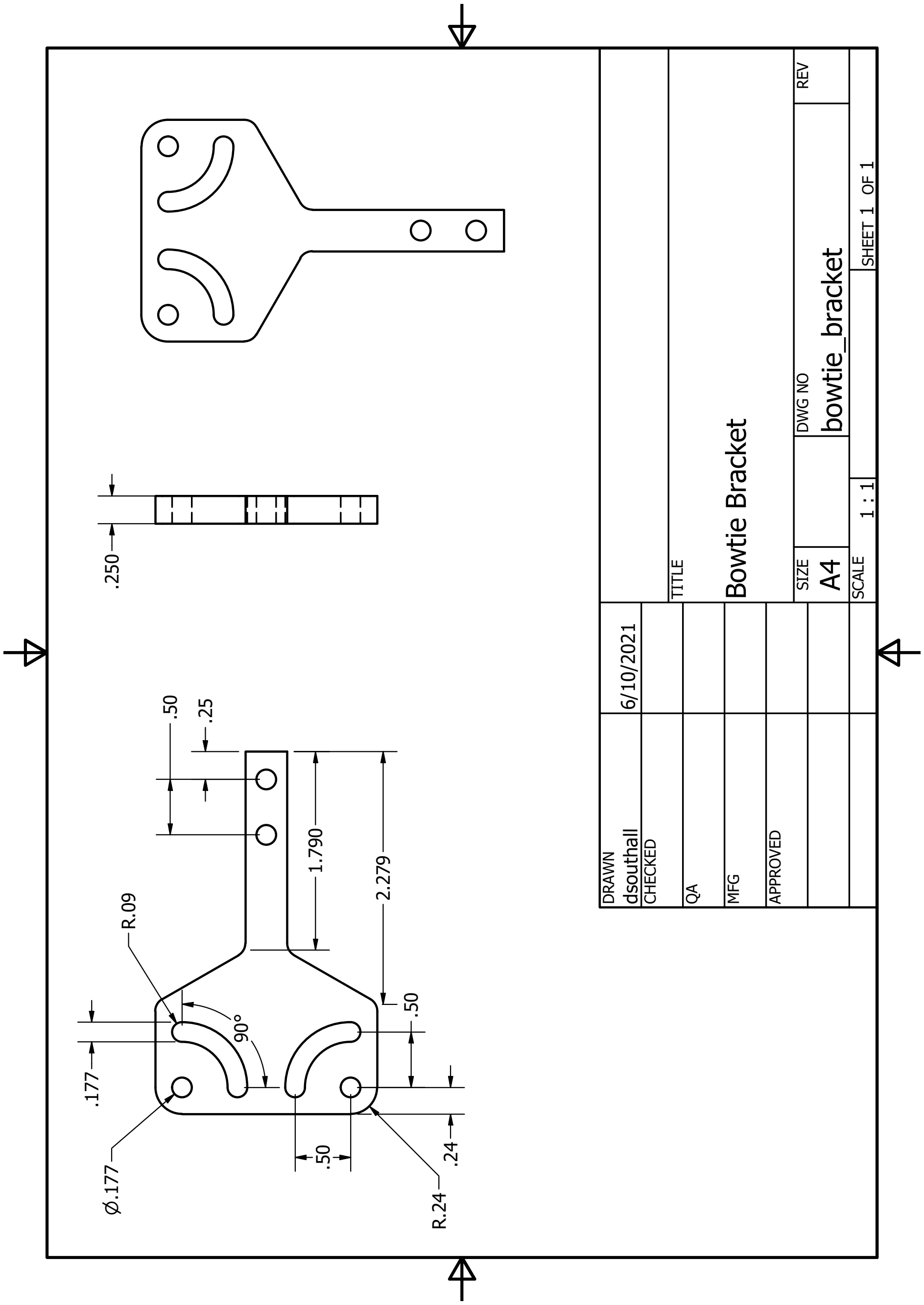

Figure B.3: This bracket was developed as a quick way to convert an existing BEACON antenna into a bow-tie antenna. The bracket could be bolted in-place where the normal element would be attached to the front-end board. Two antenna elements per bracket could then be fastened in place on the wide end of the bracket. The slot allows for customize opening angle for the bow-tie antenna elements. This antenna design was tested as a way to achieve a more broad-band pulsing antenna. Discussed further in Figure B.4.

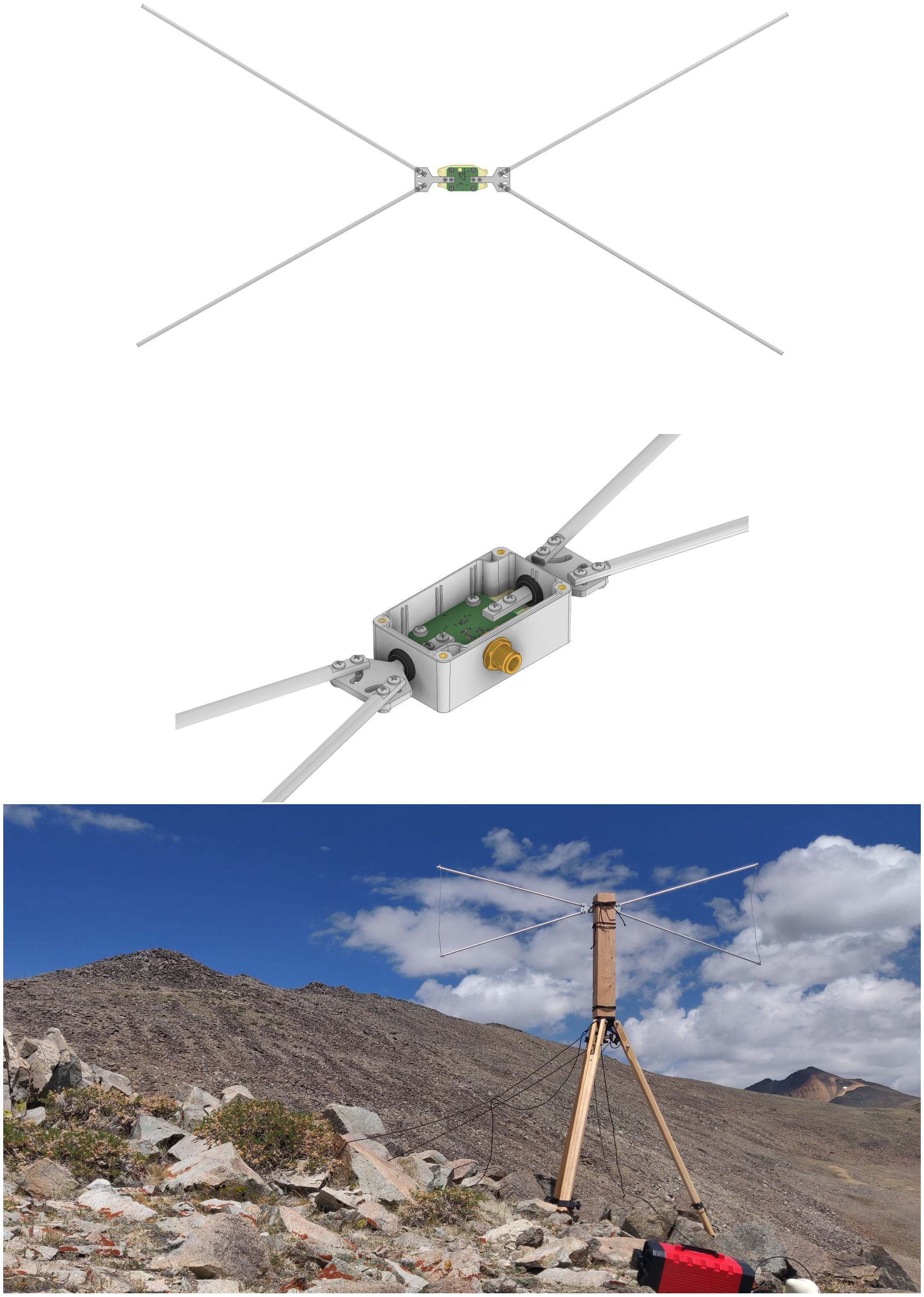

Figure B.4: Top: This a model of the modified bow-tie BEACON antenna with a 60° opening angle. Middle: A closer view of the brackets in-place within the enclosure. Bottom: The bow-tie antenna being used as a pulser during a 2021 deployment. Discussed further in Figure B.3.

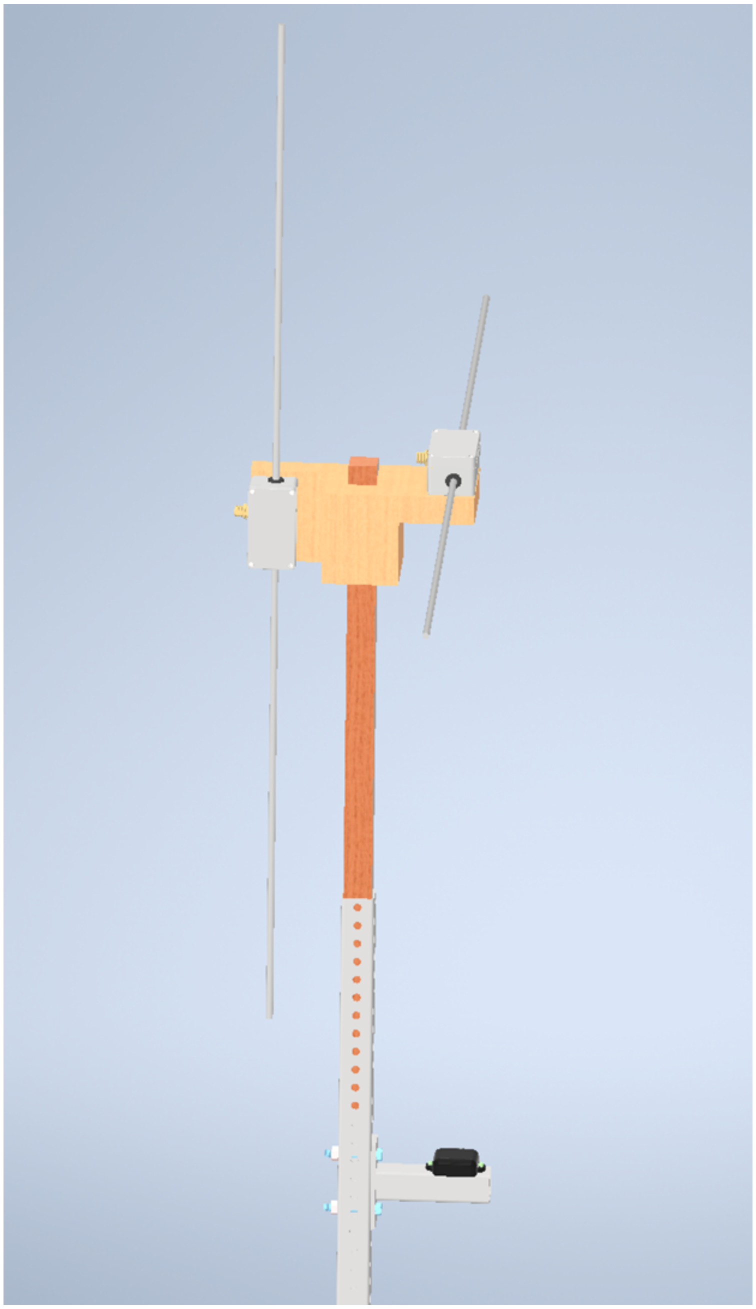

Figure B.5: A model of the GPS patch antenna and bracket which were installed on each BEACON mast during the 2021 deployment. These patch antennas would provide a consistent location for initial conditions of each antenna for the purposes of position calibration.

BIBLIOGRAPHY

[1] Raymond Davis. "A review of the homestake solar neutrino experiment". In: *Progress in Particle and Nuclear Physics* 32 (1994), pp. 13–32. ISSN: 0146-6410. DOI: https://doi.org/10.1016/0146-6410(94)90004-3. URL: https://www.sciencedirect.com/science/article/pii/0146641094900043.

[2] John N. Bahcall, M. H. Pinsonneault, and G. J. Wasserburg. "Solar models with helium and heavy-element diffusion". In: *Rev. Mod. Phys.* 67 (4 Oct. 1995), pp. 781–808. DOI: 10.1103/RevModPhys.67.781. URL: https://link.aps.org/doi/10.1103/RevModPhys.67.781.

[3] Sylvaine Turck-Chieze and Ilidio Lopes. "Toward a Unified Classical Model of the Sun: On the Sensitivity of Neutrinos and Helioseismology to the Microscopic Physics". In: 408 (May 1993), p. 347. DOI: 10.1086/172592.

[4] I Sackmann, Arnold I Boothroyd, William A Fowler, et al. "Our sun. I-the standard model: Successes and failures". In: *The Astrophysical Journal* 360 (1990), pp. 727–736.

[5] John N. Bahcall and H. A. Bethe. "Solution of the solar-neutrino problem". In: *Phys. Rev. Lett.* 65 (18 Oct. 1990), pp. 2233–2235. DOI: 10.1103/PhysRevLett.65.2233. URL: https://link.aps.org/doi/10.1103/PhysRevLett.65.2233.

[6] Y. Fukuda et al. "Evidence for Oscillation of Atmospheric Neutrinos". In: *Phys. Rev. Lett.* 81 (8 Aug. 1998), pp. 1562–1567. DOI: 10.1103/PhysRevLett.81.1562. URL: https://link.aps.org/doi/10.1103/PhysRevLett.81.1562.

[7] John N. Bahcall, Aldo M. Serenelli, and Sarbani Basu. "New solar opacities, abundances, helioseismology, and neutrino fluxes". In: *Astrophys. J. Lett.* 621 (2005), pp. L85–L88. DOI: 10.1086/428929. arXiv: astro-ph/0412440.

[8] M. Anderson et al. "Measurement of the ^{8}B solar neutrino flux in SNO+ with very low backgrounds". In: *Phys. Rev. D* 99.1 (2019), p. 012012. DOI: 10.1103/PhysRevD.99.012012. arXiv: 1812.03355 `[hep-ex]`.

[9] S. N. Ahmed et al. "Measurement of the Total Active ^{8}B Solar Neutrino Flux at the Sudbury Neutrino Observatory with Enhanced Neutral Current Sensitivity". In: *Phys. Rev. Lett.* 92 (18 May 2004), p. 181301. DOI: 10.1103/PhysRevLett.92.181301. URL: https://link.aps.org/doi/10.1103/PhysRevLett.92.181301.

[10] Abigail Vieregg et al. "Fundamental Physics with High-Energy Cosmic Neutrinos". In: *Bulletin of the AAS* 51.3 (May 31, 2019). https://baas.aas.org/pub/2020n3i215. URL: https://baas.aas.org/pub/2020n3i215.

[11] Imre Bartos and Marek Kowalski. *Multimessenger Astronomy*. 2399-2891. IOP Publishing, 2017. ISBN: 978-0-7503-1369-8. DOI: 10.1088/978-0-7503-1369-8. URL: https://dx.doi.org/10.1088/978-0-7503-1369-8.

[12] K Greisen. "End to the cosmic ray spectrum". In: *Phys. Rev. Lett* 16 (1966), pp. 748–750.

[13] GT Zatsepin and VA Kuz'min. "Upper limit of the spectrum of cosmic rays". In: *Soviet Journal of Experimental and Theoretical Physics Letters* 4 (1966), p. 78.

[14] D. V. Martynov et al. "Sensitivity of the Advanced LIGO detectors at the beginning of gravitational wave astronomy". In: *Phys. Rev. D* 93 (11 June 2016), p. 112004. DOI: 10.1103/PhysRevD.93.112004. URL: https://link.aps.org/doi/10.1103/PhysRevD.93.112004.

[15] Victor Branco Valera, Mauricio Bustamante, and Christian Glaser. "The ultra-high-energy neutrino-nucleon cross section: measurement forecasts for an era of cosmic EeV-neutrino discovery". In: (Apr. 2022). arXiv: 2204.04237 `[hep-ph]`.

[16] Peter B. Denton and Yves Kini. "Ultra-High-Energy Tau Neutrino Cross Sections with GRAND and POEMMA". In: *Phys. Rev. D* 102 (2020), p. 123019. DOI: 10.1103/PhysRevD.102.123019. arXiv: 2007.10334 `[astro-ph.HE]`.

[17] Amy Connolly, Robert S. Thorne, and David Waters. "Calculation of High Energy Neutrino-Nucleon Cross Sections and Uncertainties Using the MSTW Parton Distribution Functions and Implications for Future Experiments". In: *Phys. Rev. D* 83 (2011), p. 113009. DOI: 10.1103/PhysRevD.83.113009. arXiv: 1102.0691 `[hep-ph]`.

[18] Ivan Esteban, Steven Prohira, and John F. Beacom. "Detector Requirements for Model-Independent Measurements of Ultrahigh Energy Neutrino Cross Sections". In: (May 2022). arXiv: 2205.09763 `[hep-ph]`.

[19] M. Ahlers. "Neutrino Sources from a Multi-Messenger Perspective". In: *Proceedings, 7th Roma International Conference on Astroparticle Physics (RICAP18) Rome, Italy, September 4-7, 2018.* arXiv:1811.07633. 2018.

[20] K. Fang and K. Murase. "Linking High-Energy Cosmic Particles by Black Hole Jets Embedded in Large-Scale Structures". In: *Phys. Lett.* 14 (2018). Nature Phys.14,no.4,396 (2018), p. 396. DOI: 10.1038/s41567-017-0025-4. arXiv: 1704.00015 `[astro-ph.HE]`.

[21] K. Fang et al. "Testing the Newborn Pulsar Origin of Ultrahigh Energy Cosmic Rays with EeV Neutrinos". In: *Phys. Rev.* D90.10 (2014), p. 103005. DOI: 10.1103/PhysRevD.90.103005,10.1103/PhysRevD.92.129901. arXiv: 1311.2044 `[astro-ph.HE]`.

[22] D. Boncioli, D. Biehl, and W. Winter. "On the common origin of cosmic rays across the ankle and diffuse neutrinos at the highest energies from low-luminosity Gamma-Ray Bursts". In: *Astrophys. J.* 872 (2019), p. 110. DOI: 10.3847/1538-4357/aafda7. arXiv: 1808.07481 `[astro-ph.HE]`.

[23] Kohta Murase, Yoshiyuki Inoue, and Charles D. Dermer. "Diffuse Neutrino Intensity from the Inner Jets of Active Galactic Nuclei: Impacts of External Photon Fields and the Blazar Sequence". In: *Phys. Rev. D* 90.2 (2014), p. 023007. DOI: 10.1103/PhysRevD.90.023007. arXiv: 1403.4089 `[astro-ph.HE]`.

[24] Xavier Rodrigues et al. "Blazar origin of the UHECRs and perspectives for the detection of astrophysical source neutrinos at EeV energies". In: (2020). arXiv: 2003.08392 `[astro-ph.HE]`.

[25] K. Murase. “High energy neutrino early afterglows gamma-ray bursts revisited”. In: *Phys. Rev.* D76 (2007), p. 123001. DOI: 10.1103/PhysRevD.76.123001. arXiv: 0707.1140 `[astro-ph]`.

[26] J. Heinze et al. “A new view on Auger data and cosmogenic neutrinos in light of different nuclear disintegration and air-shower models”. In: *Astrophys. J.* 873 (2019), p. 88. DOI: 10.3847/1538-4357/ab05ce. arXiv: 1901.03338 `[astro-ph.HE]`.

[27] A. van Vliet, R. Alves Batista, and J. R. Hörandel. “Determining the fraction of cosmic-ray protons at ultrahigh energies with cosmogenic neutrinos”. In: *Phys. Rev.* D100.2 (2019), p. 021302. DOI: 10.1103/PhysRevD.100.021302. arXiv: 1901.01899 `[astro-ph.HE]`.

[28] M. Ackermann et al. “The spectrum of isotropic diffuse gamma-ray emission between 100 MeV and 820 GeV”. In: *Astrophys. J.* 799 (2015), p. 86. DOI: 10.1088/0004-637X/799/1/86. arXiv: 1410.3696 `[astro-ph.HE]`.

[29] Christian Haack and Christopher Wiebusch. “A measurement of the diffuse astrophysical muon neutrino flux using eight years of IceCube data.” In: *PoS* ICRC2017 (2018), p. 1005. DOI: 10.22323/1.301.1005. eprint: 1710.01191.

[30] Claudio Kopper. “Observation of Astrophysical Neutrinos in Six Years of IceCube Data”. In: *PoS* ICRC2017 (2018), p. 981. DOI: 10.22323/1.301.0981. eprint: 1710.01191.

[31] M. G. Aartsen et al. “Differential limit on the extremely-high-energy cosmic neutrino flux in the presence of astrophysical background from nine years of IceCube data”. In: *Phys. Rev.* D98.6 (2018), p. 062003. DOI: 10.1103/PhysRevD.98.062003. arXiv: 1807.01820 `[astro-ph.HE]`.

[32] A. Aab et al. “The Pierre Auger Observatory: Contributions to the 34th International Cosmic Ray Conference (ICRC 2015)”. In: *Proceedings, 34th International Cosmic Ray Conference (ICRC 2015): The Hague, The Netherlands, July 30-August 6, 2015.* 2015. arXiv: 1509.03732 `[astro-ph.HE]`. URL: http://lss.fnal.gov/archive/2015/conf/fermilab-conf-15-396-ad-ae-cd-td.pdf.

[33] J.A. Aguilar et al. “Design and sensitivity of the Radio Neutrino Observatory in Greenland (RNO-G)”. In: *Journal of Instrumentation* 16.03 (Mar. 2021), P03025. DOI: 10.1088/1748-0221/16/03/p03025. URL: https://doi.org/10.1088%2F1748-0221%2F16%2F03%2Fp03025.

[34] K. Hirata et al. “Observation of a neutrino burst from the supernova SN1987A”. In: *Phys. Rev. Lett.* 58 (14 Apr. 1987), pp. 1490–1493. DOI: 10.1103/PhysRevLett.58.1490. URL: https://link.aps.org/doi/10.1103/PhysRevLett.58.1490.

[35] R. M. Bionta et al. “Observation of a neutrino burst in coincidence with supernova 1987A in the Large Magellanic Cloud”. In: *Phys. Rev. Lett.* 58 (14 Apr. 1987), pp. 1494–1496. DOI: 10.1103/PhysRevLett.58.1494. URL: https://link.aps.org/doi/10.1103/PhysRevLett.58.1494.

[36] E.N. Alexeyev et al. "Detection of the neutrino signal from SN 1987A in the LMC using the INR Baksan underground scintillation telescope". In: *Physics Letters B* 205.2 (1988), pp. 209–214. ISSN: 0370-2693. DOI: https://doi.org/10.1016/0370-2693(88)91651-6. URL: https://www.sciencedirect.com/science/article/pii/0370269388916516.

[37] Yudai Suwa et al. "Observing Supernova Neutrino Light Curves with Super-Kamiokande: Expected Event Number over 10 s". In: *The Astrophysical Journal* 881.2 (Aug. 2019), p. 139. DOI: 10.3847/1538-4357/ab2e05. URL: https://doi.org/10.3847/1538-4357/ab2e05.

[38] Kate Scholberg. "Supernova Neutrino Detection". In: *Annual Review of Nuclear and Particle Science* 62.1 (2012), pp. 81–103. DOI: 10.1146/annurev-nucl-102711-095006. eprint: https://doi.org/10.1146/annurev-nucl-102711-095006. URL: https://doi.org/10.1146/annurev-nucl-102711-095006.

[39] MG Aartsen et al. "2018b. Multimessenger observations of a flaring blazar coincident with high-energy neutrino IceCube-170922A". In: *Science* 361 ().

[40] MG Aartsen et al. "All-sky search for time-integrated neutrino emission from astrophysical sources with 7 yr of IceCube data". In: *The Astrophysical Journal* 835.2 (2017), p. 151.

[41] MG Aartsen et al. "The IceCube Neutrino Observatory–Contributions to ICRC 2017 Part I: Searches for the Sources of Astrophysical Neutrinos". In: *arXiv:1710.01179* (2017).

[42] IceCube Collaboration and others. "Fermi-Lat". In: *MAGIC, AGILE, ASAS-SN, HAWC, HESS, INTEGRAL, Kanata, Kiso, Kapteyn, Liverpool Telescope, Subaru, Swift/NuSTAR, VERITAS, and VLA/17B-403 teams, Multimessenger observations of a flaring blazar coincident with high-energy neutrino IceCube-170922A, Science* 361 (2018), p. 146.

[43] Workman, RL and Beatty, JJ and Matthews, J and Wakely, SP and AUGER and HiRes and TA and others. "Review of Particle Physics". In: *Particle Data Group* (). To be published (2022). Section 30. Cosmic Rays.

[44] ENRICO Fermi. "On the Origin of the Cosmic Radiation". In: *Phys. Rev.* 75 (8 Apr. 1949), pp. 1169–1174. DOI: 10.1103/PhysRev.75.1169. URL: https://link.aps.org/doi/10.1103/PhysRev.75.1169.

[45] M Bustamante et al. "High-energy cosmic-ray acceleration". In: (2010). DOI: 10.5170/CERN-2010-001.533. URL: https://cds.cern.ch/record/1249755.

[46] Elisabete De Gouveia Dal Pino et al. "Ultra-high-energy cosmic ray acceleration by magnetic reconnection in relativistic jets and the origin of very high energy emission". In: *Proceedings of 37th International Cosmic Ray Conference — PoS(ICRC2021)*. Sissa Medialab, Aug. 2021. DOI: 10.22323/1.395.0454. URL: https://doi.org/10.22323%2F1.395.0454.

[47] Kohta Murase, Yoshiyuki Inoue, and Charles D. Dermer. “Diffuse neutrino intensity from the inner jets of active galactic nuclei: Impacts of external photon fields and the blazar sequence”. In: *Physical Review D* 90.2 (July 2014). DOI: 10.1103/physrevd.90.023007. URL: https://doi.org/10.1103%2Fphysrevd.90.023007.

[48] Kohta Murase. “Active Galactic Nuclei as High-Energy Neutrino Sources”. In: *Neutrino Astronomy*. WORLD SCIENTIFIC, Mar. 2017, pp. 15–31. DOI: 10.1142/9789814759410_0002. URL: https://doi.org/10.1142%2F9789814759410_0002.

[49] Denise Boncioli, Daniel Biehl, and Walter Winter. “On the Common Origin of Cosmic Rays across the Ankle and Diffuse Neutrinos at the Highest Energies from Low-luminosity Gamma-Ray Bursts”. In: *The Astrophysical Journal* 872.1 (Feb. 2019), p. 110. DOI: 10.3847/1538-4357/aafda7. URL: https://doi.org/10.3847/1538-4357/aafda7.

[50] Ke Fang et al. “Testing the newborn pulsar origin of ultrahigh energy cosmic rays with EeV neutrinos”. In: *Phys. Rev. D* 90 (10 Nov. 2014), p. 103005. DOI: 10.1103/PhysRevD.90.103005. URL: https://link.aps.org/doi/10.1103/PhysRevD.90.103005.

[51] C. Righi et al. “EeV astrophysical neutrinos from flat spectrum radio quasars”. In: *Astron. Astrophys.* 642 (2020), A92. DOI: 10.1051/0004-6361/202038301. arXiv: 2003.08701 `[astro-ph.HE]`.

[52] IceCube Collaboration. “IceCube-190730A - IceCube observation of a high-energy neutrino candidate event”. In: *GRB Coordinates Network* 25225 (July 2019), p. 1.

[53] A. Franckowiak et al. “Patterns in the Multiwavelength Behavior of Candidate Neutrino Blazars”. In: *Astrophys. J.* 893.2 (2020), p. 162. DOI: 10.3847/1538-4357/ab8307. arXiv: 2001.10232 `[astro-ph.HE]`.

[54] Daniel Biehl et al. “Tidally disrupted stars as a possible origin of both cosmic rays and neutrinos at the highest energies”. In: *Scientific reports* 8.1 (2018), pp. 1–9.

[55] Ke Fang and Brian D. Metzger. “High-energy Neutrinos from Millisecond Magnetars Formed from the Merger of Binary Neutron Stars”. In: *The Astrophysical Journal* 849.2 (Nov. 2017), p. 153. DOI: 10.3847/1538-4357/aa8b6a. URL: https://doi.org/10.3847/1538-4357/aa8b6a.

[56] Nicolas Busca, Dan Hooper, and Edward W. Kolb. “Pierre Auger data, photons, and top-down cosmic ray models”. In: *Physical Review D* 73.12 (June 2006). DOI: 10.1103/physrevd.73.123001. URL: https://doi.org/10.1103%2Fphysrevd.73.123001.

[57] M. Kachelriess. “The rise and fall of top-down models as main UHECR sources”. In: *20th Rencontres de Blois on Challenges in Particle Astrophysics*. 2008, pp. 215–224. arXiv: 0810.3017 `[astro-ph]`.

[58] A. Aab et al. “Measurement of the cosmic-ray energy spectrum above 2.5×10^{18} eV using the Pierre Auger Observatory”. In: *Phys. Rev. D* 102 (6 Sept. 2020), p. 062005. DOI: 10.1103/PhysRevD.102.062005.

[59] T. Abu-Zayyad et al. “THE COSMIC-RAY ENERGY SPECTRUM OBSERVED WITH THE SURFACE DETECTOR OF THE TELESCOPE ARRAY EXPERIMENT”. In: *The Astrophysical Journal* 768.1 (Apr. 2013), p. L1. DOI: 10.1088/2041-8205/768/1/l1.

[60] R.U. Abbasi et al. “Measurement of the flux of ultra high energy cosmic rays by the stereo technique”. In: *Astroparticle Physics* 32.1 (2009), pp. 53–60. ISSN: 0927-6505. DOI: https://doi.org/10.1016/j.astropartphys.2009.06.001.

[61] Lee Yacobi, Dafne Guetta, and Ehud Behar. “Implication of the Non-detection of GZK Neutrinos”. In: 823.2, 89 (June 2016), p. 89. DOI: 10.3847/0004-637X/823/2/89. arXiv: `1510.01244 [astro-ph.HE]`.

[62] David Seckel. “In-ice radio detection of GZK neutrinos”. In: *AIP Conference Proceedings*. Vol. 579. 1. American Institute of Physics. 2001, pp. 196–203.

[63] Frank G. Schröder. “Radio detection of Cosmic-Ray Air Showers and High-Energy Neutrinos”. In: *Progress in Particle and Nuclear Physics* 93 (2017), pp. 1–68. arXiv: `1607.08781 [astro-ph.IM]`.

[64] T. Huege. “Radio detection of cosmic ray air showers in the digital era”. In: *Physical Reports* 620 (2016), pp. 1–52. arXiv: `1601.07426 [astro-ph.IM]`.

[65] H. Schoorlemmer et al. “Energy and Flux Measurements of Ultra-High Energy Cosmic Rays Observed During the First ANITA Flight”. In: *Astropart. Phys.* 77 (2016), pp. 32–43. DOI: 10.1016/j.astropartphys.2016.01.001. arXiv: `1506.05396 [astro-ph.HE]`.

[66] H. Falcke et al. “Detection and imaging of atmospheric radio flashes from cosmic ray air showers”. In: *Nature* 435 (2005), pp. 313–316. DOI: 10.1038/nature03614. arXiv: astro-ph/0505383.

[67] D. Ardouin et al. “Geomagnetic origin of the radio emission from cosmic ray induced air showers observed by CODALEMA”. In: *Astropart. Phys.* 31 (2009), pp. 192–200. DOI: 10.1016/j.astropartphys.2009.01.001. arXiv: `0901.4502 [astro-ph.HE]`.

[68] P. Schellart et al. “Detecting cosmic rays with the LOFAR radio telescope”. In: *Astron. Astrophys.* 560 (2013), A98. DOI: 10.1051/0004-6361/201322683. arXiv: `1311.1399 [astro-ph.IM]`.

[69] R Monroe et al. “Self-triggered radio detection and identification of cosmic air showers with the OVRO-LWA”. In: *Nuclear Instruments and Methods in Physics Research Section A: Accelerators, Spectrometers, Detectors and Associated Equipment* 953 (2020), p. 163086.

[70] K. Bechtol et al. “SLAC T-510 experiment for radio emission from particle showers: Detailed simulation study and interpretation”. In: *Phys. Rev. D* 105.6 (2022), p. 063025. DOI: 10.1103/PhysRevD.105.063025. arXiv: `2111.04334 [astro-ph.IM]`.

[71] K. Belov et al. “Accelerator measurements of magnetically-induced radio emission from particle cascades with applications to cosmic-ray air showers”. In: *Phys. Rev. Lett.* 116.14 (2016), p. 141103. DOI: 10.1103/PhysRevLett.116.141103. arXiv: `1507.07296 [astro-ph.IM]`.

[72] G. A. Askar'yan. "Excess negative charge of an electron-photon shower and its coherent radio emission". In: *Zh. Eksp. Teor. Fiz.* 41 (1961), pp. 616–618.

[73] David Saltzberg et al. "Observation of the Askaryan Effect: Coherent Microwave Cherenkov Emission from Charge Asymmetry in High-Energy Particle Cascades". In: *Phys. Rev. Lett.* 86 (13 Mar. 2001), pp. 2802–2805. DOI: 10.1103/PhysRevLett.86.2802. URL: https://link.aps.org/doi/10.1103/PhysRevLett.86.2802.

[74] Frank G. Schröder. "Status of the radio technique for cosmic-ray induced air showers". In: *Nuclear and Particle Physics Proceedings* 279-281 (2016). Proceedings of the 9th Cosmic Ray International Seminar, pp. 190–197. ISSN: 2405-6014. DOI: https://doi.org/10.1016/j.nuclphysbps.2016.10.027. URL: https://www.sciencedirect.com/science/article/pii/S2405601416302085.

[75] J.A. Aguilar et al. "Transmission of light in deep sea water at the site of the Antares neutrino telescope". In: *Astroparticle Physics* 23.1 (2005), pp. 131–155. ISSN: 0927-6505. DOI: https://doi.org/10.1016/j.astropartphys.2004.11.006. URL: https://www.sciencedirect.com/science/article/pii/S0927650504001902.

[76] M. Ackermann et al. "Optical properties of deep glacial ice at the South Pole". In: *Journal of Geophysical Research: Atmospheres* 111.D13 (2006). DOI: https://doi.org/10.1029/2005JD006687. eprint: https://agupubs.onlinelibrary.wiley.com/doi/pdf/10.1029/2005JD006687. URL: https://agupubs.onlinelibrary.wiley.com/doi/abs/10.1029/2005JD006687.

[77] P. Allison et al. "Design and initial performance of the Askaryan Radio Array prototype EeV neutrino detector at the South Pole". In: *Astroparticle Physics* 35.7 (2012), pp. 457–477. ISSN: 0927-6505. DOI: https://doi.org/10.1016/j.astropartphys.2011.11.010. URL: https://www.sciencedirect.com/science/article/pii/S092765051100209X.

[78] A Anker et al. "Targeting ultra-high energy neutrinos with the ARIANNA experiment". In: *Advances in Space Research* 64.12 (2019), pp. 2595–2609.

[79] P. Allison et al. "Design and Performance of an Interferometric Trigger Array for Radio Detection of High-Energy Neutrinos". In: *Nucl. Instrum. Meth.* A930 (2019), pp. 112–125. DOI: 10.1016/j.nima.2019.01.067. arXiv: 1809.04573.

[80] P. Allison et al. *A low-threshold ultrahigh-energy neutrino search with the Askaryan Radio Array.* 2022. DOI: 10.48550/ARXIV.2202.07080. URL: https://arxiv.org/abs/2202.07080.

[81] S. Prohira et al. "The Radar Echo Telescope for Cosmic Rays: Pathfinder experiment for a next-generation neutrino observatory". In: *Physical Review D* 104.10 (Nov. 2021). DOI: 10.1103/physrevd.104.102006. URL: https://doi.org/10.1103%2Fphysrevd.104.102006.

[82] MG Aartsen et al. "IceCube-Gen2: the window to the extreme universe". In: *Journal of Physics G: Nuclear and Particle Physics* 48.6 (2021), p. 060501.

[83] Daniele Fargion, Andrea Aiello, and Roberto Conversano. "Horizontal tau air showers from mountains in deep valley: Traces of UHECR neutrino tau". In: *Proceedings, 26th International Cosmic Ray Conference, August 17-25, 1999, Salt Lake City: Invited, Rapporteur, and Highlight Papers.* [2,396(1999)]. 1999, p. 396. arXiv: astro-ph/9906450 `[astro-ph]`. URL: https://arxiv.org/pdf/astro-ph/9906450.pdf.

[84] Jonathan L. Feng et al. "Observability of earth skimming ultrahigh-energy neutrinos". In: *Phys. Rev. Lett.* 88 (2002), p. 161102. DOI: 10.1103/PhysRevLett.88.161102. arXiv: hep-ph/0105067.

[85] Enrique Zas. "Neutrino detection with inclined air showers". In: *New J. Phys.* 7 (2005), p. 130. DOI: 10.1088/1367-2630/7/1/130. arXiv: astro-ph/0504610.

[86] Jaime Álvarez-Muñiz et al. "The Giant Radio Array for Neutrino Detection (GRAND): Science and design". In: *Science China Physics, Mechanics and Astronomy* 63.1 (Aug. 2019). DOI: 10.1007/s11433-018-9385-7. URL: https://doi.org/10.1007%2Fs11433-018-9385-7.

[87] DONALD E. GROOM, NIKOLAI V. MOKHOV, and SERGEI I. STRIGANOV. "MUON STOPPING POWER AND RANGE TABLES 10 MeV–100 TeV". In: *Atomic Data and Nuclear Data Tables* 78.2 (2001), pp. 183–356. ISSN: 0092-640X. DOI: https://doi.org/10.1006/adnd.2001.0861. URL: https://www.sciencedirect.com/science/article/pii/S0092640X01908617.

[88] J Alvarez-Muñiz, W Carvalho Jr, and E Zas. "Monte Carlo simulations of radio pulses in atmospheric showers using ZHAireS". In: *Astroparticle Physics* 35.6 (2012), pp. 325–341.

[89] Jaime Alvarez-Muñiz et al. "Comprehensive approach to tau-lepton production by high-energy tau neutrinos propagating through the Earth". In: *Physical Review D* 97.2 (Jan. 2018). DOI: 10.1103/physrevd.97.023021.

[90] Gonzalo Parente and Enrique Zas. *Neutrino Induced Events in the Pierre Auger Detector.* 1996. DOI: 10.48550/ARXIV.ASTRO-PH/9606091. URL: https://arxiv.org/abs/astro-ph/9606091.

[91] D. Fargion et al. "Tau Air Showers from Earth". In: *The Astrophysical Journal* 613.2 (Oct. 2004), pp. 1285–1301. DOI: 10.1086/423124. URL: https://doi.org/10.1086%2F423124.

[92] X Bertou et al. "Tau neutrinos in the Auger Observatory: a new window to UHECR sources". In: *Astroparticle Physics* 17.2 (May 2002), pp. 183–193. DOI: 10.1016/s0927-6505(01)00147-5.

[93] Roshan Mammen Abraham et al. *Tau Neutrinos in the Next Decade: from GeV to EeV.* 2022. DOI: 10.48550/ARXIV.2203.05591. URL: https://arxiv.org/abs/2203.05591.

[94] A. Nepomuk Otte et al. *Trinity: An Air-Shower Imaging Instrument to detect Ultrahigh Energy Neutrinos.* 2019. DOI: 10.48550/ARXIV.1907.08727. URL: https://arxiv.org/abs/1907.08727.

[95] Anthony Brown et al. “Trinity: an imaging air Cherenkov telescope to search for Ultra-High-Energy neutrinos.” In: *PoS* ICRC2021 (2021), p. 1179. DOI: 10.22323/1.395.1179.

[96] Andres Romero-Wolf et al. *An Andean Deep-Valley Detector for High-Energy Tau Neutrinos.* 2020. DOI: 10.48550/ARXIV.2002.06475. URL: https://arxiv.org/abs/2002.06475.

[97] SH Wang et al. “TAROGE-M: Radio Observatory on Antarctic High Mountain for Detecting Near-Horizon Ultra-High Energy Air Showers”. In: *37th International Cosmic Ray Conference. 12-23 July 2021. Berlin.* 2022, p. 1173.

[98] J. W. Nam et al. “Design and implementation of the TAROGE experiment”. In: *International Journal of Modern Physics D* 25.13, 1645013 (July 2016), p. 1645013. DOI: 10.1142/S0218271816450139.

[99] P. W. Gorham et al. “New Limits on the Ultrahigh Energy Cosmic Neutrino Flux from the ANITA Experiment”. In: *Phys. Rev. Lett.* 103 (5 July 2009), p. 051103. DOI: 10.1103/PhysRevLett.103.051103. URL: https://link.aps.org/doi/10.1103/PhysRevLett.103.051103.

[100] Q. Abarr et al. “The Payload for Ultrahigh Energy Observations (PUEO): a white paper”. In: *Journal of Instrumentation* 16.08 (Aug. 2021), P08035. DOI: 10.1088/1748-0221/16/08/p08035.

[101] A. V. Olinto et al. “The POEMMA (Probe of Extreme Multi-Messenger Astrophysics) Observatory”. In: (2020). DOI: 10.48550/ARXIV.2012.07945. URL: https://arxiv.org/abs/2012.07945.

[102] P.W. Gorham et al. “The Antarctic Impulsive Transient Antenna ultra-high energy neutrino detector: Design, performance, and sensitivity for the 2006–2007 balloon flight”. In: *Astroparticle Physics* 32.1 (2009), pp. 10–41. ISSN: 0927-6505. DOI: https://doi.org/10.1016/j.astropartphys.2009.05.003. URL: https://www.sciencedirect.com/science/article/pii/S0927650509000838.

[103] PW Gorham et al. “Constraints on the diffuse high-energy neutrino flux from the third flight of ANITA”. In: *Physical Review D* 98.2 (2018), p. 022001.

[104] A Romero-Wolf et al. “Comprehensive analysis of anomalous ANITA events disfavors a diffuse tau-neutrino flux origin”. In: *Physical Review D* 99.6 (2019), p. 063011.

[105] P. W. Gorham et al. “Characteristics of Four Upward-Pointing Cosmic-Ray-like Events Observed with ANITA”. In: *Phys. Rev. Lett.* 117 (7 Aug. 2016), p. 071101. DOI: 10.1103/PhysRevLett.117.071101. URL: https://link.aps.org/doi/10.1103/PhysRevLett.117.071101.

[106] P. W. Gorham et al. “Observation of an Unusual Upward-Going Cosmic-Ray-like Event in the Third Flight of ANITA”. In: *Phys. Rev. Lett.* 121 (16 Oct. 2018), p. 161102. DOI: 10.1103/PhysRevLett.121.161102. URL: https://link.aps.org/doi/10.1103/PhysRevLett.121.161102.

[107] John F. Cherry and Ian M. Shoemaker. "Sterile neutrino origin for the upward directed cosmic ray showers detected by ANITA". In: *Phys. Rev. D* 99 (6 Mar. 2019), p. 063016. DOI: 10.1103/PhysRevD.99.063016. URL: https://link.aps.org/doi/10.1103/PhysRevD.99.063016.

[108] Guo-yuan Huang. "Sterile neutrinos as a possible explanation for the upward air shower events at ANITA". In: *Phys. Rev. D* 98 (4 Aug. 2018), p. 043019. DOI: 10.1103/PhysRevD.98.043019. URL: https://link.aps.org/doi/10.1103/PhysRevD.98.043019.

[109] Luis A Anchordoqui et al. "Upgoing ANITA events as evidence of the CPT symmetric universe". In: *arXiv preprint arXiv:1803.11554* (2018).

[110] Lucien Heurtier, Yann Mambrini, and Mathias Pierre. "Dark matter interpretation of the ANITA anomalous events". In: *Phys. Rev. D* 99 (9 May 2019), p. 095014. DOI: 10.1103/PhysRevD.99.095014. URL: https://link.aps.org/doi/10.1103/PhysRevD.99.095014.

[111] Dan Hooper et al. "Superheavy dark matter and ANITA's anomalous events". In: *Phys. Rev. D* 100 (4 Aug. 2019), p. 043019. DOI: 10.1103/PhysRevD.100.043019. URL: https://link.aps.org/doi/10.1103/PhysRevD.100.043019.

[112] Derek B. Fox et al. *The ANITA Anomalous Events as Signatures of a Beyond Standard Model Particle, and Supporting Observations from IceCube.* 2018. DOI: 10.48550/ARXIV.1809.09615. URL: https://arxiv.org/abs/1809.09615.

[113] James M. Cline, Christian Gross, and Wei Xue. "Can the ANITA anomalous events be due to new physics?" In: *Phys. Rev. D* 100 (1 July 2019), p. 015031. DOI: 10.1103/PhysRevD.100.015031. URL: https://link.aps.org/doi/10.1103/PhysRevD.100.015031.

[114] Jack H. Collins, P. S. Bhupal Dev, and Yicong Sui. "*R*-parity violating supersymmetric explanation of the anomalous events at ANITA". In: *Phys. Rev. D* 99 (4 Feb. 2019), p. 043009. DOI: 10.1103/PhysRevD.99.043009. URL: https://link.aps.org/doi/10.1103/PhysRevD.99.043009.

[115] Bhavesh Chauhan and Subhendra Mohanty. "Leptoquark solution for both the flavor and ANITA anomalies". In: *Phys. Rev. D* 99 (9 May 2019), p. 095018. DOI: 10.1103/PhysRevD.99.095018. URL: https://link.aps.org/doi/10.1103/PhysRevD.99.095018.

[116] D. Smith et al. "Experimental tests of sub-surface reflectors as an explanation for the ANITA anomalous events". In: *Journal of Cosmology and Astroparticle Physics* 2021.04 (Apr. 2021), p. 016. DOI: 10.1088/1475-7516/2021/04/016. URL: https://doi.org/10.1088/1475-7516/2021/04/016.

[117] Ian M Shoemaker et al. "Reflections on the anomalous ANITA events: the Antarctic subsurface as a possible explanation". In: *Annals of Glaciology* 61.81 (2020), pp. 92–98.

[118] Jessica Avva et al. "An in situ measurement of the radio-frequency attenuation in ice at Summit Station, Greenland". In: *Journal of Glaciology* 61.229 (2015), pp. 1005–1011. DOI: 10.3189/2015JoG15J057.

[119] Stephanie A Wissel et al. “Site characterization and detector development for the greenland neutrino observatory”. In: *34th International Cosmic Ray Conference*. 2015.

[120] JA Aguilar et al. “In situ, broadband measurement of the radio frequency attenuation length at Summit Station, Greenland”. In: *arXiv preprint arXiv:2201.07846* (2022).

[121] Adam M. Dziewonski and Don L. Anderson. “Preliminary reference Earth model”. In: *Physics of the Earth and Planetary Interiors* 25.4 (1981), pp. 297–356. ISSN: 0031-9201. DOI: https://doi.org/10.1016/0031-9201(81)90046-7. URL: https://www.sciencedirect.com/science/article/pii/0031920181900467.

[122] Amy Connolly, Robert S. Thorne, and David Waters. “Calculation of high energy neutrino-nucleon cross sections and uncertainties using the Martin-Stirling-Thorne-Watt parton distribution functions and implications for future experiments”. In: *Physical Review D* 83.11 (June 2011). DOI: 10.1103/physrevd.83.113009. URL: https://doi.org/10.1103%2Fphysrevd.83.113009.

[123] P. Allison and S. Archambault and R. Bard and J.J. Beatty and M. Beheler-Amass and D.Z. Besson and M. Beydler and M. Bogdan and C.-C. Chen and C.-H. Chen and P. Chen and B.A. Clark and A. Clough and A. Connolly and L. Cremonesi and J. Davies and C. Deaconu and M.A. DuVernois and E. Friedman and J. Hanson and K. Hanson and J. Haugen and K.D. Hoffman and B. Hokanson-Fasig and E. Hong and S.-Y. Hsu and L. Hu and J.-J. Huang and M.-H. Huang and K. Hughes and A. Ishihara and A. Karle and J.L. Kelley and R. Khandelwal and M. Kim and I. Kravchenko and J. Kruse and K. Kurusu and H. Landsman and U.A. Latif and A. Laundrie and C.-J. Li and T.C. Liu and M.-Y. Lu and A. Ludwig and K. Mase and T. Meures and J. Nam and R.J. Nichol and G. Nir and E. Oberla and A. ÓMurchadha and Y. Pan and C. Pfendner and M. Ransom and K. Ratzlaff and J. Roth and P. Sandstrom and D. Seckel and Y.-S. Shiao and A. Shultz and D. Smith and M. Song and M. Sullivan and J. Touart and A.G. Vieregg and M.-Z. Wang and S.-H. Wang and K. Wei and S.A. Wissel and S. Yoshida and R. Young. “Design and performance of an interferometric trigger array for radio detection of high-energy neutrinos”. In: *Nuclear Instruments and Methods in Physics Research Section A: Accelerators, Spectrometers, Detectors and Associated Equipment* 930 (2019), pp. 112–125. ISSN: 0168-9002. DOI: https://doi.org/10.1016/j.nima.2019.01.067. URL: https://www.sciencedirect.com/science/article/pii/S016890021930124X.

[124] B. Hokanson-Fasig. “Design Studies for the Radio Neutrino Observatory (RNO)”. In: *PoS (ICRC2019)* 913 (2019).

[125] Eric W Weisstein. “Sphere point picking”. In: *https://mathworld. wolfram. com/* (2002).

[126] Nikolai G. Lehtinen et al. “FORTE satellite constraints on ultrahigh energy cosmic particle fluxes”. In: *Physical Review D* 69.1 (Jan. 2004). DOI: 10.1103/physrevd.69.013008. URL: https://doi.org/10.1103%2Fphysrevd.69.013008.

[127] Jaime Alvarez-Muñiz, Andrés Romero-Wolf, and Enrique Zas. “Practical and accurate calculations of Askaryan radiation”. In: *Physical Review D* 84.10 (Nov. 2011). DOI: 10.1103/physrevd.84.103003. URL: https://doi.org/10.1103%2Fphysrevd.84.103003.

[128] Soebur Razzaque et al. “Coherent radio pulses from GEANT generated electromagnetic showers in ice”. In: *Phys. Rev. D* 65 (10 May 2002), p. 103002. DOI: 10.1103/PhysRevD.65.103002. URL: https://link.aps.org/doi/10.1103/PhysRevD.65.103002.

[129] S. Prohira et al. “Modeling in-ice radio propagation with parabolic equation methods”. In: *Physical Review D* 103.10 (May 2021). DOI: 10.1103/physrevd.103.103007. URL: https://doi.org/10.1103%2Fphysrevd.103.103007.

[130] Jordan C. Hanson. “Broadband RF Phased Array Design with MEEP: Comparisons to Array Theory in Two and Three Dimensions”. In: *Electronics* 10.4 (Feb. 2021), p. 415. DOI: 10.3390/electronics10040415. URL: https://doi.org/10.3390%2Felectronics10040415.

[131] M Newcomb, The ARA Collaboration. *Ice-Index Of Refraction.* URL: https://user-web.icecube.wisc.edu/~araproject/radio/#icerefraction.

[132] Sigfus J. Johnsen et al. “Greenland palaeotemperatures derived from GRIP bore hole temperature and ice core isotope profiles”. In: *Tellus Series B Chemical and Physical Meteorology B* 47.5 (Jan. 1995), pp. 624–629. DOI: 10.3402/tellusb.v47i5.16077.

[133] Robert Arthern et al. “Inversion for the density-depth profile of polar firn using a stepped-frequency radar”. In: *Journal of Geophysical Research: Earth Surface* 118 (Sept. 2013). DOI: 10.1002/jgrf.20089.

[134] Jessica Avva et al. “An in situ measurement of the radio-frequency attenuation in ice at Summit Station, Greenland”. In: *Journal of Glaciology* 61.229 (2015), pp. 1005–1011. DOI: 10.3189/2015jog15j057. URL: https://doi.org/10.3189%2F2015jog15j057.

[135] A. Aab et al. “Improved limit to the diffuse flux of ultrahigh energy neutrinos from the Pierre Auger Observatory”. In: *Phys. Rev. D* 91 (2015), p. 092008. DOI: 10.1103/PhysRevD.91.092008. arXiv: 1504.05397 `[astro-ph.HE]`.

[136] P. Allison et al. “Performance of two Askaryan Radio Array stations and first results in the search for ultrahigh energy neutrinos”. In: *Phys. Rev.* D93.8 (2016), p. 082003. DOI: 10.1103/PhysRevD.93.082003. arXiv: 1507.08991 `[astro-ph.HE]`.

[137] U.S. Ice Drilling Program. “Agile Sub-Ice Geological Drill Operations and Maintenance Manual”. In: *https://icedrill.org/library/agile-sub-ice-geological-drill-operations-and-maintenance-manual* (2019).

[138] I. Kravchenko et al. “Performance and simulation of the RICE detector”. In: *Astropart. Phys.* 19 (2003), pp. 15–36. DOI: 10.1016/S0927-6505(02)00194-9. arXiv: astro-ph/0112372 `[astro-ph]`.

[139] J. Avva et al. “Development Toward a Ground-Based Interferometric Phased Array for Radio Detection of High Energy Neutrinos”. In: *Nucl. Instrum. Meth.* A869 (2017), pp. 46–55. DOI: 10.1016/j.nima.2017.07.009. arXiv: 1605.03525 `[astro-ph.IM]`.

[140] J. Roberts et al. “LAB4D: A low power, multi-GSa/s, transient digitizer with sampling timebase trimming capabilities”. In: *Nucl. Instrum. Meth.* A925 (2019), pp. 92–100. DOI: 10.1016/j.nima.2019.01.091. arXiv: 1803.04600.

[141] UNAVCO. “Remote Station Engineering - Power Systems”. In: *https://www.unavco.org/projects/project-support/polar/remote/power/power.html* (2014), (accessed July 2019).

[142] A. Nelles for the ARIANNA Collaboration. “A wind-turbine for autonomous stations for radio detection of neutrinos”. In: *PoS* ICRC2019 (2019), p. 968.

[143] K. Steffen, J.E. Box, and W. Abdalati. “Greenland climate network: GC-Net”. In: *US Army Cold Regions Reattach and Engineering (CRREL), CRREL Special Report* (1996), pp. 98–103.

[144] NOAA. “Global Monitoring Laboratory”. In: *https://www.esrl.noaa.gov/gmd/dv/data.html* (2020).

[145] LoRA Alliance. *LoRaWAN Specification v. 1.03.* 2018.

[146] P. Meade. “JADE: An End-To-End Data Transfer and Catalog Tool”. In: *Journal of Physics: Conference Series* 898.6 (2017), p. 062050.

[147] J. A. Aguilar et al. *Triboelectric Backgrounds to radio-based UHE Neutrino Exeperiments.* 2021. DOI: 10.48550/ARXIV.2103.06079. URL: https://arxiv.org/abs/2103.06079.

[148] Aguilar, J. A. et al. “Reconstructing the neutrino energy for in-ice radio detectors - A study for the Radio Neutrino Observatory Greenland (RNO-G)”. In: *Eur. Phys. J. C* 82.2 (2022), p. 147. DOI: 10.1140/epjc/s10052-022-10034-4. URL: https://doi.org/10.1140/epjc/s10052-022-10034-4.

[149] T. Huege, M. Ludwig, and C.W. James. “Simulating radio emission from air showers with CoREAS”. In: *AIP Conf. Proc.* 1535.1 (2013). Ed. by Robert Lahmann et al., p. 128. DOI: 10.1063/1.4807534. arXiv: 1301.2132 `[astro-ph.HE]`.

[150] P. Abreu et al. “Advanced Functionality for Radio Analysis in the Offline Software Framework of the Pierre Auger Observatory”. In: *Nucl. Instrum. Meth. A* 635 (2011), pp. 92–102. DOI: 10.1016/j.nima.2011.01.049. arXiv: 1101.4473 `[astro-ph.IM]`.

[151] P. Allison et al. “First Constraints on the Ultra-High Energy Neutrino Flux from a Prototype Station of the Askaryan Radio Array”. In: *Astropart. Phys.* 70 (2015), pp. 62–80. DOI: 10.1016/j.astropartphys.2015.04.006. arXiv: 1404.5285 `[astro-ph.HE]`.

[152] K. Dookayka. “Characterizing the Search for Ultra-High Energy Neutrinos with the ARIANNA Detector”. PhD thesis. University of California, Irvine, 2011.

[153] L. Cremonesi et al. “The Simulation of the Sensitivity of the Antarctic Impulsive Transient Antenna (ANITA) to Askaryan Radiation from Cosmogenic Neutrinos Interacting in the Antarctic Ice”. In: *JINST* 14.08 (2019), P08011. DOI: 10.1088/1748-0221/14/08/P08011. arXiv: 1903.11043 `[astro-ph.IM]`.

[154] Christian Glaser et al. "NuRadioMC: Simulating the radio emission of neutrinos from interaction to detector". In: *Eur. Phys. J. C* 80.2 (2020), p. 77. DOI: 10.1140/epjc/s10052-020-7612-8. arXiv: 1906.01670 `[astro-ph.IM]`.

[155] Gary J. Feldman and Robert D. Cousins. "A Unified approach to the classical statistical analysis of small signals". In: *Phys. Rev. D* 57 (1998), pp. 3873–3889. DOI: 10.1103/PhysRevD.57.3873. arXiv: physics/9711021.

[156] D. García-Fernández, A. Nelles, and C. Glaser. "Signatures of secondary leptons in radio-neutrino detectors in ice". In: *Phys. Rev. D* 102 (8 Oct. 2020), p. 083011. DOI: 10.1103/PhysRevD.102.083011. URL: https://link.aps.org/doi/10.1103/PhysRevD.102.083011.

[157] Xavier Rodrigues et al. "Multi-wavelength and neutrino emission from blazar PKS 1502+ 106". In: *arXiv preprint* (2020). eprint: 2009.04026.

[158] S. S. Kimura et al. "High-Energy Neutrino Emission from Short Gamma-Ray Bursts: Prospects for Coincident Detection with Gravitational Waves". In: *Astrophys. J.* 848 (2017), p. L4. DOI: 10.3847/2041-8213/aa8d14. arXiv: 1708.07075 `[astro-ph.HE]`.

[159] Constantine A Balanis. *Antenna theory: analysis and design.* John wiley & sons, 2015.

[160] Edward Conrad Jordan and Keith George Balmain. *Electromagnetic waves and radiating systems.* Prentice-Hall, 1968.

[161] G. Sinclair, E.C. Jordan, and E.W. Vaughan. "Measurement of Aircraft-Antenna Patterns Using Models". In: *Proceedings of the IRE* 35.12 (1947), pp. 1451–1462. DOI: 10.1109/JRPROC.1947.234570.

[162] Timothy Miller, Robert Schaefer, and H. Brian Sequeira. "PRIDE (Passive Radio [frequency] Ice Depth Experiment): An instrument to passively measure ice depth from a Europan orbiter using neutrinos". In: *Icarus* 220.2 (Aug. 2012), pp. 877–888. DOI: 10.1016/j.icarus.2012.05.028. URL: https://doi.org/10.1016%2Fj.icarus.2012.05.028.

[163] Stephanie Wissel Katie Carter. "Designing HPol Antennas for Radio Neutrino Observatory in Greenland". In: (2020). Presented as a scientific poster as part of the graduation requirements and honors senior project.

[164] D. Southall et al. *Design and Initial Performance of the Prototype for the BEACON Instrument for Detection of Ultrahigh Energy Particles.* 2022. DOI: 10.48550/ARXIV.2206.09660. URL: https://arxiv.org/abs/2206.09660.

[165] SA Wissel et al. "Prospects for high-elevation radio detection of $0 > 10$ PeV tau neutrinos". In: *Journal of Cosmology and Astroparticle Physics* 2020.11 (2020), p. 065.

[166] P. A. Bezyazeekov et al. "Reconstruction of cosmic ray air showers with Tunka-Rex data using template fitting of radio pulses". In: *Phys. Rev. D* 97.12 (2018), p. 122004. DOI: 10.1103/PhysRevD.97.122004. arXiv: 1803.06862 `[astro-ph.IM]`.

[167] A. Aab et al. "Observation of inclined EeV air showers with the radio detector of the Pierre Auger Observatory". In: *Journal of Cosmology and Astroparticle Physics* 2018.10 (Oct. 2018), pp. 026–026. DOI: 10.1088/1475-7516/2018/10/026.

[168] Andres Romero-Wolf et al. “An Andean Deep-Valley Detector for High-Energy Tau Neutrinos”. In: *Latin American Strategy Forum for Research Infrastructure.* Feb. 2020. arXiv: 2002.06475 `[astro-ph.IM]`.

[169] M.L. Ahnen et al. “Limits on the flux of tau neutrinos from 1 PeV to 3 EeV with the MAGIC telescopes”. In: *Astroparticle Physics* 102 (Nov. 2018), pp. 77–88. DOI: 10.1016/j.astropartphys.2018.05.002.

[170] Tonia M. Venters et al. “POEMMA’s target-of-opportunity sensitivity to cosmic neutrino transient sources”. In: *Physical Review D* 102.12 (Dec. 2020). DOI: 10.1103/physrevd.102.123013.

[171] Jaime Álvarez-Muñiz et al. “The Giant Radio Array for Neutrino Detection (GRAND): Science and Design”. In: *Sci. China Phys. Mech. Astron.* 63.1 (2020), p. 219501. DOI: 10.1007/s11433-018-9385-7. arXiv: 1810.09994 `[astro-ph.HE]`.

[172] Stefan Fliescher. “Radio detection of cosmic ray induced air showers at the Pierre Auger Observatory”. In: *Nuclear Instruments and Methods in Physics Research Section A: Accelerators, Spectrometers, Detectors and Associated Equipment* 662 (2012). 4th International workshop on Acoustic and Radio EeV Neutrino detection Activities, S124–S129. ISSN: 0168-9002. DOI: 10.1016/j.nima.2010.11.045.

[173] A. Aab et al. “Nanosecond-level time synchronization of autonomous radio detector stations for extensive air showers”. In: *Journal of Instrumentation* 11.01 (Jan. 2016), P01018–P01018. DOI: 10.1088/1748-0221/11/01/p01018.

[174] R. Prechelt et al. “Analysis of a tau neutrino origin for the near-horizon air shower events observed by the fourth flight of the Antarctic Impulsive Transient Antenna”. In: *Physical Review D* 105.4 (Feb. 2022). DOI: 10.1103/physrevd.105.042001. URL: https://doi.org/10.1103%2Fphysrevd.105.042001.

[175] Roshan Mammen Abraham et al. “Tau Neutrinos in the Next Decade: from GeV to EeV”. In: (Mar. 2022). arXiv: 2203.05591 `[hep-ph]`.

[176] A.G. Vieregg, K. Bechtol, and A. Romero-Wolf. “A technique for detection of PeV neutrinos using a phased radio array”. In: *Journal of Cosmology and Astroparticle Physics* 2016.02 (Feb. 2016), pp. 005–005. DOI: 10.1088/1475-7516/2016/02/005.

[177] Aswathi Balagopal V. et al. “A Surface Radio Array for the Enhancement of IceTop and its Science Prospects”. In: *EPJ Web Conf.* 216 (2019). Ed. by G. Riccobene et al., p. 04004. DOI: 10.1051/epjconf/201921604004. arXiv: 1907.04171 `[astro-ph.IM]`.

[178] K Hughes et al. “Towards interferometric triggering on air showers induced by tau neutrino interactions”. In: *PoS (ICRC2019)* 917 (2019).

[179] Michael W. Eastwood et al. “The Radio Sky at Meter Wavelengths: m-mode Analysis Imaging with the OVRO-LWA”. In: *Astron. J.* 156.1, 32 (July 2018), p. 32. DOI: 10.3847/1538-3881/aac721. arXiv: 1711.00466 `[astro-ph.IM]`.

[180] Steven W. Ellingson et al. "The long wavelength array". In: *Proceedings of the IEEE* 97.8 (2009). Cited by: 137, pp. 1421–1430. DOI: 10.1109/JPROC.2009.2015683. URL: https://www.scopus.com/inward/record.uri?eid=2-s2.0-67651091506&doi=10.1109%2fJPROC.2009.2015683&partnerID=40&md5=00d18ae1849d5b162a46d683855f1f8f.

[181] Arie Voors. *4nec2, NEC based antenna modeler and optimizer.* 2015. URL: http://https://www.qsl.net/4nec2/.

[182] Remcom. *XFdtd 3D Electromagnetic Simulation Software.* URL: https://www.remcom.com/xfdtd-3d-em-simulation-software.

[183] W. D. Apel et al. "LOPES-3D, an antenna array for full signal detection of air-shower radio emission". In: *Nucl. Instrum. Meth. A* 696 (2012), pp. 100–109. DOI: 10.1016/j.nima.2012.08.082. arXiv: 1303.6808 `[astro-ph.IM]`.

[184] Didier Charrier. "Design of a low noise, wide band, active dipole antenna for a cosmic ray radiodetection experiment". In: (Aug. 2015). DOI: 10.1109/APS.2007.4396539. arXiv: 1508.02956 `[astro-ph.IM]`.

[185] S.W. Ellingson. "Antennas for the next generation of low-frequency radio telescopes". In: *IEEE Transactions on Antennas and Propagation* 53.8 (2005), pp. 2480–2489. DOI: 10.1109/TAP.2005.852281.

[186] G. A. Dulk et al. "Calibration of low-frequency radio telescopes using the galactic background radiation". In: *AAP* 365 (Jan. 2001), pp. 294–300. DOI: 10.1051/0004-6361:20000006.

[187] M Schafer et al. *Bringing up OpenSky: A large-scale ADS-B sensor network for research.* Apr. 2014. URL: https://opensky-network.org/about/terms-of-use.

[188] P Allison et al. "Design and performance of an interferometric trigger array for radio detection of high-energy neutrinos". In: *Nuclear Instruments and Methods in Physics Research Section A: Accelerators, Spectrometers, Detectors and Associated Equipment* 930 (2019), pp. 112–125.

[189] Andrew Zeolla et al. "Modeling and Validating RF-Only Interferometric Triggering with Cosmic Rays for BEACON". In: *PoS* ICRC2021 (2021), p. 1072. DOI: 10.22323/1.395.1072.

[190] Yanming Feng and Jinling Wang. "GPS RTK Performance Characteristics and Analysis". In: *Journal of Global Positioning Systems* 7 (June 2008). DOI: 10.5081/jgps.7.1.1.

[191] u-blox. *ZED-F9P, u-blox F9 high precision GNSS module.* English. Version UBX-18010802 R12. u-blox. 2022. 119 pp.

[192] A. Romero-Wolf et al. "An interferometric analysis method for radio impulses from ultra-high energy particle showers". In: *Astropart. Phys.* 60 (2015), pp. 72–85. DOI: 10.1016/j.astropartphys.2014.06.006.

[193] A. Aab et al. "Energy estimation of cosmic rays with the Engineering Radio Array of the Pierre Auger Observatory". In: *Phys. Rev. D* 93 (12 June 2016), p. 122005. DOI: 10.1103/PhysRevD.93.122005.

[194] D Southall et al. “Isolating Cosmic Ray Candidates with the BEACON Prototype”. In: *Contribution to the 2022 Very High Energy Phenomena in the Universe session of the 56th Rencontres de Moriond* (2022).

[195] A Zilles et al. “Radio Morphing: towards a fast computation of the radio signal from air showers”. In: *Astroparticle Physics* 114 (2020), pp. 10–21.

[196] Office of the Federal Register, National Archives and Records Administration. *14 CFR §91.225 - Automatic Dependent Surveillance-Broadcast (ADS-B) Out equipment and use*. Dec. 2020. URL: https://www.ecfr.gov/current/title-14/chapter-I/subchapter-F/part-91/subpart-C/section-91.225.

[197] Office of the Federal Register, National Archives and Records Administration. *14 CFR §91.227 Automatic Dependent Surveillance-Broadcast (ADS-B) Out equipment performance requirements*. Dec. 2020. URL: https://www.ecfr.gov/current/title-14/chapter-I/subchapter-F/part-91/subpart-C/section-91.227.

[198] D Charrier et al. “Autonomous radio detection of air showers with the TREND50 antenna array”. In: *Astroparticle Physics* 110 (2019), pp. 15–29.

[199] Jiwoo Nam et al. “Development of drone-borne aerial calibration pulser system for radio observatories of ultra-high energy air showers”. In: *PoS* ICRC2021 (2021), p. 283. DOI: 10.22323/1.395.0283.

[200] Katharine Mulrey. “Cross-calibrating the energy scales of cosmic-ray experiments using a portable radio array”. In: *PoS* ICRC2021 (2021), p. 414. DOI: 10.22323/1.395.0414.